METAMATERIAL LEAKY-WAVE ANTENNA BASED ON COMPLEMENTARY SPLIT-RING RESONATORS

Stéphanie Eggermont

Thesis submitted in partial fulfillment
of the requirements for the degree of
Docteur en sciences de l'ingénieur

Dissertation committee:
Prof. I. Huynen (ICTEAM, UCLouvain, Belgium), Supervisor
Prof. C. Craeye (ICTEAM, UCLouvain, Belgium)
Prof. F. Martin (Universitat Autonoma de Barcelona, Spain)
Prof. J.-P. Raskin (ICTEAM, UCLouvain, Belgium)
Dr. B. Stockbroeckx (ANPI, Belgium)
Prof. D. Vanhoenacker-Janvier (ICTEAM, UCLouvain, Belgium), President

December 20, 2012

METAMATERIAL LEAKY-WAVE ANTENNA BASED ON COMPLEMENTARY SPLIT-RING RESONATORS

Stéphanie Eggermont
ICTEAM Institute
Ecole Polytechnique de Louvain
ELEN Department



Université catholique de Louvain

Louvain-la-Neuve (Belgium)

To Mathias, Noah and Isalyne,
my nephews and Godchildren, our future

Contents

Acknowledgments xiii

Abstract xvii

Acronyms xix

List of Symbols xxi

Author's Publication List xxiii

1 Chapitre 1 : Introduction 1

1.1 Metamaterial concept in the wireless world 1
1.2 Scope and motivation of this research : Metamaterial Leaky Wave Antenna 2
1.3 Thesis Outline 4
Bibliography 5

2 Chapter 2 : Metamaterial Applications of CSRR 7

2.1 Introduction 7
2.2 Metamaterial Transmission Lines 8
2.3 Complementary Split Ring Resonators 16
2.3.1 Structure and model of the SRR 16
2.3.2 Structure and model of the CSRR 19
2.4 Circuit Applications of the CSRR 22
2.4.1 CSRR Filters 22
2.4.2 Miniaturisation of devices 24
2.4.3 Bandwidth improvement 26
2.4.4 Dual Band devices 27
2.4.5 Tunable devices 28
2.4.6 Nearfield probe 31
2.5 Antennas Applications using CSRR Metamaterial 32
2.5.1 Matching Network 32
2.5.2 Notch-band filter for UWB applications 32

2.5.3 Size Reduction of patch antennas 36
2.6 Conclusion 39
Bibliography 42

3 Chapter 3 : One-Dimensional Periodic Leaky Wave Antenna 47

3.1 Introduction 47
3.2 Radiation in Leaky Wave Antennas 48
3.3 Classification of Leaky Wave Antennas 55
3.3.1 Uniform Leaky Wave Antenna 55
3.3.2 Periodic Leaky Wave Antenna 56
3.3.3 Quasi-Uniform Leaky Wave Antenna 62
3.4 Metamaterial Leaky Wave Antenna 62
3.5 Conclusion 70
Bibliography 72

4 Chapter 4 : Leaky Wave Antenna based on Complementary Split Ring Resonator 75

4.1 Introduction 75
4.2 Leaky wave antenna loaded by double CSRR 76
4.2.1 Transmission line behaviour 76
4.2.2 Leaky wave radiation 81
4.2.3 Effect of edges 96
4.3 Unidirectional CSRR LWA 105
4.4 Tunable CSRR-loaded leaky wave antenna 110
4.4.1 Introduction 110
4.4.2 Concept of the electric tunability 112
4.4.3 CSRR unit cell loaded by BST thin film 113
4.4.4 CSRR unit cell loaded by varactor 115
4.4.5 Conclusion and comparison 124
4.5 Variant of CSRR-loaded LWA : CSRR with a single ring 124
4.5.1 Topology and propagation characteristics 125
4.5.2 Radiation performance 127
4.5.3 Geometrical analysis of CSRRs-loaded LWA 133
4.6 Other candidates of resonant planar LWA 148
4.7 Conclusion 151
Bibliography 153

5 Chapter 5 : Influence of the number of ring on the broadside radiation of CSRRs-loaded LWA 157

5.1 Introduction 157
5.2 Context of the work : Radiation near the broadside 158
5.3 Impact of the distribution of electric current 163
5.3.1 CSRR with two rings in the left-handed region 163
5.3.2 CSRR with two rings in the right-handed region 164
5.3.3 CSRR with one ring in the left-handed region 164
5.4 Impact of the distribution of magnetic current 167
5.4.1 CSRR with two rings in the left-handed region 168
5.4.2 CSRR with two rings in the right-handed region 168
5.4.3 CSRR with one ring in the left-handed region 170
5.5 Application to a balanced CSRR-loaded LWAs 171
5.6 Sensitivity analysis with respect of the distance between rings 178
5.6.1 Analysis of the figures of merit 178
5.6.2 Comparison of radiation shapes 183
5.6.3 Balanced CSRR-loaded LWAs with two split rings 186
5.7 Conclusion 187
Bibliography 189

6 Chapitre 6 : Conclusion and Future Works 191

Bibliography 198

Appendix A: Magnetic Tunability of Metamatreial Leaky-Wave antenna based on nanowired membranes 199

A.1 Introduction 199
A.2 Topology of Ferromagnetic Nanowired Substrate 200
A.3 Frequency tuned leaky-wave behaviour at zero DC magnetic field 200
A.4 Leaky-wave behavior based on external DC magnetic field tuning 202
A.5 Conclusion 202
Bibliography 204

Appendix B: Ferroelectric tunable LWA : first investigation 205

B.1 Introduction 205
B.2 Ferroelectric Materials 205
B.3 Experimental results of BST thin film 209

B.4 Experimental results of ink-jet silver printing on alumina substrate 210
B.5 Conclusion 212
Bibliography 213

Appendix C: Right-Leaky Region of CSRR-loaded TL with one split ring 215

C.1 Introduction 215
C.2 Propagation Characteristics 215
C.3 Radiation Performances 216
C.4 Conclusion 218

Appendix D: Parametric study of CSRR-based LWA 223

D.1 Figures of merit 223
D.2 Width C of the slot 223
D.3 Outer radius R_{out} of the outer ring 226
D.4 Opening W_{out} of the ring 233
D.5 Space e between two cells 238
D.6 Width W of the metal strip line 243
D.7 Size G of the gap 248
D.8 Opening angle χ_1 of the ring 253
D.9 Opening angle χ_2 of the ring 258
D.10 Conclusion 263

Appendix E: Other candidates of resonant planar LWA 273

E.1 Introduction 273
E.2 Nonbianisotropic spiral resonator 273
E.3 Open split ring resonators (OSRRs) 279
E.4 Open complementary split ring resonators (OCSRRs) 280
E.5 Balanced Double-split CSRR 284
E.6 Double-layers complementary split ring resonator 284
E.7 Cascade of non-uniform CSRR cell 284
E.8 CSRR with two gaps 285
E.9 Rotation of CSRR 298
Bibliography 298

Appendix F: Results of COMSOL simulation 305

F.1 CSRR-loaded LWAs with two rings 305

F.1.1 Left-leaky region 305
F.1.2 Right-leaky region 308
F.2 CSRR-loaded LWAs with one ring 311
F.2.1 Left-leaky region 311
F.2.2 Right-leaky region 312
Bibliography 312

Appendix G: Balanced CSRR-based LWA with two rings 317

G.1 Topology and propagation characteristics 317
G.2 Radiation performance 320
Bibliography 322

ACKNOWLEDGMENTS

Tout d'abord, il y a eu quelqu'un qui a cru en moi, qui m'a fait confiance pendant ces cinq longues années, qui m'a appris une méthode de travail, une rigueur, une manière de réfléchir, qui a plus d'une fois consacré ses soirées à mon travail, avec qui j'ai partagé plus que du travail, une visite extraordinaire des couloirs du Vatican par exemple ! Merci, Isabelle Huynen, pour ta disponibilité et ton aide constante. Merci d'avoir eu confiance en moi ! Merci à Danielle Vanhoenacker sans qui, non plus, cette thèse n'existerait pas, merci de m'avoir accueillie dans le service et m'avoir prodigué ta bonne humeur et tes conseils ! Merci de m'avoir accepté dans ton équipe et de m'avoir ouvert les portes du laboratoire ! Je voudrais également remercier vivement tous les membres du jury pour le temps consacré à la lecture de ce travail et leurs remarques lors de la défense privée de cette thèse. Ces commentaires auront contribué à améliorer la qualité scientifique du texte final.

Merci également à la Haute Ecole Louvain en Hainaut d'avoir cru en mon travail, spécialement au directeur Dominique Masy, Paul Lebailly, Jean-Christophe Nutte, Dominique Denis, Sarah Cooper, Philippe Vassaux de m'avoir permis de clôturer ce travail dans les meilleures conditions ! Merci à tous mes autres collègues, je pense à Salvatore, Fabrice, Valérie, Sophie, Stefano, Laurence, Jean-Baptiste, Frédéric, Annick, William, Anne-Marie, Evelyne, Félix (là j'en oublie, c'est que la liste est longue) pour leur aide, leur soutien et leurs conseils !

Merci à Nathalie Maury, à Marc Debliquy, au professeur Maurice Gonon du service Science des matériaux de l'UMONS d'avoir apporté leur temps et leur savoir pour le début d'une collaboration, pour la conception d'une partie de ce travail !

Merci à Pat Chambers pour ta concentration et ton aide, merci pour ta patience lors de tes leçons d'anglais et des nombreuses soirées que j'ai dû te prendre, je ne sais comment j'aurais clôturé ce travail sans ta participation ! Merci à Belen Montenegro-Villacieros pour ta joie de vivre et ta force de caractère, merci de m'avoir soutenue spécialement pendant notre dernière année au labo, merci pour ces pauses de thé glacés ou de barres de chocolat, remplies de fous rires, de voyages incroyables et de fougueux conseils ! Merci à Isabel Molenberg pour avoir partagé mes coups de coeur et de cafard, tes bons conseils techniques et philosophiques ! Merci à Mehdi Simoussa à qui je dédicace tout particulièrement cette thèse car elle ne serait pas là si, lors d'une conférence, tu n'avais pas pris le temps d'en discuter avec moi, merci pour ta bonne humeur et tes mille et un bons conseils, même d'un autre continent !

Merci à David Spôte à qui j'ai pu sans cesse demander un coup de main sans que tu perdes ton sourire et ta bonne humeur en te mettant en quatre pour

trouver LA solution qu'il fallait au moment où il le fallait ! Merci également à Pascal Simon, je pourrai réécrire exactement la même chose, merci pour ta disponibilité constante et la rigueur de ton travail, beaucoup d'étapes auraient été beaucoup plus compliquées sans ton expertise et ton soutien ! Merci à Marie-Christine Vandingenen pour ta disponibilité et ton écoute ! Merci à Robert et Nicolas, même si vous n'êtes plus là, vous m'avez bien aidés tous les deux, chacun à votre manière, à mes débuts ! Je ne peux évidemment oublier Jean-Pierre, Brigitte, Christel, Christian, Pierre, Isabelle, Claude, François, merci à tous ! Merci pour ces moments que vous avez pris pour écouter mes colères ou mes joies, pour votre aide professionnelle ! Plus qu'une équipe efficace, vous avez tous été pour moi une équipe humaine et ça, cela ne peut être oublié ! Merci à Marguerita, à Esther, à Judith, à Carlos, à Maribel, à Dimitri, à Dragosh, à Yann, à Aline, à Pierre, à Nicolas, à Mostafa, à César, à Ibtissem, à Olivier, à Aimad, à Lyazid, à Remy, à Xavier, à Shambdhu et à tous les autres dont j'ai croisé le chemin au moment où il le fallait et que mon stylo oublie !

Merci à Fanny, au professeur Philippe Ancia et au professeur Jean-Pierre Tshibangu de l'UMONs pour votre accueil, pour la petite place que vous m'avez offerte pendant les derniers mois d'écriture !

Merci à Nathalie pour ton soutien sans faille, ton écoute de mes coups de gueule, mes joies et mes peines ! Plus que ne le ferait une soeur, tu m'a épaulée pendant toutes ces années, je ne sais ce que je pourrais faire pour t'en remercier ! Merci également à Eric, à Fanny et Ali, pour les moments de détente d'écoute que vous m'avez apportés ! Merci également à Nadia, Rita et Mark pour l'aide efficace que vous m'avez apportée à la fin de ce travail ! Merci à Annette et Mehdia pour ces repas soleil que nous avons partagés pendant ces années, merci pour votre vue globale, la vue qu'il faut pour retirer le nez du guidon et se rendre compte du chemin que l'on a parcouru ! Merci à Carla et Jorgue, vous nous avez ouvert votre maison, vos connaissances, votre bonne humeur et votre super accueil ! Merci à toute la troupe de Passion et Différences, spécialement à Evelyne et Sophie d'avoir eu la patience de me soutenir et d'accepter mes absences liées à cette thèse !

Merci à Thierry Delmot, Laurent Berti et Damien Macq de m'avoir appris la rigueur et le courage, sans le savoir peut-être, vous avez apporté une énorme brique à ma méthode de travail.

Merci à Christine Leroy, qui en plus de m'avoir soutenue ces trois dernières années, en plus de m'avoir ouvert les portes de sa salle à manger, votre sourire constant et votre écoute m'ont été d'une aide que je ne peux quantifier ! Merci pour ces moments de calme et de concentration !

Merci à ma famille, spécialement à vous, Papa et Maman, de m'avoir supporté, soutenu, consolidé ! Vous avez été là tant dans mes moments de doute que de bonheur, vous mettant en quatre pour m'aider ! On dit qu'une maison ne doit pas se construire sur du sable, vous avez été ma fondation en diamant et ma charpente en acier ! Ce n'est plus un Merci que je peux vous envoyer; cette thèse, je vous la dois, c'est aussi simple que cela !

Les remerciements se terminent souvent par le plus gros, le plus beau, celui qui prend le plus de place, pour ne pas rendre les autres jaloux, je termine par un merci huguesque pour le soutien constant de Gauthier, mon Didou Pinguoin! Plus d'une fois tu m'as remise sur les voix. Plus d'une fois tu as été mon vent dans le dos, plus d'une fois tu m'as réparée de tous les côtés, plus d'une fois tu as été mon coach :-P, me voilà arrivée au Sacré Coeur, pfff... Que la vue est belle et ce grâce à toi ! Merci ! Tu m'as permis de m'épanouïr, même si cela signifiait pour toi un nombre impressionnant d'heures sup, d'encouragements, voir même d'aide au laboratoire où tu m'as plus d'une fois secondée sans émettre un doute quand à ta présence à des heures folles dans un laboratoire d'hyperfréquence... Si ce n'est pas là une preuvre d'amour... Merci!

Merci à toutes et tous, ceux que ma plume oublie de citer...

Sans vous tous, cette thèse ne serait probablement pas là !
Stéphanie

ABSTRACT

These last decades have seen the emergence of the metamaterial concept. Metamaterial structures present physical properties that do not exist in nature. They are especially attractive in the area of microwave RF engineering. In 1968, Veselago proposed the idea of using simultaneous negative permeability and permittivity materials. This concept was then clarified and consolidated in published works from 2000 concerning the topic of these left-handed cells, providing additional degrees of freedom for system designers. They have facilitated : a considerable decrease in the size of microwave components such as filters or couplers, an increase in system bandwidth, useful for ultra wide band applications, an easy insertion of electrical-tunable elements, these elements could influence the physical properties of an antenna with a simple DC voltage applied to the circuit, amongst other things. The focus of this work is on one-dimensional leaky wave antennas (LWAs) using the metamaterial concept. These are wave-guiding structures from which electromagnetic waves leak, as they are guided along their length, in the form of coherent radiation. Using a simple feed for a LWA, this line facilitates full-space continuous scanning with respect to variation in operating frequency.

The metamaterial concept selected in this thesis is the dual of a microstrip line, based on the complementary split ring resonator (CSRR), which is used to load the transmission line and hence permit a full-space continuous beam scanning with frequency. Full wave simulations and measurements in an anechoic chamber demonstrate a particular behavior: radiation seems to be equally split into two different directions resulting in two apparent beams in the plane of the substrate. Clearly, the radiation is not maximal in the broadside direction as predicted by the theory. The objective of this thesis is to understand the physical reasons of this behavior and the influencing parameters of interest. Other resonant structures are also considered, that are similar to the CSRR structure and CSRR-loaded ferroeletric LWA controlled by DC voltage.

ACRONYMS

TL	Transmission Line
RHM	Right-Handed Material
LHM	Left-Handed Material
PLH	Purely Left-Handed
PRH	Purely Right-Handed
CRLH	Composite Right/Left-Handed Material
SRR	Split Ring Resonator
CSRR	Complementary Split Ring Resonator
LWA	Leaky Wave Antenna
CPW	CoPlanar Waveguide
VSWR	Voltage Standing Wave Ratio
PEC	Perfect Electrical Conductor
PMC	Perfect Magnetic Conductor
DPS	Double Positive Material
SNG	Single Negative Material
SW	Surface Waves
VNA	Vector Network Analyser
BST	Barium Strontium Titanate

LIST OF SYMBOLS

ϕ	Complex propagation constant of a wave guided in a waveguide	1/m
β	Propagation constant or phase modal constant of a wave guided in a waveguide	1/m
α	Leakage factor or attenuation constant of a wave guided in a waveguide	1/m
k_0	Free Space Complex propagation constant	1/m
v_p	Phase velocity of a propagating wave	m/s
v_g	Group velocity of a propagating wave	m/s
c	Speed of light	m/s
Z_B	Characteristics Impedance of a Transmission line	Ω
θ_{MB}	Angle of the main lobe of the leaky wave antenna	$^\circ$
S_{11}	Reflection coefficient of the port 1 of the transmission line	—
S_{22}	Reflection coefficient of the port 2 of the transmission line	—
S_{21}	Transmission coefficient from port 1 to port 2 of the transmission line	—
S_{12}	Transmission coefficient from port 2 to port 1 of the transmission line	—
Z_0	Characteristic Impedance	Ω
R_s	Sheet Resistance	$\Omega/\square$
AF	Antenna Efficiency	%

AUTHOR'S PUBLICATION LIST

Journal papers

[1] **S. Eggermont** and I. Huynen, "Influence of Number of Split Rings on the Leaky Radiation of a Metamaterial Transmission Line based on Complementary Split Ring Resonators," *Microwave And Optical Technology Letters*, Volume 54, Issue 4, April 2012, Pages : 867-875.

[2] **S. Eggermont** and I. Huynen, "Leaky wave radiation phenomena in metamaterial transmission line based on complementary split ring resonators," *Microwave And Optical Technology Letters*, Volume 53, Issue 9, September 2011, Pages : 2025-2029.

[3] I. Huynen, N. Quiévy, C. Bailly, P. Bollen, C. Detrembleur, **S. Eggermont**, I. Molenberg, J.M. Thomassin, L. Urbanczyk, T. Pardoen, "Multifunctional hybrids for electromagnetic absorption," *Acta Materialia*, Volume 59, Issue 8, May 2011, Pages : 3255-3266.

Conference papers

[4] **S. Eggermont**, P. Bollen, C. Bailly, C. Detrembleur, I. Huynen, I. Molenberg, J.M. Thomassin, L. Monnereau, N. Quiévy, L. Urbanczyk, T. Pardoen, "Novel Frequency Selective Electromagnetic Absorber Combining Honeycomb Waveguide and Carbon Nanotube Composites," *Proceedings of EUCAP 2011*, Roma, Italy, April, 2011.

[5] **S. Eggermont**, I. Huynen, "Influence of Number of Rings on Radiation of CSRR-Loaded Leaky Wave Antenna," *Proceedings of EUCAP 2011*, Roma, Italy, April, 2011.

[6] N. Quiévy, I. Huynen, C. Bailly, C. Detrembleur, **S. Eggermont**, P. Bollen, I. Molenberg, J.M. Thomassin, L. Monnerau, L. Urbanczyk, T. Pardoen, "Multifunctional Hybrids for Electromagnetic Absorption," *Hybrid Materials 2011*, 6-10 Mars 2011, Strasbourg, France.

[7] **S. Eggermont**, I. Huynen, "Substrate edge effects in leaky-wave antenna based on complementary splitring resonators," *Proceedings of EUCAP 2010*, Barcelona, Spain, April, 2010.

[8] **S. Eggermont**, R. Platteborze, I. Huynen, "Analysis of Radiation in a Metamaterial Leaky Wave Antenna Based on Complementary Split Ring

Resonator," *Proceedings or Metamaterial's 2009*, London, UK, September 2009.

[9] **S. Eggermont**, R. Platteborze, I. Huynen, "Investigation of Metamaterial Leaky Wave Antenna Based on Complementary Split Ring Resonators," *Proceedings of European Microwave Conference*, Roma, Italy, October 2009.

[10] J. Spiegel, **S. Eggermont**, I. Huynen, "Investigation on Ferromagnetic Nanowired Substrates for Leaky-Wave Antennas," *Proceedings of Metamaterial's 2008*, Pampluna, September 2008.

[11] N. A. Ozdemir, **S. Eggermont**, I. Huynen, D. Dancila, "Investigation of A 2-D Lattice of Spiral Resonators and Metallic Strip Wires as a Planar Left-Handed Structure," *Proceedings of Metamaterial's 2008*, Pampluna, September 2008.

[12] **S. Eggermont**, I. Huynen., "Radiation Phenomena in Metamaterial Transmission Line (TL) based on Complementary Split Ring Resonators (CSRRs)," *URSI Benelux Meeting*, Brussel, Belgium, April 2008.

[13] **S. Eggermont**, I. Huynen., "Investigation of radiation phenomena in composite right and left handed (CRLH) transmission line (TL) based on Complementary Split Ring Resorators (CSRRs)," *Proceedings of Young Scientific Metamaterial Meeting 08*, Barcelona, Spain, February 2008.

European Patent

[14] C. Bailly, P. Bollen, C. Detrembleur, **S. Eggermont**, I. Huynen , I. Molenberg, L. Monnereau, N. Quiévy, J.M. Thomassin, L. Urbanczyk, T. Pardoen, "Hybrid material for electromagnetic absorption," *Europeen Patent*, EP10 175 887, Sept 09, 2010.

CHAPTER 1

INTRODUCTION

1.1 METAMATERIAL CONCEPT IN THE WIRELESS WORLD

Nowadays, high-tech companies promise ever more sophisticated technological applications to the consumer. In the home, technologies such as wireless printers, automatic lawnmowers, automatic window shutters or even multi-purpose robots are becoming more and more commonplace. Key to these technologies is the need for highly integrated systems of sensors.

Consider for example even a highly confined environment such as a car, the Volkswagen Golf 6 in 2011 comprised 70 sensors with more than a third of these relying on microelectronic technology [1][1]. However, more luxurious models such as the Audi Q7 v12 TDI comprised 118 sensors[2][1]. An important application of vehicular sensors is combustion control, which is integral in the worldwide drive to reduce carbon footprints. Also, in terms of worldwide research funding, collision avoidance systems, based on radar, are another important technology.

[1]The car sensors comes from microelectronic, micro-optic or micro-mecanic[2]
[2]The contactors are not included in this calculation. The list includes : opening of the door : 6, motor : 30, warming seats : 10, additional heating : 1, air-conditioning : 26, tyres : 4, trunk plate : 9, Autoradio + GPS : 6, directional lighting : 2, direction : 2, Airbag system : 7, ABS : 7, comfort : 6, steering wheel : 2 [1].

Those typical examples ask for efficient techniques ensuring a reliable transfer and processing of the various data collected by multiparametric sensors.

This increase in sensors brings with it an increased requirement for efficient data transfer. Wireless RF technology provides a solution to this because of both the level of sophistication of todays's signal processing techniques for high-speed data transfer as well as the simple fact that it does not rely on cumbersome cabling to establish a connection. A very important aspect of wireless technology is the design of the RF front-end antenna. Antennas play a more and more important role in the economic development of telecommunications in the industrial environmental (sensor network), in the area of transport (GPS, mobile phone, radar...) and in the home (TV receptor, domotic, wireless-LAN...) [3].

The integration of the RF front-end and the antenna has been rendered possible because of microstrip printed technology, which enables the hybrid integration of planar passive RF components, e.g., lines, couplers, filters, low-profile antennas, with the SMD (Surface Mounted Device) digital microprocessor [4]. Significant research on the popular patch antenna started in the 1970s and these low-profile structures can be realized on the same substrate as the RF front-end by using the inexpensive fabrication process known as *photo-lithography technology* [5].

In 1968, **Veselago [6] proposed the idea of using simultaneous negative permeability and permittivity materials** among others to construct microstrip antennas. This work was then clarified and strengthened in published work from 2000 concerning the topic of ***metamaterials***. Circuits based on electromagnetic metamaterials comprise artificial structures that achieve novel electromagnetic, radiofrequency or optical properties. These improvements have answered to the specifications of the miniaturization of the sensor environment nowadays. More specifically, this work addressed the ideas of decreasing the beam squinting for the planar antenna array [7], creating electrically small antennas using a zero-degree phase-shifting line wrapped in a closed loop [8] and improving the antenna gain by suppressing surface waves using the electromagnetic band-gap [3]. Among the metamaterial antennas, leaky wave antennas have been studied and my thesis proposes to go further in this area.

1.2 SCOPE AND MOTIVATION OF THIS RESEARCH : METAMATERIAL LEAKY WAVE ANTENNA

The focus of this work is on **one-dimensional leaky wave antennas (LWAs)**. These are wave-guiding structures from which electromagnetic waves leak, as they are guided along their length, in the form of coherent radiation.

The first leaky wave antenna, invented by W.W. Hansen in 1940 is a simple rectangular waveguide with a long slot. The concept is a wave propagating along an electrically long guiding structure. Radiation phenomena do not depend on a resonating-wave mechanism, indeed the energy is leaked out gradually in the form of coherent radiation, and so creates a sharp directional beams with a fre-

quency scanning over a large bandwidth. Continuous, discontinuous or periodic apertures are realised on the waveguide to allow the radiation. Its advantages are its **inexpensive cost**, due to its simple structure, its **easy integration**, especially for planar printed LWA, its **ability to be flush-mounted on different structures**. This kind of antennas are part to the family of the *travelling waves antennas*, so as the *surface waves antennas*, creating an end-fire radiation and the *slot arrays antennas*, creating a frequency scanning in a narrow bandwidth.

For a planar structure (created on the planar substrate), the radiation pattern beamwidth is fixed by the antenna width. The propagation constant and the leakage factor of the structure establish the beam direction, the beamwidth, the radiation efficiency and the variation of the scan angle with frequency. The main advantage of the LWA compared to the array antennas is the feeding network. Indeed, in a LWA, a single feed point is sufficient, for example a transmission line or a waveguide connection. LWAs can be classified into three basic classes according to the geometry of the antenna : first, an *uniform* geometry along its length, secondly a *periodic* geometry along the length. Finally the last class of LWA is called an quasi-uniform antenna, indeed the geometry is modulated along the length but the period of the modulation is smaller than the guided wavelength of the travelling wave.

Metamaterial LWAs are classified in this last family. By applying Veselago's concept of negative permeability and permittivity, a periodic planar transmission line has been created, which is referred to as a *Left-hand transmission line*. This metamaterial TL is the dual adaptation of the conventional transmission line (TL) model, so a combination of times-unit-length series capacitance and a times-unit-length shunt inductance. The series capacitance can be realized by a inter-digital capacitor or a simple gap, the shunt inductance can be realized by a stub inductance or by a resonant structure. The main interesting properties of this TL is to present a frequency bandwidth in which the phase and the group velocities are anti-parallel. Using a simple feed for a LWA, this line facilitates full-space continuous scanning with respect to variation in operating frequency [9].

The main drawback of the structure presented in [10] is the obligation to realize a *via* through the substrate. This via introduces additional fabrication steps and, above all, resistive leakages. In order to avoid these disadvantages, the authors of [11] have chosen to analyze a transmission line based on Complementary Split Ring Resonators. Indeed this TL produces a similar frequency behaviour with the inductance being etched on the ground plane of the substrate without the existence of a via through the substrate. Two concentric split rings, referred to as a *Complementary Split Ring Resonator*, are etched, for example, on the reverse side of the substrate of a host line to synthesize a left-handed transmission line. This structure can be viewed as an electric dipole excited by an electric field while exhibiting negative values of dielectric permittivity around its resonance.

To my best knowledge, it is the first time that a TL loaded by CSRR is investigated as a leaky wave antenna. The use of this structure for antenna design

purposes could, for example, improve impedance matching issues, filter undesirable frequencies for ultra wide band applications or decrease the size of patch antennas. During this thesis, my investigation demonstrates a particular behavior : radiation seems to be equally splitted into two different directions resulting in two apparent beams in the plane of the substrate. Clearly, the radiation is not maximal in the broadside direction as predicted by the theory. The objective of this thesis is to understand the physical reasons of this behavior and the influencing factors. Another objective concerns the creation of a LWA controlled by a DC voltage, working at one frequency. This concept is obtained by the introduction of ferrolectric film or electronic discrete components. Finally similar resonant structures as non-bianisotropic spiral resonators, open split ring resonators are examined as candidates for metamaterial LWA and compared to the CSRR-loaded LWA.

1.3 THESIS OUTLINE

The structure of this thesis is as follows :

- **Chapter 2** introduces the **metamaterial concept**, with a particular emphasis on the CSRR cell.
- **Chapter 3** presents the state of the art of the **one-dimensional LWAs**.
- **Chapter 4** is focussed on the characteristics of the **transmission line loaded by the CSRR** and its radiation properties. The impact of the **surface waves** on the radiation properties are also described. It introduces the work realized on the LWAs based on the ferroelectric materials, in the aim of creating a **DC-voltage tunable LWA, working at a fixed frequency**. Next, a variant of the CSRR structure, called a **CSRR cell with a single ring**, is presented. Based on this structure, parametric study analyses the influence of fabrication geometry on antenna performance. This work is applied to the synthesis of a novel **balanced LWAs** and these are then validated by experiment. **Other resonant structures** are investigated as a potential candidates to be used in metamaterial LWA topologies.
- **Chapter 5** is devoted to the physical understanding of the radiation behavior of this antenna. Full wave simulation and measurement of the CSRR structure with two rings show, in the left-leaky region, a frequency beam steering simultaneously in the plane of the substrate, ($\theta = 90°$) X-Y plane, and in its normal plane, ($\Phi = 0°$) X-Z plane. The physical explanation comes from the particular current distribution on metal strips and ring slots, which creates a zero in the total radiated field in the broadside direction. A sensitivity analysis w.r.t. the distance between the rings is created to examine the impact of the coupling between rings on the radiation properties of the structure. Indeed the radiation pattern of TL loaded by CSRR

structure with one ring does not present the split into two different directions.

Bibliography

[1] *Elsa Win Software, Official database for diagnostics and repair of Volkswagen, Audi, Seat and Skoda cars, version 3.70*, VAG Group.

[2] R. B. GmbH, *Les capteurs en automobile, Serie jaune, Cahier technique, Electricite et electronique en automobile.* BOSCH, 2002.

[3] F. Yang and Y. Rahmat-Samii, *Electromagnetic Band Gap Structures in Antenna Engineering.* Cambridge University Press, 2008.

[4] K. Gupta and P. S. Hall, *Analysis and Design of Integrated Circuit-Antenna Modules.* John Wiley and Sons Inc Publication, 2000.

[5] D. Pozar, "Microstrip antennas," *Proceedings of IEEE*, no. 1, Jan. 1992.

[6] V. G. Veselago, "The electrodynamics of substances with simultaneously negative values of ϵ and μ," *SOV PHYS USPEKHI*, vol. 10, no. 4, 1968.

[7] G. Eleftheriades and M. Antoniades, *Antenna Applications of Negative Refractive Index Transmission Line (NRI-TL) Metamaterials.* in Balanis C.A. (Ed), Wiley, 2008, ch. Modern Antenna Handbook, pp. 677 – 736.

[8] N. Engheta and W. Ziolkowski, *Metamaterials, Physics and Engineering Explorations.* IEEE Press, Wiley and Sons Inc Publication, 2006.

[9] C. Caloz and T. Itoh, *Electromagnetic metamaterial : Transmission line and microwave applications.* Wiley, 2006.

[10] S. L. C. Caloz and T. Itoh, "A novel leaky-wave retrodirective reflector using short/ matched terminations," *Proceedings of European Microwave Conference*, pp. 1071–1074, Oct. 2003, Munich, Germany.

[11] M. Gil, J. Bonache, J. Garcia-Garcia, and F. Martin, "Composite right/left handed (crlh) transmission lines based on complementary split ring resonators (csrrs) and applications," *Proc. Metamaterials 2007*, pp. 22–24, Oct. 2007, Roma, Italy.

CHAPTER 2

METAMATERIAL APPLICATIONS OF CSRR

METAmaterials are exotic composites that have been engineered to have properties that may not be found in naturally occurring materials [1]. The prefix, '*Meta*', is derived from the Greek word for, '*Beyond*' [2] and examples of such realizable properties include: negative refractive index and cloaking against electromagnetic waves.

Following [2], this unconventional behavior comes from macroscopic composites having man-made, three-dimensional, periodic cellular architecture and are often generated by artificially fabricated inclusions or inhomogeneities embedded in a host medium or connected to or embedded on a host surface. This work concerns the interaction of the metamaterial concept in planar structure domain with antenna applications, more specifically classical leaky wave antenna. The objective of this chapter is to introduce the metamaterial concept and the planar structure used in the rest of this work.

2.1 INTRODUCTION

During the last decade, the microwave field has seen the emergence of metamaterial structures, especially in the area of antenna, offering new technological advances, like, decreasing the size with sub-wavelenght structure [3], improving the directivity of patch antennas [4] or increasing the bandwidth of broadband

UWB antennas. As presented in [5], Caloz's group was the first in 2002 to propose a metamaterial planar periodic structure to improve the performances of leaky wave antennas (LWAs). By the introduction of planar transmission lines loaded with reactive elements named Composite Right and Left Handed (CRLH) transmission lines (TL), the possibility of creating backward and forward scanning LWAs is explored in [5–7], using the left-handed band for backward scanning. Recently, we proposed a CRLH TL based on Complementary Split Rings Resonators (CSRRs) loading a host microstrip line [8] in order to obtain a LWA [9]. First proposed in [10] to create broadband and tunable filters, CSRRs are also used in various microwave applications, e.g. power dividers [11] or hybrid couplers [12], but also for antenna applications for bandwidth enlargement of microstrip patch antennas [13], for band-notched UWB antennas [14] or for size reduction of patch antennas [15].

This chapter is divided in two parts, the first section introduces the concept of metamaterial in the 1D periodic structure. The second section focusses its attention on the complementary split ring resonator and its different microwave applications, especially in the antenna domain.

2.2 METAMATERIAL TRANSMISSION LINES

Circuits based on electromagnetic metamaterials comprise artificial structures that achieve novel electromagnetic, radiofrequency or optical properties. These properties have been unobserved in known naturally occurring materials. Examples of such properties are negative permittivity and permeability. These in turn lead to alterations in the phenomena that are normally governed by Snell's law or that are normally expected due to the Doppler effect [16]. These particular aforementioned materials are called *left-handed materials* (LHMs) and were first identified by V.G. Veselago [17]. Their applications can be found in lenses for high resolution imaging systems, as well as in compact filters and antennas, etc. The goal of this section is to describe how a subwavelength filter may be realized by using a metamaterial adaptation of the conventional transmission line (TL) model. Consider the conventional model for a lossless TL and its *dual*, which are compared in Figs. 2.1(a) and 2.1(b) respectively. As will be seen, an interesting feature of the TL dual is that its physical dimensions are not directly related to the wavelength of the signal that is being propagated along it [5].

In order to describe the TL dual properly, the distinction between '*right-hand*' (or conventional) propagation and '*left-hand*' propagation must be made. To do this, it is necessary to start with some fundamental concepts from electromagnetic theory. Firstly, consider now the permittivity, ε, of a material, which is defined as the ratio of electric displacement D and intensity of the electric field E. It is expressed in Farad per meter [F/m], usually as the product of the vacuum permittivity ε_0 (which is equal to 8.854×10^{-12}F/m) and the relative permittivity ϵ_r (dimensionless) of the material. Similarly, consider also the permeability, μ, of a material, which is defined as the ratio of the magnetic induction B and

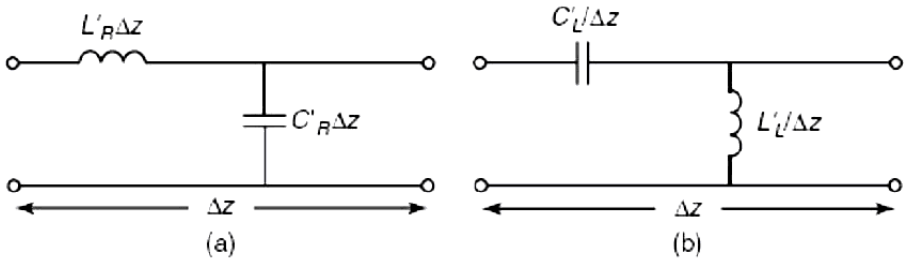


Figure 2.1. *(a) Model of a classical lossless transmission line (named right-handed TL) - (b) Model of the dual lossless transmission line (named left-handed TL) [16].*

magnetic field H. It is expressed in Henry per meter [H/m], usually as the product of the permeability of vacuum μ_0 (which is equal to $4\pi \times 10^{-7}$ H/m) and the relative permeability μ_r (dimensionless) of the material.

The relationships between all of these terms may be expressed from Maxwells equations for monochromatic electromagnetic radiation in vacuum, which can be written as:

$$\vec{k} \times \vec{E}(\vec{r}) = \omega\mu\vec{H}(\vec{r}) \tag{2.1}$$

$$\vec{k} \times \vec{H}(\vec{r}) = -\omega\epsilon\vec{E}(\vec{r}) \tag{2.2}$$

where $\vec{k}$ represents the wave number [rad/m], where $\vec{E}(\vec{r})$ et $\vec{H}(\vec{r})$ represent respectively the electric and magnetic fields and where ω is the frequency [rad/s].

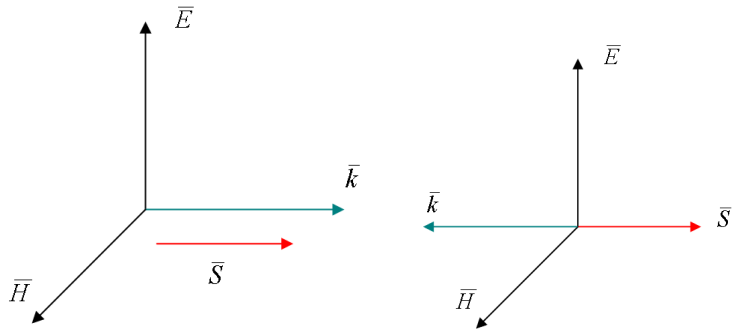
In any normal naturally occurring material, the relative permittivity, ε, and the relative permeability, μ, are both positive. It follows, by observing the equations (2.1) and (2.2) that the triad $(\vec{E}, \vec{H}, \vec{k})$ is in the direct orientation. This type of material is referred to here as a, *right-handed material*, (RHM) and is illustrated in Fig. 2.2(a).

In this configuration, the energy and the wavefronts move in the same direction. This implies vectors of group velocity v_g and phase velocity v_p, which will be defined more precisely later, are parallel in the same direction. The Poynting vector $\vec{S}$ is a vector whose direction indicates the direction of propagation of an electromagnetic wave in an isotropic medium and whose magnitude is the power density carried by this wave. It may be expressed as:

$$\vec{S}(\vec{r}) = \frac{1}{2}\mathbb{R}\left\{\vec{E}(\vec{r}) \times \vec{H}(\vec{r})^*\right\} \tag{2.3}$$

and it should be clear that this vector is parallel to the wave vector $\vec{k}$.

In contrast, in the case of a "left-handed" material (LHM) where both ϵ_r and μ_r are negative [16], equations (2.1) and (2.2) show that the triad $(\vec{E}, \vec{H}, \vec{k})$ is not in the direct orientation (Fig. 2.2(b)) as the vector wave $\vec{k}$ is in opposition [5].



(a) Right-Hand material ***(b)*** Left-Hand material

Figure 2.2. *Representation of the triad ($\vec{E}$, $\vec{H}$, $\vec{k}$) with the Poynting vector $\vec{S}$(red arrow).*

In particular this reflects a phase velocity opposite to that observed previously, however the Poynting vector remains in the same direction as in the case of right handed (conventional) signal propagation.

Finally, note that this triad ($\vec{E}$,$\vec{H}$,$\vec{k}$) is obtained by using the right hand in the event of a "right-handed" material and by using the left-hand in the case of a "left-handed" material, this justifies their name.

We now consider how a classical lossless distributed TL model can be applied to the case of the conventional RHM. This model comprises a combination of a per-unit length series inductance L_R [H/m] and a per-unit length shunt capacitance C_R [F/m] (Fig. 2.1 (a)). This is true in the case where the length of the line is very large compared to the wavelength of [16]. Real inductance and capacitance can be obtained multiplying these values by the line section $\triangle z$ i.e. either $L_R.\triangle z$ and $C_R.\triangle z$. The series impedance per unit meter of the RHM is therefore:

$$Z_R = j\omega L_R \ [\Omega/m] \tag{2.4}$$

Similarly, the shunt admittance per unit meter of the RHM is:

$$Y_R = j\omega C_R \ [S/m] \tag{2.5}$$

with C_R expressed in $[F/m]$.

The TL equivalent to the pure LHM, i.e. the TL dual, will be the combination of a times-unit-length series capacitance C_L [F.m] and a times-unit-length shunt inductance L_L [H.m] (Fig. 2.1 (b)). Real inductance and capacitance will be obtained by dividing these previous values by the corresponding line segment $\triangle z$. The series impedance per unit length of the LHM is therefore:

$$Z_L = 1/j\omega C_L \ [\Omega/m] \tag{2.6}$$

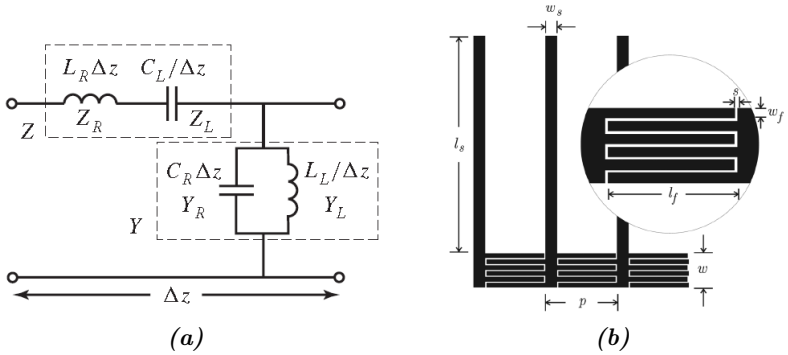


Figure 2.3. *(a) : Model of a CLRH TL dual [5]; (b) : Top View of a TL based on 3 CRLH cells (series capacitance is realized by an interdigital capacitor of six fingers, shunt inductance is realized by a stub line, the different dimensions are defined in [7]).*

Similarly, the shunt admittance per unit length of the LHM is :

$$Y_L = 1/j\omega L_L \ [S/m] \tag{2.7}$$

with L_L expressed in $[H.m]$. The series capacitance can be realized by a interdigital capacitor or a simple gap, the shunt inductance can be realized by a stub inductance (Fig. 2.3(b)).

Having described RHMs and LHMs in some detail, it should now be stipulated that any practical attempt to realize a metamaterial transmission line based on the concept of the TL dual will unfortunately include the creation of an RHM TL component due to the presence of parasitic inductive and parasitic capacitive elements, which would, by definition, not be expected. Thus Fig. 2.3(a) may be thought of as a circuit diagram for the metamaterial transmission line since it depicts what could be described as a realistic lossless TL dual because it comprises both RHM and LHM TL circuits. In effect, the metamaterial transmission line is a *Composite Right and Left Handed* (CRLH) material. The parasitic inductance is due to the fact that currents flow in the upper metallic layers of the capacitive fingers, which in turn create a magnetic flux. Furthermore, the parasitic capacitance is due to the appearance of non-zero potentials that occur between the metallic plates of the inductive stub lines and the ground plane of the material upon which they are printed. As a result of these parasitic components, the total series impedance, Z, and shunt admittance, Y, of the metamaterial transmission

line may be written as:

$$Z = j\left(\omega L_R - \frac{1}{\omega C_L}\right)\ [\Omega/m] \tag{2.8}$$

$$Y = j\left(\omega C_R - \frac{1}{\omega L_L}\right)[S/m] \tag{2.9}$$

Careful inspection of equations 2.8 and 2.9 reveals that in a low frequency regime, i.e. $\omega \to 0$, the series "right-handed" impedance is low, i.e. $Z_R \to 0$, as is the shunt "right-handed" admittance, i.e. $Y_R \to 0$. Thus it may be concluded that the metamaterial transmission line supports left-hand signal propagation at low frequencies. Using a similar analysis, it is trivial to show that in a high frequency regime, i.e. $\omega \to \infty$, the metamaterial transmission line supports right-hand signal propagation.

In order to gain a more detailed insight into the behaviour of the metamaterial transmission line, recall that a transmission line is characterised by a voltage, $V(z,t)$, and a current $I(z,t)$, which are functions of the space along the transmission line itself, z, and time, t (Fig. 2.4). The variations in $V(z,t)$ and $I(z,t)$ are described by the telegrapher's equations, which, in the context of the metamaterial transmission line, may be written as [18]:

$$\frac{dV(z,t)}{dz} = -ZI(z,t) = -j\omega\left(L_R - \frac{1}{\omega^2 C_L}\right)I \tag{2.10}$$

$$\frac{dI(z,t)}{dz} = -YV(z,t) = -j\omega\left(C_R - \frac{1}{\omega^2 L_L}\right)V \tag{2.11}$$

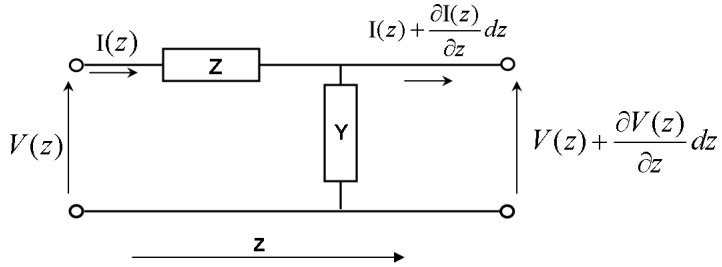


Figure 2.4. *Variation of voltage and current waves along a transmission line modelised by its series impedance and shunt admittance [18].*

By solving the equations (2.10) and (2.11) simultaneously, we obtain the wave equations of second order :

$$\frac{d^2V(z,t)}{dz^2} - \gamma^2 = 0 \tag{2.12}$$

$$\frac{d^2I(z,t)}{dz^2} - \gamma^2 = 0 \tag{2.13}$$

γ is the complex propagation constant, this complex number characterizes the transmission line under consideration. Its expression is:

$$\gamma \cong \alpha + j\beta = \sqrt{ZY}\ [rad/m] \tag{2.14}$$

where α is the attenuation constant (also called the leakage factor in the field of the leaky wave antennas) and β is the propagation constant (also defined as the modal phase constant), α and β are both real numbers. The complex propagation constant is involved in the analytical expression of wave currents and voltages that are solutions of the system of equations (2.12) and (2.13) :

$$V(z) = V_0^+ \exp(-\gamma z) + V_0^- \exp(\gamma z)\ [V] \tag{2.15}$$

$$I(z) = I_0^+ \exp(-\gamma z) + I_0^- \exp(\gamma z) \tag{2.16}$$

$$= \frac{\gamma}{Z}\left(V_0^+ \exp(-\gamma z) - V_0^- \exp(\gamma z)\right)\ [A] \tag{2.17}$$

It remains to define the characteristic impedance, Z_C, that links the modules of the currents and voltages as follows :

$$Z_C(\omega) = \sqrt{\frac{Z(\omega)}{Y(\omega)}}\ [\Omega] \tag{2.18}$$

Based on the equations (2.10), (2.11) and (2.14), the complex propagation coefficient, γ, can also be written [5]:

$$\gamma = js(\omega)\sqrt{\left(\frac{\omega}{\omega_R}\right)^2 + \left(\frac{\omega_L}{\omega}\right)^2 - \kappa\omega_L^2}\quad [rad/m] \tag{2.19}$$

With :

$$\omega_R = \frac{1}{\sqrt{L_R C_R}}\quad [rad/s] \tag{2.20}$$

$$\omega_L = \frac{1}{\sqrt{L_L C_L}}\quad [rad/s] \tag{2.21}$$

$$\omega_s = \frac{1}{\sqrt{L_R C_L}}\quad [rad/s] \tag{2.22}$$

$$\omega_p = \frac{1}{\sqrt{L_L C_R}}\quad [rad/s] \tag{2.23}$$

$$\kappa = L_R C_L + L_L C_R \tag{2.24}$$

$$s(\omega) = \begin{cases} -1 & if \quad \omega < min(\omega_s, \omega_p) \\ 1 & if \quad \omega > max(\omega_s, \omega_p) \end{cases} \tag{2.25}$$

The equations (2.22) and (2.23) represent the resonance frequencies of series and shunt impedances, respectively. It is interesting to note in equation (2.14) that , despite the fact that we had previously assumed a lossless transmission

line (absence of resistance R and reactance G in parallel with respectively L_R and C_R), the complex propagation constant may, depending on frequency, however, be purely real, provided that the term under the square root is negative. Thus, we speak of pass-band when $\gamma = j.\beta$ is purely imaginary (the transmission is possible) and stop-band when $\gamma = \alpha$ is purely real (the signal is attenuated, the transmission is impossible). Computed from (2.19), Fig. 2.5 presents the dispersion diagram (β, ω) and attenuation diagram (α, ω) of a CRLH metamaterial transmission line [5].

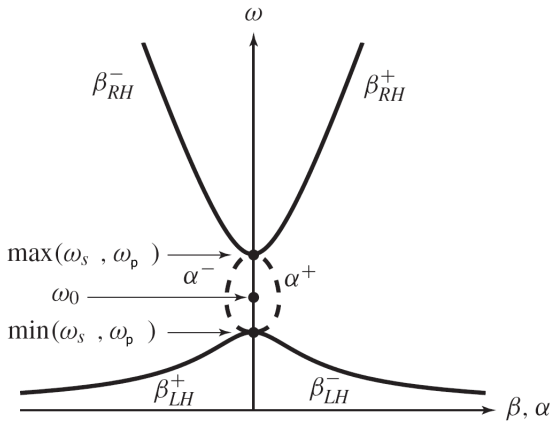


Figure 2.5. *Dispersion (solid) and attenuation (dotted) diagram for a CRLH line computed from (2.19) in the configuration where energy propagates along +z and -z directions. The labels "RH" and "LH" indicate the RH and LH frequency branches, respectively.* ω_s *and* ω_p *are the resonance frequencies of series and parallel impedances , respectively computed from equations (2.22) and (2.23),* ω_0 *is the frequency of maximum attenuation [5].*

Some interesting observations concerning Fig. 2.5 are now highlighted. Firstly, it is clear that the stop-band, where signal transmission is forbidden and where points lying on its curve are defined by a pair (α,ω), is bounded by the terms: max(ω_s,ω_p) and min(ω_s,ω_p). The resonant frequency of maximum attenuation, denoted by ω_0, can be found in the centre of the stop-band, it may be calculated from

$$\omega_0 = \frac{1}{\sqrt[4]{L_R C_R L_L C_L}} \quad [rad/s] \tag{2.26}$$

Also for a pair (β,ω), in the pass-band where signal propagation is allowed, the phase velocity[1], v_p, of a signal being propagated can be calculated by computing the slope of the line drawn between the point defined by the pair (β,ω) itself and

[1] The phase velocity, v_p, also called the velocity of propagation with which energy is propagated, is defined as the ratio of the pulsation, ω, and the propagation constant β [19]

the origin. Furthermore, the group velocity[2], v_g, of the signal being propagated, is computed from the slope of the tangent to part of the curve where the pair (β,ω) lies. Thus, for a LHM (lower curve), both slopes are considered with an opposite sign, the two vectors are in opposition (so they are called anti-parallel) while they have identical signs for the RHM (upper curve), so the two vectors are not in opposition(they are called parallel).

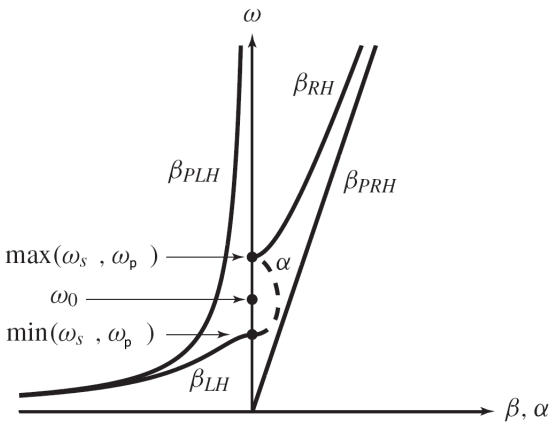


Figure 2.6. *Dispersion (solid) and attenuation (dotted) diagram for a CRLH line, a pure left-handed line (β_{PLH}) and a pure right-handed line ((β_{PRH})) computed from (2.19) in the configuration where energy propagates along +z direction. The labels "RH" and "LH" indicate the RH and LH frequency branches, respectively. ω_s and ω_p are the resonance frequencies of series and parallel impedances, respectively computed from equations (2.22) and (2.23), ω_0 is the resonance frequency of maximum attenuation [5].*

Fig. 2.6, for its part, presents the dispersion curves of a CRLH line compared to the dispersion curves of a purely left-handed (PLH) and purely right-handed (PRH) lines. It should be noted that the dispersion curve of the CRLH line approaches the dispersion curve of a PLH line for $\omega \to 0$ while it approaches the dispersion curve of a PRH line for $\omega \to \infty$.

A final feature visible on the attenuation diagram should be set as it will be useful when the antenna design will be considered. This concerns whether or not the circuit, which in turn makes up the material, can be deemed *balanced* or not. Balanced circuits/materials are defined as having parallel and series resonances that occur at the same resonance frequency. Alternatively, the circuit/material is said to be *unbalanced*.

[2]The group velocity, v_p, is the phase velocity of the wave envelope [20]. An observer has to move along the line with this velocity to observe the envelope of a modulated signal with a constant phase [21]. The phase and group velocities are different in a dispersive media. [20]

To conclude here, the design of a band-pass filter comprising subwavelength components has been described in this section. The filter is based on the concept of the TL line dual. The device itself is a metematerial transmission line, which was further concluded to be a CLRH material due to the presence of the TL dual itself along with its associated parasitics. This device is useful because the unusual frequency dependence of the guided wavelength and the (low-frequency, anti-parallel)/(high-frequency,parallel) existing between the phase and the group velocities in CRLH structures, any CRLH applications of this concept will be presented later in this section and in the next chapter.

2.3 COMPLEMENTARY SPLIT RING RESONATORS

The main part of this work is based on a metamaterial structure called *Complementary Split Ring Resonator* (CSRR), the planar complement and dual of the more well-known subwavelength resonator called the *Split Ring Resonator* (SRR). This section will introduce briefly the SRR and CSRR behaviour and different applications of the CSRR in the microwave domain, especially in the area of antenna design.

2.3.1 Structure and model of the SRR

The *Split Ring Resonator* (SRR) structure shown in Fig. 2.7(a) was proposed by Pendry to create metamaterial medium [22] and was reworked by the group of Martin for microstrip lines. This particular approach is referred to as a *resonant-type metamaterial transmission lines* based on sub-wavelength resonators [23]. These resonators consist of two concentric split rings, printed on a conventional dielectric substrate at microwave frequencies. When impinged upon by a magnetic flux varying in time directed along the Z-axis, the cutting of each ring causes a current to go from one ring to another through the spacing between the two rings, taking the form of a strong displacement current to occur between the two rings [23]. The slots between rings therefore behave as a distributed capacitance. Near the resonance, the particle reacts to an external magnetic field not only as a strong magnetic dipole, but also as a strong electric dipole. Indeed, when the SRR particle is excited at resonance, charges in the upper half of the SRR particle must be the images of charges at its lower half, as shown in Fig. 2.7(a). So two parallel electric dipoles directed along the y-axis are generated at each SRR half ring. Following this statement, the SRR resonance can also be excited by an external electric field directed along the y-axis. To summarise, the basic SRR topologies exhibit cross-polarization effects. This means that both SRRs and CSRRs can be magnetically and/or electrically excited if the rings are properly oriented [24].

The lossless model of the SRR structure is given in Fig. 2.7(b), the inductance represents the self-inductance of the metallic strips of the split rings and the capacitance represents the capacity between the two lines of each half-ring. It is valid as long as the perimeter of the ring can be considered small with regard

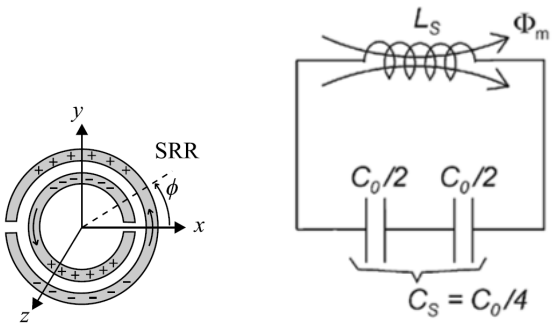


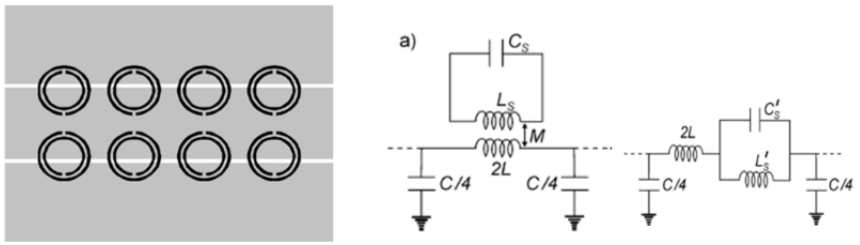
Figure 2.7. *(a) : Representation of the structure named Split Ring Resonator (grey color represents the metallic strips); (b) : LC model of SRR [23].*

to a half-wavelength, and the capacitance associated with the cuts on each ring can be neglected.

Similarly to the dual transmission line approach, these resonators are used as loading elements, they are etched for example on the reverse side of the substrate of a host line to synthesise a left-handed transmission lines. Resonant-type metamaterial transmission lines also exhibit a composite right/left-handed (CRLH) behavior [23]. Fig. 2.8(a) presents a CoPlanar Waveguide (CPW) line loaded with SRRs with the aim of obtaining a material with negative effective permeability in a certain frequency band above the resonance of the SRRs. The location and the direction of the SRR are chosen in such way that the magnetic field generated by the current flowing through the line exhibits a significant component in the axial direction of the rings, achieving a high magnetic coupling.

Due to the small electrical dimensions of SRRs at resonance, the CPW loaded lines can be described by means of lumped-element equivalent circuits [24]. The equivalent model of the structure is included in Fig. 2.8(b), L and C are the inductance and capacitance per unit length of the line, the SRR is modeled by an LC resonant circuit (with inductance L_s and capacitance C_s) magnetically coupled to the line by a mutual inductance M. Simplifications can be applied to this equivalent circuit, the simplified equivalent model is given in Fig. 2.8(c). [24] shows that the dispersion diagram of the CPW TL loaded by SRR has the characteristics of a stopband around the resonance frequency of the SRR with a level of rejection that depends on the number of SRR pairs etched in the line.

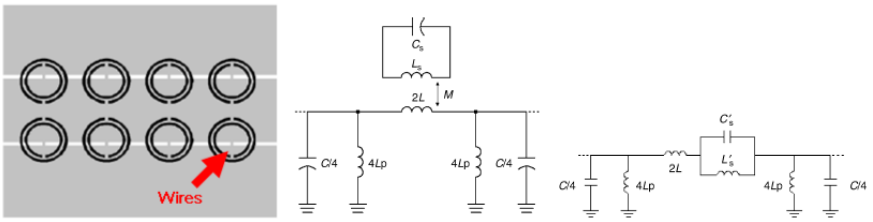
This aforementioned stopband can be switched to a passband by periodically inserting metallic strips between the central CPW strip and ground planes, as shown in Fig. 2.9(a). These additional strips make the structure behave as a microwave plasma with a negative effective permittivity below the plasma frequency. The effect of the resonators coupled to the coplanar waveguide, together



(a) *(b)* *(c)*

Figure 2.8. *(a) : Representation of a CPW line loaded by SRR structures; (b) : Equivalent π-circuit model of the SRR loaded negative permeability TL; (c) : Circuit model that results after transformation of the series branch (grey color represents the metallic layer of the CPW line, black color represents the metallic layer of the SRR in the backside of the susbtrate) [24].*

with the metallic strips acting as shunt inductances, gives rise to a LH transmission band around the resonance frequency of the resonators, where the series reactance is capacitive and the shunt reactance is inductive. The equivalent model, shown in Fig. 2.9(b), is the same as the previous structure, except the metallic strips modelled by L_p. Simplifications can be applied to this equivalent circuit, the simplified equivalent model is given in Fig. 2.9(c), we can now compare this scheme to the structure of CRLH TL illustrated in Fig. 2.3(a).



(a) *(b)* *(c)*

Figure 2.9. *(a) : Layout of the fabricated SRR loaded CPW structure with shunt metal strips, forming a left-handed SRR-based TL where it has been found that by aligning the slits of the SRRs with the wire shorts, an optimum result in terms of in-band losses is obtained (grey color represents the metallic layer of the CPW line, black color represents the metallic layer of the SRR in the reverse side of the susbtrate) [24]; (b) : Equivalent π-circuit model of the SRR loaded negative permeability TL; (c) : Circuit model that results after transformation of the series branch [23].*

2.3.2 Structure and model of the CSRR

Resonant-type artificial transmission lines can also be implemented with complementary split-ring resonators (CSRRs). These resonators can be excited by a time-varying electric field. In order to ensure such excitation, CSRRs are generally etched on the ground plane of a microstrip line [25].

The SRR structure presented in the previous paragraph has its complement. This dual structure is called a *Complementary Split Ring Resonator* (CSRR), also known as a *slotted split-ring resonator* or a *dual split-ring resonator* and it is shown in Fig. 2.10. The shape of the SRR is used to create slots in the ground plane, replacing the metal parts of the original structure with slots, and the slots with metal plates. This negative image of the SRR presents electromagnetic properties that are almost the dual of those of the SRR. Due to symmetry considerations, it can be demonstrated that if the thickness of the metal plate is zero and its conductivity is infinity, i.e. has the characteristics of a perfect electrical conductor, then the slots behave as perfect magnetic conductors [23]. According to the principle of Babinet, in such complementary structures, electric and magnetic fields, currents, etc. interchange their roles [25]. So if the SRR structure can be viewed as a resonant magnetic dipole, excited by an axial magnetic field structure, then CSRR can be viewed as its dual, i.e as an electric dipole that resonates at the same frequency and can be excited by an electric field while exhibiting negative values of the dielectric permittivity around its resonance. By etching the complementary rings in the ground plane under a signal strip, a significant component of the electric field results parallel to the rings axis, as desired, to excite the CSRR.

The model of the CSRR, shown in Fig. 2.10 is also composed of a LC resonant circuit. The inductance, L_S, of the SRR structure (Fig. 2.7(b)) is replaced by a capacitor, C_C, created by a disk, of radius equal to $r_0 - c/2$, surrounded by the ground plane at a distance c from its edge, where r_0 is the averaged radius, shown in Fig. 2.7(b). The two series capacitances, $C_0/2$, of the SRR model are replaced by two shunt inductances, $L_0/2$. These shunt inductances are the inductances per unit length of the two coplanar lines connecting the inner disk to the ground plane [23].

A left-handed TL can be created from a classical microstrip line loaded with CSRR cells to create a material with negative permittivity but, as was seen previously, it is also necessary to add a second element to provide the negative permeability to create backward propagation. This element can be a capacitive gap or an interdigital capacitor etched on the microstrip line just above the CSRR. These gaps or interdigital capacitors make the structure behave as a magnetic plasma, with negative valued permeability up to a frequency that depends on the resonator formed by the gap capacitance and the per-unit inductance of the line. A basic cell is presented in Fig. 2.11(a) and can be modeled by the equivalent circuit of Fig. 2.11(b). The inductance of the microstrip line is represented by L and the CSRR by the parallel combination of L_c and C_c, as shown in Fig. 2.10. The gap is modelled by the capacitance, C_g. Also, the

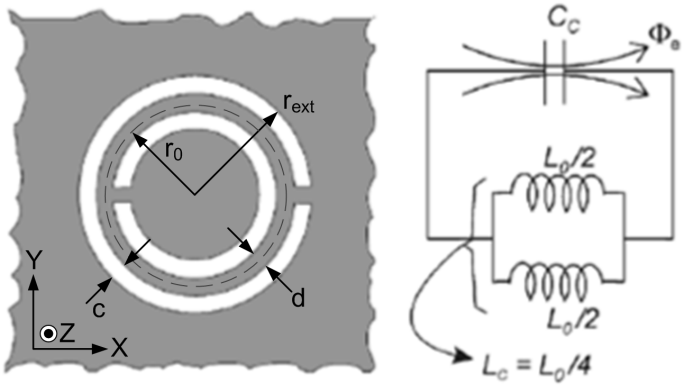


Figure 2.10. *3D view and LC model of the Complementary Split Ring Resonator (grey color represents the metallic layer) [23]*

coupling that occurs between the line and the resonator is modelled separately by the capacitance C [3]. The LH TL can be realized by the cascade of several of these elementary cells as shown in Fig. 2.11(c). The transmission and reflection characteristics of this line will be presented in more details in the third chapter of this work.

From the T-model of Fig. 2.11(b), we can extract the propagation properties of the LH TL. From [26], we can compute the phase shift ϕ and the characteristic impedance, Z_0 of the unit cell :

$$cos\phi = 1 + \frac{Z_s(j\omega)}{Z_p(j\omega)} \tag{2.27}$$

$$Z_0 = \sqrt{Z_s(j\omega)(Z_s(j\omega) + 2Z_p(j\omega))} \tag{2.28}$$

where Z_s and Z_p are respectively the series and shunt impedance of the T-model. Applied to Fig. 2.11(b), the expression of those impedances are [27]:

$$Z_s = j\omega\frac{L}{2} + \frac{1}{j\omega 2C_g} \tag{2.29}$$

$$Z_p = \frac{1}{j\omega C} + j\omega\frac{L_c}{1 - \omega^2 C_c L_c} \tag{2.30}$$

Similarly to the section 2.2, we can define the series resonance ω_s and the shunt resonance ω_p as [25]:

$$\omega_s = \frac{1}{\sqrt{LC_g}} \tag{2.31}$$

$$\omega_p = \frac{1}{\sqrt{L_c C_c}} \tag{2.32}$$

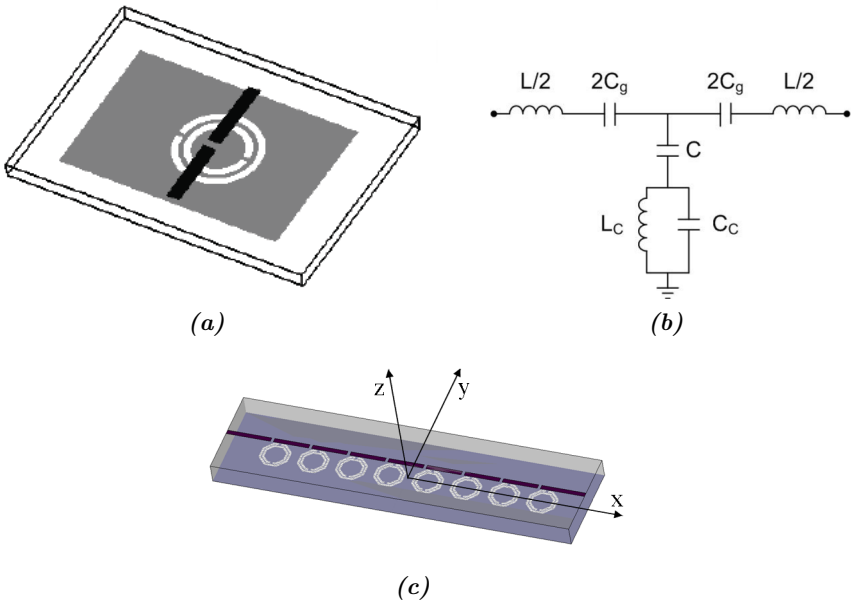


Figure 2.11. *(a) : 3D view of a unit cell of microstrip line loaded by CSRR and gaps (black color represents the upper metallic layer of the microstrip line, grey color represents the metallic layer of the ground plane) [25]; (b) : Equivalent T-model of microstrip line loaded by CSRR and gaps [23]; (c) : 3D view of the cascade of 8 elementary cells (black color represents the upper metallic layer of the microstrip line, mauve color represents the metallic layer of the ground plane).*

As already presented in section 2.2, these two frequencies define the limit of the upper left-handed and lower right-hand band limits : the lower one is the upper limit of the left-handed band, the larger one sets the lower limit for the right-handed band. The lower limit of the left-handed band is defined by ω_L, calculated in [23] as :

$$\omega_L = \frac{1}{\sqrt{L_c(C_c + (\frac{4}{\frac{1}{C_g}+\frac{4}{C}}))}} \tag{2.33}$$

In addition, we have also to define the transmission zero frequency [25] as :

$$\omega_z = \frac{1}{\sqrt{L_c(C_g + C)}} \tag{2.34}$$

These definitions allow us to calculate the characteristic impedance and the propagation constant as follows :

$$cos\phi = 1 + \frac{C}{C_g}\frac{(1-\omega^2 C_g L)(1-\omega^2 C_c L_c)}{1-\omega^2(C_c+C)L_c} \tag{2.35}$$

$$Z_0 = \sqrt{\frac{L}{C}\frac{\omega^2-\omega_s^2}{\omega^2} + \frac{L}{C_c}\frac{(\omega^2-\omega_s^2)}{(\omega^2-\omega_p^2)} - \frac{L^2}{4}\frac{(\omega^2-\omega_s^2)^2}{\omega^2}} \tag{2.36}$$

These parameters are shown in Fig. 2.12 for the unit cell represented in Fig. 2.11(a). The comparison with Fig. 2.6 shows that the resonant-type TL has all conditions to be a theoretical CRLH TL, presenting left-handed and righ-handed bands. A significant aspect of the CSRR structure is the fact that equations 2.35 and 2.36 depend on five parameters, namely the five reactive elements depicted in Fig. 2.11(b). As presented in [10], it is also possible to create a balanced structure by fixing ω_s equal to ω_p (shown in Fig. 2.13(a)).

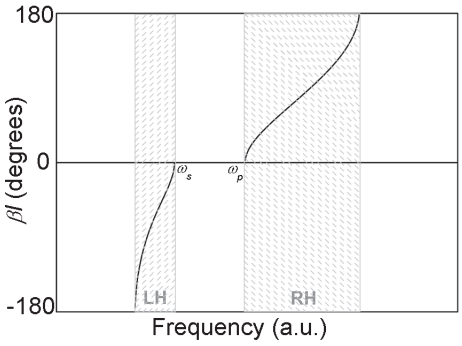
2.4 CIRCUIT APPLICATIONS OF THE CSRR

As discussed previously, CSRRs are miniature resonant structures that can facilitate both left-hand and right-hand propagation and whose design parameters can be engineered in such a way as to influence the properties of the metamaterial TL with more degrees of freedom compared to classical TL. The focus of this section is to describe further microwave applications of CSRRs where a number of advantageous features of CSRR-based components will be highlighted. These features are: very sharp frequency responses for effective filter design, component miniaturization for the design of power dividers or antennas, increased bandwidth of operation for microwave coupling devices and nearfield probes. Along with these, the ability to construct with CSRR structures dual-band power dividers with reasonably arbitrary frequencies of operation and efficient tunable microwave devices. It should be noted that similar properties can also be achieved with the more conventional SSR structure however this work focuses primarily on the more recent CSRR structure with only occasional mention of the SSR case. Thus for more detailed discussions of these properties in relation to the SSR, the interested reader is referred to [3, 12, 23, 25].

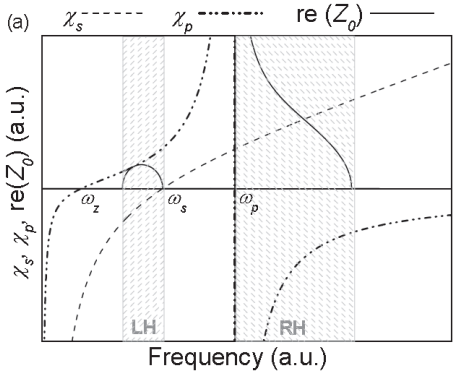
2.4.1 CSRR Filters

Any resonant type of TL is a frequency-selective structures by nature. As a result, the first types of applications using CSRR as particles in one-dimensional metamaterials concerned the design of compact microwave filters. They could be narrowband, wide-bandpass and reconfigurable filters.

The first applications of sub-wavelength resonators to the design of filtering microwave devices consisted in their use to load a host transmission line to create a stop band centred on various desired frequencies. Using the narrow band with



(a)

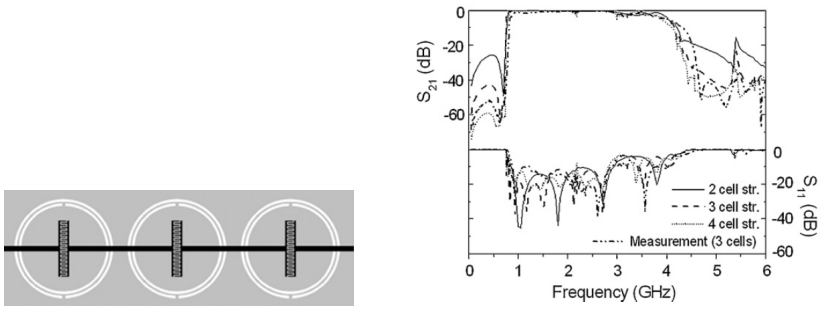


(b)

Figure 2.12. *(a) : phase shift of the unit cell shown in Fig. 2.11(a) calculated from 2.35; (b) : impedance characteritic Z_0, series χ_s and parallel χ_s reactances of the unit cell shown in Fig. 2.11(a) calculated respectively from 2.36, 2.29 and 2.30 ; series (ω_s) and shunt (ω_p) resonance frequencies and zero transmission frequency (ω_z) are defined in equations 2.31, 2.32 and 2.34 [25].*

left-hand propagation, transmission lines simply loaded with SRRs or CSRRs are able to inhibit signal propagation in a narrow band in the vicinity of resonance. Indeed the single left-handed SRR- or CSRR-loaded lines exhibit highly selective stop-bands with a rejection level depending on the number of stages. The resonators can be tuned to reject the signal at slightly different frequencies and, thus, give rise to a rejection band with a certain bandwidth, which can be to some extent controlled with the number of resonators. But the control of the width of the stop-band unfortunately depends on the distance between adjacent resonators, because inter-resonator coupling enhances this width.

As bandpass structures, the artificial lines with negative permeability and negative permittivity of Fig. 2.11(a) and Fig. 2.13(a) (showing a balanced case) also exhibit some limitations. Namely, the typical frequency responses measured on these left-handed lines are very selective at the lower edge of the band, due to the presence of a transmission zero, but the transition band is smooth at the upper band edge, as shown in Fig. 2.13(b) [3]. The frequency response is thus asymmetric. It should also be highlighted that the bandwidth cannot be easily controlled and it is difficult to achieve wide bands. However the approaches outlined in [3], [25] and [23], among others, do present different modifications to improve the performances of these types of filters for specific applications such as the ultra-wideband (UWB) protocol.



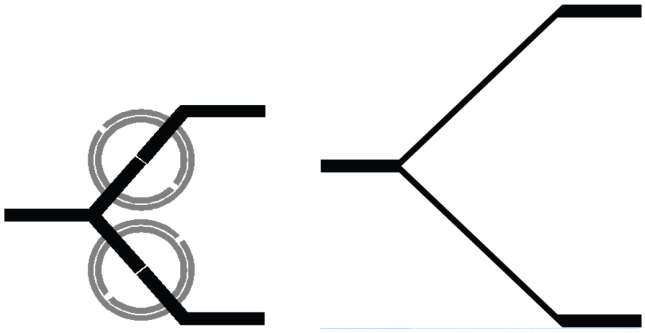
(a) *(b)*

Figure 2.13. *(a) : Topology of balanced TL loaded by 3 CSRRs for high pass filtering structure (grey color represents the metallic upper layer, black color represents the metallic layer of the ground plane); (b) : S-parameters for balanced TL of Fig. 2.13(a) loaded by different numbers of CSRRs cells, showing that left-handed lines are very selective at the lower edge of the band but the transition band is smooth at the upper band edge [3].*

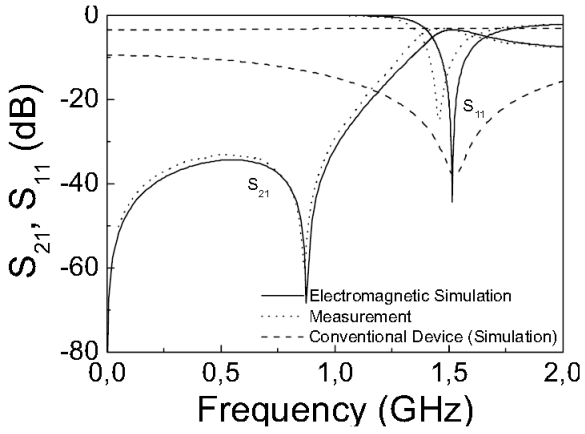
2.4.2 Miniaturisation of devices

An example of **miniaturization** of microwave devices based on subwavelength resonators is the Y-junction power divider based on CSRR shown in Fig. 2.14(a). This narrow-band device is composed of two 90° impedance inverters with a phase shift of 90° and with an impedance characteristics of $\sqrt{2}.Z_0$, where Z_0 is the reference impedance of the ports, equal to 50 Ω, so the impedance characteristics of the inverters must be equal to 70.7 Ω. Conventional devices are shown in Fig. 2.14(b) on a classical RF substrate, the length of two lines is equal to 21 mm. CSRR-based structures are optimised to obtain the same electrical characteristics, but the length of the inverter is 12.9mm, which represents a significant miniaturisation of 50% [11]. The simulated and measured frequency

responses of both topologies are shown in Fig. 2.14(c). They exhibit similar loss levels at the design frequency, thus the miniaturization does not affect the device perfomances at the desired frequency but does however reduce significantly the operational bandwidth as careful inspection of Fig. 2.14(c) reveals.



(a) *(b)*



(c)

Figure 2.14. *(a) : Topology of CSRR-based power divider; (b) : Topology of classical power divider (grey color represents the slots created in the ground plane, black color represents the upper metallic layers); (c) : Simulated and measured frequency responses of the power dividers based on the CSRR topology of Fig. 2.14(a) and based on conventional topology of Fig. 2.14(b) [11].*

2.4.3 Bandwidth improvement

Contrary to the previous example, miniaturization does not always mean a reduction of the bandwidth. Consider a rat race hybrid coupler, which is a four-port network with a phase shift of 180° between the two output ports [26]. A conventional topology is shown in Fig. 2.15(b). A signal at one desired frequency is applied to port 2 where it is then split into two in-phase components at port 3 and port 4, and port 1 will be isolated. If this signal is applied now to port 1, it will be split into two components at port 3 and port 4 with a phase difference of 180°, port 2 will be isolated. So to make a rat race hybrid, four line sections have been realised with fixed phase-shift.

The principle used in metamaterial structure to obtain a compact broadband microwave component is based on the possibility of fixing independently the phase-shift ϕ_n and the group delay v_p of a metamaterial structure. In conventional lines, the dispersion diagram is simply a straight line with the slope given by the phase velocity v_p of the line. This phase velocity depends on the geometry of the microstrip TL and the expression for the phase shift of a classical line is the following [23]:

$$\phi_n \quad = \quad \beta.l = \frac{\omega_n}{v_p} \tag{2.37}$$

where l is the length of the line and ω_n is the desired frequency. The bandwidth is the frequency interval in which the difference between the phase shift and its nominal value is smaller than a predetermined value. So following 2.37, the bandwidth is directly linked to the derivative of the phase, also known as the group delay. Thus in order to obtain broad bandwiths, a short line length is inevitably required. Ultimately however, the line length is imposed by the desired phase-shift.

In a CSRR-based device, it is possible by an optimisation of the four reactive elements of the model of Fig. 2.11(b) to fix a desired phase shift at the operating frequency with a phase velocity as small as possible, thus facilitating quite a short line length. The topology is presented in 2.15(a). The metamaterial counterpart of this coupler can be implemented by substituting the 270° ($3\lambda/4$) line section by the CSRR-cell structure of Fig. 2.11(b) designed to provide the required characteristic impedance (70.7Ω) and phase (-90°) at the operating frequency. By replacing the line section of 270° with a left-handed line section of -90°, the dispersion diagram has been controlled to make the phase difference between lines remain almost constant over a wider range [12]. The three others ($\lambda/4$) line sections are implemented also with the CSRR-based devices designed to provide the required characteristic impedance (70.7Ω) and phase (+90°) at the operating frequency, so working in their right-handed band. Power splitting, isolation and matching of the metamaterial hybrid are similar to the ones of a conventional one. The improvement of the bandwidth is validated by the analysis of the phase balance, $\phi(S_{41}) - \phi(S_{31})$ shown in Fig. 2.15(c) and $\phi(S_{42}) - \phi(S_{32})$ shown in Fig. 2.15(d). The phase balance variation with frequency is smaller for

the CSRR-based hybrid and hence the operating bandwidth is enhanced with size reduction by a factor of 3.

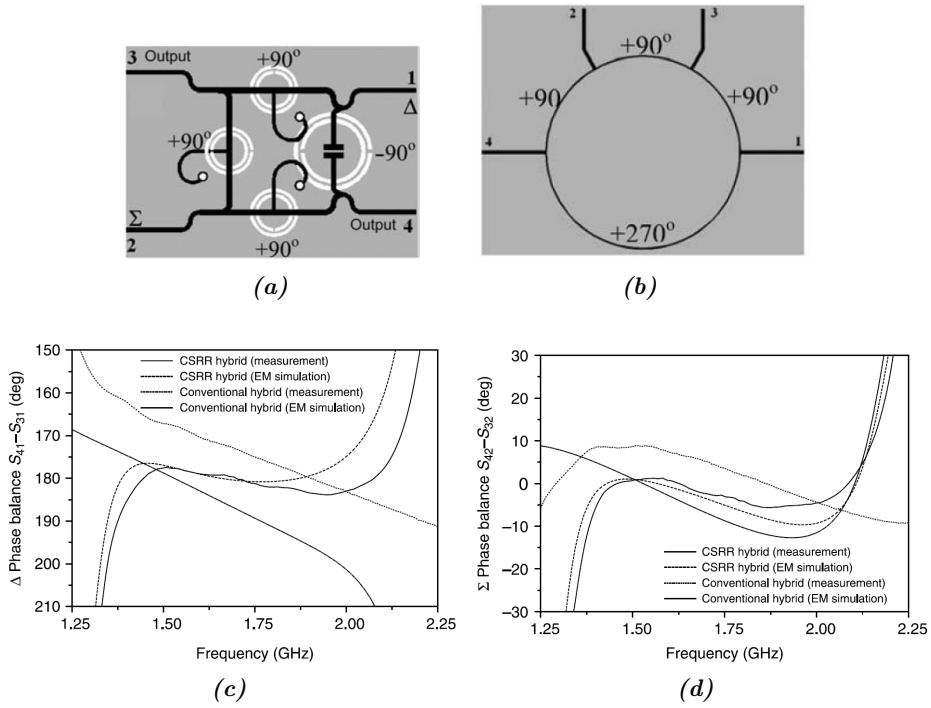


Figure 2.15. *(a) : Topology of CSRR-based rat-race Hybrid Coupler; (b) : Topology of conventional rat-race Hybrid Coupler (grey color represents the metallic layer of the ground plane, black color represents the upper metallic layers); (c) : Comparison of the measured and simulated phase balance* $\phi(S_{41}) - \phi(S_{31})$ *for the metamaterial and conventional rat-race Hybrid Coupler shown respectively in Fig.2.15(a) and in Fig.2.15(b); (d) : Comparison of the measured and simulated phase balance* $\phi(S_{42}) - \phi(S_{32})$ *for the metamaterial and conventional structureshown respectively in Fig.2.15(a) and in Fig.2.15(b) [23].*

2.4.4 Dual Band devices

Having clarified the concepts of left and right hand propagation previously, the manipulation of the dispersion diagram to facilitate dual-band operation at reasonably arbitrary frequencies is now considered. The main principle behind this device is the fact that the four independent parameters described by the model outlined in Fig. 2.11(a) can be engineered so that the device itself has two independent pass-bands. [28] has presented a dual-band. Fig. 2.16(a) presents

the structure with the required phase ϕ_1 = -90°, ϕ_2 = 90° and characteristic impedances (Z_1, Z_2) both equal to 35.35 Ω at the two frequencies of interest (f_1, f_2). f_1 and f_2 are chosen respectively in the left-handed band and in the righ-handed band. Thus we have 4 imposed conditions with 5 unknowns based on relations 2.35 and 2.36. The measured and simulated S-parameters, shown in Fig. 2.16(a), present good performance for matching and power splitting with a broad bandwidth at the upper frequency. The length of a conventional Y-junction power divider operative at the first frequency and fabricated in the same substrate is 31.4 mm, against 17.7 mm for the metamaterial divider. So this concept combines size reduction of factor two and dual-band use. This principle can be also applied to create dual-band rat-race hybrid coupler or power splitter [29].

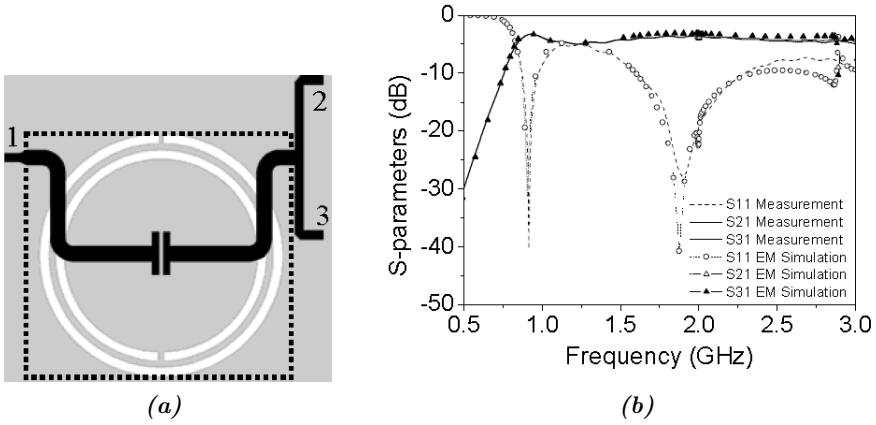


Figure 2.16. *(a) : Topology of CSRR-based Dual-Band Y-junction power divider; (b) : Comparison of the measured and simulated S-parameters for the metamaterial dual band power divider shown in Fig.2.16(a) [28].*

2.4.5 Tunable devices

Previous to this, the engineering of the lumped components of the metamaterial structure has been the primary focus of device construction and engineering. In contrast here, the addition of other components to the lumped structure, such as varactor diodes, ferroelectric capacitors or microelectromechanical (MEMS) will be described whose principle function will be seen to be that of electrical tuning. The combination of a planar SSR structure with a varactor diode placed between its inner and outer ring is presented [30]. In [31], its CSRR counterpart is shown in Fig. 2.17(a); a varactor diode C_{var} and a lumped capacitance C_L is added to the structure of Fig. 2.11(a) (without gaps in the upper metal to create a stopband fiter) between the internal and external metallic regions of the

CSRR. The second series capacitance is used for the polarisation of the diode and its value must be higher than the maximum achievable capacitance of the varactor diode. The model of this new structure is presented in Fig. 2.17(b). In addition to C_{var} and C_L, the model comprises L_V, the inductance of the vias and R_D, taking to account the varactor losses. Fig. 2.17(c) shows the simulation and the measurement of a TL loaded by 3 varactor-loaded CSRRs for different bias voltage with a tuning range of 45%. The bias voltage has the effect of decreasing the value of C_{var}, but at the same time increases the in-band losses.

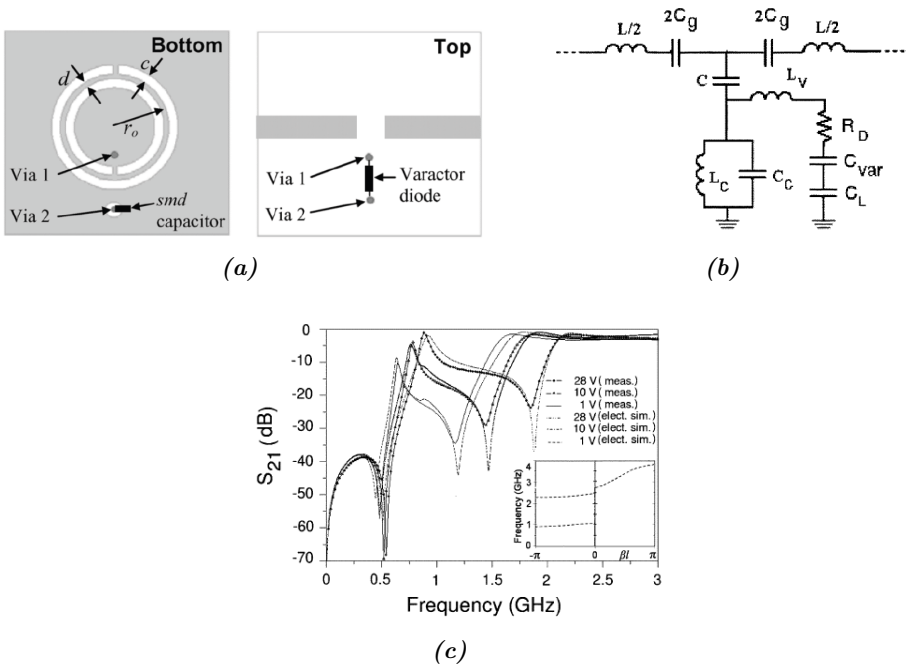


Figure 2.17. *(a) : Topology of the varactor-loaded CSRR (left : view of the ground plane, right : view of the upper metallic layer, grey color represents the metallic layer) ; (b) : lumped equivalent model of the unit cell of varactor-loaded CSRR of Fig. 2.17(a); (b) : simulation and measurement of S_{11} parameter of TL loaded by 3 unit cells of Fig. 2.17(a) for different diode-bias voltages [31].*

It is also possible to consider coplanar waveguide structures (CPWs) loaded with complementary split-ring resonators and can be tuned with the addition of MEMS switches which, when properly biased, allow the modification of the resonance frequency of the CSRRs. In place of electronical lumped element, [32] proposes a solution based on integrated RF-MEMS bridges. The rectangular shaped CSRR is etched onto the central strip of a CPW and RF-MEMS are placed on top of them and uses an electrically floating bridge anchored directly

on the substrate in holes of the CPW ground planes, as depicted in Fig. 2.18. Its voltage evolves freely between those applied to the strip and ground planes of the CPW. A representation of the tunable notch filter operating at Q-band are given in Fig. 2.18(a). The central frequency of the stop-band is varied between 39 and 48 GHz (Q-band), for corner actuation voltages of 17V (called down-state, the bridge is in idle-state) and 0V (called up-state, the bridge is actuated), as illustrated in Fig. 2.18(d).

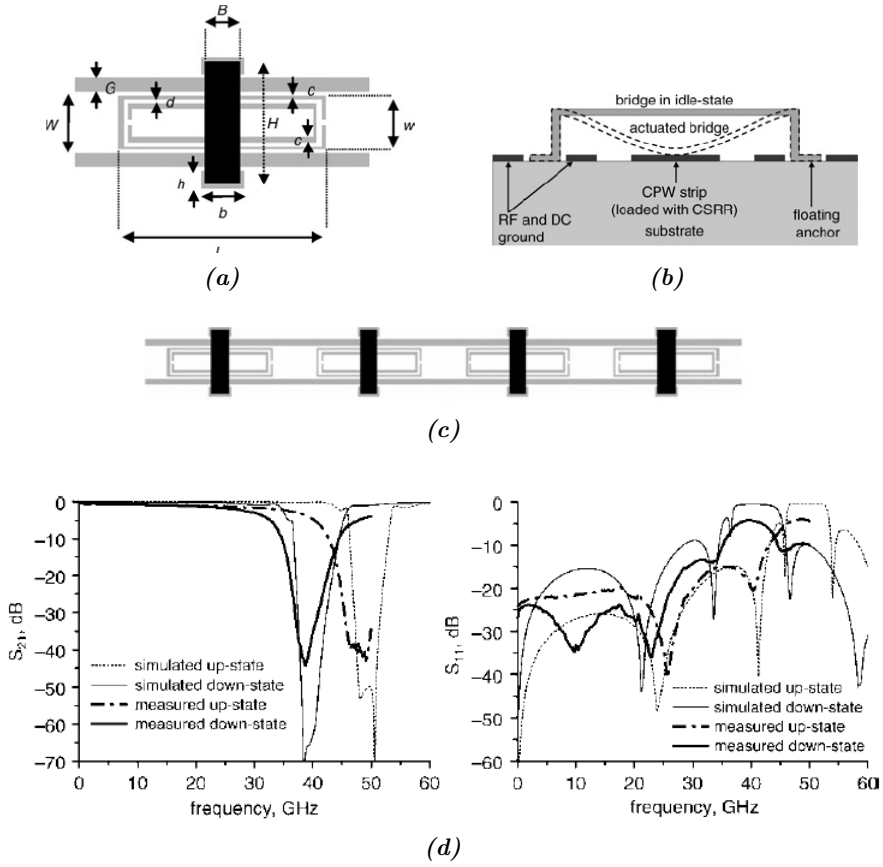


Figure 2.18. *(a),(b) : Topology and cross-section of the MEMs-loaded CSRR cell; (c) : Topology of the CPW loaded by 4 MEMs-loaded CSRR cell; (d) : simulation and measurement of S parameter of CPW loaded by 4 unit cells of Fig. 2.18(a) for different bias voltages [32].*

2.4.6 Nearfield probe

This last application, described in [33], concerns the use of metamaterial planar structure as a nearfield probe or detector. Various resonators included CSRRs and SRRs etched on the ground plane of a microstropline (Fig. 2.19(a)) are considered for LC resonant structures. The subwavelength particule creates a high field confined in an electrically small volume. The resonance frequency and the amplitude and the phase of the scattering parameters of the TL based on CSRR are direct images of the shape (Fig. 2.19(b)), size or permittivity of the sample placed under it. The small dimension of CSRR increases the probe resolution.

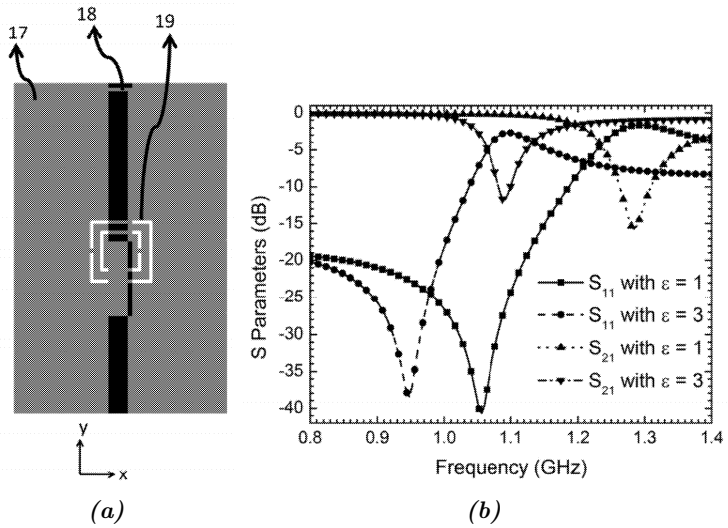


Figure 2.19. *(a) : Excitation structure for CSRR sensor (CSRR* ***19*** *etched on the ground plane* ***17*** *of a microstripline* ***18****); (b) : S-Parameters of Fig. 2.19(a) for different relative permittivity of the sample under test placed under the CSRR [33].*

2.5 ANTENNAS APPLICATIONS USING CSRR METAMATERIAL

Having focused previously on a broad range of applications for CSRR metamaterials, this section focuses primarily on their usefulness in the domain of antenna design. Three specific applications will be considered. Firstly, it will be shown how they can be applied to the problem of improving impedance matching in an antenna matching network. Further to this, their application to the construction of a notch-band filter for UWB antenna applications is discussed. Finally, the usefulness of CSRRs in reducing the size of planar antennas is described.

2.5.1 Matching Network

In [13], it is shown how a CSRR may be used as an RLC network to improve the impedance matching with the aim of increasing the bandwidth of a planar antenna (Fig. 2.20). The impedance matching is achieved by creating a network of two stages. The first stage consists of a series reactance to form a series RLC locus on the Smith Chart. This is implemented by modifying the length of the transmission-line between the base of the monopole and the second stage of the matching network. This has the effect of adjusting the reactance of the monopole. The second stage, which is based on a transmission line loaded by CSRR, forms a loop on the Smith Chart that brings the impedance locus below the given VSWR level by cancelling out the susceptance at two separate points using a shunt inductance and capacitance. The correspondence between the geometry and the equivalent circuit are as follows: the size of the CSRR is proportional to the total shunt inductance and capacitance of the LC resonator. Also the dimensions of the microstrip line are proportional to the shunt capacitance. The position of the CSRR relative to the edge of the ground plane adjusts the amount of transmission line between the strip and the CSRR, which affects the frequency at which the antenna is matched. By tuning the size of the CSRR and the microstrip dimensions, the CSRR can be used to cancel out the appropriate amount of susceptance to form the desired loop on the Smith Chart. Furthermore by adjusting the location of the CSRR, the desired frequency band can be matched. The authors of [13] developed a simple LC model for the CSRR and Fig. 2.21(a) shows the comparison between the modelled and measured S parameters. [34] uses the exact same principle to create a dual-band microstrip feed line antenna by taking advantage of the right-handed and left-handed behaviour of the CSRR (Fig. 2.21(b)).

2.5.2 Notch-band filter for UWB applications

Unlike the previous case, the CSRR will now be used to eliminate a given bandwidth by using its transmission zero characteristic. In the context of the ultra wide band (UWB) protocol (high data-rate, low-cost, low power consumption and easy connection among a large number of multimedia devices), antennas are broadband with a bandwidth between 3.1 and 10.6 GHz with a compact size,

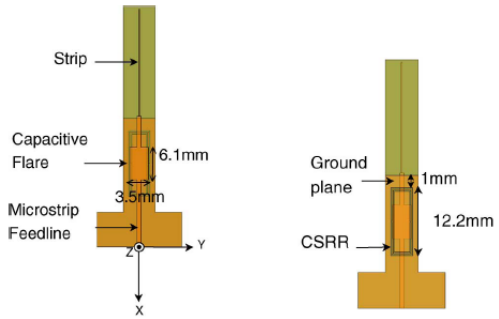
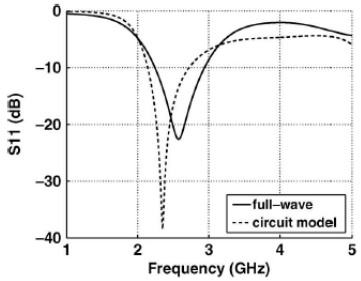
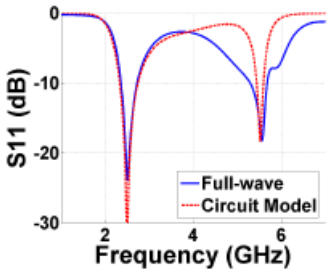


Figure 2.20. *Schematics of the microstrip feed line antenna with a CSRR-microstrip matching network with dimensions, (a) : Top view with coordinate system, (b) : Bottom view [13].*



(a) Microstrip feed line antenna of Fig. 2.20(a) [13]

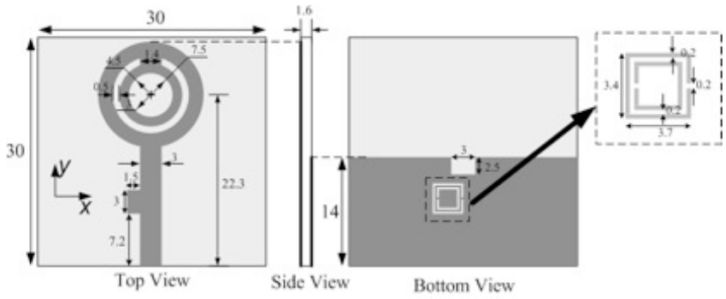


(b) Dual-band microstrip feed line antenna Antenna [34]

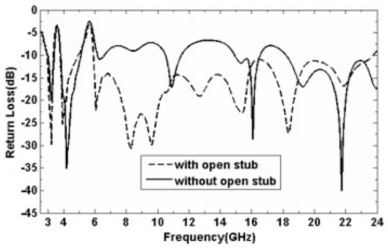
Figure 2.21. *S_{11} parameter of the simulated monopole and matching network compared to the S_{11} parameter found using the circuit model.*

a low cost with a non-dispersive, omnidirectional radiation pattern and a relatively uniform gain. However to avoid unwanted interferences, UWB antennas have to be blind to other nearby narrow-band communication systems working in the same bandwidth, as for example IEEE 802.11a Wireless LAN in Europe in the frequency band of 5.15-5.825 GHz or IEEE 802.16 WiMax operating in frequency band of 3.3-3.6 GHz. Etched with different geometries on the patch or the ground of the antennas, the CSRR, by virtue of its subwavelength size and its resonance properties, is a good candidate for this kind of notch-band rejection [14, 35–43].

From [35], Fig. 2.22(a) presents a UWB antenna where two notch-bands are easily achieved by etching a C-shaped slot in the annular patch and by etching a CSRR structure in the ground plane. The radiation component is an annular patch with a C-shaped slot that is fed by a 50 Ω microstrip line. CSRR slots in the ground plane, together from the open stub extended from feed line, can achieve band-stop filtering property at 5.5GHz with good out-off-band flatness (Fig. 2.22(b)). Adding CSRR to reject possible interferences with other communication systems for UWB applications is also presented in [37], where the behaviour of a monopole antenna is modified by a transmission line loaded with CSRR. However in contrast to what has been outlined in [37], the approach of [35] also proposes improvements in the return loss by the addition of a capacitive load in the form of an open circuit stub. Also in [35], the positioning of the CSRRs is adjusted such that there is an improvement in the shape of the response of the stop-band. The schematic pertaining to this adjustment is shown in Fig. 2.23. To summarise, CSSR can be considered as an UWB filter [44].



(a) Geometry (unit:mm) [35]



(b) Simulated return loss [35]

Figure 2.22. *Dual band-notched UWB antenna based on CSRR (in (a), dark grey region depicts the metal layer, light grey region depicts the substrate layer).*

Another approach is the elliptical-slot antenna with 5.2 GHz/5.8 GHz band-notched characteristics, which is proposed in [36] (Fig. 2.24(a)). The elliptical-slot design facilitates a wider workable bandwidth than the circular-slot design.

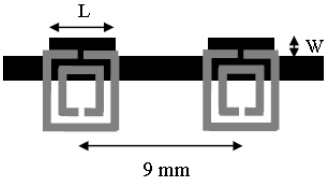
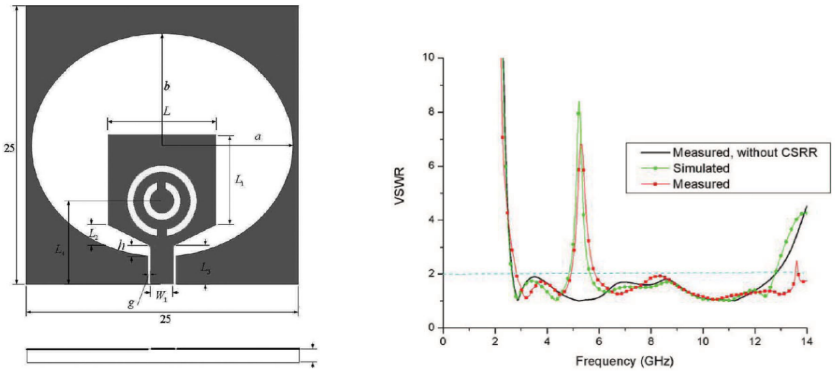


Figure 2.23. *Layout of CSRR-microstrip structure adding to a monopole antenna for UWB application (the dark and grey regions represent the microstrip line and CSRRs etched in the ground plane, respectively) [37].*

Notch-band filtering is achieved by embedding CSRR slots on the radiative patch. The centre frequency of the notch-band filter can be changed by adjusting the radius of the CSRR. Inside the elliptical slot, there is an embedded foursquare patch, which can be truncated to two right-angled triangles. The elliptical-slot antenna itself is fed by a 50Ω microstrip line, which connects to an SMA connector, and two feed lines with a gap on each side to form a transmission line with 50Ω characteristic impedance. This structure uses the property that CSRR creates the strongest resonance when parallel polarization occurs, where the parallel polarization means that the E-field is aligned parallel with the x-y plane and the H-field is aligned with the center axis z of the CSRR. The resonance frequency is tuned with the average of circumferential length of the CSRR, i.e. fabricating the CSRR to have a certain average circumference is how the resonant frequency is set. The measured and simulated voltage standing wave ratio (VSWR) for this proposed elliptical-slot antenna are shown in Fig. 2.24(a). Details of this antenna structure may also be found in [14, 39, 41].

Further to this, an approach is presented [38, 40, 42] where similarly the CSRR is applied to UWB antenna design but where there are four notch-bands in the antenna frequency response. A schematic of the design approach is presented in Fig. 2.25(a) [38]. The resonators in this study have co-directional split ring gaps to make possible a compact UWB antenna. A coplanar waveguide (CPW) feed is applied to the antennas, the first notch-band is realised by embedding symmetrically the CSRRs in this antenna feed location. To achieve the second notch-band, the antenna employs a CSRR which has a split gap at the bottom part of the radiative patch. The third and fourth notch-bands are realized by the inner ring and outer ring of the CSRR being placed at the bottom of the monopole antenna. The measured and simulated VSWRs are plotted in Fig. 2.25(b). By applying three co-directional CSRRs, the minimized mutual coupling among each nocth-band can be achieved. Because of this specific topology, it is also possible to load the monopole antenna with a quadruple notch-band filter in order to create a compact antenna with a single-layer of substrate and a single sided metal plane. The benefit of this approach is a simpler fabrication process at a moderate cost price.



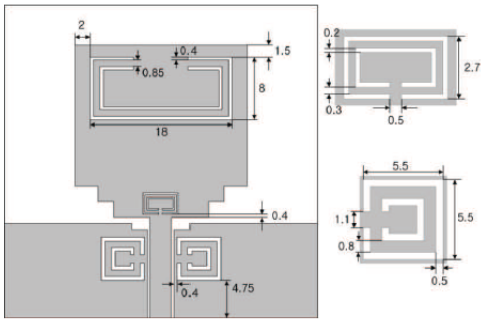
(a) Geometry [36] *(b)* Simulated and measured VSWR [36]

Figure 2.24. *UWB elliptical-slot antenna with 5.2 GHz/5.8 GHz band-notched characteristic (in (a), dark regions represent the metal layer).*

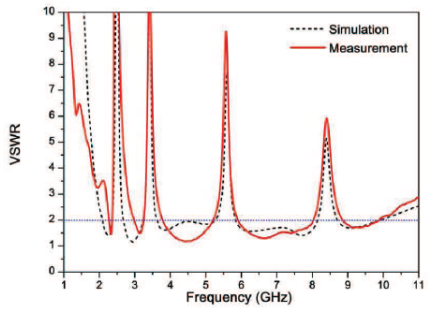
2.5.3 Size Reduction of patch antennas

The last kind of CSRR application concerns the size reduction of patch antennas [45–50]. Based on the idea of the metamaterial subwavelength cavity presented in [51], the patch in [45] is constructed as a 1D cavity from a combination of a classical double positive substrate (DPS - with positive permittivity and positive permeability) and a single negative substrate (SNG - with negative permittivity) between two perfectly conducting layers. Negative permittivity has been achieved by placing CSRRs in the ground plane of the microstrip antenna. A level of return loss has been achieved in these antennas equivalent to that would be normally observed in antennas twice their size as a result of implementing the CSRRs in this manner. The presence of the CSRRs does however create more backside radiation, but [15] presents methodology to minimize it.

In [46], the CSRR structure is applied to microstrip patch antennas to decrease their size with the aim of realizing compact antennas with improved impedance bandwidth. The ground plane is loaded with CSRRs, which behave as an electric dipole excited by an axial electric field and exhibit strong dispersion near the resonance frequency reducing the guided wavelength significantly. The solid metal ground plane is replaced with a ground plane with periodically etched CSRRs (Fig. 2.27(a)). The CSRR loaded antenna shows higher backside radiation resulting in a reduced broadside gain. It is also observed that more ripples are introduced in the antenna pattern and the cross polarization level is increased. In spite of this conclusion, the fabricated antenna achieves a 69% reduction in the resonant frequency compared to other antennas of equivalent size as well as 67% improvement in the bandwidth compared to more conventional antennas.



(a) Geometry (unit:mm) [38]

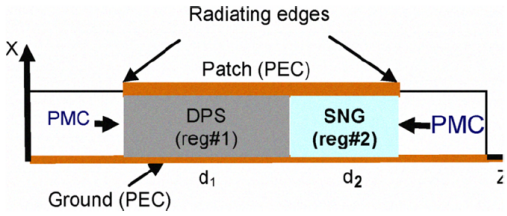


(b) Simulated and measured VSWR [38]

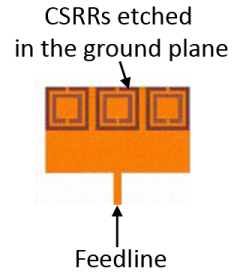
Figure 2.25. *Quadruple-band rejection ultra-wideband (UWB) antenna with three co-directional CSRRs (in (a), grey regions represent the metal layer).*

Likewise, [49] presents a loaded circular patch antenna using multiple CSRRs (Fig. 2.28(a)). The metal ground plane is replaced with etched ground plane with one CSRR. The antenna is excited by a coaxial feed. The operation frequency is selected to be the frequency at which the CSRR shows resonant behavior. The circular patch antenna of the same dimension without CSRR in the ground operates at 6.7 GHz as illustrated in Fig. 2.28(b). The CSRR-based structure is giving an area reduction of 83% as compared to conventional circular patch antennas.

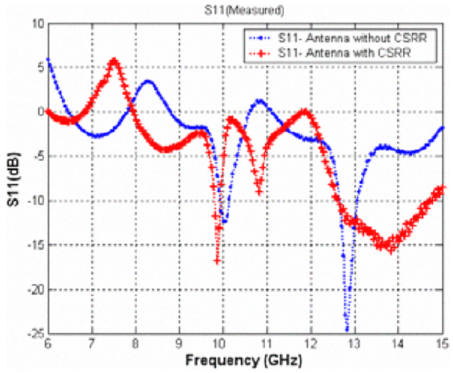
Another approach to size reduction in patch antennas is presented in [50]. Here, an open-ended transmission line is loaded by an interdigital capacitor and a CSRR at resonant frequencies under $\beta.d = m.\pi$ conditions. Recall that β is the propagation constant of the TL whereas d is size of the CSRR unit cell, m is an integer. These conditions allow for the formation of standing waves on the TL. The proposed CRLH resonant antenna and its measured and simulated



(a) Schematic View [45]



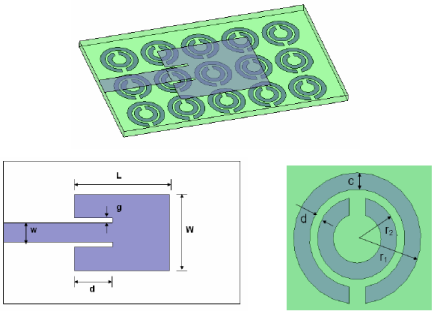
(b) Planar Layout of configuration [45]



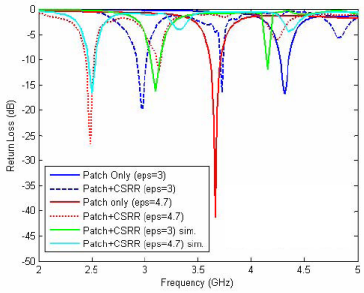
(c) Measured return loss [45]

Figure 2.26. *CSRR loaded microstrip patch antenna using phase compensation (in (a), grey region on the left represents the double positive substrate (DPS), blue region on the right represents single negative substrate (SNG), brown region represents the metal layer. In (b), brown region represents the shape of the metal layer of the patch, the black regions represents the slots etched in the ground plane, playing the role of the single negative substrate).*

reflexion characteristics are shown respectively in Fig. 2.29(a) and in Fig. 2.29(b). A quarter-wave transformer is inserted between 50Ω feed line and the patch for impedance matching. The footprint area of the proposed antenna is 72% smaller than that of a conventional patch antenna with a geometrical tunability of the resonance frequency. Even though the peak gain is 3 dB lower than that of a conventional one, the radiation efficiency is the same, and the proposed antenna has omnidirectional radiation pattern.

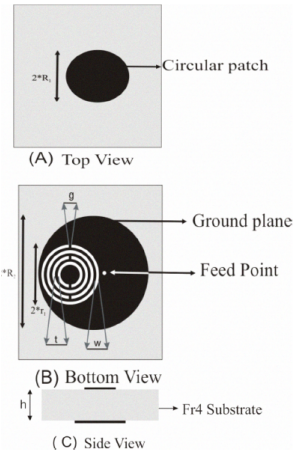


(a) Geometry [46]

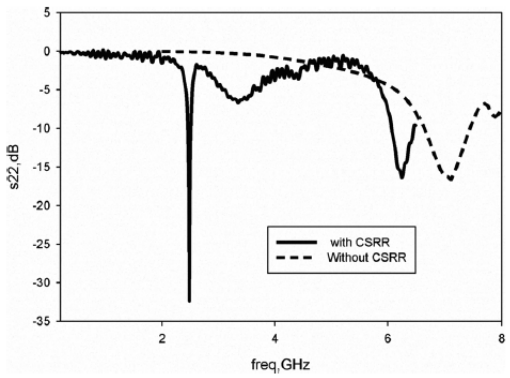


(b) Measured return loss [46]

Figure 2.27. *CSRR loaded microstrip patch antenna (in (a), green region represents the substrate layer, grey regions represent slots etched in the ground plane, blue region represents the upper metal layer of the patch antenna).*



(a) Geometry [49]

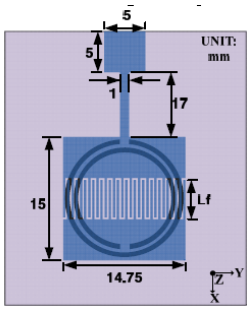


(b) Reflection characteristics of antenna with and without CSRR [49]

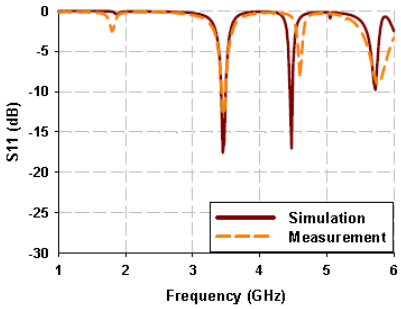
Figure 2.28. *Circular patch antenna loaded by multiple CSRR (in (a), black regions represent the metal layer, grey regions represent the substrate layer).*

2.6 CONCLUSION

This chapter focused on a particular metamaterial structure known as the complementary split ring resonator (CSRR). It has first introduced the concept of left-hand propagation where a wave phase velocity is in opposition to the direc-



(a) Geometry of [50]



(b) Reflection characteristics [50]

Figure 2.29. *CRLH resonant antenna (in (a), light blue region represent the upper metal layer, dark blue regions represent the slot etched in the ground plane, grey regions represents the substrate layer).*

tion indicated by its Poynting vector. This phenomenon was seen to occur when the positions of the conventional lumped components of the lossless transmission line model were interchanged. Thus left-hand propagation is facilitated when an artificial structure or metamaterial, comprising a number of series capacitances and shunt inductances, is created. Owing to this, this structure is referred to as the transmission line dual. Furthermore, in reality such a structure has parasitic elements that in fact allow the right-hand or conventional propagation. Therefore, such a metamaterial may thus be described as a composite left/right hand (CLRH) material.

The CSRR is in fact an example of a cell of CLRH material whose left and right hand propagation characteristics can be readily engineered and may be implemented as a microstrip. CSRRs offer a number of advantageous degrees of freedom such as size reduction due to the small electrical size of their constitutive elements, improved workable of bandwidth, multi-band operation due to the left and right handed propagation. Also advantageous is the fact that the CSRRs can be combined with other electrical components to facilitate ease of electrical tuning. CSRRs were also seen to provide improved designs for most classical microwave devices such as power dividers, phase shifters, hybrid couplers, filters, antennas.

Finally in this chapter, some considerable attention was given to the specific application of CSRRs to the domain of antenna design since this is the principle focus of the work described in this thesis. Some recent techniques were described including the use of CSRRs in improving antenna matching networks. The use of CSRRs in providing better compatibility of ultra-wideband antennas with other systems along with their role in reducing the size of patch antennas were both described also.

To the best of our best knowledge, no structure in the state of the art applies the CSRR concept to leaky wave antenna. This kind of antenna is the subject of the next chapter, where the application of metamaterials for this type of antenna will be investigated.

Bibliography

[1] N. Engheta and W. Ziolkowski, *Metamaterials, Physics and Engineering Explorations*. IEEE Press, Wiley and Sons Inc Publication, 2006.

[2] B. A. Munk, *Metamaterials, Critique and Alternatives*. IEEE Press, Wiley and Sons Inc Publication, 2009.

[3] M. Gil, J. Bonache, and F. Martín, "Metamaterial filters: A review," *Metamaterials*, vol. 2, pp. 186 – 197, 2008.

[4] F. Yang and Y. Rahmat-Samii, *Electromagnetic Band Gap Structures in Antenna Engineering*. Cambridge University Press, 2008.

[5] C. Caloz and T. Itoh, *Electromagnetic metamaterial : Transmission line and microwave applications*. Wiley, 2006.

[6] A. Grbic and G. V. Eleftheriades, "Experimental verificiation of backward-wave radiation from a negative refractive index metamaterial," *Journal of Applied Physics*, vol. 92, no. 10, pp. 5930 – 5935, Nov. 2002.

[7] S. Paulotto, P. Baccarelli, F. Frezza, and D. R. Jackson, "Full-wave modal dispersion analysis and broadside optimization for a class of microstrip CRLH leaky-wave antennas," *IEEE Transactions on Microwave Theory and Techniques*, vol. 56, no. 12, pp. 2826–2837, Dec. 2008.

[8] M. Gil, J. Bonache, J. Garcia-Garcia, and F. Martin, "Composite right/left handed (crlh) transmission lines based on complementary split ring resonators (csrrs) and applications," *Proc. Metamaterials 2007*, pp. 22–24, Oct. 2007, Roma, Italy.

[9] S. Eggermont and I. Huynen, "Leaky wave radiation phenomena in metamaterial transmission line based on complementary split ring resonators," *Microwave And Optical Technology Letters*, vol. 53, no. 9, pp. 2025 – 2029, Sep. 2011.

[10] M. Gil, J. Bonache, J. Selga, and J. G.-G. F. Martin, "Broadband resonant-type metamaterial transmission lines," *Microwave and Wireless Components Letters, IEEE*, vol. 17, no. 2, pp. 97 – 99, Feb. 2007.

[11] M. Gil, J. Bonache, I. Gil, J. García-García, and F. Martín, "Artificial left-handed transmission lines for small size microwave components: Application to power dividers," *Proc. 36th European Microwave Conference (EUMA 2006)*, pp. 1135 – 1138, Sep. 2006, Manchester, UK.

[12] J. Bonache, G. Siso, M. Gil, and F. Martin, *Dispersion Engineering in Resonant Type Metamaterial Transmission Lines and Applications*. in S. Zoudhi, A. Sihvola, A.P. Vinogradov, NATO Science for Peace and Security

Series-B, Springer, 2008, ch. Metamaterial And Plasmonics : Fundamentals, Modelling, Applications, pp. 269 – 280.

[13] M. Selvanayagam and G. V. Eleftheriades, "A compact printed antenna with an embedded double-tuned metamaterial matching network," *IEEE Transactions on Antennas and Propagation*, vol. 58, no. 7, pp. 2354 – 2361, Jul. 2010.

[14] J. Kim, C. Cho, and J. Lee, "5.2 GHz notched ultra-wideband antenna using slot-type SRR," *Electronics Letters*, vol. 42, 2006.

[15] A. Limaye and J. Venkataraman, "Size reduction in microstrip antennas using left-handed materials realized by complementary split-ring resonators in ground plane," *Proc. IEEE Antennas and Propagation Society International Symposium*, Jun. 2007, Rochester, USA.

[16] A. Lai, T. Itoh, and C. Caloz, "Composite right/left-handed transmission line metamaterials," *IEEE Microwave magazine*, Sep. 2004.

[17] V. G. Veselago, "The electrodynamics of substances with simultaneously negative values of ϵ and μ," *SOV PHYS USPEKHI*, vol. 10, no. 4, 1968.

[18] A. Vander-Vorst, *Transmission propagation et rayonnement.* De Boek Université.

[19] T. Edwards, *Foundations for Microstrip Circuit Design.* John Wiley and Sons, 1992.

[20] J. Kraus and D. Fleisch, *Electromagnetics with applications.* Mc Graw-Hill, 1999.

[21] A. V. Vorst and D. Vanhoenacker-Janvier, *Bases de l'ingenierie Micro-Onde.* Deboeck Universite, 1996.

[22] J. J. B. Pendry, A. J. Holden, D. J. Robbins, and W. J. Stewart, "Magnetism from conductors and enhanced nonlinearphenomena," *IEEE Transaction on Microwaves Theory and Techniques*, vol. 47, no. 11, November 1999.

[23] M. S. R. Marques, F. Martin, *Metamaterials With Negative Parameters, Theory, Design and Microwave Applications.* Wiley, 2008.

[24] J. D. Baena, J. Bonache, F. Martín, R. M. Sillero, F. Falcone, T. Lopetegi, M. A. G. Laso, J. García-García, I. Gil, M. F.Portillo, and M. Sorolla, "Equivalent-circuit models for split-ring resonators and complementary split-ring resonators coupled to planar transmission lines," *IEEE Transaction on Microwaves Theory and Techniques*, vol. 53, no. 4, pp. 1451 – 1460, Apr. 2005.

[25] M. G. Barba, *Doctoral Thesis on Resonant-type metamaterial transmission lines and their application to microwave device design.* Escola Technica Superior d'Enginyeria, Universitat Autonoma de Barcelona, 2009.

[26] D. M. Pozar, *Microwave Engineering.* Wiley, 1997.

[27] M. Gil, J. Bonache, I. Gil, J. Garcia-Garcia, and F. Martin, "On the transmission properties of left-handed microstrip lines implemented by complementary split rings resonators," *International Journal of Numerical Modelling : Electronic Networks, Devices and Fields*, vol. 19, no. 2, pp. 87 – 103, Mar. 2006.

[28] G. Siso, J. Bonache, and F. Martín, "Dual-band y-junction power dividers implemented through artificial lines based on complementary resonators," *Proc. IEEE MTT-S International Microwave Symposium Digest*, pp. 663– 666, Jun. 2008, Atlanta, USA.

[29] G. Siso, J. Bonache, and F. Martin, "Composite right/left-handed metamaterial transmission mines with unconventional dispersion and applications," *Microwave And Optical Technology Letters*, vol. 52, no. 4, pp. 904 – 909, Apr. 2010.

[30] I. Gil, J. Bonache, J. Garcia-Garcia, and F. Martin, "Tunable metamaterial transmission lines based on varactor-loaded split-ring resonators," *IEEE Transactions on Microwave Theory and Techniques*, vol. 54, no. 6, pp. 2665 – 2674, Jun. 2006.

[31] A. Vélez, J. Bonache, and F. Martin, "Varactor-loaded complementary split ring resonators (*vlcsrr*) and their application to tunable metamaterial transmission lines," *IEEE Microwave and Wireless Components Letters*, vol. 18, no. 1, pp. 28 – 30, Jan. 2008.

[32] I. Gil, F. Martín, X. Rottenberg, and W. D. Raedt, "Tunable stop-band filter at q-band based on rf-mems metamaterials," *Electronics Letters*, vol. 43, no. 21, pp. 1153 – 1154, Oct. 2007.

[33] M. S. Boybay and O. M. Ramahi, "Metamaterial particles for near-field sensing applications," *United States Patent Application*, no. 20120086463 A1, publication Date: 04/12/2012, Filing Date: 10/12/2010.

[34] M. Selvanayagam, D. Choudhury, and G. V. Eleftheriades, "A dual band wi-fi antenna using a metamaterial CSRR matching particle," *Proc. Antennas and Propagation Society International Symposium (APSURSI'2010)*, Jul. 2010, Toronto, Canada.

[35] M. Zhang, X. Zhou, J. Guo, and W. Yin, "A novel ultra-wideband planar antenna with dual-notched performance," *Microwave And Optical Technology Letters*, vol. 52, no. 1, pp. 90 – 92, Jan. 2010.

[36] L. Liu, Y. Z. Yin, C. Jie, J. P. Xiong, and Z. Cui, "A compact printed antenna using slot-type CSRR for 5.2GHz/5.8GHz band-notched UWB application," *Microwave And Optical Technology Letters*, vol. 50, no. 12, Dec. 2008.

[37] A. Ali and Z. Hu, "Broadband antenna with frequency notch characteristic based on complementary split-ring resonators," *Proc. Antennas and Propagation Society International Symposium*, Jun. 2007, Honolulu, USA.

[38] D.-O. Kim, N.-I. Jo, H.-A. Jang, and C.-Y. Kim, "Design of the ultrawideband antenna with a quadruple-band rejection characteristics using a combination of the complementary split ring resonators," *Progress In Electromagnetics Research*, vol. 93 - 107.

[39] I.-T. Tang, D.-B. Lin, G.-H. Liou, and J.-H. Horng, "Miniaturized 5.2GHz notched UWB CPW-FED antenna using dual reverse split trapezoid slots," *Microwave And Optical Technology Letters*, vol. 50, no. 3, pp. 652 – 655, 2008.

[40] J.Ding, Z. Lin, Z. Ying, and S. He, "A compact ultra wide band slot antenna with multiple notch frequency bands," *Microwave And Optical Technology Letters*, vol. 59, no. 12, pp. 3056 – 3060, 2007.

[41] W. Lui, C. Cheng, and H. Zhu, "Improved frequency notched ultrawideband slot antenna using square ring resonator," *IEEE Transactions on Antennas and Propagation*, vol. 55, no. 9, pp. 2445 – 2450, Sep. 2007.

[42] X. Li, L. Yang, S.-X. Gong, and Y. Yang, "Ultra-wideband monopole antenna with four-band-notched characteristics," *Progress In Electromagnetics Research Letters*, vol. 6, pp. 27 – 34, Jun. 2009.

[43] Z.-W. Yu, G.-M. Wang, J.-G. Liang, and X.-J. Gao, "Miniaturized patch antennas loaded with complementary split-ring resonators and reactive impedance surface," *Microwave And Optical Technology Letters*, vol. 52, no. 10, pp. 2387 – 2390, Oct. 2010.

[44] A. Ali and Z. Hu, "Metamaterial resonator based wave propagation notch for ultrawideband filter applications," *Antennas and Wireless Propagation Letters, IEEE*, vol. 7, pp. 210 – 212, Aug. 2008.

[45] J. Venkataraman, A. Wyant, A. W. Chen, A. Limaye, and G. Shieh, "Small microstrip patch antennas," *Proc. Applied Electromagnetics Conference (AEMC)*, Dec. 2009, Rochester, USA.

[46] Y. Lee, S. Tse, Y. Hao, and C. G. Parini, "A compact microstrip antenna with improved bandwidth using complementary split-ring resonator (CSRR) loading," *Proc. Antennas and Propagation Society International Symposium*, Jun. 2007, Honolulu, USA.

[47] Y. Dong and T. Itoh, "Miniaturized patch antennas loaded with complementary split-ring resonators and reactive impedance surface," *Proc. European Conference on Antenna and Propagation (EUCAP)*, pp. 27 – 34, Apr. 2011, Roma, Italy.

[48] ——, "Design and characterization of miniaturized patch antennas loaded with complementary split-ring resonators," *IEEE Transactions on Antennas and Propagation*, vol. 60, no. 2, pp. 772 – 785, 2012.

[49] D. Laila, R. Sujith, V. Deepu, C. K. Aanandan, K. Vasudevan, and P. Mohanan, "Compact CSRR based patch antenna for wireless applications," *Proc. Applied Electromagnetics Conference (AEMC)*, pp. 1 – 3, Dec. 2009, Kolkata, Bengali.

[50] J. Ha, J. Kim, and J. Choi, "Design of a small resonant antenna using metamaterial based on transmission line approach," *Proc. Antennas and Propagation Society International Symposium (APSURSI)*, Jul. 2010, Toronto, Canada.

[51] N. Engheta, "An idea for thin subwavelength cavity resonators using metamaterials with negative permittivity and permeability," *IEEE Antennas and Wireless Propagation Letters*, vol. 1, no. 1, pp. 10–13, 2002.

CHAPTER 3

ONE-DIMENSIONAL PERIODIC LEAKY WAVE ANTENNA

This chapter will introduce the theory of one-dimensional leaky wave antennas (LWAs). First the general theory of travelling waves along a waveguide will be presented. Subsequently, the main properties of different types of LWAs will be presented, including uniform, periodically-loaded and quasi-uniform antennas. Considerable attention will be given to the novel metamaterial LWAs.

3.1 INTRODUCTION

The first leaky wave antenna was invented by W.W. Hansen in 1940 [1]. This rectangular waveguide with a long slot is in fact older than the first bipolar transistor (Bell Labs, 1948). Its first application concerned aircraft and missile radar applications. The basic working principle is based on a wave propagating along an electrically long guiding structure and leaking out gradually energy in the form of coherent radiation [2]. Its advantages are the ability to offer sharp directional beams with a frequency scanning over a large bandwidth [2], as well as the ability to offer simple inexpensive structure with low profile. As a result of its low profile, it can be flush-mounted on different structures such as vehicles, cellular base stations, or mobile devices [2]. It offers also an easy integration [3], especially for printed LWA integrated in the same substrate with other circuits and devices [2]. In 2002, metamaterial principles of Veselago, presented in the

first chapter, were applied to the planar LWA by Caloz's group, enabling, using the concept of the TL dual, a complete full space scanning based on the frequency tuning of the fundamental mode of a planar waveguide [4].

The first section discusses the radiation mechanism in a leaky wave antenna. The second section presents the classification of the LWAs and their properties. In the third section, different metamaterial LWAs are presented.

3.2 RADIATION IN LEAKY WAVE ANTENNAS

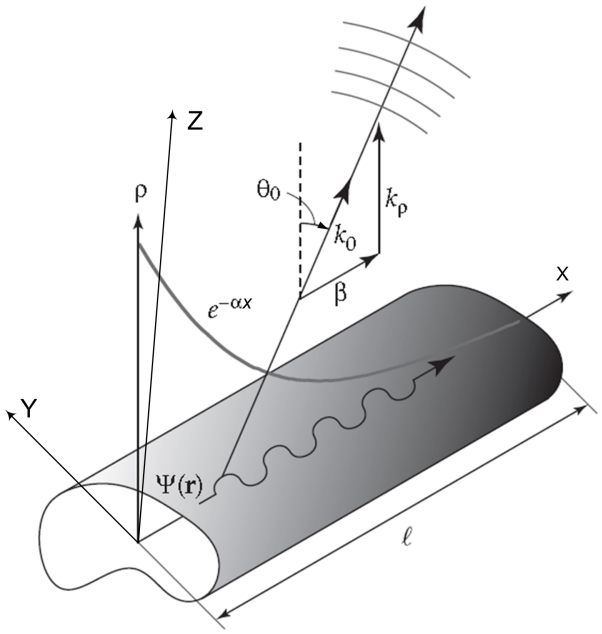


Figure 3.1. *Conceptual view of radiation phenomena in a leaky wave antenna [5].*

A leaky wave antenna is a kind of waveguide along which a travelling wave leaks out radiating power. The travelling wave forms the basis of different classes of antennas, including the leaky wave antennas, surface wave antennas or slot arrays [6]. Radiation phenomena do not depend on a resonating-wave mechanism. As illustrated in Fig. 3.1, the direction of the propagation (axis of the waveguide) is X. The transverse coordinates are represented by $\overrightarrow{\rho} = \mathrm{y}.\overrightarrow{y} + \mathrm{z}.\overrightarrow{z}$. Continuous, discontinuous or periodic apertures are realised on the waveguide to allow the radiation. In a waveguide terminated by an appropriate matched load to avoid backward wave [7], the field of a wave travelling along the guiding structure is

expressed as [5]:

$$\psi(\rho, x) \quad = \quad \psi_0(\rho) e^{-\gamma x} \tag{3.1}$$

where γ is the longitudinal complex propagation constant along x and, as defined in 2.14, is equal to :

$$\gamma \quad = \quad \alpha + j\beta = -jk_x \tag{3.2}$$

where α is the attenuation constant, also called the leakage factor, β is the propagation number and k_x is the longitudinal wavenumber. α corresponds to the loss of the propagating wave, leaking power along the structure. A wave travelling toward the positive x direction with a positive group velocity (called *forward wave*) is represented by the spatial variation $e^{-j|\beta|x}$, similarly a wave travelling toward the negative x direction (called *backward wave*) is represented by the spatial variation $e^{+j|\beta|x}$. α and β are both real numbers and depend on the cross-sectional geometry of the waveguide.

The basic structure of all travelling wave antennas is similar, but their performances can be different. Further to this, the LWA may be compared to :

- *Surface waves antennas or slow wave antennas* : a slow wave, the dominant mode of an open waveguide for example, is guided in the structure and in fact radiation appears only at discontinuities. Thus a surface wave antenna radiates normally at the end of the waveguide, creating an end-fire radiation [6]. This class includes wires in free space or over ground plane, helixes, dielectric slabs or rods [8]. Their gain is approximately 20 dB with a narrow bandwidth and a limited control pattern shape [9] with a significant sidelobe level [8].

- *Slot arrays antennas* : a slot array antenna, used for radar communications and navigation applications, is formed by narrow nonconductive slits etched or milled into the host metallic ground plane of a waveguide [10]. In common with LWAs, the antenna has the ability of frequency scanning but in narrow bandwidth because the frequency response of the antenna is based on the resonance of the individual slot [6].

The boundary conditions, extracted from Maxwell's equations, indicate that the tangential part of the complex wavenumber vector $\overrightarrow{k} = k_\rho \overrightarrow{\rho} + k_x . \overrightarrow{x}$ is continuous at the interface between the waveguide and the free space. Thus the waveform in the free space just above the antenna exhibits the same x dependence of equation 3.1 and can be expressed as :

$$\psi(\rho, x) \quad = \quad \psi_0 e^{-\gamma x} e^{-jk_\rho \rho} \tag{3.3}$$

where ψ_0 is a constant. k_ρ, depends on the propagation constant, β, and if it is assumed that $\alpha \ll \beta$, then in accordance the approach of [11], it may be written as :

$$k_\rho \quad = \quad \sqrt{k_0^2 - k_x^2} = \sqrt{k_0^2 - \beta^2} \tag{3.4}$$

where k_0 is the free space propagation constant.

The working condition for a leaky wave antenna is derived from 3.4. For the frequency bands where k_ρ is imaginary, the wave is evanescent along the unbounded ρ direction [12], i.e. decays exponentially along ρ away from the interface and is guided in the antenna (slow wave) and in this case, the structure does not radiate. Contrary, for the frequency bands where k_z is real, the travelling waves are faster than the speed of light, c (the phase velocity v_p of the wave is higher than c), the equation 3.1 indicates then an oscillator wave contribution toward free space (called a *fast wave*). To extract the radiation condition, it is also possible to analyse the dispersion diagram : if $|\beta| < k_0$, the antenna radiates, the frequency band, in which this condition is met, is described as the fast-wave region or the leaky wave region. The region of the dispersion diagram where the condition $|\beta| < k_0$ is called the **radiation cone** and is illustrated in Fig. 3.2.

The region where $-k_0 < \beta < 0$ will be denominated the **left-leaky region**. The region where $0 < \beta < k_0$ will be denominated the **right-leaky region**.

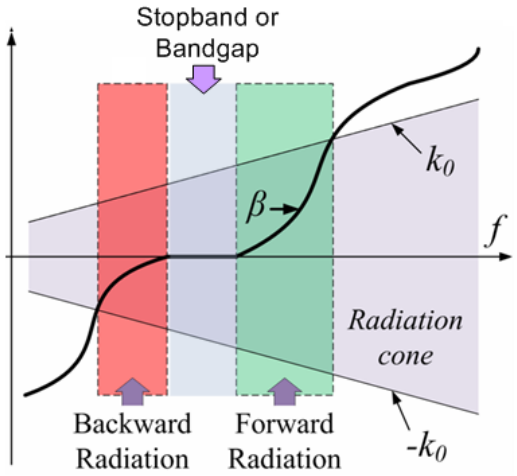


Figure 3.2. *Conceptual view of dispersion diagram of a leaky wave antenna where the magenta area represents the radiation cone defined by the free-space propagation constant k_0, illustrating two radiation frequency bands : backward radiation ($-k_0 < \beta < 0$, LH range) and forward radiation ($0 < \beta < k_0$, RH range).*

The direction of the main beam of the antenna, defined from the normal direction and illustrated in Fig. 3.3, is given by [11]:

$$\theta_{\mathsf{MB}} = \arcsin(\frac{\beta(\omega)}{k_0}) = \arcsin(\frac{c.\beta(\omega)}{\omega}) \tag{3.5}$$

The relation 3.5 shows the ability of a leaky wave antenna to present a nonlinear scanning of the main beam as a function of frequency. The leakage factor, α, influences the radiation. This factor includes the effect of radiative, ohmic and dielectricl losses. If α is larger, the rate of decay of the wave magnitude along the structure will be larger and therefore the length of the antenna, before which all the power is radiated out, will be smaller. As a result of this, the antenna will be less directive. Thus a small leakage factor means high directivity if the other structures are negligible. The antenna length is related to the directivity but not to the operation frequency, contrary to resonating-wave antennas. For a planar structure (created on the planar substrate), the radiation pattern beamwidth is fixed by the antenna width [13]. Theoretical or experimental determination of β and α is essential to establish the properties of the LWA such as : the beam direction, the beamwidth, the radiation efficiency and the variation of the scan angle with frequency [14]. The aperture distribution is defined as the radiated power distribution along the line of elements. The sidelobes are essentially created by a finite antenna length. To obtain the desired sidelobe level with a given length, the antenna aperture distribution must be a compromise between a slow variation of α value and a fixed β value [8]. The LWA bandwidths are typically in the range of 15% and 30% [15]. The main advantage of the LWA compared to the array antennas is the feeding network. Indeed, this feeding network can be a transmission line or a waveguide connection [13]. They also need a simple inexpensive structure with low profile and with an easy integration [3].

As discussed later in this chapter, a conventional uniform LWA, a purely RH structure, only provides a positive frequency scanning from broadside where θ_{MB} is equal to zero ($\beta = 0$) to end-fire direction where θ_{MB} is equal to 90° ($\beta = k_0$) as illustrated in Fig. 3.3.

The expression of the beamwidth measured between half-power points is [8]:

$$\Delta\theta \simeq \frac{1}{\frac{L}{\lambda_0}\cos\theta_{\mathsf{MB}}} \quad [\mathsf{rad}] \tag{3.6}$$

Narrow beams are usually obtained with LWAs whose aperture is long compared to the wavelength [16]. LWA with narrow radiating aperture is equivalent to a current source in the far-field with a cone beam making an angle 90°-θ_{MB} with respect to the wave propagation axis. The typical pattern of 1D printed LWA with a ground plane inserted underneath it is an unidirectional fan beam [6]. Fig 3.4 illustrates the radiation shape of a line source of current with a grounded dielectric slab inserted underneath. The expression of the current is equal to $e^{-jk_x x}$. Assuming a working frequency above the cut-off of TE_1 surface waves, TM_0 surface waves are created in the substrate. If the propagation constant of the wave is smaller than the wavenumber of the surface waves, k_{TM_0}, then leakage into the surface wave occurs. The angular sector of scanning depends on the LWA topology. A solution to obtain a pencil beam is the creation of a LWA array [16]. Conical beams can be obtained by 2D layer configuration, this topic is not discussed in this thesis, the interested reader is referred to [14].

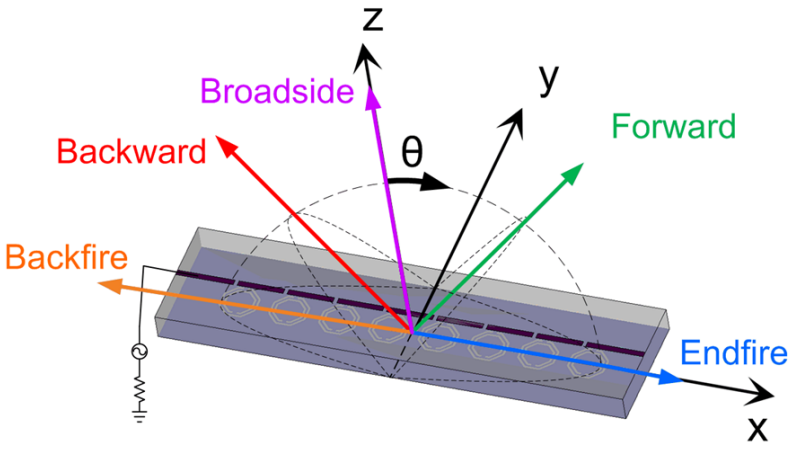


Figure 3.3. *Sketch of a TL used as LWA illustrating the five radiation regions : backfire ($\beta = -k_0$), backward ($-k_0 < \beta < 0$, LH range), broadside ($\beta = 0$), forward ($0 < \beta < k_0$, RH range), endfire ($\beta = k_0$).*

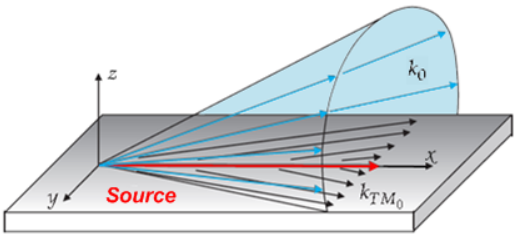


Figure 3.4. *Conceptual view of the unidirectional fan beam of a 1D printed LWA with a ground plane inserted underneath it (the LWA is modelled by a line source with a current varying as $e^{-jk_x x}$, represented by the red arrow. The blue arrows represent the direction of the leaky wave radiation. The black arrow represents the direction of the TM_0 surface waves propagating in the susbtrate) [5].*

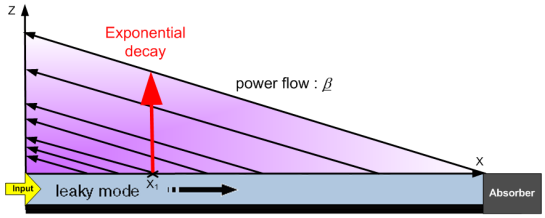
The radiation of a LWA is referred to as *improprer* for the forward quadrant and as **proper** for the backward quadrant. The explanation comes from the sign of the leakage factor, α_ρ, of the wave in the free-space region, this value can be extracted from the equation 3.4 after squaring both sides :

$$k_\rho^2 = (\beta_\rho - j\alpha_\rho)^2 = k_0^2 - (\beta - j\alpha)^2 \tag{3.7}$$

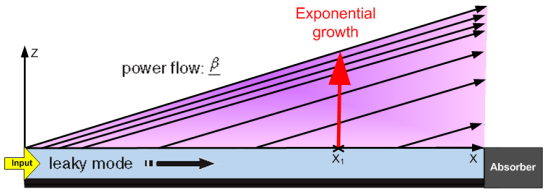
α_ρ is obtained from the imaginary part of the equation 3.7 :

$$-2\beta_\rho\alpha_\rho = 2\beta\alpha \tag{3.8}$$

For a forward propagation, α, β and β_ρ are positive and then α_ρ becomes negative. Thus the wave, decreasing exponentially along the x axis, must increase exponentially in the radial direction in the free space region and this is the reason to refer to this leaky wave as, 'improper'. For a backward propagation (introduced in the chapter 2), α is positive, β is negative, then α_ρ becomes positive. In this case, the wave decays exponentially in both directions, along the x axis and in the air. The leaky wave is then referred to as, 'proper'. The forward propagation seems physically abnormal, however the ray diagram, presented in [14], explains this behaviour for the simple case of the layered structure illustrated in Fig. 3.5. A travelling wave propagates in this guiding structure, which is terminated by an absorber to avoid reflection. The black arrows represent the direction of power flow in the free-space region and the spacing between arrows indicates the magnitude of the time-average Poynting vector. Thus the arrows are closer in the input region, compared to the absorber region, because the power flow of the wave is larger. Fig. 3.5(b) illustrates the forward propagation, at the point x_1. The power level seems to be increasing vertically along the red arrow, which explains the exponential increase created by the negative α_ρ value. The proper wave is illustrated in Fig. 3.5(a), at the point x_1. The power level seems to be decreasing vertically in the red arrow direction, which explains the exponential decrease created by the positive α_ρ value.



(a) Backward Propagation [14]



(b) Forward Propagation [14]

Figure 3.5. *Conceptual view of leaky wave propagation in a layered structure matched by an absorber. The black arrows represents the direction of power flow in the air region. The spacing between arrows indicates the magnitude of the time-average Poynting vector. At point x_1, in (a), the power decreases vertically from the aperture in the red arrow direction, the leaky wave is called proper. At point x_1, in (b), the power increases vertically from the aperture in the red arrow direction, the leaky wave is called improper.*

3.3 CLASSIFICATION OF LEAKY WAVE ANTENNAS

LWAs can be classified into three basic classes according to the geometry of the antenna [6]:

- *uniform* LWAs, in which the LWA geometry is uniform along its length,
- *periodic* LWAs, in which the LWA geometry is modulated along its length.
- *quasi-uniform* LWAs in which the LWA geometry is modulated along the length but the period of the modulation is smaller than the guided wavelength of the travelling wave.

3.3.1 Uniform Leaky Wave Antenna

The first category, the uniform LWA, describes LWAs with an invariant transverse cross section along the propagation axis. Only a small, smooth and continuous variation of the cross section is realised to allow continuous leaking power from the antenna. The radiating modes, called leaky modes, are the dominant or higher-order fast-wave ones. Their propagation constant, β is always positive and non-zero for all frequencies, therefore the frequency scanning is allowed only in the forward quadrant [5].

An example of uniform LWA, the first LWA proposed in 1940 by W. W. Hansen [1], is illustrated in Fig. 3.6 and consists of rectangular waveguide with a longitudinal slot in the narrow wall of the waveguide [6]. The propagating fast-wave mode is the fundamental TE_{10} mode, where the propagation constant β is equal to [8]:

$$\beta = \sqrt{k_0^2 - (\frac{\pi}{a})^2} \tag{3.9}$$

where a is the waveguide dimension illustrated in Fig. 3.6. The effective aperture of LWA waveguide will be the whole length if the leakage factor α is small enough so that the power has not effectively leaked away before reaching the end of the antenna [6]. If the waveguide is fed at one end, the broadside radiation is not possible because the frequency of broadside direction is then the cutoff frequency of the waveguide. A double feed network with waves propagating in both directions is necessary to obtain broadside radiation [14]. The frequency scanning is not possible too close to endfire (illustrated in Fig. 3.3) because of the presence of higher-order modes [8]. The radiation properties are influenced by the dielectric inside the waveguide. The scanning law, depicted in Fig. 3.6(b) is influenced by the permittivity of this dielectric [17]. Indeed the beamwidth is constant for a frequency increase for air-filled waveguides, contrary to the dielectric-filled wavdeguides. It may also be observed that for a fixed bandwidth, the angle scanning is higher for a dieletric-filled waveguide than for a air-filled waveguide [8].

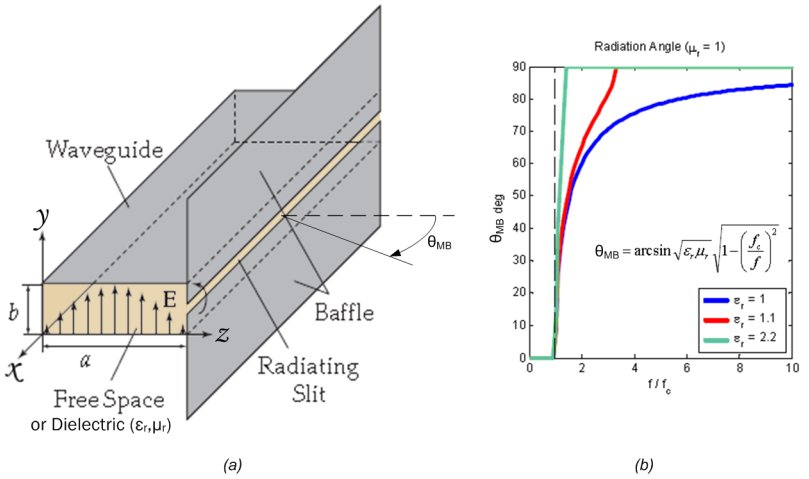


Figure 3.6. *Example of a uniform LWA : Rectangular waveguide with a longitudinal slit in the narrow wall of the waveguide and with a ground plane baffle, operating in the weakly-perturbed TE_{10} dominant mode (a) Topology [5] (b) Scanning law for different permittivity values of the dieletric inside the waveguide for a wave propagating along the x-axis [17].*

3.3.2 Periodic Leaky Wave Antenna

The second category of LWA, the periodic LWA presents a periodic modulation of the waveguide along the axis of propagation in the form of periodic discontinuities (created by metallization, slots, permittivity of permeability transitions) [5]. This radiation phenomenon can be explained intuitively by the fact that a slow wave, travelling along the length of the structure, radiates only at discontinuities and therefore creates a continuous radiation, based on periodic discontinuities [14]. A periodic LWA can be viewed as a surface wave antenna with a periodic array of discontinuities on the guide in such way that the first harmonic becomes a fast radiating wave [6].

This radiation phenomenon can also be described mathematically by the Bloch-Floquet expansion where the wave is viewed as a superposition of an infinite number of plane waves. As explained in [18], in a infinite periodic structure, where p is the length of a unit cell, the expression of a wave travelling along the guiding structure, along the axis x, can be expressed at the point $x + mp$ (where m is an integer), using the equation 3.1, as :

$$\psi(x + mp) \quad = \quad e^{-\gamma mp}\psi(x) \tag{3.10}$$

By multiplying both terms by $e^{+\gamma x}$, this expression can be written with simple manipulations as :

$$\psi(x)e^{+\gamma x} = \psi(x+mp)e^{+\gamma(x+mp)} \tag{3.11}$$

The function $\psi(x)e^{+\gamma x}$, called $\xi_\gamma(x)$, is a periodic function of period, p for any complex propagation constant, γ. By using the Fourrier's theory, we can write it as :

$$\xi_\gamma(x) = \sum_{m=-\infty}^{+\infty} \xi_{\gamma m} e^{-j(2m\pi/p)x} \tag{3.12}$$

where

$$\xi_{\gamma m} = \frac{1}{2\pi}\int_{-\pi}^{+\pi} \xi_\gamma(x) e^{+j(2m\pi/p)x} dx \tag{3.13}$$

If reflections are present, both positive-going and negative-going waves exist along the line. So the global wave in a periodic structure is viewed as the superposition of infinite numbers of space harmonics, called the Floquet's series :

$$\psi(x) = e^{-\alpha(\omega)x} \sum_{m=-\infty}^{+\infty} \xi_{\gamma m}^{+} e^{-j\beta_m x} + e^{+\alpha(\omega)x} \sum_{m=-\infty}^{+\infty} \xi_{\gamma m}^{-} e^{+j\beta_m x} \tag{3.14}$$

where α is the leakage factor, previously defined in this chapter and where the propagation constant, β_m is equal to

$$\beta_m(\omega) = \beta_0(\omega) + 2m\pi/p \tag{3.15}$$

β_0 is the propagation constant of the fundamental mode and can be also viewed as the original β of the dominant mode of the uniform dielectric waveguide modified by the addition of the holes. So the wave is viewed as a superposition of infinite number of plane waves, called *space harmonics*. The modal electric field of an infinite-width periodically-loaded structure (with an absence of topology and field variations along y-axis) in the air region, for a wave propagating only along the x-axis, is [12] :

$$\underline{E}(x,y,z) = e^{-\alpha(\omega)x} \sum_{m=-\infty}^{+\infty} \underline{A}_m(z) e^{-j\beta_m x} e^{-jk_{zm}z} \tag{3.16}$$

where

$$k_{zm} = \sqrt{k_0^2 - (\beta_m - j\alpha)^2} \tag{3.17}$$

The fundamental mode is generally a guided slow wave. In contrast the higher mode can be designed to radiate [5]. Assuming $\alpha \ll \beta_m$, the radiation condition is then $|\beta_m/k_0| < 1$, we can rewrite the equation 3.5 as [6]:

$$\frac{\beta_m}{k_0} = \frac{\beta_0}{k_0} + \frac{2m\pi}{k_0.p} = \frac{\beta_0}{k_0} + \frac{m\lambda_0}{p} \tag{3.18}$$

The analysis of equation 3.18 shows that the radiation condition is achieved for a negative value of m and a suitably chosen factor $\frac{\lambda_0}{p}$. The value m=-1 is often obtained [6].

Contrary to the uniform LWAs, periodic LWAs can radiate in the backward and forward quadrants, depending on the sign of β_{-1}. Indeed, the expression for the LWA main beam of equation 3.5 can be written :

$$\sin(\theta_{\mathsf{MB}}) \quad = \quad \frac{\beta_{-1}}{k_0} = \frac{\beta_0}{k_0} - \frac{2\pi}{k_0 p} = \frac{\beta_0}{k_0} - \frac{\lambda_0}{p} \tag{3.19}$$

Depending on the numerical relationship between $\frac{\lambda_0}{p}$ and $\frac{\beta_0}{k_0}$, a frequency scanning is possible from backfire to endfire [14]. To excite this higher order emode, carefully designed feeding networks are necessary in order to match this space harmonic contribution without the creation of spurious radiations due to surface waves at the feed transition [11].

The frequency scanning is divided in three parts as depicted in Fig.3.2 : the *backward frequency scanning* (in which θ_{MB} increases from -90° to 0°), the *open stop band* (α increases and drops to zero, β is close to zero) and *forward frequency scanning* (in which θ_{MB} increases from 0° to 90°). In the stop band, for frequency bands for which β is equal to zero, a standing-wave regime appears in the structure and indeed the wave is reflected back to the source. Futhermore, the leakage factor drops sharply to zero and the Bloch impedance becomes purely imaginary [19]. The input match to the antenna is poor and the radiation efficiency and the gain also become poor [14]. The optimisation of the broadside radiation is possible with the suppression of the stop band. For microstrip LWAs, this may be achieved by using double-stub techniques, which are based on the cancellation of two reflected waves. Another possible method is the use of U-shaped stubs, which are based on parallel U-stubs in conjunction with gaps. In this case, these act as both a radiating element and a phase shifter. Impedance transformer can also be used, it is based on a matching network between the parallel and series impedances, so between the Bloch impedance of the radiating elements and the line impedance, using a quarter-wavelength or a matching stub Finally, metamaterial LWAs may offer another method for this type of optimisation and these are discussed later in this chapter [19].

Having discussed the general theory of periodic LWAs, two open periodic structures can now be described. The first type combines structures that are completely surrounded by free space, such as periodically modulated slow-wave antennas, travelling-wave slots or dipole arrays, with metal gratings on a grounded dielectric slab. Their main properties are expressed in the equation 3.16 and the radiation is only possible into the free space. The second type combines a finite-width structure with a dielectric substrate into which surface waves can leak power because of the finite width of the metallization and the unbounded grounded substrate in the y-direction. Open periodic structures printed on a grounded dielectric slab with a transverse variation along y, as illustrated in Fig. 3.7(a), belong to this class. In addition to space leakage, surface leakage is

allowed, thus equation 3.16 must be modified to take into account the transverse variation of the field along y. The modal electric field in the air region is [12] :

$$\underline{E}(x,y,z) \quad = \quad e^{-\alpha(\omega)x} \sum_{m=-\infty}^{+\infty} \underline{a}_m(y,z) e^{-j\beta_m x} \tag{3.20}$$

where

$$\underline{a}_m(y,z) \quad = \quad \int_{-\infty}^{+\infty} \underline{A}_m(k_y) e^{-jk_{zm}z} e^{-jk_y y} dk_y \tag{3.21}$$

and

$$k_{zm} \quad = \quad \sqrt{k_0^2 - k_y^2 - (\beta_m - j\alpha)^2} \tag{3.22}$$

The above cutoff TM_0 surface-wave mode is defined by k_{TM_0}. Assuming a working frequency such that this mode is dominant, therefore $k_{TM_0} > k_0$, the previous relation brings then six leakage regimes of one space harmonic depeding on the value of β_m. These regimes are illustrated in Fig. 3.7 [20] :

- *Slow wave regime* : $|\beta_m| > k_{TM_0} > k_0$: the space harmonic is guided in the structure along the x-axis, the waves along the z-axis and y-axis are evanescent, defined by $k_{zm} = -j\alpha_{zm}$ and $k_{ym} = -j\alpha_{ym}$.

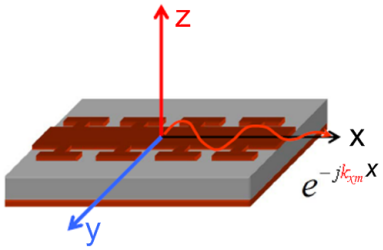
- *Backward surface leaky-wave regime* : $-k_{TM_0} < \beta_m < -k_0$: the space harmonic radiates into the dominant surface-wave mode of the substrate, and not into free space. The wave along the z-axis is evanescent in free space, defined by $k_{zm} = -j\alpha_{zm}$. As illustrated in Fig. 3.7(b), the propagation direction of the surface waves is defined by :

$$\theta_s \quad = \quad \arcsin(\frac{\beta_m}{k_{TM_0}}) \tag{3.23}$$

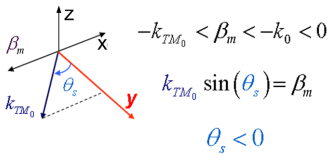
- *Backward spatial and surface leaky-wave regime* : $-k_{TM_0} < -k_0 < \beta_m < 0$: the space harmonic radiates simultaneously into the dominant surface-wave mode of the substrate and into free space. The propagation direction of the surface waves and the free space wave are defined respectively by eq. 3.23 and eq. 3.19 as illustrated in Fig. 3.7(c).

- *Forward spatial and surface leaky-wave regime* : $0 < \beta_m < k_0 < k_{TM_0}$: the space harmonic radiates simultaneously into the dominant surface-wave mode of the substrate and into the free space. The propagation direction of the surface waves and the free space wave are defined respectively by eq. 3.23 and eq. 3.19 as illustrated in Fig. 3.7(d).

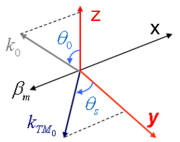
- *Forward surface leaky-wave regime* : $k_0 < \beta_m < k_{TM_0}$ the space harmonic radiates into the dominant surface-wave mode of the substrate, and not



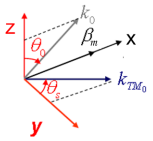
(a) 1-D open periodic structures printed on a grounded dielectric slab



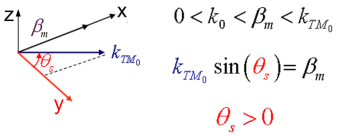
(b) Backward Surface Leaky-Wave Regime



(c) Backward Spatial and Surface Leaky-Wave Regime



(d) Forward Spatial and Surface Leaky-Wave Regime



(e) Forward Surface Leaky-Wave Regime

Figure 3.7. *Example of finite-width structure with dielectric substrate into which surface waves can leak power because of the finite width of the metallization and the unbounded grounded substrate in the y-direction and its propagation regimes. It is assumed that a space harmonic radiates only into the TM_0 mode of the substrate. k_{TM0} is the wavenumber of the dominant TM_0 surface wave [20].*

into the free space. The wave along the z-axis is evanescent in free space, defined by $k_{zm} = -j\alpha_{zm}$. The propagation direction of the surface waves is illustrated in Fig. 3.7(e).

Fig. 3.8 illustrates an example of a periodic LWA. The fundamental slow mode is the dominant TE_{10} mode, characterized by $\beta_{10}^{TE} = \sqrt{\varepsilon_r k_0^2 - (\pi/a)^2}$. The fast radiating space harmonic is the mode $m = -1$ [5]. An air-filled waveguide has the disadvantage of radiation absence for endfire and backfire directions, corresponding to $\beta/k_0 = \pm 1$ because of a mode coupling [19].

A computationally efficient method based on an array factor approach is presented in [4] to determine the radiation pattern of a periodic structure. The LWA

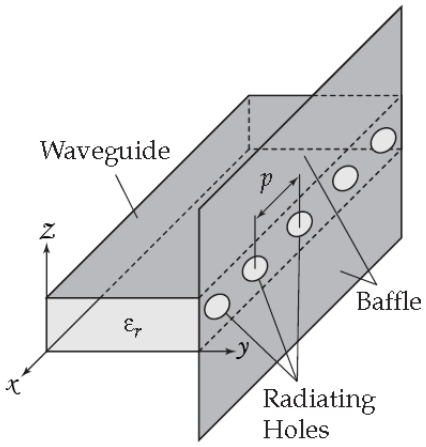


Figure 3.8. *Example of periodic LWA : Rectangular waveguide with periodic array of holes in the narrow wall of the waveguide and with a ground plane baffle, filled with dielectric [5].*

is approximated by a phased array antenna with a distance between elements close to zero, so the LWA radiation pattern is computed from the array factor.

As illustrated in Fig. 3.9(a), supposing a M-element linear array with uniform amplitude, $\psi_m = \psi_0 \ \forall m$, and spacing, p with a progressive phase function, ξ_m, the total field is obtained by multiplying the array factor of the isotropic sources by the field of a single element. The expression of the array factor, AF, is written as [21]:

$$AF = \sum_{m=1}^{M} \psi_m e^{j(m-1)(k_0 p \sin\theta + \xi_m)} \tag{3.24}$$

To correspond to a LWA, the phase function ξ_m and the magnitude function ψ_m have to be modified [4]:

$$\xi_m = -(m-1)k_0 p \sin\theta_{\mathsf{MB}} \tag{3.25}$$

$$\psi_m = \psi_0 e^{-\alpha(m-1)p} \tag{3.26}$$

The expression for the radiation pattern corresponds to [4]:

$$R(\theta) = E(\theta)AF(\theta) \tag{3.27}$$

$$= E(\theta) \sum_{m=1}^{M} \psi_m e^{j(m-1)k_0 p \sin\theta + j\xi_m} \tag{3.28}$$

where M is the number of unit cells and θ_{MB} is the main beam, given by 3.19. If the period p is much smaller than the guided wavelength, the field of the single cell, $E(\theta)$ corresponds to the field of an incremental period.

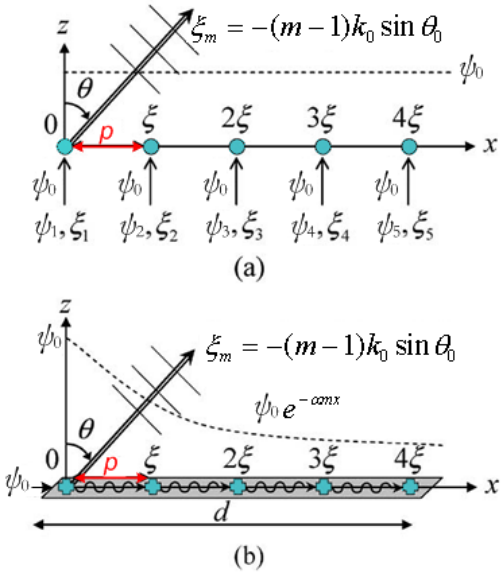


Figure 3.9. *Conceptual view of the array factor approach : (a) M-element linear array with uniform amplitude, $\psi_m = \psi_0\ \forall m$, and spacing, p with a progressive phase function, ξ_n, (b) Periodic LWA, with period p, a phase function $\xi(\theta_0)$ and an exponential magnitude function $\psi(x) = \psi_0 e^{-\alpha x}$ where α is the leakage factor [4].*

3.3.3 Quasi-Uniform Leaky Wave Antenna

The geometrical characteristics of quasi-uniform antenna are similar to the periodic LWA, unless the structure is geometrically modulated with a period smaller than the guided wavelength. In this case, there is the capability to create a fast-wave dominant (m=0) space harmonic [5]. This fundamental mode radiates, contrary to the case of the periodic LWA. Thus Fig. 3.8 with subwavelength spacing between the holes could be considered as a quasi-uniform LWA. To model the structure as a uniform LWA, an equivalent uniform surface impedance replaces the wall of the waveguide carrying the holes. Metamaterial LWAs, which can be classified into this category, are described in the next section.

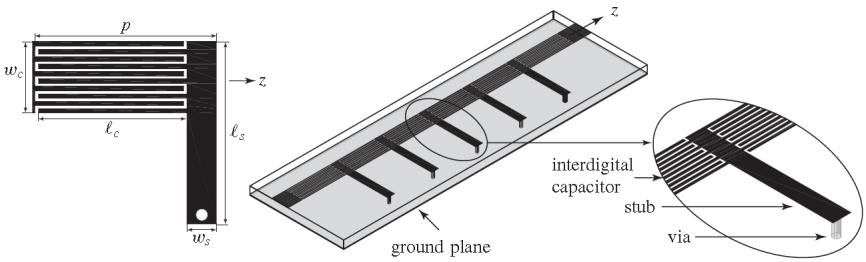
3.4 METAMATERIAL LEAKY WAVE ANTENNA

A metamaterial LWA can be considered as a quasi-uniform LWA in which the LWA has the topology of a periodic LWA but combines the radiation properties of a uniform LWA with the ability of full-space scanning. In fact, the geometry is modulated along the length but the period of the modulation is smaller

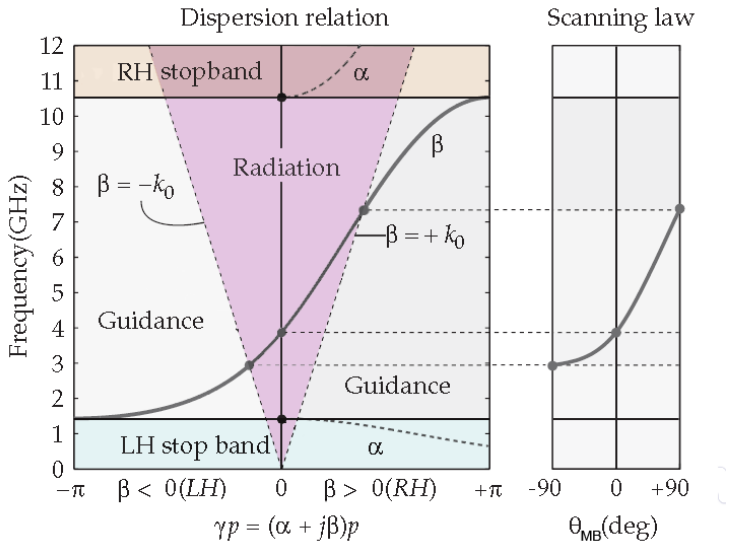
than the guided wavelength of the travelling wave [5]. Caloz's group was the first to introduce the concept of 1D planar periodic LWA in which the fundamental quasi-TEM mode of the microstrip line becomes a fast wave with the properties of backward and forward radiation [14]. As viewed in the section 3.3.2, the wave of the periodic structure is the superposition of infinite numbers of space harmonics, following the Floquet's theory. In the metamaterial artificial TL, only the fundamental mode radiates significantly, the contribution of non-zero space harmonics are poor, the $m = -1$ mode, for example, is a slow wave [5]. The 1-D planar antenna is based on the CRLH TL presented in the section 2.2, illustrated in Fig. 3.10(a). Referring to the model described in the section 2.2 in Fig. 2.3(a), the propagation constant, $\beta(\omega)$ of a lossless CRLH TL is equal to :

$$\beta(\omega) \quad = \quad \frac{1}{p}\sqrt{\omega\sqrt{L_R C_R} - \frac{1}{\omega\sqrt{L_L C_L}}} \tag{3.29}$$

This is shown in Fig. 3.10(b) for a balanced structure, i.e. the band-gap or stop-band between LH and RH bands is equal to zero. To obtain this condition, the series and shunt branches resonate at the same frequency [19]. Thus the dispersion diagram in the radiation cone is divided between a negative hyperbolic LH contribution in lower frequencies and a positive linear RH contribution in higher frequencies [5]. Because of these two bands, the continuous full-space scanning, i.e. from $\theta_{\mathsf{MB}} = -90°$ to $\theta_{\mathsf{MB}} = 90°$ is possible for a frequency increase from $\omega = -\beta c$ to $\omega = \beta c$. In [18], a realized TL of 24-cells is presented to achieve a leaky wave radiation between 3.1 GHz and 6.3 GHz with a 61% bandwidth. Fig. 3.11(a) shows the measured dispersion diagram, the transition between LH and RH propagation appears at 3.9 GHz. The gain value is reported in [22] to be above 6 dB, the sidelobe level is greater than 10 dB and the radiation efficiency is higher than 40 %. Fig. 3.11(b) presents the measured radiation pattern for three noticeable frequencies to prove the frequency scanning ability.

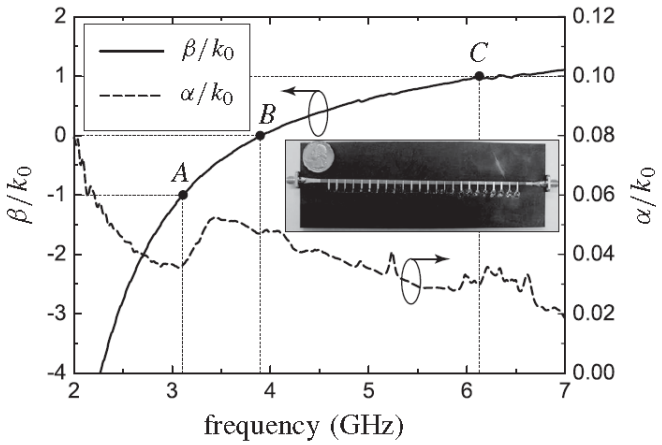


(a) Topology [18]

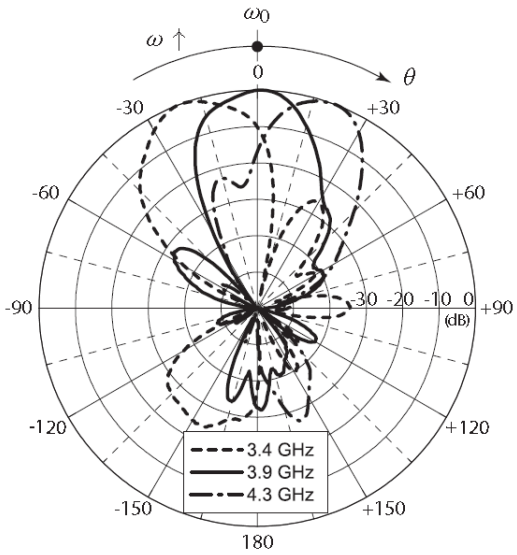


(b) Dispersion Diagram and scanning law [5]

Figure 3.10. *Caloz Group's Balanced CRLH LWA (the structure has been already presented in the section C.2), θ_{MB} is calculated from eq. 3.19 : the balanced structure creates a full space scanning [18].*

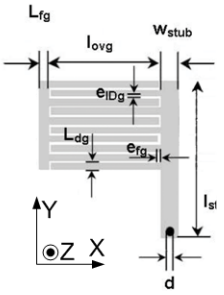


(a) Photo and measured dispersion and attenuation diagrams [18]

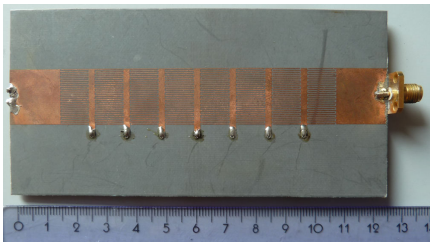


(b) Measured radiation patterns [18]

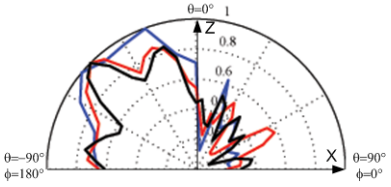
Figure 3.11. *Metamaterial balanced TL of 24 cells illustrated in Fig. 3.10(a) (dimensions are described in [18], the point A represents the backfire radiation, so $\beta = -k_0$, the point B represents the broadside radiation and the point C represents the endfire radiation.)*



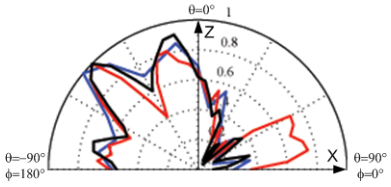
(a) Topology [23]



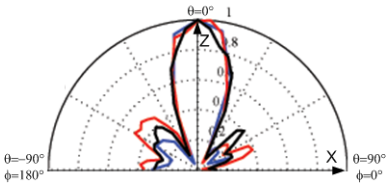
(b) Photo of LWA design of 8 cells, working around 1 GHz



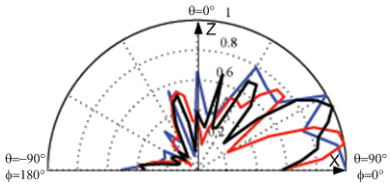
(c) 1189 MHz



(d) 1224 MHz



(e) 1320 MHz



(f) 1502 MHz

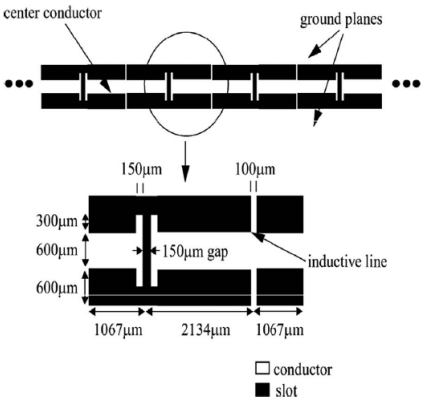
Figure 3.12. *Metamaterial planar LWA inspired by Fig. 3.10(a) working around 1 GHz, the parameters of the cell are : Number of finger $N = 83$, $L_{dg} = 0.2mm$, $l_{ovg} = 14mm$, $e_{IDg} = 0.1mm$, $e_{fg} = 0.1mm$, $L_{fg} = 0.1mm$, $l_{st} = 31.6mm$, $W_{stub} = 3mm$, $d = 0.5mm$, substrate between upper metal and ground plane has following characteristics: $\varepsilon_r = 2.33$, $h = 1.54$ mm, $tg\delta = 0.003$ (in the LWA topology of 3.12(a), grey regions represent metal layers and black circle represents the via between the upper metal layer and the ground plane). Measured radiation patterns for the CRLH LW antenna of Fig. (b) at four frequencies in the leaky wave bands for X-Z ($\phi = 0°$) plane: (c) : $f = 1189$ MHz, (d) : $f = 1224$ MHz, (e) : $f = 1320$ MHz,(f) : $f = 1502$ MHz. The three curves represent the measurement of three identical realisations of the same antenna [23].*

To verify the metamaterial concept, an antenna similar to the one of Caloz has been realised at UCL in our group [23]. This example of balanced TL, which

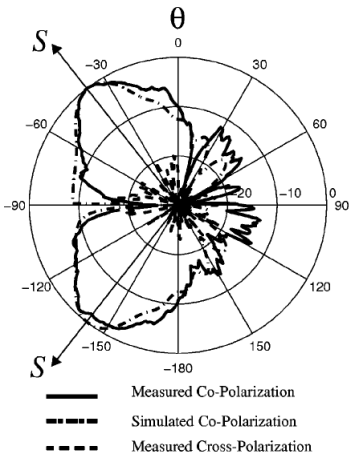
is based on 8 CRLH cells is illustrated in Fig. 3.12(b). It operates at approximately 1 GHz [23]. The radiation patterns are measured from transmission measurements between a log-periodic antenna and the antenna under test with the Agilent PNA-X N5242A vector network analyser in an anechoic chamber for four noticeable frequencies in the LH and RH bands (Fig. 3.12).

In [24], the leaky wave antenna is based on the CPW technology (Fig. 3.13(a)). The series capacitor of the purely LH TL (Fig. 2.1) is created with gaps in the CPW feed line. The shunt inductors are realised with narrow lines and wires connect the center signal line to the ground plane thus incorporating shunt inductances without the need for via-holes. Backward radiation is simulated and observed experimentally in Fig. 3.13(b). To decrease the backside radiation and create a unidirectional antenna, the authors introduce a long metallic through underneath the antenna, in the signal line axis, as shown in Fig. 3.13(c) [25]. This through exhibits the same behaviour as a waveguide operated below its cutoff frequency of the dominant TE_{10} mode.

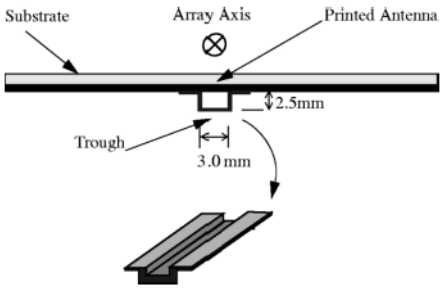
Using the similar concept to the previous idea, the metamaterial transmission line presented in [26] uses the SRR particle to load a CPW in a manner identical to the structure presented in the section 2.3.1 in Fig. 2.9(a). Wires connect periodically the strip to the ground plane, creating the negative permittivity of the LHM. Underlying SRRs are made on the back side of the antenna thus creating the negative permeability of the LHM in a narrowband above the SRR resonance frequency. The topology of this SRR-loaded LWA is shown in Fig. 3.14(a). The simulated dispersion diagram is shown in Fig. 3.14(b). The LH band is defined by the area where the slope of the dispersion diagram is negative, i.e. the group and phase velocities are anti-parallel. To understand the frequency scanning, the structure is simulated with Mentor Graphics IE3D software for LH frequencies in the radiation cone, illustrated in 3.14(b). As expected, a beam steering from backfire to broadside is observed between 7 GHz and 7.23 GHz.



(a) Geometry [24]

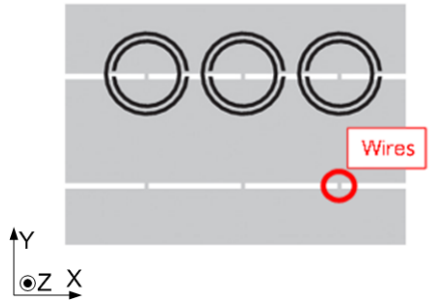


(b) Simulated and measured E-plane far-field patterns of backward-wave radiating meta-material [24]

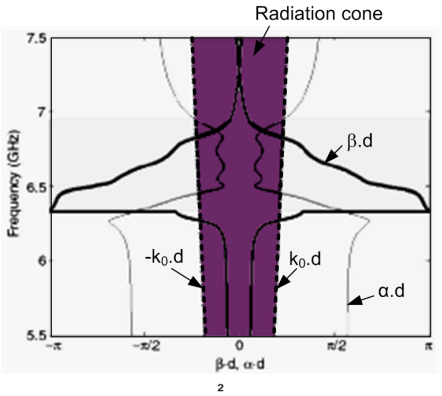


(c) Topology of unidirectional LWA [25]

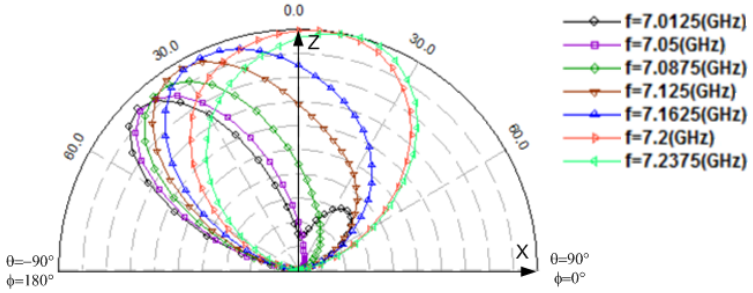
Figure 3.13. *CPW Leaky Wave Antenna (in (a), black regions represent the CPW slots, white regions represent the CPW metal layers, the dimensions of the structure are described in [24].)*



(a) Geometry [26]



(b) Dispersion Diagram [26]



(c) Simulated Radiation Pattern in X-Z ($\phi = 0°$) plane

Figure 3.14. *SRR-loaded CPW LWA. In (a), black regions represent the metal layer made on the backside, grey regions represent the CPW metal layers. The dimensions of the structure are described in [26], the asymmetry of the structure is chosen by the designer. The dispersion diagram is calculated from full-wave electromagnetic simulation (using CST Microwave Studio) of an entire three cells. The magenta area represents the radiation cone defined by the free-space propagation constant k_0. In the IE3D simulation of Fig. (c)an infinite substrate is assumed.*

3.5 CONCLUSION

A leaky wave antenna is a kind of waveguide along which a travelling wave leaks out radiating power and the radiation phenomena do not depend on a resonating-wave mechanism. Continuous, discontinuous or periodic apertures are realised on the waveguide to allow the radiation. For the frequency bands where the velocity of the wave is slower than the speed of light, the wave is evanescent along the unbounded free-space direction [12] and is guided in the antenna. This type of wave is referred to as a slow wave and in this case the structure does not radiate. Contrary to this, for frequency bands where the velocity of the travelling waves is faster than the speed of light, the waves, referred to as fast waves, radiate into free space in a coherent manner at specific angles depending on the frequency. The antenna length is related to the directivity and not to the operation frequency, contrary to resonating-wave antennas. Theoretical or experimental determination of the propagation constant and the leakage factor is essential to establish the properties of the LWA, such as the beam direction, the beamwidth, the radiation efficiency, the variation of the scan angle with frequency.

A LWA can be classified according to the following parameters [16] :

- beam scanning (in one or two dimensions, in the forward or the backward quadrants),
- beam shape (fan beam, pencil beam, conical beam, wide beam),
- geometry (uniform, periodic, quasi-uniform)
- waveguiding structures (metallic, dielectric, printed, planar waveguides, microwaves and millimeter waves guides).

In this work, the LWAs are classified according to geometry [6]:

- *uniform* LWA, in which the LWA geometry has an invariant transverse cross section along the propagation axis. The radiating mode is the dominant leaky mode with a positive propagation constant, allowing therefore frequency scanning in the forward quadrant.
- *periodic* LWA, in which the LWA geometry exhibits a periodic modulation of the waveguide along the axis of propagation in the form of periodic discontinuities (created by metallization, slots, permittivity of permeability transitions). The radiation phenomenon can be described mathematically by the Bloch-Floquet expansion where the wave is viewed as a superposition of infinite number of plane waves. The fundamental mode is generally a guided slow wave whereas the higher mode can be designed to radiate. Contrary to the uniform LWA, periodic LWA can radiate in the backward and forward quadrants, depending on the sign of the radiating space harmonic. A standing wave regime could appear for frequencies at broadside

radiation, in the stop-band region, between the backward regime and the forward regime. The finite-width structure with dielectric substrate can also suffer from the presence of surface waves that can leak power because of the finite width of the metallization and the unbounded grounded substrate in the transverse direction.

- *quasi-uniform* LWA in which the LWA geometry is modulated along the length but the period of the modulation is smaller than the guided wavelength of the travelling wave. Metamarial LWAs are included in this category. The fundamental mode radiates significantly and the contribution of non-zero space harmonics is poor. Contrary to the conventional periodic LWAs, the leakage factor may vary significantly near broadside but drops not sharply to zero on the stop band, avoiding the standing wave regime. The creation of a balanced TL, for which the resonance frequencies of the series and parallel impedances are equal, eliminates the stop-band, i.e. the band-gap between LH and RH bands, and allows a continuous full-space spatial scanning.

Bibliography

[1] W. W. Hansen, "Radiating electromagnetic waveguide," U.S. Patent 2 402 662, Sep. 25, 1940.

[2] M. A. Antoniades and G. V. Eleftheriades, "A cps leaky-wave antenna with reduced beam squinting using nri-tl metamaterials," *IEEE Transactions on Antennas And Propagation*, vol. 56, no. 3, pp. 708 – 721, Mar. 2008.

[3] G. Lovat, "General properties of planar leaky-wave antennas," in *European School of Antennas, High-frequency techniques and Travelling-wave antennas*, La Sapienza University of Rome, Roma, Feb. 2005.

[4] C. Caloz and T. Itoh, "Array factor approach of leaky-wave antennas and application to 1-d/2-d composite right/left-handed (crlh) structures," *IEEE Microwave and Wireless Components Letters*, vol. 14, no. 6, pp. 274 – 276, Jun. 2004.

[5] C. Caloz, D. R. Jackson, and T. Itoh, *Leaky-Wave Antennas.* in Frank B. Gross (Ed), Mc Graw Hill, 2011, ch. Frontiers in Antennas : Next Generation, Design and Engineering, pp. 339 – 410.

[6] A. A. Oliner and D. R. Jackson, *Leaky-Wave Antennas.* in John L. Volakis (Ed), Mc Graw Hill, 2007, ch. Antenna Engineering Handbook, Fourth Edition, pp. 11.1 – 11.56.

[7] S. J. Orfanidis, *Electromagnetic Waves and Antennas.* Prentice-Hall, 2003.

[8] F. Frezza, "Introduction to travelling-wave antennas," in *European School of Antennas, High-frequency techniques and Travelling-wave antennas*, La Sapienza University of Rome, Roma, Apr. 2008.

[9] F. J. Zucker, *Surface-Wave Antennas.* in John L. Volakis (Ed), Mc Graw Hill, 2007, ch. Antenna Engineering Handbook, Fourth Edition, pp. 10.1 – 10.32.

[10] R. A. Gilbert, *Waveguide Slot Antenna Arrays.* in John L. Volakis (Ed), Mc Graw Hill, 2007, ch. Antenna Engineering Handbook, Fourth Edition, pp. 9.1 – 9.36.

[11] C. Caloz and T. Itoh, *CRLH Metamaterial Antennas, Part II : Leaky-Wave and Resonant Antennas.* in F. Capolino, CRC Press Inc, 2009, ch. Applications of Metamaterials, pp. 16–1 – 16–21.

[12] P. Baccarelli, S. Paulotto, D. R. Jackson, and A. A. Oliner, "A new brillouin dispersion diagram for 1-d periodic printed structures," *IEEE Transactions on Microwave And Techniques*, vol. 55, no. 7, pp. 1484 – 1495, Jul. 2007.

[13] T. A. Milligan, *Modern Antenna Design, Second Edition.* IEEE Press, J. Wiley And Sons INC. Publication, 2005.

[14] D. Jackson and A. Oliner, *Leaky Wave Antennas.* in Balanis C.A. (Ed), Wiley, 2008, ch. Modern Antenna Handbook, pp. 325 – 368.

[15] W. L. Stutzman and G. A. Thiele, *Antenna Theory and Design, 2nd Edition.* John Wiley and Sons, 1998.

[16] A. Galli, "Leaky-wave antennas : Fundamentals," in *European School of Antennas, High-frequency techniques and Travelling-wave antennas*, La Sapienza University of Rome, Roma, Feb. 2005.

[17] T. Bertuch, "Dispersion properties of periodically loaded parallel-plate waveguides, analysis and leaky-wave antenna application," in *European School of Antennas, High-frequency techniques and Travelling-wave antennas*, La Sapienza University of Rome, Roma, Apr. 2011.

[18] C. Caloz and T. Itoh, *Electromagnetic metamaterial : Transmission line and microwave applications.* Wiley, 2006.

[19] P. Burghignoli, "1-d periodic leaky-wave antennas: Radiation properties and design aspects," in *European School of Antennas, High-frequency techniques and Travelling-wave antennas*, La Sapienza University of Rome, Roma, Apr. 2011.

[20] ——, "Modal analysis of 1-d periodic planar leaky-wave antennas (3-d fields): Surface and spatial leaky-wave regimes," in *European School of Antennas, High-frequency techniques and Travelling-wave antennas*, La Sapienza University of Rome, Roma, Apr. 2011.

[21] C. Balanis, *Antenna Theory, 3rd edition.* Wiley, 2005.

[22] G. Mumcu, K. Sertel, and J. L. Volakis, *Metamaterial Antennas.* in Frank B. Gross (Ed), Mc Graw Hill, 2011, ch. Frontiers in Antennas: Next Generation, Design and Engineering, pp. 203 – 239.

[23] P. Collin and N. Serra, "Travail de fin d'etudes, localisation de tag-rf en metamateriaux a l'aide d'un reseau lineaire d'antennes dipoles," Université catholique de Louvain, Ecole Polytechnique de Louvain, Tech. Rep., Jun. 2007, promoteur : Isabelle Huynen, Christophe Craeye.

[24] A. Grbic and G. V. Eleftheriades, "Experimental verification of backward-wave radiation from a negative refractive index metamaterial," *Journal of applied physics*, vol. 92, no. 10, pp. 5930 – 5935, Nov. 2002.

[25] ——, "Experimental verificiation of backward-wave radiation from a negative refractive index metamaterial," *Journal of Applied Physics*, vol. 92, no. 10, pp. 5930 – 5935, Nov. 2002.

[26] I. Arnedo, J. Illescas, M. Flores, T. Lopetegi, M. Laso, F. Falcone, J. Bonache, J. Garcia-Garcia, F. Martin, J. Marcotegui, R. Marques, and

M. Sorolla, "Forward and backward leaky wave radiation in split-ring-resonator-based metamaterials," *IET Microwave, Antennas, Propagation, Special Issue on Metamaterials LHM*, vol. 1, no. 1, pp. 65 – 68, Feb. 2007.

CHAPTER 4

LEAKY WAVE ANTENNA BASED ON COMPLEMENTARY SPLIT RING RESONATOR

This chapter presents the analysis of the radiation of the leaky wave antenna (LWA) based on Complementary Split Ring Resonators (CSRRs) and some variants of this structure.

4.1 INTRODUCTION

As seen in the previous chapter, LWAs are based on a travelling wave in a guiding structure as the main radiating mechanism. Most LWAs have the property that the beam scans with frequency. They offer the advantage of elementary nature [1], since no complicated feed network is required, as for example in a planar antenna array. Over the past years, transmission line metamaterial structures, loaded with reactive elements, were proposed as backward and forward scanning LWAs [2–4]. To the best of our knowledge, very little work on Complementary Split Rings Resonators (CSRRs) structures for travelling wave antennas has been reported yet. In this chapter, the radiation phenomena in a CRLH TL based on CSRRs, presented in the section 2.3, are investigated in order to obtain a LWA.

The first section presents this leaky wave antenna, first the propagation characteristics and secondly the radiation performance of a LWA created from a CRLH TL based on CSRRs. Full-wave simulation and measurement of the radiation performances are presented for a LWA, created from a transmission line

loaded by gaps and CSRRs. Some of the results discussed in the current chapters were published in the conference proceeding [5] and in the article [6].

The second section presents a solution of unidirectional LWA using the CSRR concept. The third section analyses a tunable CSRR loaded LWA, using ferroelectric film or varactor component. Secondly, a special emphasis is put on the influence of a geometrical parameter, namely the number of concentric split rings of the CSRR, on the radiation properties of a LWA based on CSRRs. The work reported here is the subject of the following article : [7].

Finally the aim of the last section is to analyse an exhaustive list of similar structures with the objective of using them as classical full-scanned (eventually balanced[1]) LWAs with a broadside radiation.

4.2 LEAKY WAVE ANTENNA LOADED BY DOUBLE CSRR

4.2.1 Transmission line behaviour

4.2.1.1 Topology

The sub-wavelength resonators considered in this chapter is shown in Fig. 4.1(a)-(b), this structure has been already presented in the section 2.3 and are used to load a microstrip line with the aim of creating a CRLH TL. We analyse the radiation behaviour of this structure as a LWA. As reminder, the series gaps of Fig. 4.1(a) provide the negative effective permeability of the structure, whereas the CSRRs are responsible for the negative effective permittivity and hence the periodic structure can be considered as a CRLH line. In fact, it exhibits similar characteristics : it has right-hand and left-hand frequency bands [3], which depends on the respective capacitive or inductive behaviour of the series and parallel branches of the equivalent circuit [8].

4.2.1.2 Dimensionning

We have implemented the structure of Fig. 4.1(a) on a dielectric substrate, which is Rogers RT5870 ($\varepsilon_r = 2.33$, $h = 0.5$ mm, $tg\delta = 0.003$) with low permittivity and weak losses to assure good radiation performances, the substrate is deliberately chosen electrically thin in order to avoid strong excitation of substrate higher modes. The CRLH unit cell is designed for left-hand leaky-wave antenna operation at approximately 3 GHz. The parameters of the cell are: $r_{in} = 3.5$ mm, $r_{out} = 4.5$ mm, $G = 1$ mm, $C = 0.5$ mm, $D = 0.5$ mm, $W_{out} = 1$ mm, $W_{in} = 1$ mm, $W = 1.47$ mm. W dimension is chosen to create a TL impedance characteristic, Z_0, around 3 GHz [9]. C and D dimensions are limited by minimal fabrication limits of the UCL process. The size of the TL is fixed to 16 CSRR cells and is a compromise between the directivity of the LWA and the conditions of fabrication (the maximal length of the TL is around 20 cm). The

[1] A balanced metamaterial TL does not present a stop-band between the right and left leaky regions. Therefore a balanced LWA presents, as a result, a full-space frequency scanning [3]. This concept is presented in sections 2.2 and 3.4

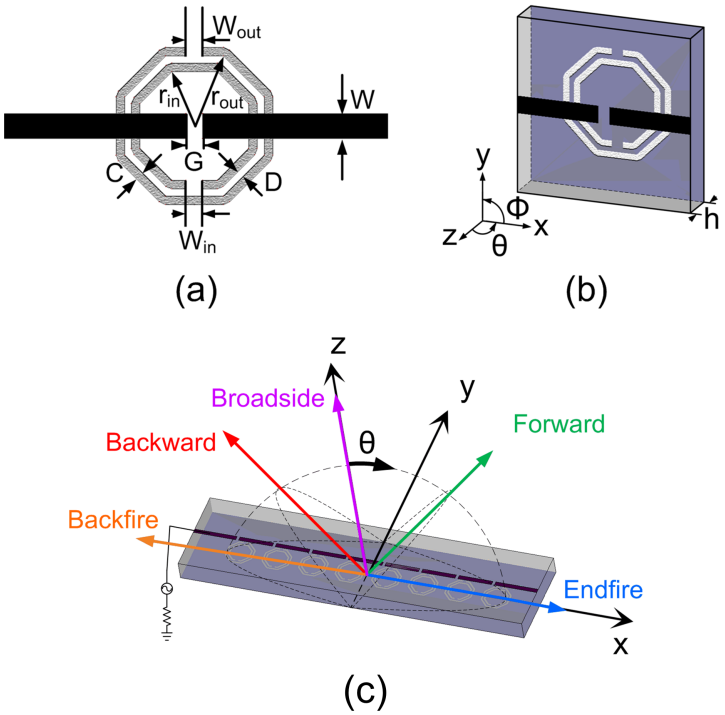


Figure 4.1. *CSSR structure (ground plane is depicted in grey whereas upper metal is depicted in black. The substrate between upper metal and ground plane has the following characteristics:* $\varepsilon_r = 2.33$, $h = 0.5$ *mm,* $tg\delta = 0.003$ *: (a) Layout (dimensions are:* $r_{in} = 3.5$ *mm,* $r_{out} = 4.5$ *mm,* $G = 1$ *mm,* $C = 0.5$ *mm,* $D = 0.5$ *mm,* $W_{out} = 1$ *mm,* $W_{in} = 1$ *mm,* $W = 1.47$ *mm) (b) 3D view, (c) View of transmission line created by a cascade of 8 cells with source (distance between CSRRs : 2.5 mm)*

other parameters are optimised from simulation in order to target the desired frequency range. Fig. 4.2 shows the fabricated TL based on 16 CSRRs, lying on a Rogers RT5870 substrate. The distance between CSRRs and substrate edges is fixed to 95 mm in order to approach the condition of an infinite substrate, which is assumed in IE3D simulation, and in order to avoid spurious radiation from the reflection of surface waves at the substrate edges [5]. This will be discussed in more detail in the next section. The ring shape is a hexagon for two reasons: firstly to avoid memory overflow from the full-wave electromagnetic simulations when finite ground plane and substrate option is activated and secondly to facilitate further parametric study of the structure.

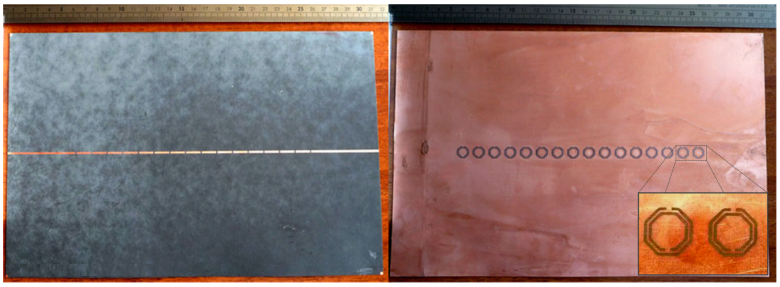


Figure 4.2. *Photos of cascade of 16 cells, corresponding to the layout described in Fig. 4.1(a). Left : strip metal and right : ground plane (antenna length = 20cm).*

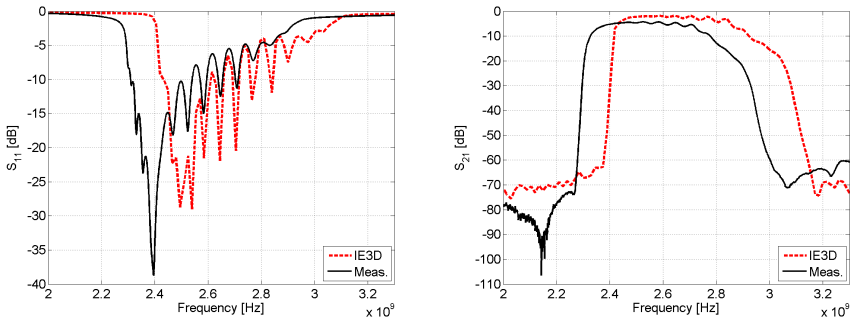
4.2.1.3 Simulation tools

The full-wave electromagnetic simulations are done with IE3D software [10] and the COMSOL solver [11]. Mentor Graphics IE3D is a EM platform using the full-Wave 3D Method-of-Moments (MoM). COMSOL Multiphysics (formerly FEMLAB) is a Multiphysics Finite Element Method solver. IE3D is the main software used in this work, due to its speed and its ability to perform parametric analyses. IE3D offers also useful modelling tools to analyse the radiation performances of the structure. IE3D also present an parametric analysis, used in the section 4.5.3. However, contrary to COMSOL solver, the IE3D software can not handle lumped elements such as the varactors with DC voltages, which are useful for the tunable antenna described in the next chapter. The COMSOL solver has also a tool to simulate the electric distribution across the ring, this tool will be used in the next chapter to understand the some specific behavior of the analysed antennas. As a result of this, it will often be necessary to compare the results generated by the *IE3D approach*, which as noted previously assumes an infinite substrate, and the data extracted from the *COMSOL solver*.

4.2.1.4 Propagation Characteristics

The S-parameters are simulated with COMSOL solver and with IE3D software (with the assumption of infinite substrate and ground planes) and are measured using a Vector Network Analyser (VNA) Agilent PNA-X N5242A and a 40 GHz Universal Test Fixture. The calibration is realised with an Agilent Electronic Calibration (ECal) Module N4691-60006 based on a *SOTL* technique (Short Open Through Line) [12]. The next two sections are devoted to the analysis of the left-hand and the right-hand bands. For a reason of thesis compactness, the results of the COMSOL simulation of CSRR-loaded LWAs are presented in annex F.

Left-hand band. Fig. 4.3 illustrates the comparison between simulation and experimental results for the left-hand band of the LWA created from a CRLH TL based on CSRRs. Discrepancies between measurements and IE3D simulations are probably explained by fabrication tolerances and the influence of meshing. Globally the analysis of the propagation characteristics and the radiation performances, presented in the next section, have presented quite the same behaviour except this frequency shift, so discrepancies are neglected.



(a) S_{11} ***(b)*** S_{21}

Figure 4.3. *S-parameters of TL loaded by 16 CSRRs of Fig. 4.1(a) measured (black solid), simulated with IE3D (red dashed) in the left-hand band. The COMSOL simulation is illustrated in Fig. F.1.*

The propagation characteristics are extracted from S-parameters by the following methodology. The impact of the access lines is firstly removed by using the de-embedding technique of two lines described in [13]. Then the $ABCD$ matrix is calculated from the S-matrix [14]. The $ABCD$ matrix of a TL defines the relationship between the voltage and current waves at the access ports of the TL, which are referred to here as port 1 and port 2. This relationship may be written as [15]:

$$\begin{bmatrix} V_1 \\ I_1 \end{bmatrix} = \begin{bmatrix} A & B \\ C & D \end{bmatrix} \cdot \begin{bmatrix} V_2 \\ I_2 \end{bmatrix} = \begin{bmatrix} \cosh \phi_{TL} & Z_0 \sinh \phi_T L \\ Z_0^{-1} \sinh \phi_{TL} & \cosh \phi_{TL} \end{bmatrix} \cdot \begin{bmatrix} V_2 \\ I_2 \end{bmatrix} \quad (4.1)$$

where Z_0 is the characteristic impedance and ϕ_{TL} is determined from the complex propagation constant γ as [14]:

$$\phi_{TL} = acosh(\frac{A+D}{2}) = \gamma N L \quad (4.2)$$

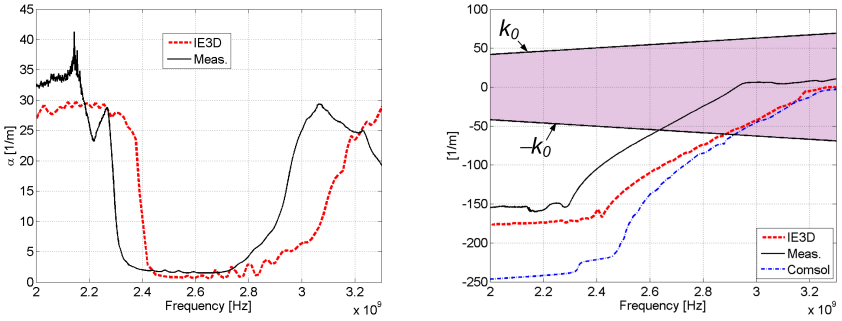
where L is the length of one unit cell and N the number of cells used to load the TL. The leakage factor, α, and the propagation constant, β, may then be

written as:

$$\alpha = \frac{Re(\phi)}{NL} \tag{4.3}$$

$$\beta = \frac{Im(\phi)}{NL} \tag{4.4}$$

Fig. 4.4 illustrates the leakage factor α and the propagation constant β of the equivalent TL, extracted from the S-parameters of the cascade of 16 cells similar to Fig. 4.1(c).

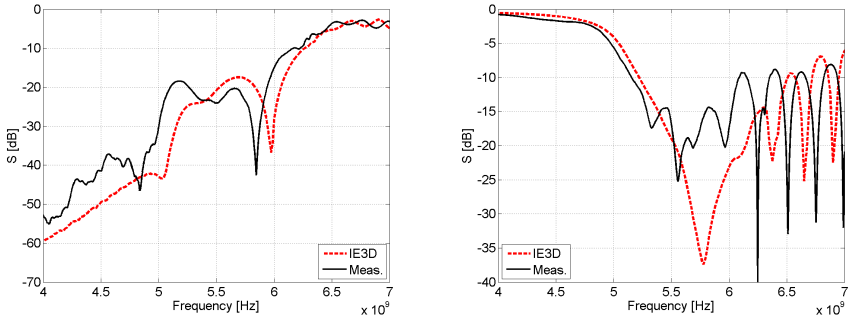


(a) Leakage factor α ***(b)*** Propagation constant β

Figure 4.4. *Propagation characteristics as calculated from the S-parameters shown in Fig. 4.3 using eqs. 4.4 and 4.3 of the TL loaded by 16 CSRRs depicted in Fig. 4.1. The calculations shown pertain to the measured case (black solid), the IE3D case (red dashed) and the COMSOL case (blue dashdot) in the left-hand band. The magenta area represents the radiation cone defined by the free-space propagation constant k_0. The COMSOL simulation of the leakage factor is illustrated in Fig. F.2.*

Right-hand band. The TL loaded by CSRR and gaps is also analysed in the right-hand region. Globally the behaviour as a leaky wave is similar to the classical theory discussed in the previous chapter. The same methodology, which was explained in the previous section, is applied to extract the propagation characteristic. The S parameters were measured with the same setup and simulated with the same assumption and are shown in Fig. 4.5. The dispersion diagram and the leakage factor are shown in Fig. F.5. Discrepancies between measurements and IE3D simulations are explained by fabrication tolerances. Discrepancies between COMSOL simulation, presented in annex F, and measurements are explained by the influence of too simplified meshing, indeed the simulated structure must be long enough to radiate the main part of the energy, but it includes small dimensions around the CSRR. So for memory reasons, we had to accept to decrease the

meshing characteristics of the simulation. That creates a shift in lower frequencies of the S-parameters, but globally the analysis of the propagation characteristics, shown in Fig. 4.6(b) and the radiation performances, presented in the next section, have presented quite the same behaviour except this frequency shift, so we have kept this simulation for the section of the physical explanation.



(a) S_{21} *(b)* S_{11}

Figure 4.5. *S-parameters of TL loaded by 16 CSRRs of Fig. 4.1 measured (black solid), simulated with IE3D (red dashed) in the right-hand band. The COMSOL simulation is illustrated in Fig. F.4*

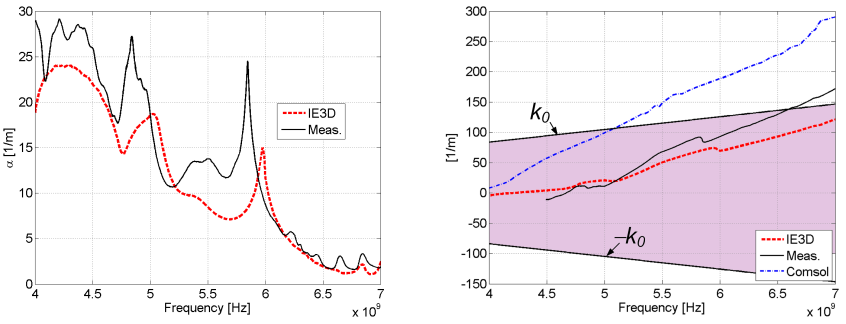
4.2.2 Leaky wave radiation

As explained in the previous chapter, LWAs support a fast wave on the guiding structure when β is lower than the free-space propagation constant, k_0, i.e. when β is within the radiation cone of Fig. 4.4(b). The leaky wave is therefore fundamentally a radiating type of wave, which radiates power continuously in free space as it propagates on the guiding structure. Generally, β controls the beam angle, while α controls the beamwidth [1]. The expression of the main beam θ_{MB} of LWA is [1]:

$$\sin(\theta_{\mathrm{MB}}) \quad = \quad \frac{\beta}{k_0} \tag{4.5}$$

Depending on the value of β, the beam angle can theoretically be scanned from -90° (backfire) to 90° (endfire) as shown in Fig. 4.1(c).

From Fig. 4.4, it is concluded that our LWA, using the 16-cells structure similar to depicted in Fig. 4.1(c), should operate as a backward LWA from $\theta_{\mathrm{MB}} =$ -90° ($\beta = -k_0$), backfire, to $\theta_{\mathrm{MB}} = 0°$ ($\beta = 0$), broadside. This type of operation can be seen to occur between 2.84 GHz and 3.11 GHz according to the IE3D simulation, between 2.9 GHz to 3.275 GHz according to the COMSOL simulation



(a) α *(b)* β

Figure 4.6. *Propagation characteristics as calculated from the S-parameters shown in Fig. 4.5 using eqs. 4.4 and 4.3 of the TL loaded by 16 CSRRs depicted in Fig. 4.1. The calculations shown pertain to the measured case (black solid), the IE3D case (red dashed) and the COMSOL case (blue dashdot) in the right-hand band. The magenta area represents the radiation cone defined by the free-space propagation constant* k_0*. The COMSOL simulation of the leakage factor is illustrated in Fig. F.2.*

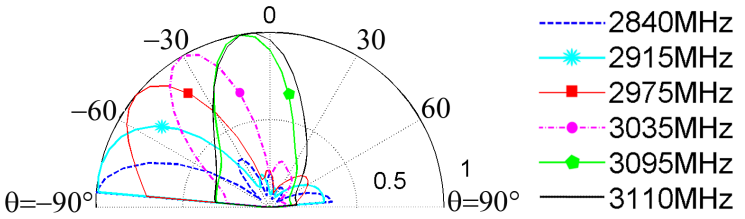
and between 2.7 GHz and 2.92 GHz according to the measurement. This region of left-hand band will henceforth be referred to as the, "left-leaky region".

From Fig. F.5, right-hand leakage radiation appears from $\theta_{\mathsf{MB}} = 0°$ ($\beta = 0$) to $\theta_{\mathsf{MB}} = 90°$ ($\beta = k_0$) between 4.8 GHz and 6.3 GHz according to the measurement results, between 4.8 GHz and 6.4 GHz according to the IE3D simulation and between 4 GHz and 5.1 GHz according to the COMSOL simulation. This region of right-hand band will henceforth be referred to as the, "right-leaky region".

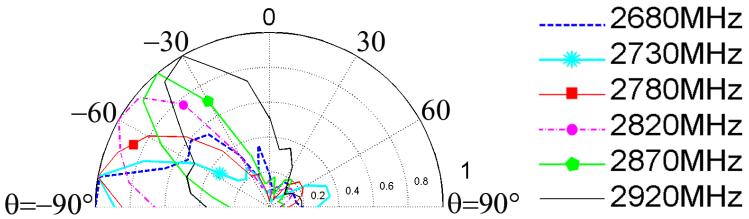
The radiation performance of this LWA will be simulated in the section 4.2.2.1 and will be measured in the section 4.2.2.2. Section 5.1 in chapter 5 will contain a physical explanation for the radiation near the broadside direction.

4.2.2.1 *Simulation results*

IE3D software from Zeland is used to simulate the 3D radiation pattern of the TL based on the 16 cells from Fig. 4.1(a) in the left-leaky region. The structure is simulated assuming an infinite substrate. To validate the results of this software and to avoid this hypothesis of infinite substrate, COMSOL solver is also used to simulate the radiation pattern of this structure, the result is shown in Fig. F.3. Fig. F.3(a) shows 2D views of the IE3D-simulated radiation pattern for the left-leaky region in the ($\phi = 0°$) X-Z plane, validating the frequency beam scanning in the left-leaky region.



(a) IE3D Simulation



(b) Measurement

Figure 4.7. *Normalized 2D radiation pattern in (ϕ = 0°) X-Z plane for the TL based on 16 cells of Fig. 4.1(a) simulated with IE3D (with the assumption of infinite substrate) (a), and measured (b) for different frequencies in the left-leaky region. The COMSOL simulation is illustrated in Fig. F.3(a).*

Left-Leaky Region : Fig. 4.8 shows corresponding 2D views of the simulated radiation pattern in the (θ = 90°) X-Y plane. Fig. 4.9 shows 3D views of the simulated radiation pattern at three illustrative frequencies of interest in the left-leaky region :

- The radiation pattern was first simulated at 2.84 GHz because it is the lowest frequency of the left-leaky region, corresponding to $\beta = -k_0$, therefore to θ_{MB} = -90° from (4.5).
- Secondly 2.975 GHz was used because this frequency is in the middle of the left-leaky region.
- Finally 3.11 GHz was used because this frequency is close to the upper frequency of the left-leaky region, corresponding to $\beta = 0$, therefore to $\theta_{\mathrm{MB}} = 0°$ from (4.5).

These simulations into Fig. 4.9, combined with the ones in Fig. 4.8, clearly show that ***radiation seems to be equally splitted into two different directions resulting in two apparent beams in the plane of the substrate***: one beam steering from $\phi = 180°$ to $\phi = 90°$ and the other steering from $\phi = 180°$ to $\phi = 90°$. ***Clearly, the radiation is not maximal in the broadside direction as predicted by the theory.***

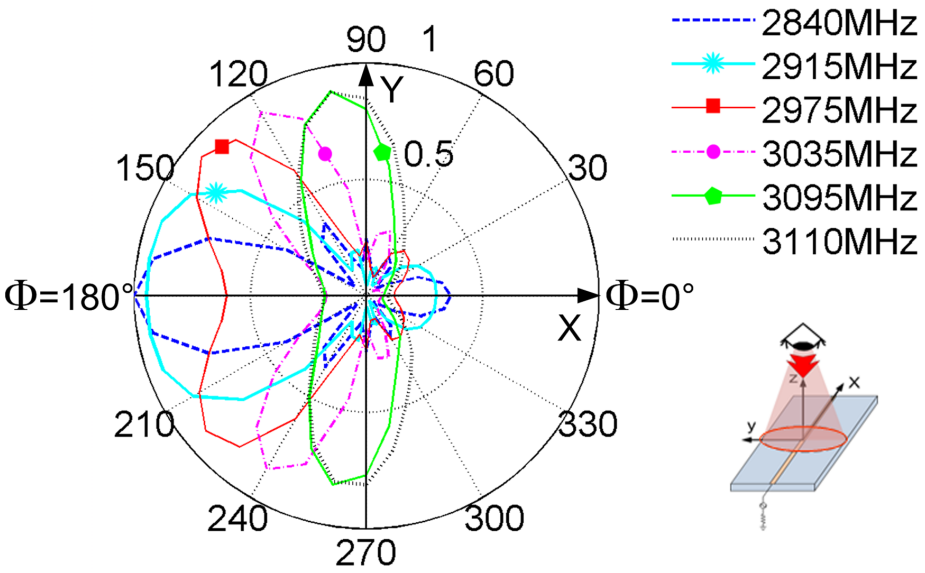


Figure 4.8. *Normalized 2D radiation pattern in ($\theta = 90°$) X-Y plane for the TL based on 16 cells of Fig. 4.1(a) simulated with IE3D (with the assumption of infinite substrate) for different frequencies in the left-leaky region.*

Right-Leaky Region : The frequency scanning capabilities are illustrated in the right-leaky region by Fig. 4.10, showing the 2D radiation pattern in the ($\phi = 0°$) X-Z plane using both IE3D. Fig. 4.11 shows the 3D view of the radiation pattern simulated with IE3D software at three illustrative frequencies of interest in the right-leaky region :

- The radiation pattern was first simulated at 4.805 GHz because it is the lowest frequency of the right-leaky region, corresponding to $\beta = 0$, therefore to $\theta_{\mathrm{MB}} = 0°$ from (4.5).
- Secondly 5.405 GHz was used because this frequency is in the middle of the right-leaky region.
- Finally the upper frequency of the right-leaky region, corresponding at 6.3 GHz, so corresponding to $\beta = k_0$, therefore to $\theta_{\mathrm{MB}} = 90°$ from (4.5) was used.

In this case, the radiation is ***maximal in the broadside direction as predicted by the theory*** for the lowest frequency of the right-leaky region. This approach agrees on a frequency scanning ability in the right-hand region.

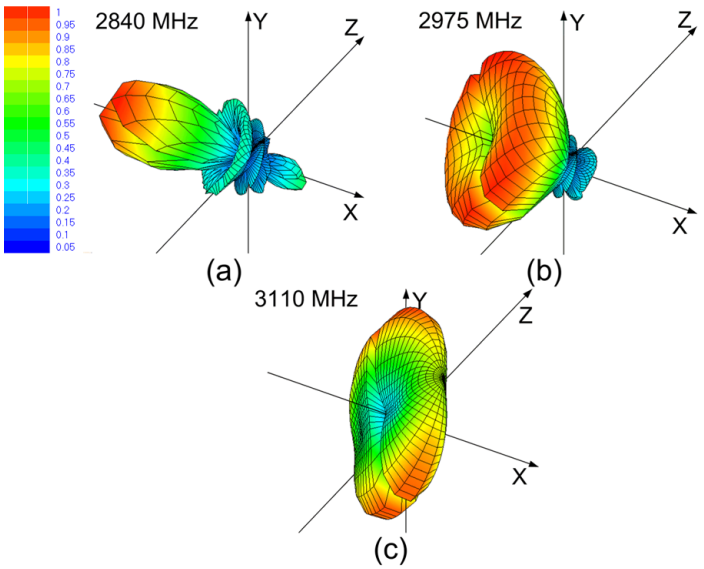
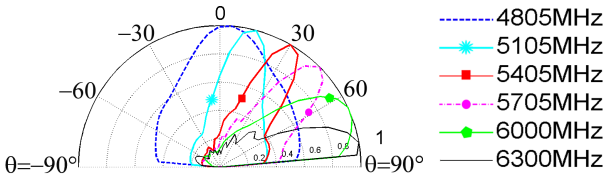
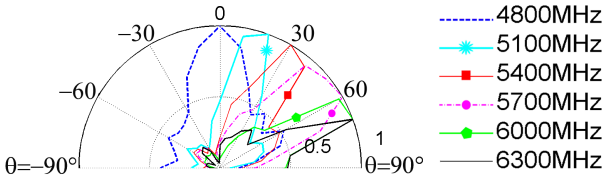


Figure 4.9. *Normalized 3D radiation pattern for the TL based on 16 cells of Fig. 4.1(a) simulated with IE3D software assuming an infinite substrate at 3 frequencies in the left-leaky region. Color bar: blue corresponds to zero, red corresponds to 1 : (a) 2.84 GHz ($\beta = -k_0$), (b) 2.975 GHz, (c) 3.11 GHz ($\beta \approx 0$).*



(a) IE3D Simulation



(b) Measurement

Figure 4.10. *Normalized 2D radiation pattern in ($\phi = 0°$) X-Z plane for the TL based on 16 cells of Fig. 4.1(a) simulated with IE3D (with the assumption of infinite substrate) (a) and measured (b) for different frequencies in the right-leaky region.*

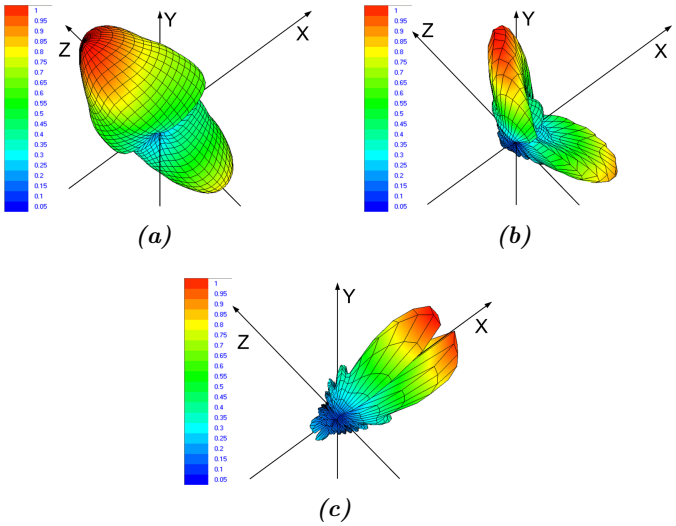
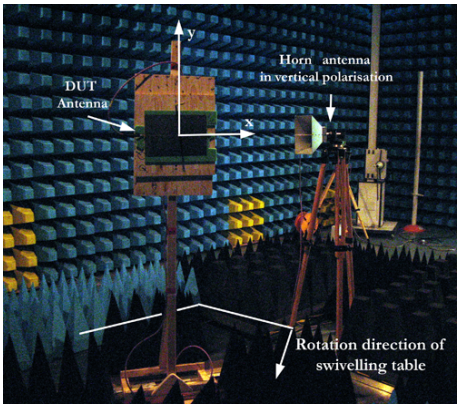
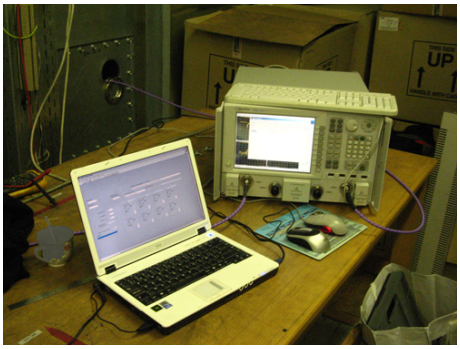


Figure 4.11. *Normalized 3D radiation pattern for the TL based on 16 cells of Fig. 4.1(a) simulated with IE3D assuming an infinite substrate at 3 frequencies in the right-leaky region. Color bar: blue corresponds to zero, red corresponds to 1 : (a) 4.805 GHz ($\beta = 0$), (b) 5.405 GHz, (c) 6.3 GHz ($\beta \approx k_0$).*

4.2.2.2 Experimental Results



(a)



(b)

Figure 4.12. *Photos of the measurement set-up in the anechoic chamber (left : view of a horn antenna Schwarzbeck BBHA 9120D and the antenna under test with the swivelling table inside the ANPI anechoic chamber; right : view of the VNA Agilent PNA-X N5242A and the computer commanding the swivelling table outside the anechoic chamber).*

Setup Environment : The radiation patterns are also measured from transmission measurements between a horn antenna Schwarzbeck BBHA 9120D and the antenna under test with the same VNA (used to extract the propagation characteristics in the previous section) in an anechoic chamber. The setup is shown in Fig. 4.12. The antenna under test is placed on a rotating table, controlled by a computer (controlling also the VNA). The measurement is repeated for different angles ϕ and θ to create 2D and 3D radiation patterns. The characteristics of the horn antenna are de-embedded following the methodology presented in [16].

Left-Leaky Region : Recall that Fig. 4.7(b) illustrates corresponding 2D views of the measured radiation pattern for the left-leaky region in the ($\phi = 0°$) X-Z plane, validating the frequency beam scanning in the left-leaky region. Indeed, the qualitative agreement between Fig. 4.7(a), Fig. F.3(a) and Fig. 4.7(b) is very good, given that in all likelihood there would occur frequency shifts between measurements and simulations due to fabrication tolerances.

Fig. 4.13, Fig. 4.14 and Fig. 4.15 show 3D views of the measured radiation pattern at three illustrative frequencies of interest in the left-leaky region :

- 2.73 GHz was first measured because it is the lowest frequency of the left-leaky region, corresponding to $\beta = -k_0$, therefore to θ_{MB} = -90° from (4.5).
- Secondly 2.82 GHz was measured because this frequency is in the middle of the left-leaky region.
- Finally 2.92 GHz is measured because this frequency is the upper frequency of the left-leaky region, corresponding to $\beta = 0$, therefore to $\theta_{MB} = 0°$ from (4.5).

Comparison between Fig. 4.13(b), Fig. 4.14(b) and Fig. 4.15(b) shows again a **frequency beam steering in the ($\phi = 0°$) X-Z plane**. Comparison between Fig. 4.13(c), Fig. 4.14(c) and Fig. 4.15(c) shows a ***simultaneous frequency beam steering in the plane of the substrate, created by the absence of maximal broadside radiation for upper frequencies of the left-leaky region***. Moreover, the qualitative agreement between 3D views of Fig. F.3 and of Fig. 4.13-4.14-4.15 is very good, again recalling the frequency shift between measurements and simulation due to fabrication tolerances. It is worth mentioning that the radiation is weaker at 2.92 GHz due to poor matching of the structure at that frequency ($|S_{11}| < -2\,dB$). Indeed matching deteriorates at the upper limit of the left-leaky region in such a structure, as observed in Fig. 4.3.

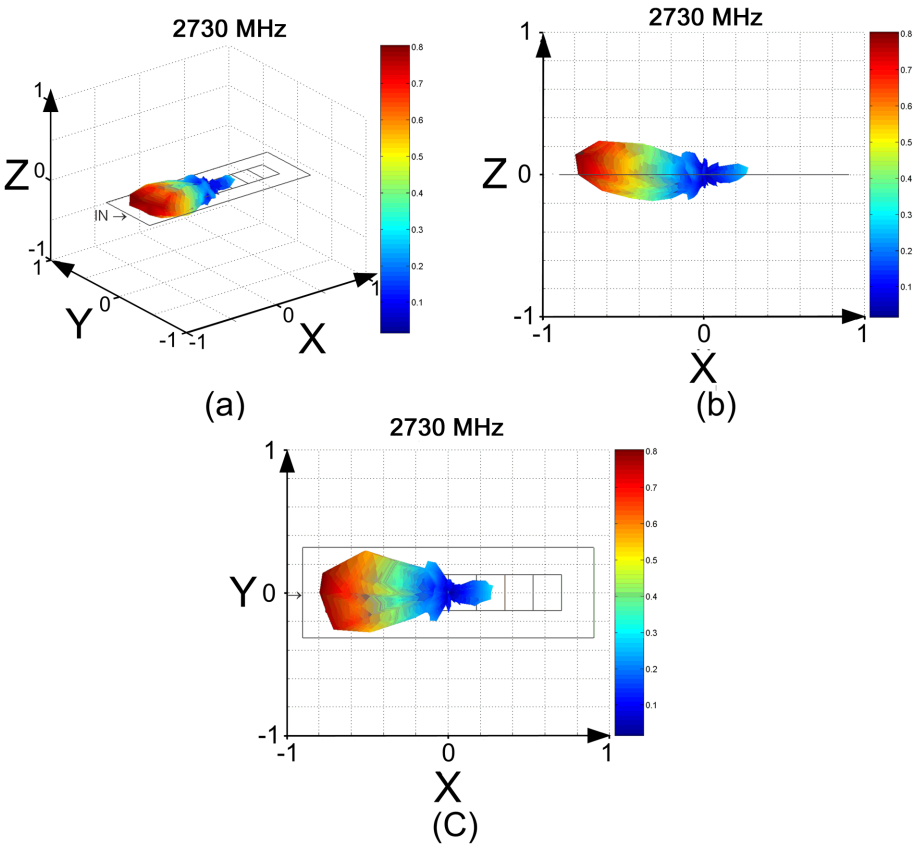


Figure 4.13. *3D view (a), 3D view of ($\phi = 0°$) X-Z plane (b) and 3D top view along the z-axis (c) of measurement of normalised radiation pattern of Fig. 4.2 at 2.730 GHz, corresponding to lowest frequency of the* ***left-leaky region****. Color bar: dark blue corresponds to zero, dark red corresponds to 0.8.*

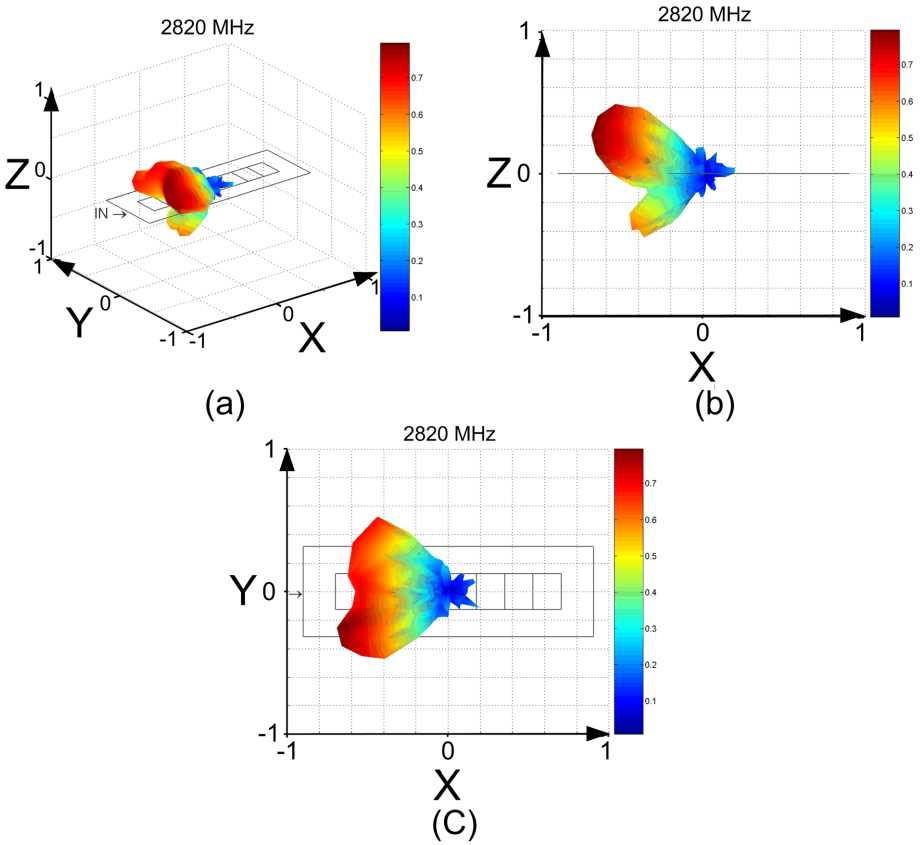


Figure 4.14. *3D view (a), 3D view of ($\phi = 0°$) X-Z plane (b) and 3D top view along the z-axis (c) of measurement of normalised radiation pattern of Fig. 4.2 at 2.820 GHz, corresponding to the center of the* ***left-leaky region****. Color bar: dark blue corresponds to zero, dark red corresponds to 0.8.*

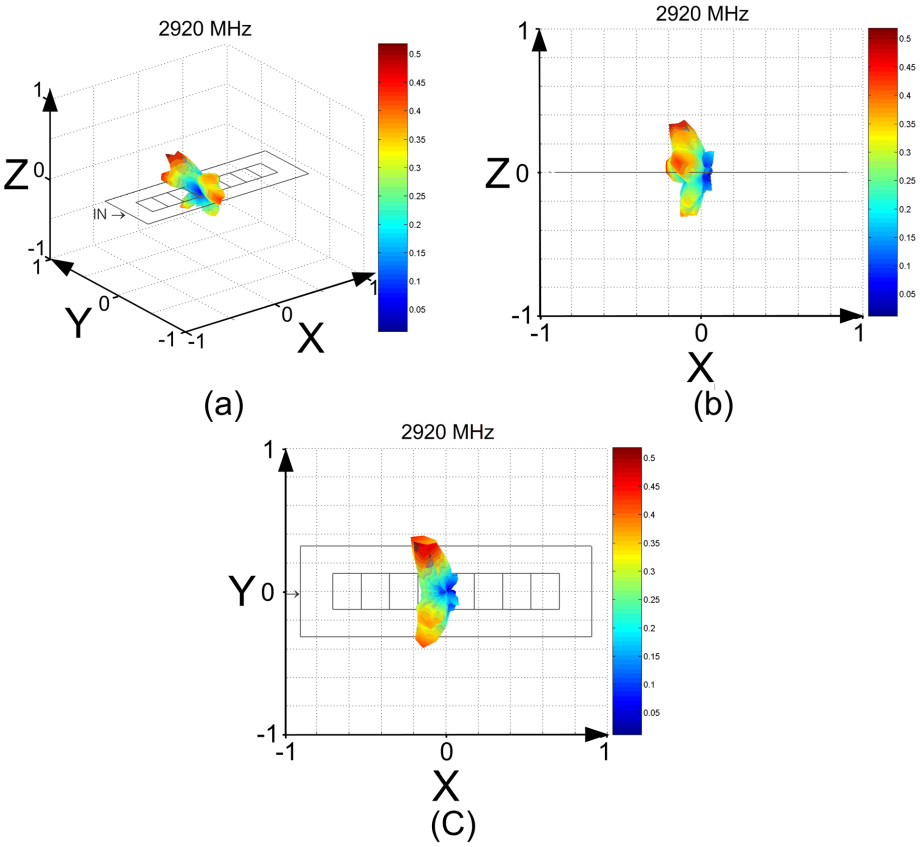


Figure 4.15. *3D view (a), 3D view of ($\phi = 0°$) X-Z plane (b) and 3D top view along the z-axis (c) of measurement of normalised radiation pattern of Fig. 4.2 at 2.920 GHz, corresponding to upper frequency of the* ***left-leaky region****. Color bar: dark blue corresponds to zero, dark red corresponds to 0.55.*

Right-Leaky Region : The frequency scanning capabilities are illustrated in the right-leaky region by Fig. 4.10, which shows the 2D radiation pattern in the ($\phi = 0°$) X-Z plane for the measurement in the anechoic chamber. Fig. 4.16, Fig. 4.17 and Fig. 4.18 show 3D views of the measured radiation pattern at three illustrative frequencies of interest in the right-leaky region :

- 4.8 GHz was first measured because it is the lowest frequency of the right-leaky region, corresponding to $\beta = 0$, therefore to $\theta_{\mathsf{MB}} = 0°$ from (4.5).
- Secondly 5.4 GHz was measured because this frequency is in the middle of the right-leaky region.
- Finally 6.3 GHz is measured because this frequency is the upper frequency of the right-leaky region, corresponding to $\beta = k_0$, therefore to $\theta_{\mathsf{MB}} = 90°$ from (4.5.

We can also conclude that ***the radiation at the lower frequency of the right-hand band does not show a zero in the broadside direction***.

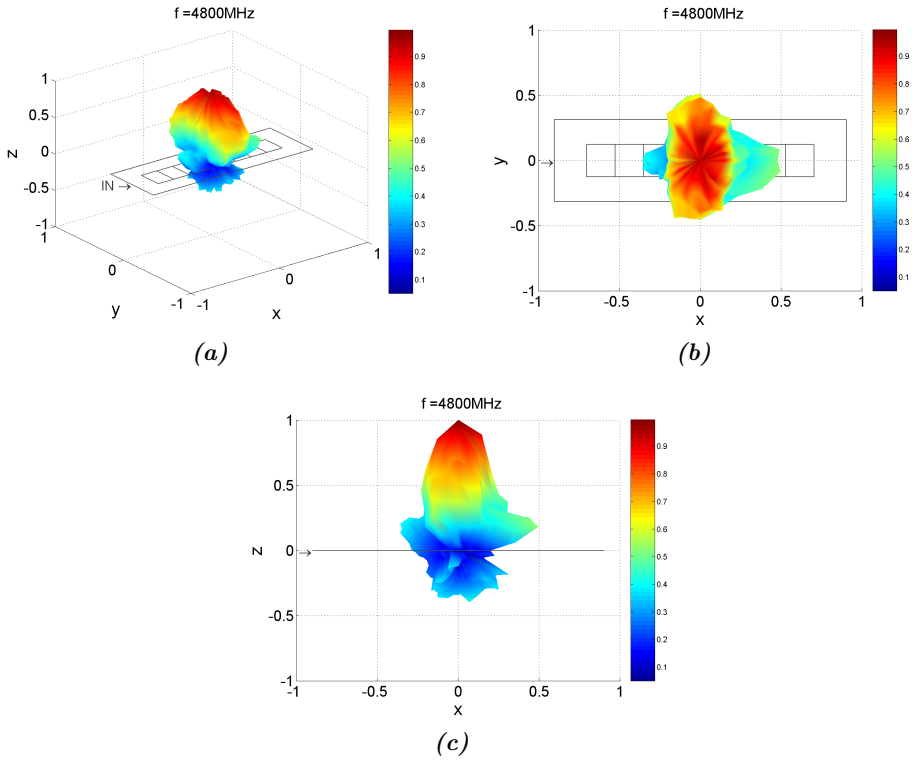


Figure 4.16. *3D view (a), 3D view of ($\phi = 0°$) X-Z plane (b) and 3D top view along the z-axis (c) of measurement of normalised radiation pattern of Fig. 4.2 at 4.8 GHz, corresponding to lowest frequency of the* ***right-leaky region****. Color bar: dark blue corresponds to zero, dark red corresponds to 1.*

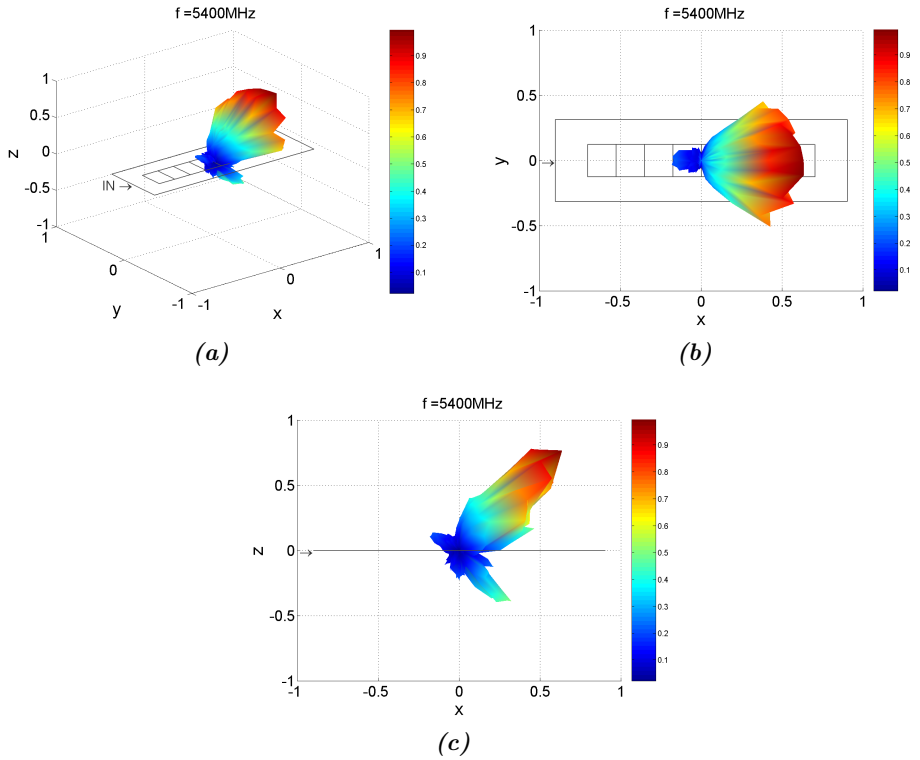


Figure 4.17. *3D view (a), 3D view of ($\phi = 0°$) X-Z plane (b) and 3D top view along the z-axis (c) of measurement of normalised radiation pattern of Fig. 4.2 at 5.4 GHz, corresponding to the center of the right-leaky region. Color bar: dark blue corresponds to zero, dark red corresponds to 1.*

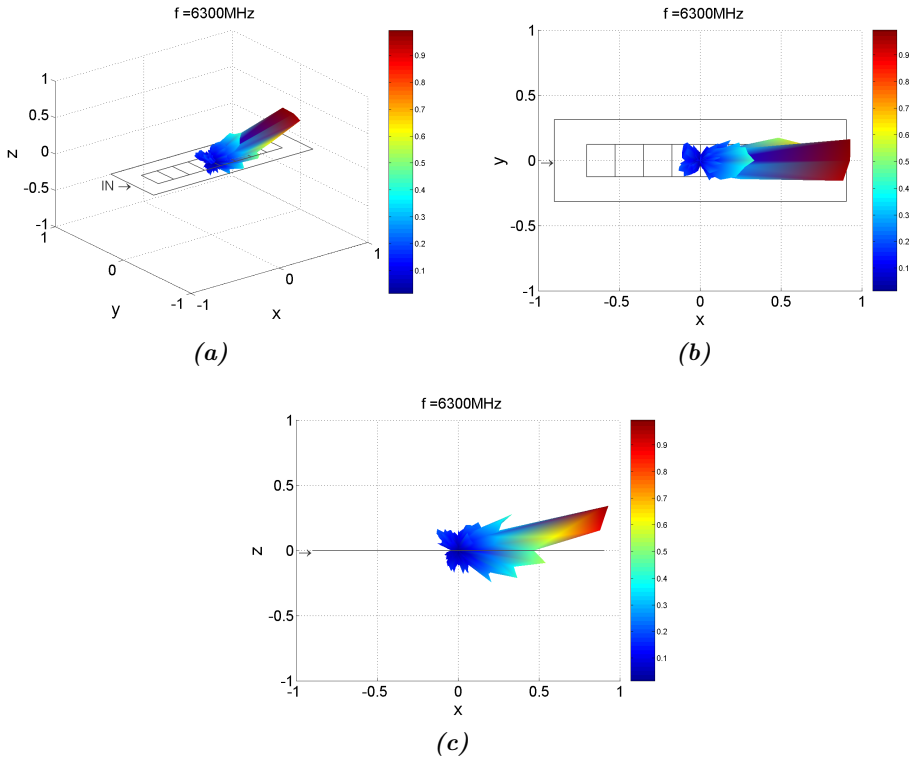


Figure 4.18. *3D view (a), 3D view of ($\phi = 0°$) X-Z plane (b) and 3D top view along the z-axis (c) of measurement of normalised radiation pattern of Fig. 4.2 at 6.3 GHz, corresponding to upper frequency of the right-leaky region. Color bar: dark blue corresponds to zero, dark red corresponds to 1.*

4.2.3 Effect of edges

The focus of this section is on the effect of the finite extent of the substrate. Due to the presence of surface waves (SWs) on the substrate, it would be expected that parasitic interferences would probably appear as the physical dimensions of the substrate itself interact with the SWs. First, by computation, simulations and nearfield measurements the presence of surface waves will be verified. Finally a model based on electrical dipoles is created to verify the shape of this interference. The objective is to improve the understanding of the influence of surface waves and to avoid their parasitic interferences in our design with the objective to distinguish the SW effects from the LWA radiation.

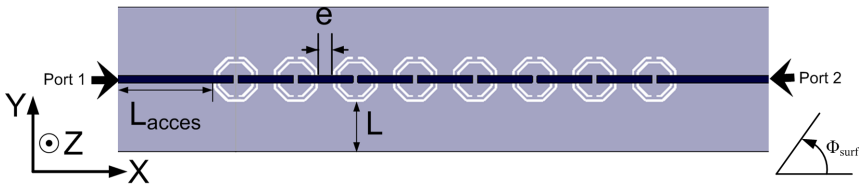


Figure 4.19. *Layout of a cascade of 8 cells where the ground plane is depicted in grey and the upper metal upper metal is depicted in black. The substrate between the upper metal and the ground plane has the following characteristics:* $\varepsilon_r = 2.33$, $h = 0.5$ *mm,* $tg\delta = 0.003$. *The dimensions are:* $r_{in} = 3.5$ *mm,* $r_{out} = 4.5$ *mm,* $G = 1$ *mm,* $C = 0.5$ *mm,* $D = 0.5$ *mm,* $W_{out} = \pi.r_{out}/32$, $W_{in} = \pi.r_{in}/32$, $W = 1.47$ *mm,* $e = 2.5$ *mm,* $L_access = 70$ *mm. The distance between CSRRs and edges is* $L = 15$ *mm.*

The analysis performed for different distances between CSRRs and the substrate edges shows that in narrow substrates destructive interference occurs between free-space leaky wave radiation and surface wave modes, reflected at substrate edges. We use the 8-cell structure shown in Fig. 4.19 as a LWA. The size of the TL is imposed by the maximal XY deviation of the nearfield measurement, presented later in this section. Fig. 4.20 illustrates the leakage factor α and the propagation constant β of the equivalent TL, extracted from the S-parameters simulated with IE3D for the cascade of 8 cells shown in Fig. 4.19. Free space leakage radiation occurs between 2.72 GHz and 2.95 GHz for the left-hand band and this region will be referred to as the left-leaky region in this section. The angle of the main beam θ_{MB} (Fig. 4.21) is determined according to equation 4.5. Full-wave simulations and measurements of the radiation pattern have been presented previously in this section and have shown a minimum in the broadside direction, thus creating a rotating beam which splits in the plane of the substrate [6], as will be shown in Fig. 4.22 with $L = 65$ mm in order to approach the condition of an infinite substrate.

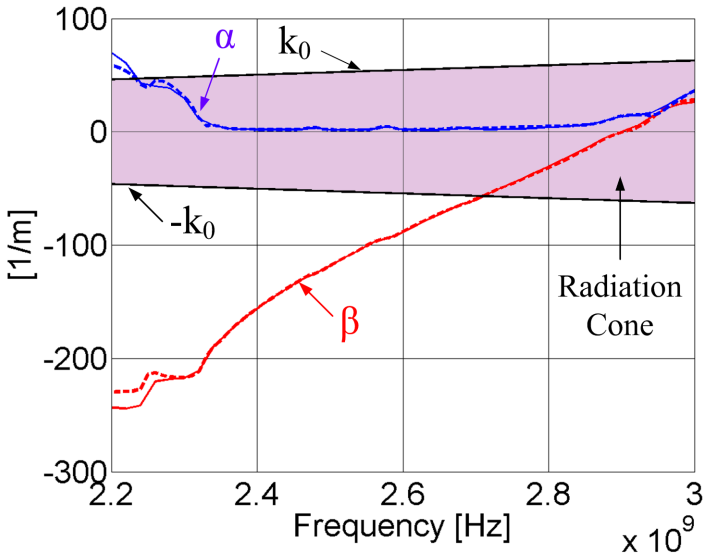


Figure 4.20. *Dispersion diagram for the cascade of 8 cells of Fig. 4.19 simulated with IE3D (with finite substrate) for L = 15 mm (dotted) and L = 65 mm (solid). The magenta cone shows the leaky radiation region, delimited by the lines $|\beta| < k_0$. The radiation band is situated between 2.72 GHz and 2.95 GHz for the left leaky region.*

SWs propagating in the substrate plane are responsible for a decrease in the free-space radiated power and also cause interferences in the radiation. Propagation characteristic $\beta_{surf} = j.\gamma_{surf}$ of TM SW mode is calculated, taking into account the substrate thickness h, from the following Helmholtz equation [17]:

$$\varepsilon_r \cdot \sqrt{\beta_{surf}^2 - k_0^2} + \sqrt{\beta_{surf}^2 - \varepsilon_r . k_0^2} . tanh(h . \sqrt{\beta_{surf}^2 - \varepsilon_r . k_0^2}) = 0 \qquad (4.6)$$

Numerical solution of this equation shows that β_{surf} is close to k_0 in the left-hand leaky region. SW angle Φ_{surf}, illustrated in Fig. 4.19, is calculated from [17]:

$$\Phi_{surf} = arccos(\frac{\beta}{\beta_{surf}}) \qquad (4.7)$$

The comparison of θ_{MB} and Φ_{surf} is shown in Fig. 4.21 and confirms the correlation between the SW direction and the beam steering in the plane of the substrate (decrease of Φ_{surf} with frequency). This behaviour, explained in the section 3.2 in Fig. 3.4 and illustrated in the combination of Fig. 4.8 and Fig. 4.7(a) results in a fan beam having a narrow shape in the X-Z plane and a broad shape in the cross plane, as confirmed in the previous measured radiation patterns presented in Fig. 4.13, 4.14 and 4.15.

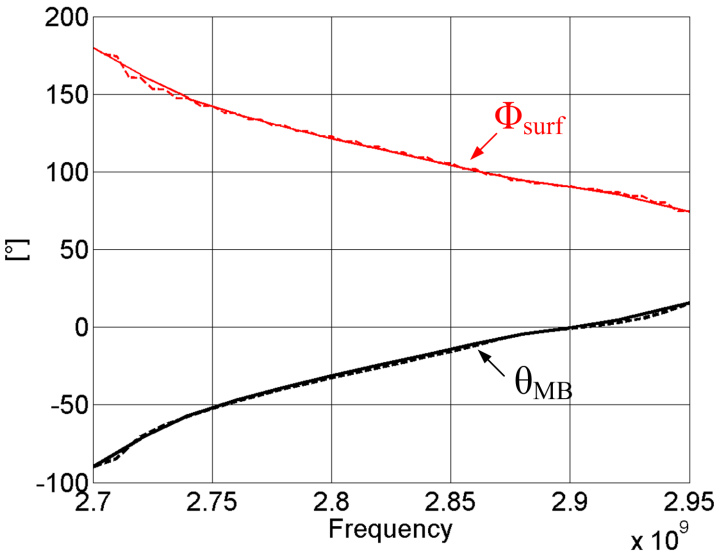


Figure 4.21. *Angle of SW Φ_{surf} in ($\theta = 90°$) X-Y plane calculated from (4.7) and angle of the main beam θ_{MB} in ($\phi = 0°$) X-Z plane calculated from (4.5), both applied to the simulation results of Fig. 4.20 for the leaky wave band with $L = 15mm$ (dotted) and $L = 65mm$ (solid).*

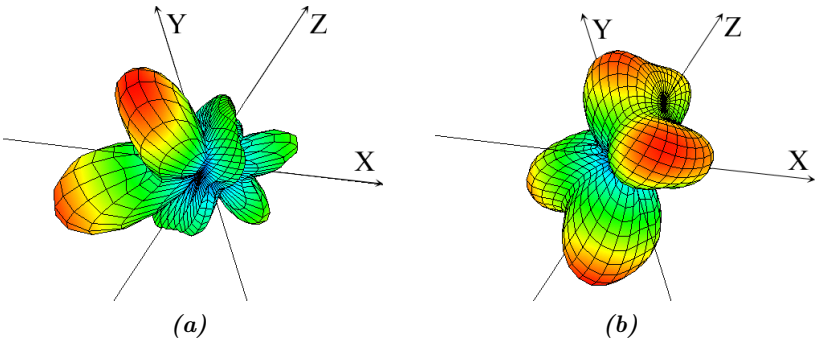


Figure 4.22. *IE3D simulation of 3D radiation pattern for TL based on 8 cells of Fig. 4.19 at 2.7 GHz (a) and at 2.95 GHz (b), the condition of finite substrate is chosen for the IE3D simulation, with $L = 65$ mm in order to approach the condition of an infinite substrate.*

Nearfield distribution is simulated with COMSOL Multiphysics based on Finite Element Method for 4 frequencies in the left-leaky region. This region is

shifted towards higher frequency between 2,95 GHz and 3,35 GHz, due to coarse meshing imposed by computer memory limitation. Fig. 4.23 and Fig. 4.24 show the distribution of magnetic field H_y for 2 different values of distance L between CSRRs and edges (L=65mm and L=15mm). The first case (wide substrate, Fig. 4.23) shows clearly the minima of the wave fronts of the SW. These wave fronts are perpendicular to the direction of propagation of the SW indicated by the black arrow. Fig. 4.23 also proves the rotation of the direction of propagation of the SWs with respect to frequency, as predicted by (4.7) and shown at Fig. 4.21. This behaviour can be also seen in the second case (narrow substrate, Fig. 4.24) however the SWs are then reflected on the substrate edges, locally increasing the field concentration at the edges and creating spurious additional radiation.

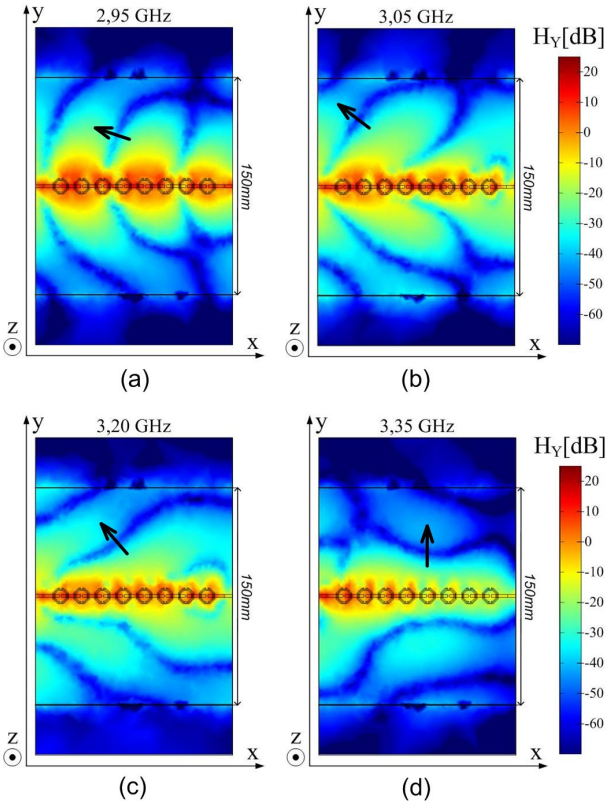


Figure 4.23. *Nearfield distribution of magnetic field H_y in the structure of Fig. 4.19 simulated with COMSOL assuming L = 65mm for 4 frequencies in the left leaky region : (a) 2,95 GHz, (b) 3,05 GHz, (c) 3,20 GHz and (d) 3,35 GHz. The black arrow shows the direction of propagation of SW.*

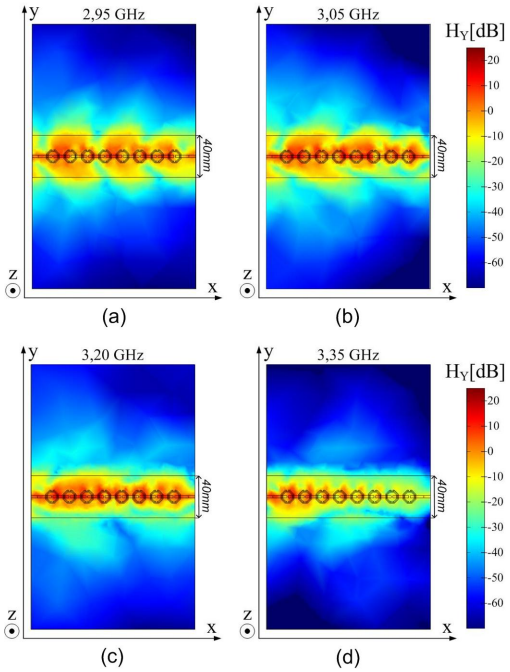


Figure 4.24. *Nearfield distribution of magnetic field H_y in the structure of Fig. 4.19 simulated with COMSOL assuming $L = 15$mm for 4 frequencies in the left leaky region : (a) 2,95 GHz, (b) 3,05 GHz, (c) 3,20 GHz and (d) 3,35 GHz. The black arrow shows the direction of propagation of SW. Due to edges reflection, direction of surface waves propagation is not visible.*

> ***Setup Environment :*** *Measurement is done with the fabricated TL based on 8 CSRRs depicted in Fig. 4.19, lying on a Rogers RT5870 substrate. The antenna under test is connected to the Agilent PSG E8267D signal generator and a nearfield probe is connected to an Agilent PSA E4440A spectrum analyser. With a controlled X-Y table, the topology of the near field is measured. Fig. 4.25 and Fig. 4.26 show the measured distribution of magnetic field H_y for 2 different values of distance L between CSRRs and edges (L=15mm and L=65mm). Measurement validates the behaviour of the COMSOL simulation.*

In this section IE3D simulations are done for 2 different values of distance L between CSRRs and edges ($L = 15$mm and $L = 65$mm). Fig. 4.20 shows the comparison of dispersion diagrams, while Fig. 4.21 shows the comparison between the extracted values of θ_{MB} and Φ_{surf}. In both figures, the edge distance L has no significant influence. This is however not the case for the radiation pattern.

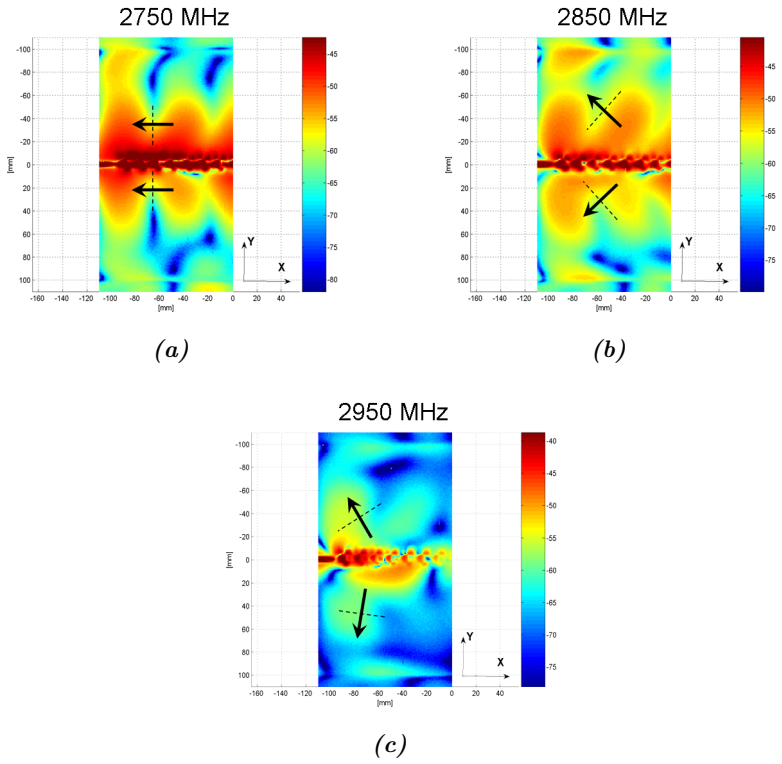


Figure 4.25. *Measured Nearfield distribution of magnetic field H_y in the structure of Fig. 4.19 assuming $L = 65$mm for 3 frequencies in the left leaky region : (a) 2,75 GHz, (b) 2,85 GHz, (c) 2,95 GHz. The black arrow shows the direction of propagation of SW.*

Fig. 4.22 and Fig. 4.27 indeed show its simulation with IE3D at two frequencies in the left-hand band for respectively $L = 65$mm and $L = 15$mm. In the first case, SWs do not cause any interference and the leaky waves create the expected 3D beam steering with frequency observed in Fig. 4.22 and explained in [6]. In the second case, reflection of SW at edges creates parasitic radiation that partially masks the leaky wave radiation (Fig. 4.27). This explanation is supported by the following theoretical reasoning.

Let us assume that the reflection of surface waves at substrate edges can be modelled as cascaded pairs of infinitesimal horizontal current dipoles with equal magnitude and same direction, oriented along x-axis as shown in Fig. 4.28. The total field radiated by a pair is equal to the sum of the field radiated by each

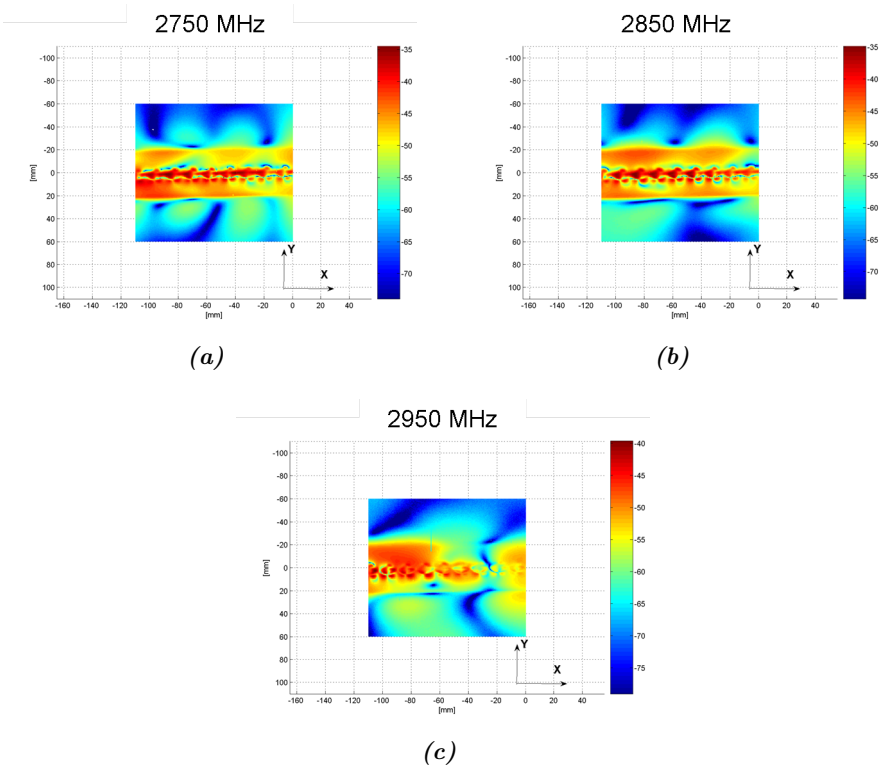


Figure 4.26. *Measured Nearfield distribution of magnetic field H_y in the structure of Fig. 4.19 assuming $L = 15mm$ for 3 frequencies in the left leaky region : (a) 2,75 GHz, (b) 2,85 GHz, (c) 2,95 GHz. Due to edges reflection, direction of surface waves propagation is not visible.*

dipole of the pair and in the ($\phi = 0°$) X-Z plane (Fig. 4.29(a)) it is given by [16]:

$$E_t = E_1 + E_2 \tag{4.8}$$

$$= \overrightarrow{a_\theta} j\eta \frac{kI_0 l}{4\pi} \left(\frac{e^{-j(kr_1 - \zeta/2)}}{r_1} \cos\theta_1 + \frac{e^{-j(kr_2 + \zeta/2)}}{r_2} \cos\theta_2 \right) \tag{4.9}$$

Where η is the intrinsic impedance of the medium (120π for free-space), I_0 is the magnitude of the current: $I(x) = a_x.I_0$; k is the propagation constant of the medium; l is the length of the dipole, r_1 and r_2 are the distances from the source 1 and 2 respectively to the observation point; ζ is the difference in phase excitation between the elements, $\zeta = 0$ due to their symmetric excitation by SW. Assuming farfield observations in the X-Z plane: $\theta = \theta_1 = \theta_2$ and for phase and amplitude variation: $r_1 = r_2 = r$. Fig. 4.29(b) represents the total field E_t.

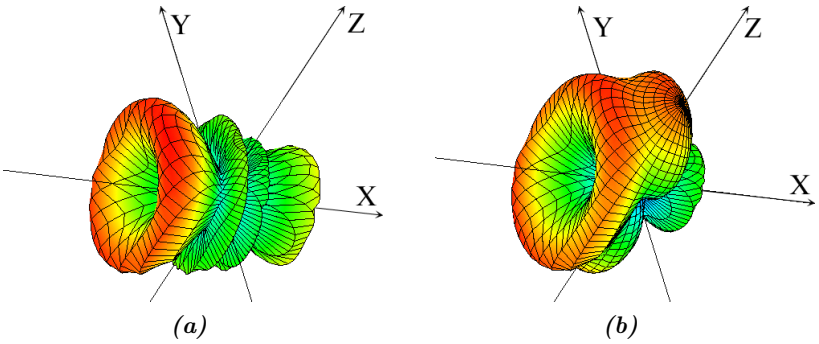


Figure 4.27. *IE3D simulation of 3D radiation pattern for TL based on 8 cells of Fig. 4.19 at 2.7 GHz (a) and at 2.95 GHz (b), the condition of finite substrate is chosen for the IE3D simulation, for L = 15 mm.*

A maximum in the radiation pattern occurs at $\theta = 0°$ along the z-axis, as was observed in Fig. 4.27.

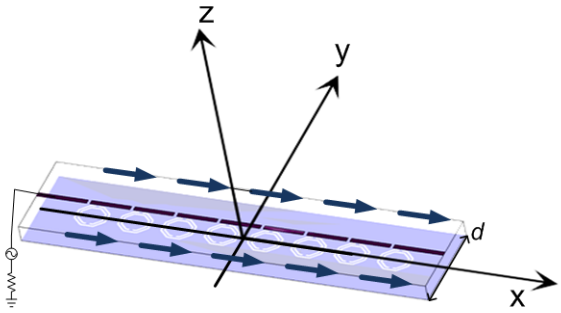


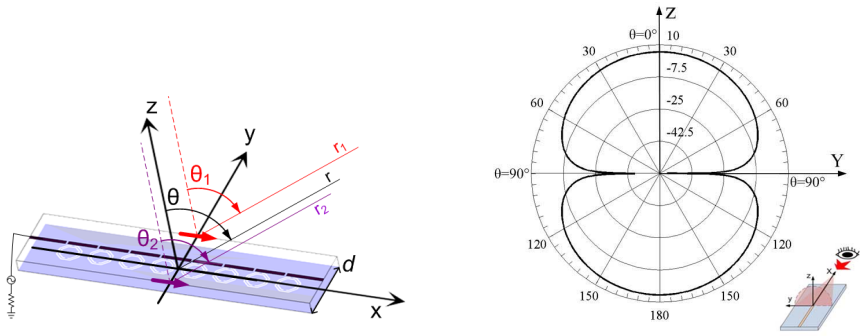
Figure 4.28. *Impact of SW reflection at the edges, modeled by infinitesimal horizontal dipoles oriented along x-axis.*

The total field is also computed in the ($\phi = 90°$) Y-Z plane (Fig. 4.30(b)) and it is given by [16]:

$$E_t = E_1 + E_2 \tag{4.10}$$

$$= \overrightarrow{a_\theta} j\eta \frac{kI_0 l}{4\pi} \left(\frac{e^{-j(kr_1 - \zeta/2)}}{r_1} sin\phi_1 + \frac{e^{-j(kr_2 + \zeta/2)}}{r_2} sin\phi_2 \right) \tag{4.11}$$

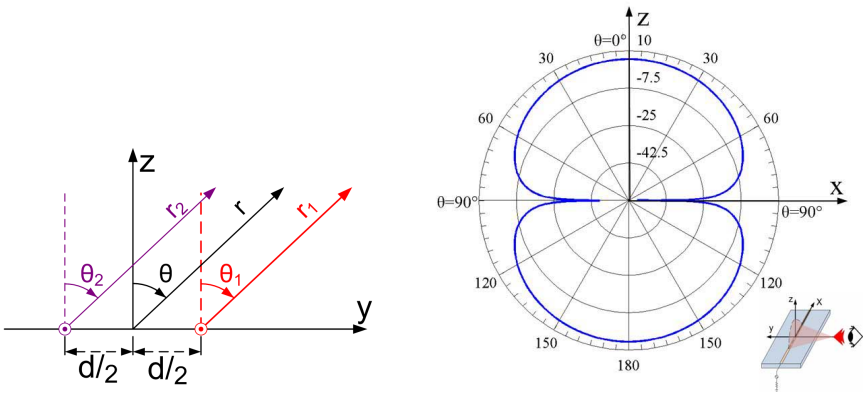
Assuming farfield observations for Y-Z plane: $\theta = \theta_1 = \theta_2$, for amplitude variation: $r_1 = r_2 = r$, for phase variation : $r_2 = r + d/2.sin\theta_2$ and $r_1 =$



(a) *(b)*

Figure 4.29. *Schematic view (a) and normalised total farfield (b) of two infinitesimal horizontal dipoles oriented along x-axis observed in the X-Z plane.*

$r - d/2.sin\theta_1$. Fig. 4.30(b) represents the total field E_t. Again a maximum of the radiation pattern occurs at $\theta = 0°$ along the z-axis, as observed in Fig. 4.27.



(a) *(b)*

Figure 4.30. *Schematic view (a) and normalised total farfield (b) of two infinitesimal horizontal dipoles oriented along x-axis observed in the Y-Z plane.*

Conclusion : This section has discussed surface radiation phenomena in a metamaterial transmission line based on series capacitive gaps and CSRRs

periodically loading a host microstrip line and acting as a leaky-wave antenna. Radiation created by the free space leaky wave mode also induces the TM surface wave mode in the substrate plane, as confirmed by COMSOL simulations. The analysis performed for different distances between CSRRs and the edges shows that ***in a narrow substrate, interference occurs between free-space leaky wave radiation and field radiated from equivalent dipoles created at substrate edges by reflection of SWs.*** The latter induces radiation at the broadside that overcomes the leaky wave beam steering. So in order to analyze the radiation beam of the CSRR LWA at the upper frequency in the broadside direction as presented in the previous section and in order to avoid a parasitic interference in this particular direction, it is necessary to choose a reasonable distance between the LWA cells and the edges. This was chosen conservatively to be four times longer than the maximum guided wavelength to be considered as an infinite substrate. A quantitative study must be realized to design the structure with minimal distance between the CSRRs and the substrate edges.

4.3 UNIDIRECTIONAL CSRR LWA

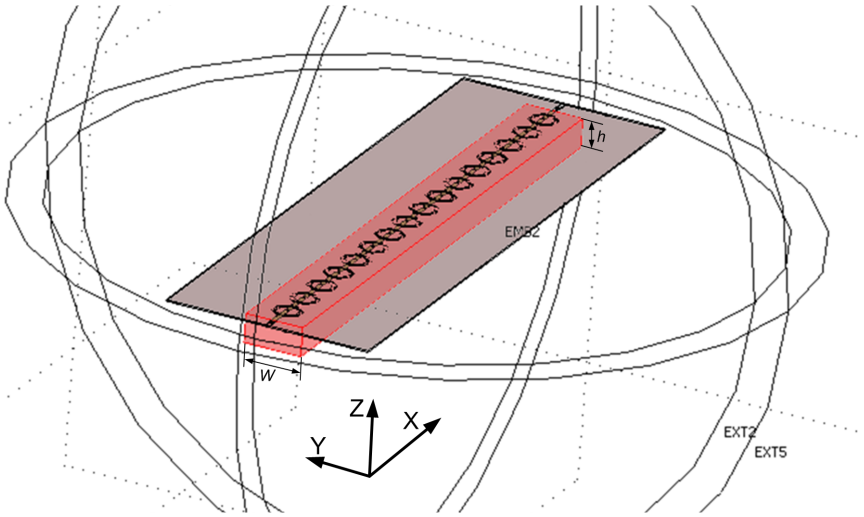


Figure 4.31. *View of transmission line created by a cascade of 16 cells of an unidirectional leaky wave antenna (depicted in grey) with a metallic trough (depicted in pink) placed on the ground plane in front of the CSRR cell (the dimensions of the antenna are the same as Fig. 4.1 and the dimensions of the metallic trough are : $W = 2$ cm, $h = 1$ cm).*

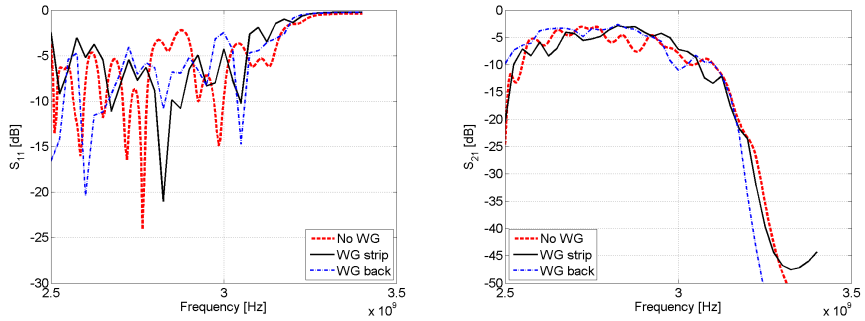
One disadvantage of the LWA based on CSRRs is the bidirectional radiation. We have applied the concept proposed by the Eleftheriades's group, described in

the section 3.4 illustrated in Fig. 3.13(c) detailled in [18] and in [19] to suppress the radiation from one side : *a narrow, long metallic trough is placed either on the ground plane in front of the CSRR cell (Fig. 4.31), or on the microstrip in front of the gap.* The trough, placed on the transverse LWA dimension, has the same effect as a waveguide below the cut-off frequency of dominant TE_{10} mode.

Simulation tool : IE3D has the ability to handle finite substrate and ground plane but it takes too much time to simulate. The presence of a waveguide obliges us to consider finite substrates, that is the reason why this part is simulated with COMSOL.

Simulated S-parameters and antenna efficiency[2] are compared in Fig. 4.32 and Fig. 4.33 for both configurations of the LWA without electrical trough. This comparison does not show any evidence of spurious resonances appearing throughout the entire bandwidth or any significant degradation.

Fig. 4.34 and Fig. 4.35 show 3D views of the simulated radiation pattern at three illustrative frequencies of interest in the the left-leaky regions for both configurations. The comparison with Fig. F.3 shows that this technique works well and the radiation from one side is suppressed without antenna efficiency degradation.



(a) S_{11} *(b)* S_{21}

Figure 4.32. *S-parameters of TL loaded by 16 CSRRs of an LWA of Fig. 4.31 simulated with COMSOL with a metallic trough placed on the ground plane in front of the CSRR cell ('WG Back', blue dashdot), placed on the microstrip in front of the gap ('WG Strip', black solid) and without any trough ('No WG', red dashed).*

[2] As presented by *C.A. Balanis*, the antenna efficiency takes into account losses at the input terminals and within the structure of the antenna. This definition is used for all the thesis. We consider that the structure is long enough to radiate all the energy before the end of the antenna, so losses go mainly in the substrate.

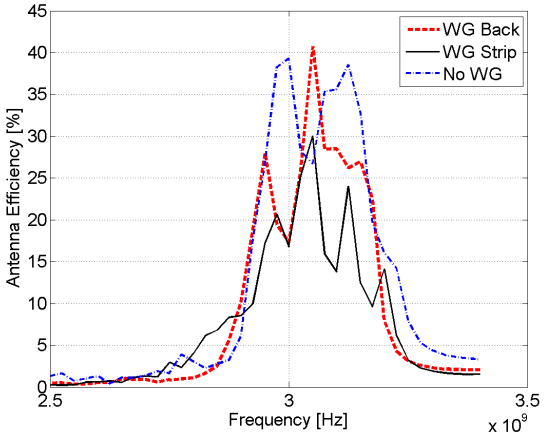
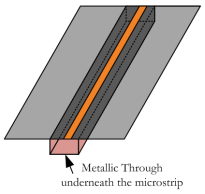
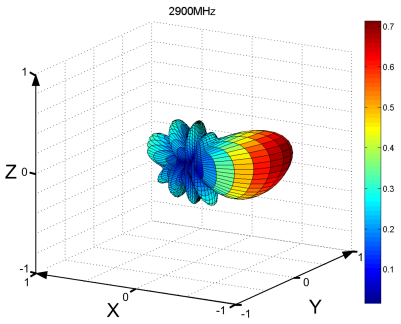


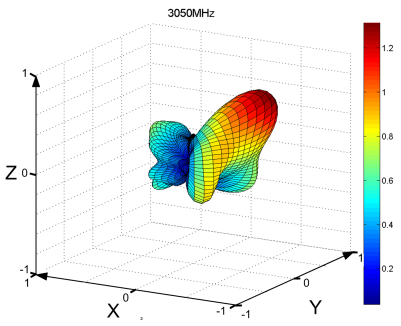
Figure 4.33. *Antenna efficiency AF of TL loaded by 16 CSRRs of an LWA of Fig. 4.31 simulated with COMSOL with a metallic trough placed on the ground plane in front of the CSRR cell ('WG Back', blue dashdot), placed on the microstrip in front of the gap ('WG Strip', black solid) and without any trough ('No WG', red dashed).*



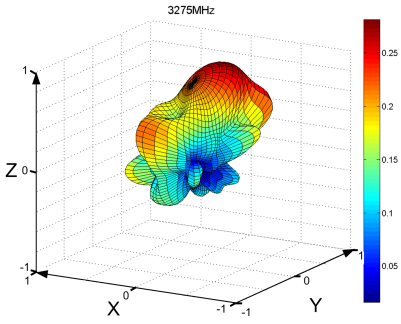
(a) Schematic view (ground plane is underneath the structure)



(b) 2900MHz

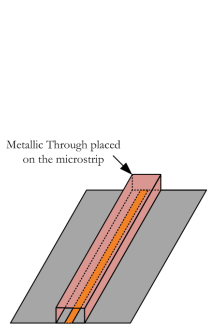


(c) 3050MHz

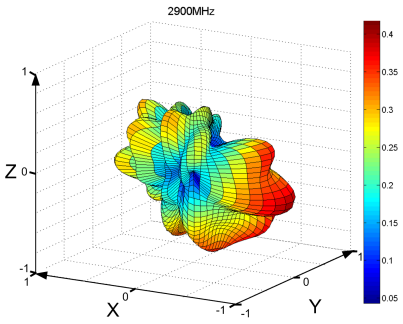


(d) 3275MHz

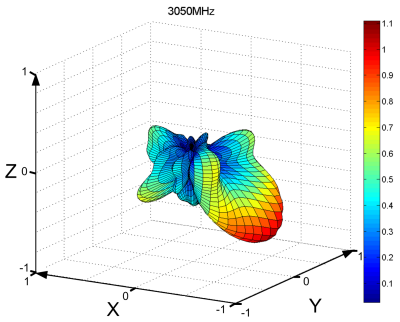
Figure 4.34. *Schematic view and normalized 3D radiation pattern for the TL based on 16 cells of an unidirectional LWA* ***with a metallic trough placed on the ground plane in front of the CSRR cell*** *Fig. 4.31 simulated with COMSOL solver at 3 frequencies in the left-leaky region. Color bar: blue corresponds to the minimum, red corresponds to the maximum.*



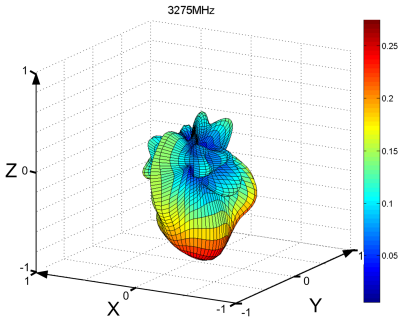
(a) Schematic view (ground plane is underneath the structure)



(b) 2900MHz



(c) 3050MHz



(d) 3275MHz

Figure 4.35. *Schematic view and normalized 3D radiation pattern for the TL based on 16 cells of an unidirectional LWA* ***with a metallic trough placed on the microstrip in front of the gap*** *(inverse of Fig. 4.31) simulated with COMSOL solver at 3 frequencies in the left-leaky region. Color bar: blue corresponds to the minimum, red corresponds to the maximum.*

4.4 TUNABLE CSRR-LOADED LEAKY WAVE ANTENNA

This section presents the concept of an electronically controlled leaky wave antenna. A novel approach, namely ferroelectric materials as well as CSRRs, is considered. The objective is the creation of frequency independent LWAs with an alternative scanning mechanism to frequency tuning.

Simulation tool : Contrary to COMSOL solver, the IE3D software can not handle lumped elements such as the varactors with DC voltages, which are useful for the tunable antenna. This limitation explains why all simulations of this chapter are realised with the COMSOL solver.

4.4.1 Introduction

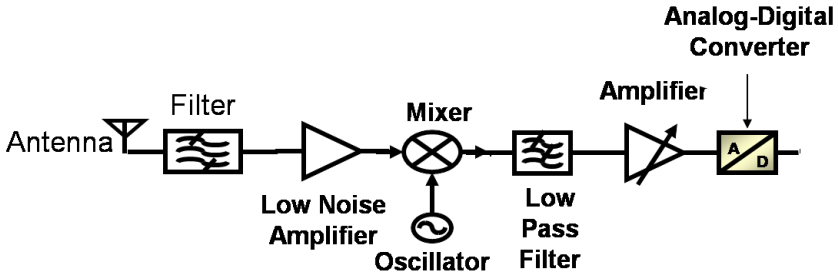


Figure 4.36. *Architecture of RF heterodyne receivers : the RF signal is received from the antenna and is sent to a channel-select filter. Then, the signal is amplified by a low noise amplifier, this amplification is necessary to avoid signal degradation in the downconversion mixing : the signal band is translated to much lower frequencies (intermediate frequency) to be treated by the analog-digital converter [20].*

The control of beam scanning using frequency could be interesting for example for localisation application but has the drawback to impose a broadband functionality to the other blocks of the RF transceiver in modern communication systems. Indeed, as shown in Fig. 4.36, the antenna is the first block of the architecture of a RF heterodyne receiver. In this kind of structure, narrowband structure generally is required for effective channelizing and means a compromise between high quality factor and cost [20]. So this chapter is devoted to the development of LWAs operating at fixed frequency and using another scanning control. In the past, significant efforts have been directed in this direction [3, 21–23]. This chapter presents a solution based on LWA using CSRRs and ferroelectric tunabilities.

This section is focused on the ferroelectric tunability of a resonant-type leaky wave antenna. Our approach was to tune the series capacitance C_g of the CSRR-

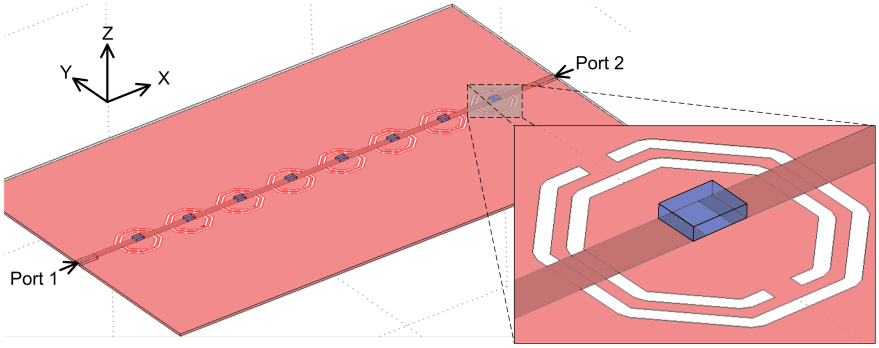


Figure 4.37. *Conceptual 3D view of TL based on 8 CSSR cells with serie tunable components (ground plane is depicted in rose, the tunable component is depicted in blue, whereas upper metal is depicted in grey).*

loaded unit cell of Fig. 4.39(b) by the introduction of a varactor, based on a ferroelectric thin film of Barium Strontium Titanate (BST) or a lumped varactor diode, placed on the gap of the microstrip line, as illustrated in Fig. 4.37. Creating this kind of simple structure is the first step to realize more complicated structure as Fig. 4.38.

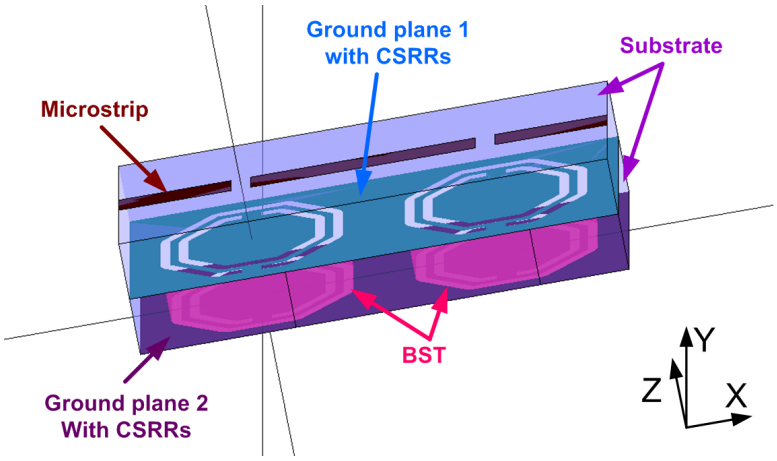


Figure 4.38. *Conceptual 3D view of TL based on 2 Double-layers complementary split ring resonator, presented in the appendix E.6, with ferroelectric film created inside the ring shapes. Electronic tunability is obtained with a DC voltage applied between the ground plane 1 and the ground plane 2.*

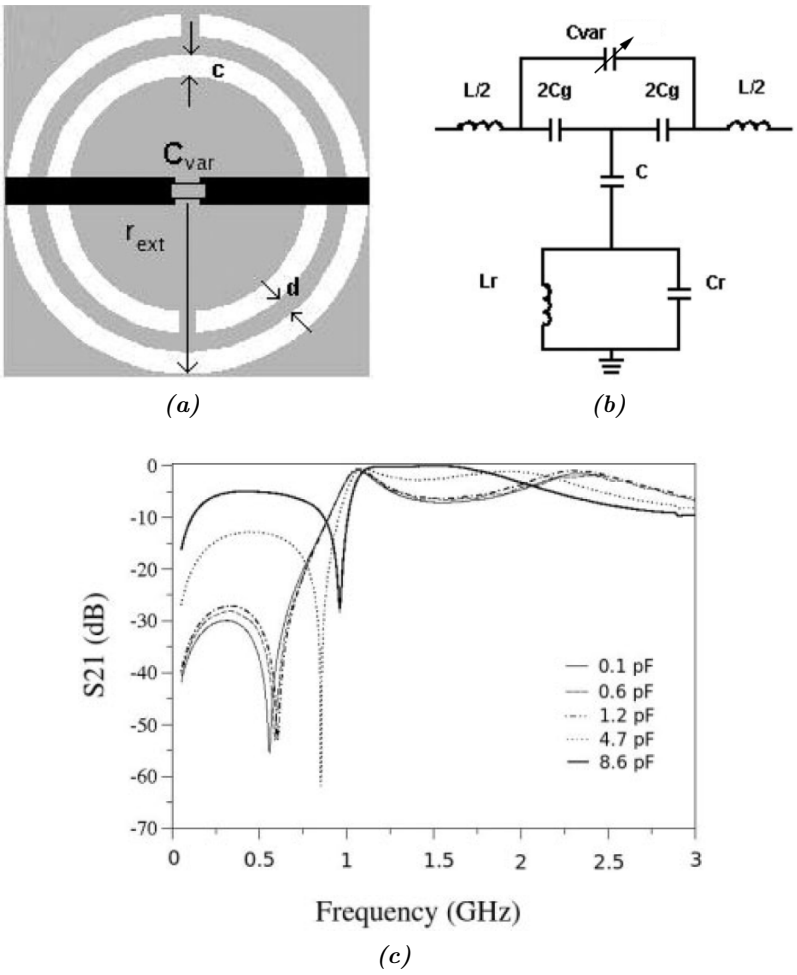


Figure 4.39. *(a) : Topology of the unit cell of a TL loaded by CSRR and by a gap (where a varactor is placed on the gap, grey regions represent the metal layer of the ground plane, black regions represents the metal layer of the microstrip line); (b) : Equivalent model of the unit cell of (a) (where C_{var} represents the tunable capacitance) ;(c) Measurement of S-Parameters of the unit cell of (a) with different values of the serie capacitance [24].*

4.4.2 Concept of the electric tunability

Tunable CSRR-loaded unit cell has already been presented in section 2.4.5 in order of designing tunable compact notch filters, leaky wave antenna or matching networks. Our approach is based on [24] where a tunable capacitance C_{var} is

placed on the gap created on the upper metal of the CSRR-loaded unit cell (Fig. 4.39(a)). A DC voltage, applied between the two ports of the TL, influences the propagation characteristics as illustrated in Fig. 4.39(c) by affecting the C_{var} value and therefore by affecting the effective permeability of the TL. An equivalent model taking into account this tunable capacitance is illustrated in Fig. 4.39(b). The inductance of the microstrip line is represented by L and the CSRR by the parallel combination of L_c and C_c, the gap by a capacitance C_g. The coupling between the line and the resonator is represented by the capacitance C [25]. On the one hand, as demonstrated in [24], the position of the typical transmission zero f_z, defined by eq. 2.34 and present at a frequency smaller than the left-handed transmission band of these lines, can be modified by the C_{var} variation. On the other hand, as C_{var} increases, the lower limit of the left-handed band decreases while the upper limit of the left-handed band is maintained more or less unaltered.

Our approach is to insert this tunable capacitance in the CSRR-loaded leaky wave TL presented in the chapter 6 based on a ferroelectric BST thin film described in the section 4.4.3 and based on a varactor lumped element, described in the section 4.4.4.

4.4.3 CSRR unit cell loaded by BST thin film

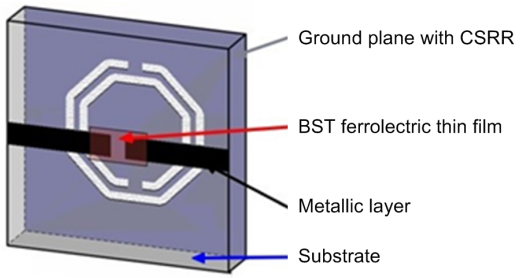


Figure 4.40. *Conceptual 3D view of CSSR structure with BST ferroelectric thin film (ground plane is depicted in grey, BST film is depicted in rose, whereas upper metal is depicted in black).*

The objective[3] of this section is to create a tunable leaky wave antenna based on Complementary Split Ring Resonator and on ferroelectric capacitance. This capacitance is created from a thin film of Barium Strontium Titanate (BST), placed on the gap of the microstrip line (Fig.4.40). A DC voltage is applied

[3]This work has been done in collaboration of Céline Marlier, Marc Debliquy, Maurice Gonon and Nathalie Maury from the University of Mons, Belgium. The context of this work was the topic of a student project of second bachelor and of a student project of third master [26].

between the two access ports. The circuit is realised with the inkjet printing technique on alumina substrate. The ferroelectric material is the Barium Strontium Titanate (BST) because of its high permittivity and its acceptable dielectric losses. The first investigation of this topic concerns the fabrication steps, described in the appendix B.

The chosen composition of the ferroelectric thin film is $Ba_{0.6}Sr_{0.4}TiO_3$, presenting a high permittivity peak at room temperature. The RF sputtering technique is used to deposit the thin film because this technique has the advantage of dense deposition and not so high annealing temperature. It is followed by annealing treatment. Alumina substrate is chosen because of its low permittivity for antenna application and because it is not damaged by the annealing treatment used after the sputter deposition technique. In a first step, interdigital capacitors are realized to test the tunable capability of the BST samples and to extract the BST thin film permittivity. The extracted value corresponds to the classical value.

The second part of this project concerns the metallic line fabrication based on the metal inkjet technique. This new technique has the advantages of high resolution and low cost metallization on various substrate. Silver is the selected metal because of its good conductivity, its good resistance to oxidation (cause of loss of electrical conductivity) and its high fusion temperature, higher temperature than the annealing temperature of BST sputter deposition technique. The resistivity of the silver inkjet printing is measured by the creation of microstrip meander line, in order to provide a comparison of the resistivity versus the number of the successive printing layers. Resistivity decreases as the number of successive printing layers increases, but the increase of successive printing layers suffers from a precision decrease.

In a first step, interdigital capacitors are realized to test the tunable capability of the BST samples and to extract the BST thin film permittivity. Fig. 4.41 shows photographs of the first samples. The 500 nm thick BST film is placed between the golden electrodes (obtained by evaporation) and the alumina substrate, as illustrated in the conceptual section view of Fig. 4.41(c). The thickness $h_{Alumine}$ of the alumina substrate is equal to 1 mm, its permittivity $\varepsilon_{Alumine}$ is equal to 6. The chosen BST composition is $Ba_{0.6}Sr_{0.4}(TiO3)_{1.1}$ with a post-deposition annealing at 700°C. Fig. 4.41(b) shows the tunable interdigital capacitor. With the aim to extract the permittivity of the BST thin film, the same interdigital capacitor is realized without BST material (Fig. 4.41(a)).

The 2-ports impedance matrix without bias voltage is measured at 1 kHz. In a first step, the measured value of the impedance for this classical capacitance of Fig. 4.41(a) is equal to 16.17 $M\Omega$. In [26], a simple model for low frequencies, neglecting the losses effect, assumes that the impedance of this capacitance is equal to :

$$Z = \frac{1}{j\omega C_A} \tag{4.12}$$

where C_A is the capacitance between electrodes, assuming that the electric field effect is mainly concentrated along the alumina substrate.

Next, the measured value of the impedance for the tunable capacitance of Fig. 4.41(b) is equal to 8.3 $M\Omega$ for bias voltage equal to 0 V and to 7.1 $M\Omega$ for bias voltage equal to 10 V. In [26], a simple model for low frequencies, neglecting the losses effect and the fringing field around the periphery, assumes that the BST film capacitance is in series with the alumina substrate capacitance. Assuming also that the alumina substrate capacitance is extracted from 4.12, given by the expression of the measured global impedance :

$$Z = \frac{1}{j\omega C_A} + \frac{1}{j\omega C_{BST}} \tag{4.13}$$

where C_{BST} is the part of the capacitance due to the BST film. From this model, assuming that the permittivity of the BST thin film is directly extracted from the parallel plate capacitor formula, detailed in [26], this permittivity is close to 11000 for a bias voltage of 0 V. This value is of the same order of magnitude as that obtained for the BST thin film at 1 kHz reported in the literature [27]. The sensitivity of the BST film seems to decrease because of the small film thickness. However no accurate value of permittivity in presence of bias voltage could be extracted because of the poor sensitivity of the BST capacitance in expression 4.13.

RF measurements have not been possible, due to a delay in the fabrication process. A radiation analysis of a TL loaded by CSRRs and lumped series varactors is developed in parallel with this work, with the aim to examine the electronic control of tunable series capacitor on the LWA radiation performances.

4.4.4 CSRR unit cell loaded by varactor

This part summarises the work done on TL loaded by CSRRs and series varactor diode, used as an electronically tunable LWA. A tunable lumped capacitor is soldered to the serie gap, as illustrated in Fig. 4.39(a), and biased by a DC voltage in order to influence the guided LWA wavelength and to reconfigure the direction of the LWA main beam.

This section is divided in three parts : a short description of the main varactor characteristics is presented in 4.4.4.1. Then the influence of the bias voltage, applied on the varactor, on the propagation characteristics, is analysed in the section 4.4.4.2 based on Comsol simulations and on measurements. Finally, the radiation properties of a frequency-independent LWA, using an electronic control mechanism for the beam scanning, is presented in the section 4.4.4.3.

4.4.4.1 Varactor diode

A varactor is a voltage controlled capacitor created by a diode used in its reverse region. The reverse-biased PN junction exhibits a charge-storage effect. As the voltage across the pn junction changes, the charge stored in the depletion layer

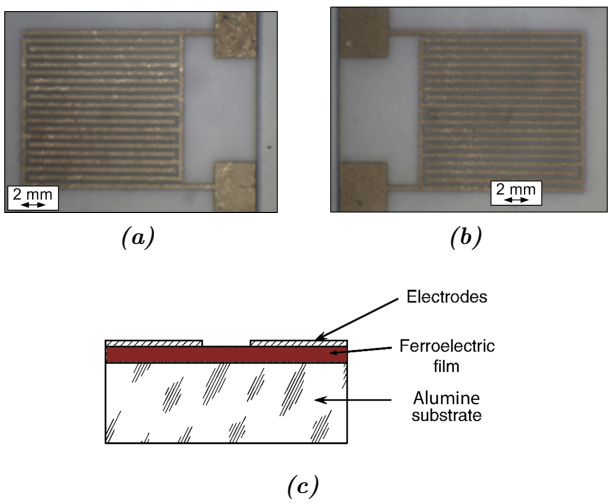


Figure 4.41. *(a) : Photo of interdigital capacitance on alumina substrate. (b) : Photo and (c) : Conceptual section view of interdigital capacitance on alumina substrate with 500 nm thick BST film placed between the golden electrodes and the alumina substrate (alumina substrate : thickness $h_{Alumine}$ = 1 mm, permittivity $\varepsilon_{Alumine}$ = 6) [26, 28].*

changes accordingly. This effect is modeled by the depletion-layer or junction capacitance C_j [29]:

$$C_j = \frac{C_{j0}}{(1+\frac{V_R}{V_0})^m} \tag{4.14}$$

where m is the grading coefficient, a constant optimized around 3.5 showing a strong correlation between C_J and the voltage V_R, where V_R is the reverse voltage applied to the diode, where V_0 is the junction built-in potential, in the range of 0.6 V to 0.8 V, C_{j0} is the value of C_f obtained for zero applied voltage. So equation 4.14 shows that C_f is function of the reverse-bias voltage V_r. A typical voltage capacitance curve is shown in Fig. 4.42. The tuning range depends on the range of the control voltage; its minimum value is zero and the maximum value is limited by the breakdown voltage of the junction and the available DC voltage value on the chip [30].

The chosen SMD varactor, used for RF applications, is the hyperabrupt junction tuning varactors SMV1232 [31]. Its spice model is shown in Fig. 4.43.

4.4.4.2 *Electronic control of propagation characteristics*

Firstly the propagation characteristics of 8-cells TL loaded by varactors and CSRRs is simulated with the Comsol software. The varactor is replaced by an

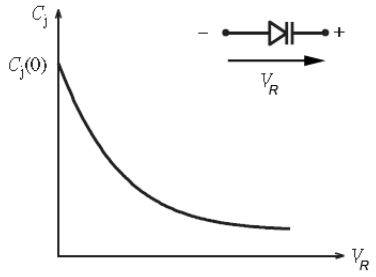
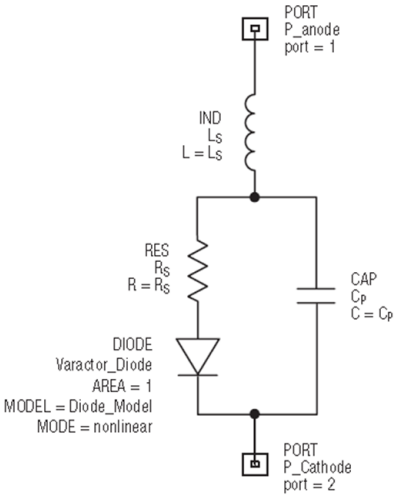
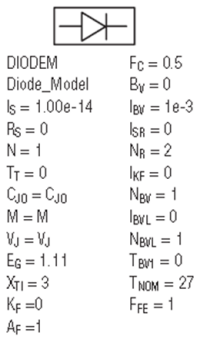


Figure 4.42. *Symbol and typical control voltage versus capacitance curve of a p-n junction varactor following eq. 4.14 (C_f is the depletion-layer or junction capacitance, V_R is the reverse voltage applied to the diode, C_{j0} is the value of C_f obtained for zero applied voltage) [30].*





Capacitance vs Reverse Voltage

V_R (V)	C_T (pF) SMV1232
0	4.15
0.5	3.22
1.0	2.67
1.5	2.28
2.0	1.97
2.5	1.72
3.0	1.51
3.5	1.35
4.0	1.22
4.5	1.13
5.0	1.05
5.5	0.99
6.0	0.94
6.5	0.90
7.0	0.86
7.5	0.84
8.0	0.81
9.0	0.78
10.0	0.76
11.0	0.75
12.0	0.74
13.0	0.73
14.0	0.73
15.0	0.72

Figure 4.43. *Spice Model of the hyperabrupt junction tuning varactors SMV1232 ($C_{J0} = 4.2$ pF, $V_J = 1.7$ V, $M = 0.9$, $C_P = 0$, $R_s = 1.5\ \Omega$, $L_s = 0.7$ nH) [31].*

impedance, $Z_{varactor}$, similar to the model illustrated in Fig. 4.43 and equal to :

$$Z_{varactor} = R_s + \frac{1}{j\omega C_{var}} + j\omega L_s \tag{4.15}$$

where R_s is fixed to 1.5 Ω and L_s equal to 0.7 nH, following [31]. C_{var} represents the diode of Fig. 4.43, the C_{var} value is replaced by discrete value, extracted from the table of Fig. 4.43. The bias voltage varies from 0 V to 5 V, so for the TL loaded by 8 tunable CSRRs, the total bias voltage varies from 0 V to 40 V. The layout of the simulated 8-cells TL is illustrated in Fig. 4.40.

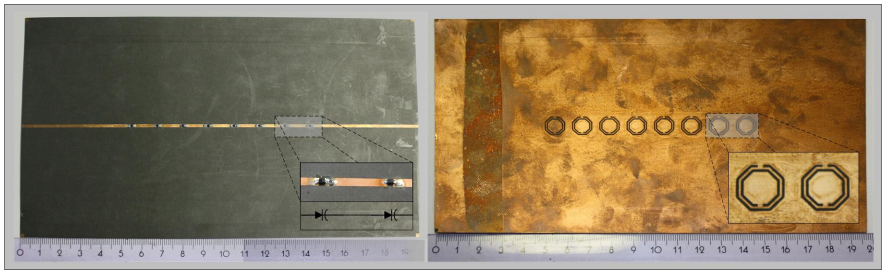
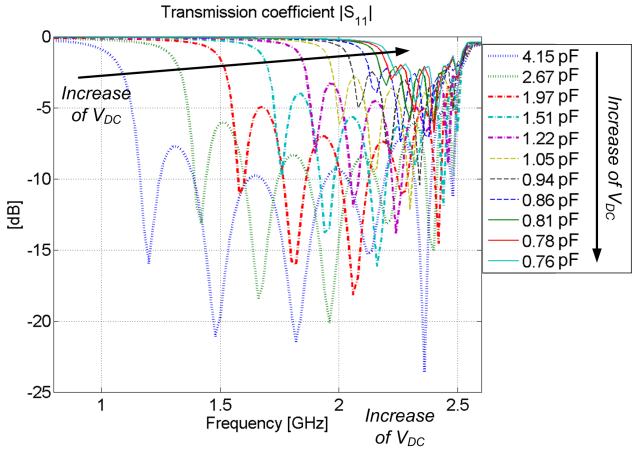


Figure 4.44. *Photos of cascade of 8 cells loaded by CSRRs and varactors SMV1232, corresponding to the layout illustrated in Fig. 4.37. Left : strip metal, with a zoom on two cells, and right : ground plane, with zoom on two cells (antenna length = 10cm).*

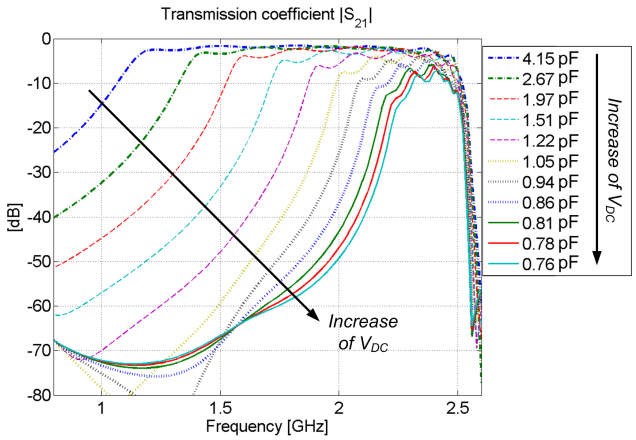
Fig. 4.45 shows the simulated S-parameters for bias DC voltage from 0 V to 40 V. The lower frequency of the LH band increases as the bias voltages increases. But it is important to notice that the upper frequency increases also slightly as the bias voltages increases.

The dispersion diagram is extracted with the methodology presented in the previous chapter. Fig. 4.46 presents the leakage factor, α, and the propagation constant, β for different bias voltages. We can conclude that the left leaky region is translated in higher frequencies as the DC bias voltage increases. So we can find one specific frequency (at 1.72 GHz) at which β increases approximatively from $-k_0$ to k_0, depending on the bias voltage. So it is possible to create LWAs with a complete spatial scanning at a fixed frequency for which the bias voltage alters the guided waves and reconfigures the direction of the main beam.

> ***Setup Environment :*** *Fig. 4.44 shows photos of the tunable LWA realization. SMV1232 varactor are soldered on the gap of the transmission line based on eight CSRRs. The structure is measured using a Vector Network Analyser (VNA) Agilent PNA-X N5242A and a 40 GHz Universal Test Fixture. A voltage source is connected to the bias inputs of the second port of the VNA (with a compliance of 0.1 mA). A DC voltage is applied between port 1 and port 2 to change the value of the varactor capacitance. Fig. 4.47 shows the measurement of S-parameters. The propagation characteristics, shown in Fig. 4.48, are extracted with the same methodology described in the previous chapter. Discrepancies between measurements and simulations are explained by fabrication tolerances and by the pre-*



(a) $|S_{11}|$ Parameter

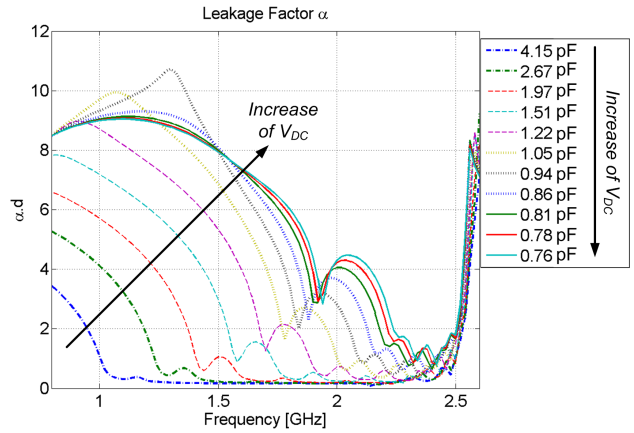


(b) $|S_{21}|$ Parameter

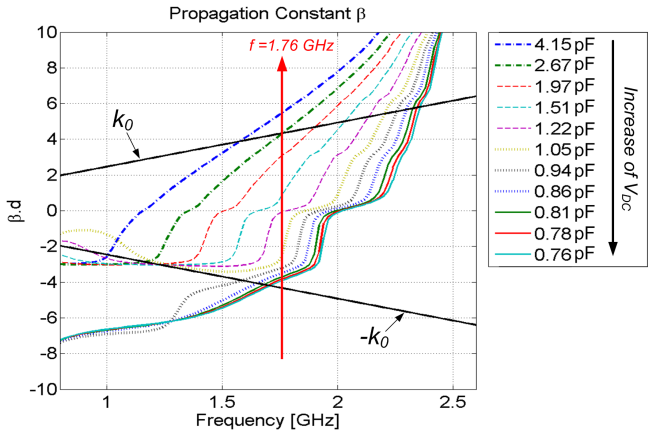
Figure 4.45. *S-parameters of TL loaded by 8 CSRRs and by varactors SMV1232 simulated with Comsol in the left-handed band for different DC voltages V_{DC} impressed on its access.*

cision of the varactor RF model. Indeed parasitic elements, created for example by soldering, are not included in the varactor RF model.

Measurements confirm the simulated behaviour : ***the left-leaky region is translated in higher frequencies as the DC bias voltage increases*** and it would be possible to find a frequency for which β increases from $-k_0$ to k_0 as the bias voltage decreases.

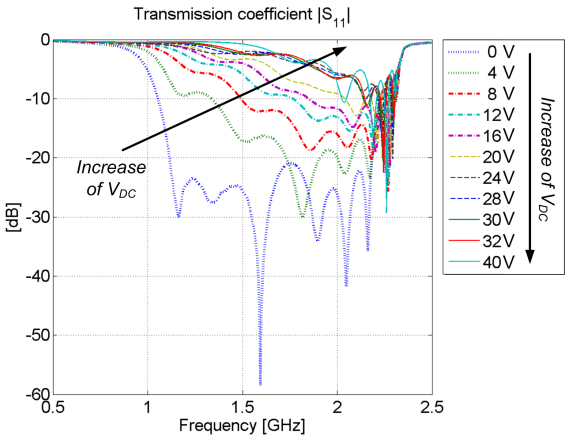


(a) Leakage Factor α

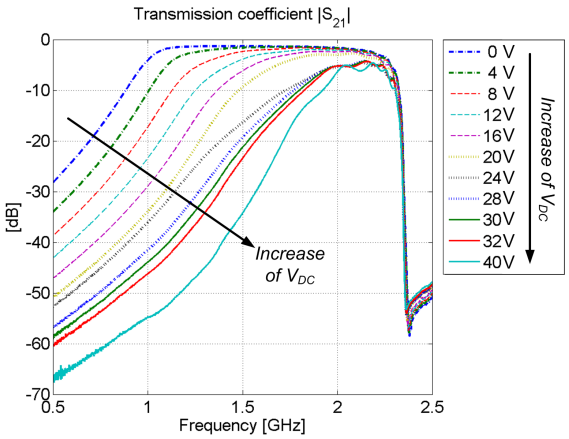


(b) Propagation Constant β

Figure 4.46. *Propagation characteristics extracted from S-parameters of TL loaded by 8 CSRRs and by varactors SMV1232 simulated with Comsol in the left-handed band for different DC voltages V_{DC} impressed on its access.*

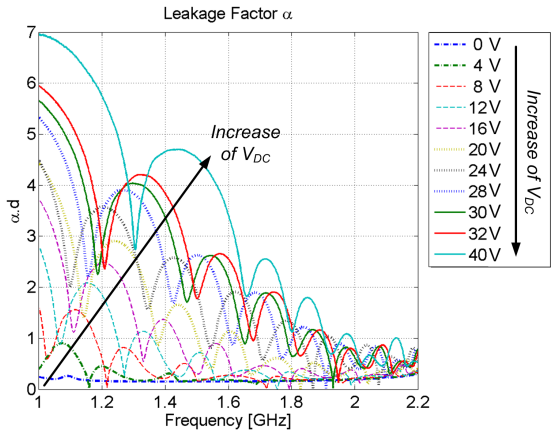


(a) $|S_{11}|$ Parameter

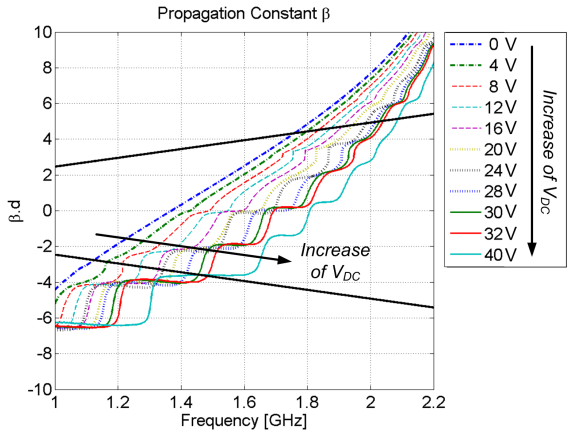


(b) $|S_{21}|$ Parameter

Figure 4.47. *S-parameters of TL loaded by 8 CSRRs and by varactors SMV1232, illustrated in Fig. 4.44 and measured in the left-handed band for different DC voltages V_{DC} applied across each gap.*



(a) Leakage Factor α

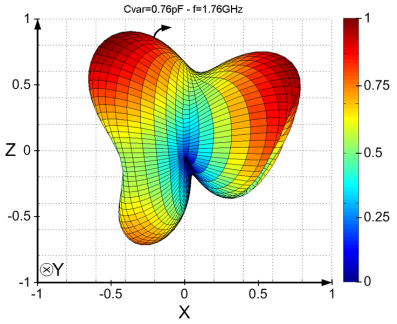


(b) Propagation Constant β

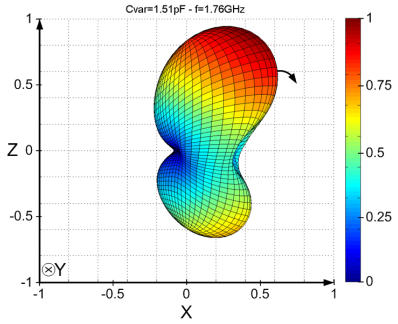
Figure 4.48. *Propagation characteristics extracted from S-parameters of TL loaded by 8 CSRRs and by varactors SMV1232, illustrated in Fig. 4.44 and measured in the left-handed band for different DC voltages V_{DC} applied across each gap.*

4.4.4.3 Electronic control of radiation performances

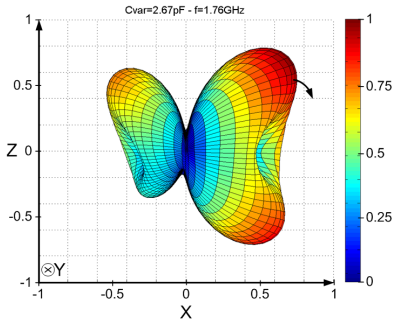
Comsol is also used to simulate the radiation pattern of 8-cells TL loaded by varactors and CSRRs to verify the voltage controlled scanning at a fixed frequency. The chosen frequency is 1.76 GHz, its radiation pattern is shown in Fig. 4.49 for three bias voltages. The simulation does confirm that an electronic control may also be used to steer the beam of the leaky-wave antennas (shown by the black array in the figure). The simulation tool is unable to handle structures above a certain length. It is clear that the structure has been chosen too short to radiate all power (the optimal dimension would include 16 CSRR cells, here we had to accept the length including only 8 CSRR cells). This explains the presence of a secondary beam in the opposite direction.



(a) $C_j = 0.76$ pF - $V_{DC} = 40$ V



(b) $C_j = 1.51$ pF - $V_{DC} = 12$ V



(c) $C_j = 2.67$ pF - $V_{DC} = 4$ V

Figure 4.49. *Normalized 3D radiation pattern for the TL based on 8 cells of Fig. 4.37 simulated with Comsol solver at 1.76 GHz for three values of the varactor (for bias voltage from 4 V to 40 V. Color bar: blue corresponds to the minimum, red corresponds to the maximum, the black arrow illustrates the rotation of the main beam.*

4.4.5 Conclusion and comparison

This section has presented an electrically tunable LWA based on CSRR. A DC bias voltage is used to modify the serie capacitor of the CSRR cell. The first objective is to realise the tunable capacitor by covering the microstrip gap with a ferroelectric BST thin film. The fabrication has suffered delay, inhibiting RF measurements. To verify the concept of the integration of electronically tunable elements into the resonant leaky-wave antennas to create frequency independent scanning, a lumped varactor diode replaces the BST film, placed in parallel with the microstrip gap. Propagation characteristics, predicted by full-wave simulations and validated by measurements conclude that the left-leaky region is translated in higher frequencies as the DC bias voltage increases and it would be possible to find a frequency for which β increases from $-k_0$ to k_0 as the bias voltage decreases. Full wave simulation has also allowed us to verify the voltage controlled scanning of the main beam of the LWA at a fixed frequency.

The thesis presents also another solution of ferromagnetic tunable LWA but not using CSRRs structure. It is presented in the annex A. A novel topology of leaky-wave antenna, where frequency scanning is obtained by a left-handed behaviour induced by negative permeability of the substrate. The ***ferromagnetic nature of nanowires allows also beam scanning of the LWA antenna at fixed frequency*** in the Ka band, by applying an external DC magnetic field. For the future, two challenges of this structure must be answered : the first one is the application of the high external DC magnetic field without interference with the antenna radiation and the second one is the production of a sufficiently long structure to obtain a good directivity.

At the present state it is not possible to conclude about pros and cons of each solution. Further research would be necessary to provide a valid comparison and figures of merit : for this information is still missing on some antenna characteristics such as radiation efficiency, directivity, loss influence of the substrate, gain, influence of the magnetic field applied in the ferromagnetic solution, tunable sensitivity of the DC voltage or of the magnetic field.

4.5 VARIANT OF CSRR-LOADED LWA : CSRR WITH A SINGLE RING

A good candidate for the realisation of a metametarial LWA without the absence of broadside radiation at the upper frequency of the left leaky region is a CSRR cell with a single ring. In this section, the analysis is extended by examining the influence of a geometrical parameter, namely the number of concentric split rings of the CSRR, on the radiation properties of a LWA based on CSRRs. Firstly, the topology and the propagation characteristics of the structure are presented for TL based on CSRRs. Afterwards, the radiation performances are investigated. In the next chapter the electric and magnetic current distribution is modelled to provide a physical explanation for this performance.

Finally, one of the advantages of the LWA based on CSRR is the number of geometrical degrees of freedom but these advantages could also be viewed as

complicated opportunity for a designer to find, for a specific application, the good compromise between particular bandwidths, an appropriate antenna efficiency AF, an arbitrary directivity, etc. The third part of this section should improve the understanding of the effects of the CSRRs dimensions on the radiation properties of a single ring LWA. This analysis will then be used to create a balanced structure.

Simulation tools : IE3D is the software used in this section, due to its speed and its ability to perform parametric analyses. IE3D also present an parametric analysis, used in the third section. However, the results of the COMSOL simulation of CSRR-loaded LWAs with a single ring are presented in annex F. Indeed these results will be only used in the next chapter to extract the magnetic current distribution.

4.5.1 Topology and propagation characteristics

We present here a structure similar to the one shown Fig. 4.1. The structure here is in fact a microstrip host line loaded with series gaps and with CSRRs in its ground plane with one split ring. A schematic of this structure is presented in Fig. 4.50. The periodic structure is considered as a CRLH line given that it actually exhibits similar characteristics with right-hand and left-hand frequency bands that depend on the respective capacitive or inductive behaviour of series and parallel branches of the equivalent circuit as introduced previously in the section 2.3.2.

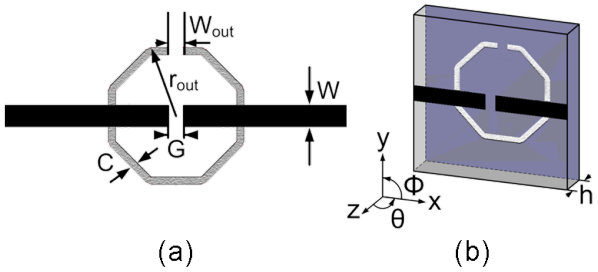


Figure 4.50. *CSSR structure with one split ring (ground plane is depicted in grey whereas upper metal is depicted in black. The substrate between upper metal and ground plane has following characteristics:* $\varepsilon_r = 2.33$, $h = 0.5$ *mm,* $tg\delta = 0.003$ *: (a) Layout (dimensions are:* $r_{out} = 4.5$ *mm,* $G = 1$ *mm,* $C = 0.5$ *mm,* $W_{out} = 1$ *mm,* $W = 1.47$ *mm) (b) 3D view.*

We have designed the structure of Fig. 4.50 on a the same substrate, namely a Rogers RT5870 substrate ($\varepsilon_r = 2.33$, $h = 0.5$ mm, $tg\delta = 0.003$). The unit cell has the same geometry, except that the inner ring is removed. The parameters of the cell are: $r_{out} = 4.5$ mm, $G = 1$ mm, $C = 0.5$ mm, $D = 0.5$ mm, $W_{out} = 1$ mm,

W_{in} = 1 mm, W = 1.47 mm. Full wave simulations are performed with IE3D software and COMSOL solver, which are in turn validated with measurements. Fig. 4.51 shows photos of the demonstrator. Following the analysis done in the section 4.2.3, the distance between the edges of the substrate and the CSRR ring is fixed to 95 mm, in order to approach the condition of an infinite substrate and to avoid spurious radiation from reflection of surface waves at substrate edges.

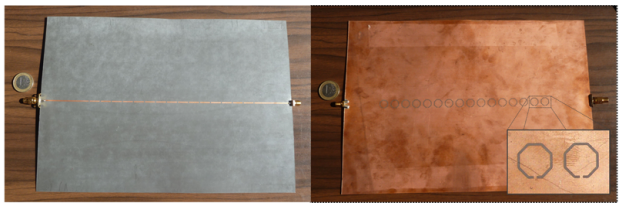
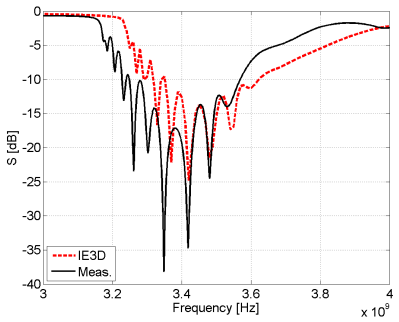


Figure 4.51. *Photos of a cascade of 16 CSRRs with one ring, corresponding to layout described in Fig. 4.50(a). Left : strip metal and right : ground plane (antenna length = 20cm).*

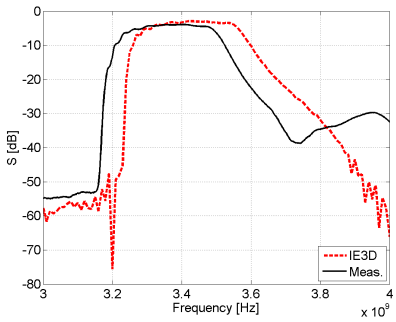
Fig. 4.52 shows the comparison of the S-parameters between measurement and simulations performed with IE3D. Discrepancies between measurements and simulations are explained again by fabrication tolerances and the influence of meshing.

The propagation characteristics are extracted from S-parameters by the methodology explained in section 4.2. Fig. 4.53 shows the leakage factor α and the propagation constant β of the equivalent TL, extracted from the S-parameters simulated for the cascade of 16 cells similar to Fig. 4.1(c). We can now analyse the radiation pattern in the left-leaky region. From these propagation characteristics, the leakage radiation appears to occur between 3.46 GHz and 4 GHz for the case of the measurements and between 3.55 GHz and 4.14 GHz for the case of the IE3D.

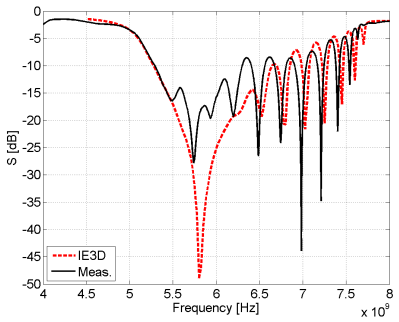
Fig. 4.52 presents the comparison of S-parameters for a TL loaded by 16 CSRRs, each of them comprising of just one split-ring, for the case of the right-hand band. Structures based on CSRRs with two split-rings create right-hand bands at lower frequencies (in Fig. 4.5), but the frequency shift is smaller than in the case of the left-hand band (Fig. 4.3 : CSRR with two split rings, Fig. 4.52 : CSRR with one split ring). The leakage factor is extracted from 4.3 in Fig. 4.53(c) and the propagation constant is extracted from 4.4 in Fig. 4.53(d). From the radiation cone, the right-leaky region is determined to be between 5.25 GHz and 7.73 GHz for IE3D simulation between 5.147 GHz and 7.475 GHz for the measurements.



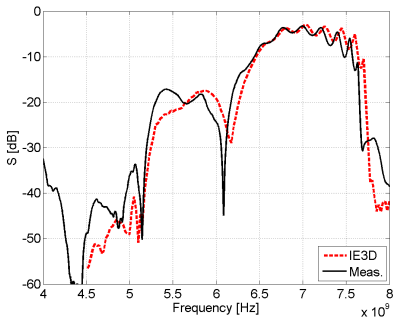
(a) S_{11} in the left-hand band



(b) S_{21} in the left-hand band



(c) S_{11} in the right-hand band



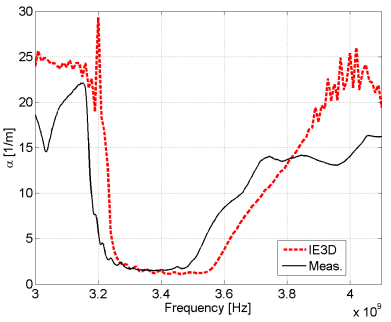
(d) S_{21} in the right-hand band

Figure 4.52. *S-parameters of TL loaded by 16 CSRRs with one ring of Fig. 4.50 measured (black solid), simulated with IE3D (red dashed) and simulated with COMSOL (blue dashdot).*

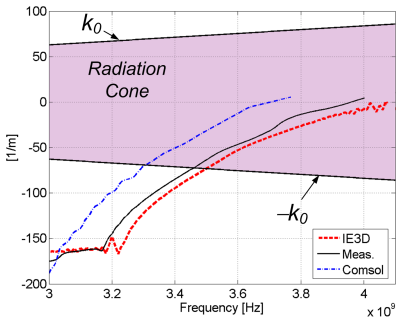
4.5.2 Radiation performance

Firstly we focus our attention on the simulated and measured radiation pattern in the left-leaky region. Subsequently, experimental and simulation results will be presented in the right-hand band.

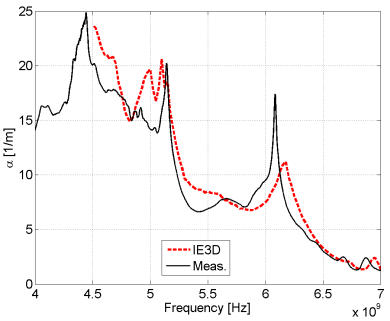
> ***Setup Environment :*** *The IE3D software is used to simulate the radiation pattern of the TL based on 16 cells depicted in the schematic in Fig. 4.50. The measured 2D radiation patterns of CSRR-based TL with one split ring depicted in Fig. 4.51 are obtained from transmission measurements between a Rohde & Schwarz HL024A1/S1 Crossed Log-Periodic Antenna and the antenna under test using the same VNA (Fig. 4.54).*



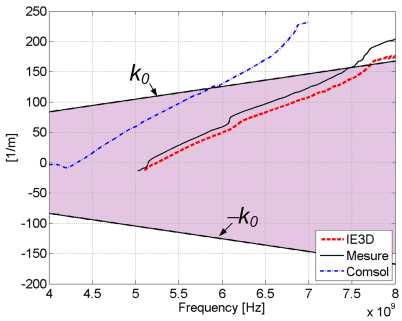
(a) Leakage factor α in the left-hand band



(b) Propagation constant β in the left-hand band



(c) Leakage factor α in the right-hand band



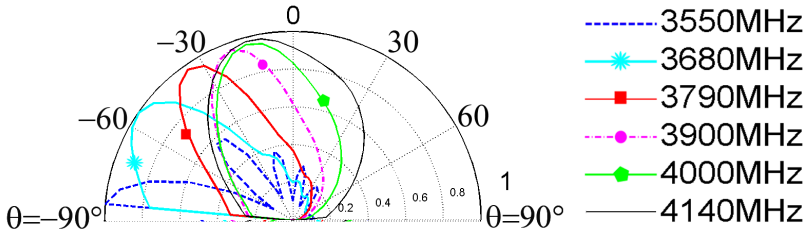
(d) Propagation Constant β in the right-hand band

Figure 4.53. *Propagation characteristics as calculated from the S-parameters shown in Fig. 4.52 using eqs. 4.4 and 4.3 of the TL loaded by 16 CSRRs with one split ring depicted in Fig. 4.50. The calculations shown pertain to the measured case (black solid), the IE3D case (red dashed) and the COMSOL case (blue dashdot) in the left-hand band. The magenta area represents the radiation cone defined by the free-space propagation constant k_0.*

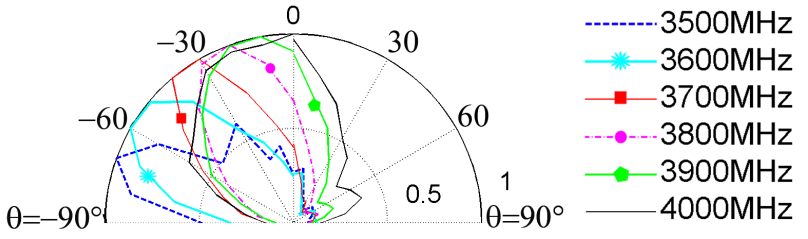
Fig. 4.55(a) shows corresponding 2D views of the simulated radiation pattern in the ($\phi = 0°$) X-Z plane, demonstrating its frequency scanning capability, also validated by measurement in Fig. 4.55(b). In accordance with Fig. 4.53(b) and with equation 4.5, the main beam scanning occurs from θ = -90° to $\theta = 0°$ with increasing frequency in the left-leaky region. Indeed, the qualitative agreement between Fig. 4.55(a) and Fig. 4.55(b) is very good, especially given that there is always inherently a frequency shift between measurements and simulation due to fabrication tolerances and meshing influence.



Figure 4.54. *Photos of the measurement setup in the UCL anechoic chamber (on the left, antenna under test and on the right, Rohde & Schwarz HL024A1/S1 Crossed Log-Periodic Antenna.*



(a) IE3D

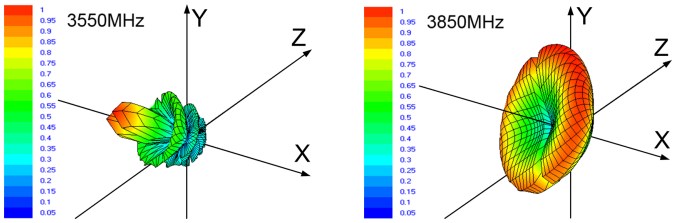


(b) Measurement

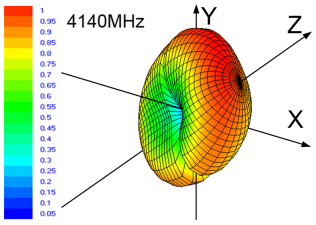
Figure 4.55. *Normalized 2D radiation pattern in ($\phi = 0°$) X-Z plane for the TL based on 16 cells with one split ring illustrated in Fig. 4.50(a) simulated with (a) IE3D (with the assumption of infinite substrate) and (b) measured for different frequencies in the left-leaky region.*

In order to facilitate the comparison with radiation patterns of CSRRs with two split rings, the simulated 3D radiation pattern is shown in Fig. 4.56 for three frequencies in the left-leaky region region. These patterns are derived the

IE3D software. Globally the antenna behaves like the classical leaky antenna introduced in the chapter 3.



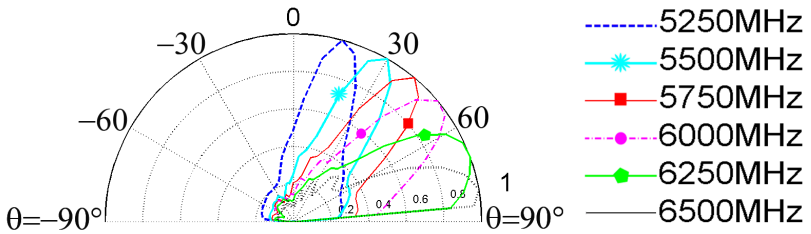
(a) 3550MHz *(b)* 3850MHz



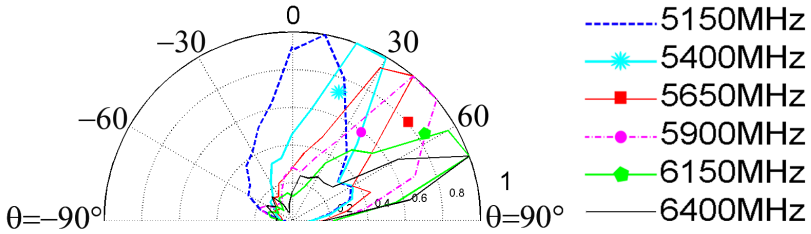
(c) 4140MHz

Figure 4.56. *Normalized 3D radiation pattern for the TL based on 16 cells similar to the one depicted in Fig. 4.51(a) simulated with IE3D assuming an infinite substrate at 3 frequencies in the left-leaky region. Color bar: blue corresponds to the minimum, red corresponds to the maximum*

Concerning the right-leaky region, the simulated and measured radiation patterns are shown in Fig. 4.57 in the ($\phi = 0°$) X-Z plane to verify the frequency scanning from $\beta = 0$ (where the main beam is oriented in the broadside direction of Fig. 4.1(c)) to $\beta = k_0$ (where the main beam is oriented in the endfire direction of Fig. 4.1(c)). Fig. 4.58 presents the 3D view of the radiation pattern simulated in IE3D (for a reason of the thesis compactness, the COMSOL results are shown in the appendix C). Remarkably, the behaviour of TL with one split ring is similar to that of the TL with two split rings (Fig. 4.11). To conclude, the influence of the number of rings on the radiation pattern is negligible in the right-hand band. The antenna efficiency AF, illustrated in Fig. 4.59, is always similar given any arbitrary number of rings.

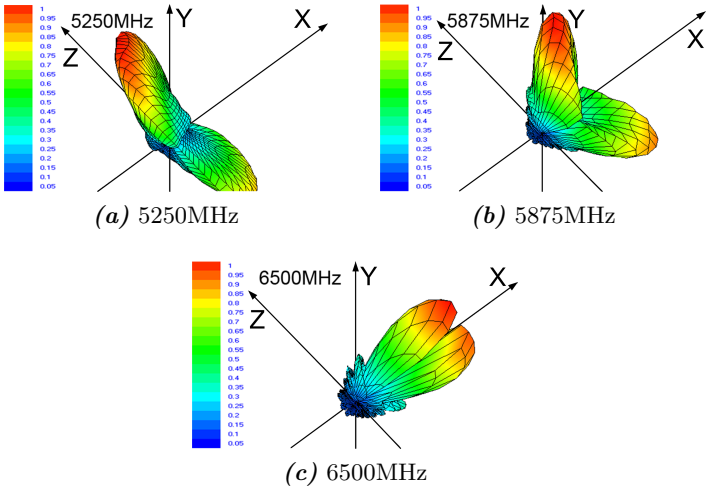


(a) IE3D Simulation



(b) Measurement

Figure 4.57. *Normalized 2D radiation pattern in ($\phi = 0°$) X-Z plane for the TL based on 16 cells similar to the one depicted in Fig. 4.50(a), (a) simulated with IE3D (with the assumption of infinite substrate), (b) measured for different frequencies in the right-leaky region.*



(a) 5250MHz *(b)* 5875MHz

(c) 6500MHz

Figure 4.58. *Normalized 3D radiation pattern for the TL based on 16 CSRRs with one split ring similar to the one depicted in Fig. 4.51(a) simulated with IE3D assuming an infinite substrate at 3 frequencies in the right-leaky region. Color bar: blue corresponds to zero, red corresponds to 1.*

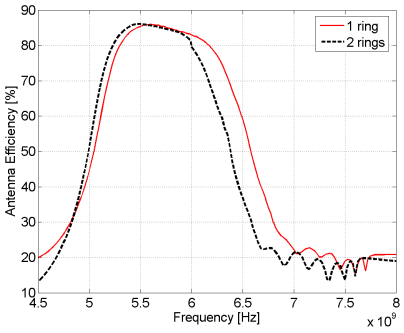


Figure 4.59. *Antenna efficiency AF of the cascade of 16 cells based on one split ring (red/solid) similar to the one depicted in Fig. 4.51(a) and on two split rings (black/dotted) of Fig. 4.1(a) extracted from simulation with IE3D assuming an infinite substrate.*

4.5.3 Geometrical analysis of CSRRs-loaded LWA

4.5.3.1 Figures of merit

A parametric study on a single ring CSSR structure has been realised to show the influence of each dimension on the antenna properties, in order to facilitate a design in view of the high number of degrees of freedom. The metamaterial detractors claim the bad impact of the leakage on the metamaterial components. This work has also the objective to give the opportunity to a RF designer to choose the dimensions of a filter, for example, to decrease the radiation leakages if the application environment imposes drastic EMC specifications.

The CSRR-based LWA based on eight cells, illustrated in Fig. 4.60(c), is simulated with IE3D Library, which is the 2nd layout editor of Mentor Graphics IE3D, assuming an infinite substrate. The IE3D Library is a full-wave EM simulator based on 3D integral equation, method of moment [32]. A simulated structure corresponds to a parameterized set of pre-defined objects, contained in the IE3D library. For example, the CSRR cell is created by putting together one ring, for which the (X,Y,Z) position, the inner and outer radius are user-defined, and a straight strip used as a boolean object (to create the split of the ring), for which the (X,Y,Z) position, the length and the width are also user-defined. The TL based on 8 gaps and 8 CSRR cells are realized with parameterized objects based on equations using the followed tuning variables :

- the width C of the slot,
- the outer radius R_{out} of the ring,
- the opening W_{out} of the ring,
- the space e between two cells,
- the width W of the metal strip line,
- the size G of the gap,
- the opening angle χ_1 of the ring, which indicates the direction of the ring opening ($\chi_1 = 0°$: the ring is opened along the y axis).
- the opening angle χ_2 of the ring : the hexagonal ring appears from χ_2 to 360°-χ_2. This dimension is redundant with the opening W_{out}.

For each case, the dispersion diagram and the radiation are simulated in the left- and right-leaky regions. The left-leaky region is defined between the frequency f_{LH1} for which the propagation constant, β, of the TL is equal to $-k_0$ and the frequency f_{LH2} for which β is equal to zero. In order to find this specific point, it has been necessary to add the condition to cancel the derivative of β. The right-leaky region is defined between the frequency f_{RH1} for which β is equal to zero and the frequency f_{RH2} for which β is equal to k_0. For frequencies for which the unit cell length is larger than the guided wavelength, f_{RH2} is derived

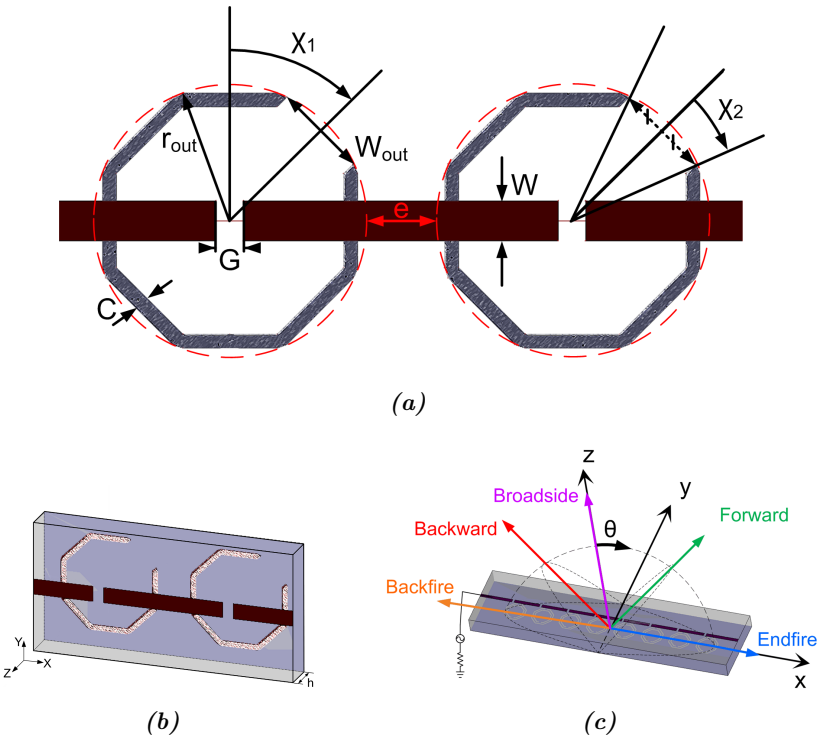


Figure 4.60. *CSSR structure with one split ring (ground plane is depicted in grey whereas upper metal is depicted in dark brown, substrate between upper metal and ground plane has following characteristics:* $\varepsilon_r = 2.33$, $h = 0.5$ *mm,* $tg\delta = 0.003$ *: (a) Layout, (b) 3D view, (c) View of transmission line created by a cascade of 8 cells with source and specific axes (initial dimensions are:* $R_{out} = 5$ *mm,* $G = 1$ *mm,* $C = 0.5$ *mm,* $W_{out} = 1$ *mm,* $W = 1.47$ *mm,* $e = 2.5$ *mm,* $\chi_1 = 0°$, $\chi_2 = \arcsin(W_{out}/2R_{out})$*)*

from the antenna efficiency AF. f_{RH2} is then the frequency for which the antenna efficiency AF is equal to a third of the antenna efficiency AF maximum in the right leaky region. In order to compare the parametric study of the structure, Eight figures of merits are chosen for both leaky regions :

- **Width of the leaky region [Hz]** defined as the difference between the lower and the upper frequency of the leaky region,

- **Slope of the leaky region [1/(Hz.m)]** defined as the average slope of the propagation constant, β (β is calculated from 4.4). This slope is the image of the sensitivity of the LWA main beam angle to the frequency. In

both leaky regions, this slop corresponds to :

$$\text{Slope of the Left Leaky Region} = \frac{\beta(f_{LH2}) - \beta(f_{LH1})}{f_{LH2} - f_{LH1}} \quad (4.16)$$

$$\text{Slope of the Right Leaky Region} = \frac{\beta(f_{RH2}) - \beta(f_{RH1})}{f_{RH2} - f_{RH1}} \quad (4.17)$$

- **Maximum of the leakage factor [1/m]** defined as the maximum of leakage factor, α, for the leaky region. α is calculated from 4.3.
- **Maximum of the S_{11}-parameter [dB]** defined as the maximum magnitudes of the S_{11} for the leaky region. The magnitude of S_{11}-parameter in dB provides information on the antenna matching, lower its value is, better the matching is.
- **Extrema of the characteristics impedance Z_B [Ω]** defined as the maximum and the minimum of the real and imaginary parts of the characteristic impedance Z_B for the leaky region, this factor is especially important for the filter design or for antenna design as patch antenna for impedance matching issues. Z_B is calculated from the ABCD matrix, defined in . This relationship may be written as [15] :

$$Z_B = \frac{B}{\sinh(acosh(\frac{A+D}{2})} \quad (4.18)$$

- **Maximum of the antenna efficiency** AF [%] defined as the maximum of antenna efficiency for the leaky region.
- **Maximum of the total field gain [dBi]** defined as the maximum of the maximum total field gain for the leaky region.
- **Maximum of the total field directivity [dBi]** defined as the maximum of the maximum total field directivity for the leaky region,

These figures of merit have the objective of analysing the radiation performances (such as directivity, gain and efficiency) and the impedance matching of the TL (to determine the matching load at the LWA end to absorb the no-radiated energy and to improve the input matching to optimize the input energy), to compare the frequency scanning between the left and the right leaky regions.

The complete results of this analysis are presented in the appendix D.

4.5.3.2 Analysis of the parametric study

A synthesis of the parametric study is presented in the table 4.1. This table is created from the analysis presented in the section D.10 of annex D.

Example for RF filter designer : To illustrate how to use the information provided by those various tables, consider, for example, the design of a RF filter,

Synthesis of Parametric study					
Figures of Merit	***Leaky Region***	***Most influencing parameter***	***Less influencing parameter***	***Increase of the figure of merit***	***Decrease of the figure of merit***
Width of the Leaky region	LH	R_{out}	C, W	C, W, χ_2, W_{out}	χ_1, R_{out}, e
	RH	R_{out}	C	C, W_{out}, G, χ_1	R_{out}, e, W
Slope of Leaky region	LH	χ_1	C	R_{out}, e, G, χ_2, χ_1	W_{out}
	RH	χ_2	W_{out}	C, R_{out}, W, χ_2	G, χ_1
Maximal leakage factor	LH	W_{out}	R_{out}	R_{out}, G, χ_1	W_{out}, e, W
	RH	W	W_{out}, e	R_{out}, G, χ_1	W_{out}, e, W
Maximum of S_{11}	LH	χ_2, W	R_{out}, C	G, χ_2, χ_1	W_{out}, W, C
	RH	χ_2	R_{out}, W_{out}	G, e	C, W_{out}, W
Max. **of** $Re(Z_B)$	LH	χ_1	W, R_{out}	G	W_{out}, e, W, C
	RH	C	R_{out}, W_{out}	G, C	W
Max. ***of*** $Im(Z_B)$	LH	χ_1	e, R_{out}	W_{out}, e, W, C	G
	RH	χ_1	e, R_{out},	W	G, C
Antenna Efficiency	LH	χ_1	R_{out}	C, W_{out}	R_{out}, G, e
	RH	W	W_{out}	C, G	e, W, χ_2
Maximal Gain	LH	χ_2	G	W_{out}	R_{out}, W, e
	RH	W	W_{out}	e	R_{out}, W_{out}, W, χ_2
Maximal directivity	LH	χ_2	W_{out}	e, W_{out}, W	R_{out}, G
	RH	e	W_{out}	e	R_{out}, W_{out}, W, χ_2

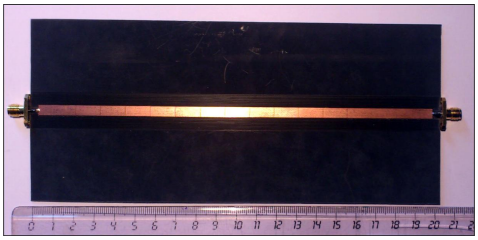
Table 4.1. *Synthesis of the parametric analysis*

using this technology, with as objective to avoid any radiation because of EMC specifications. As explained previously, for the LH band, the parameters that influence this antenna efficiency AF the most are χ_1, χ_2 and W with less influence from the parameters : W and e (Table D.7). For the RH band, the parameters that influence this figure of merit the most are W and e with less influence from the parameter, R_{out} and W_{out} (Table D.8). So, according to Fig.D.61, it is necessary to fix the absolute value of χ_1 larger than 60°, to obtain the lowest possible antenna efficiency AF. With the same approach, according to Fig.D.70(a), it is necessary to fix χ_2 smaller than 10°. One has to pay attention to the dimension, W, indeed its value influences the extrema of the antenna efficiency AF, so it can be the smallest or the highest possible, according to Fig.D.43.

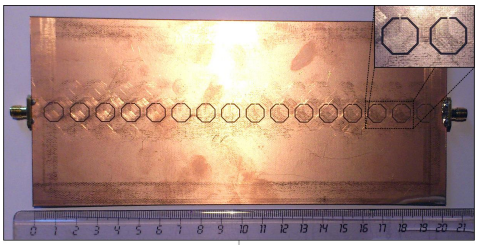
Example for RF antenna designer : This analysis is useful since it allows the antenna designer to develop an antenna with high directivity and good antenna efficiency AF in the left-leaky region. Analysis of table D.7 shows that the extrema of antenna efficiency AF are mostly influenced by χ_2, χ_1 and W and weakly influenced by R_{out} and C for the left-leaky region. Analysis of table D.11 shows that the extrema of antenna efficiency AF are mostly influenced by χ_2, χ_1 and C and weakly influenced by G and e for the left-leaky region. So the remaining degrees of freedom are G and e. For the other parameters :

- The analysis of Fig. D.70(a), D.72(a) shows that the best choice for χ_2 is between 30° and 70°.
- The analysis of Fig. D.61(a), D.63(a) shows that the best choice for χ_1 is close to 30°.
- The analysis of Fig. D.43(a), D.45(a) shows that the best choice for W is between 1,5 and 4,5 mm.
- The analysis of Fig. D.7(a), D.9(a) shows that the best choice for C is approximately 3 mm.

4.5.3.3 Application to a balanced CSRR-loaded LWAs



(a) Front Face

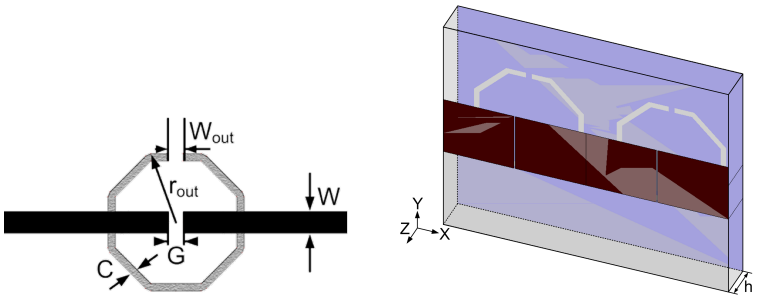


(b) Back Face

Figure 4.61. *Photos of the cascade of 16 cells, corresponding to the layout described in Fig. 4.62. (a) : strip metal and (b) : ground plane (antenna length = 20cm).*

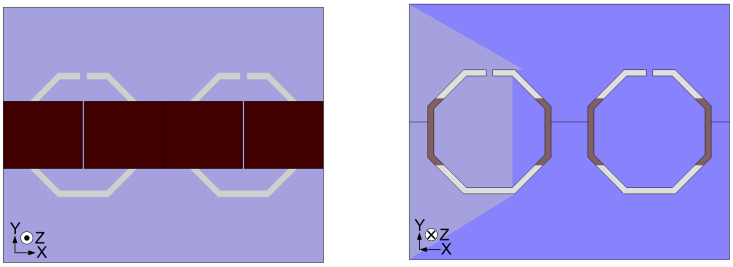
Topology and propagation characteristics. We use the analysis previously conducted on the CSRR to create a *balanced* structure. The approach is only focussed on eliminating the stop-band bandwidth between the left and right leaky region. The chosen figure of merit is only the influence of the dimensions on the frequency behaviour of the S-parameter. The concept of the balanced leaky wave antenna is introduced here. The concept of *balanced* design has been described in section 2.2. Due to fabrication tolerances, the width C of the slot and the outer radius R_{out} of the ring are fixed respectively to 0.5 mm and 4.5 mm. The aim is to decrease the lower frequency of the RH region and to decrease the higher frequency of the LH band with the aim of eliminating the stopband between both leaky regions. It is now known that a high value of W and low values of G and χ_1 cause a decrease the stop-band. After optimisation, the results are showed in Fig. 4.62 and in Fig. 4.61.

S-parameters are simulated with the Comsol solver and the IE3D software (with the assumption of infinite substrate and ground planes) and are measured using an Agilent PNA-X N5242A Vector Network Analyser (VNA) along with a 40 GHz Universal Test Fixture. The calibration is realised with an Agilent Electronic Calibration (ECal) Module N4691-60006 based on the *SOTL* technique



(a) Topology (grey : slot, black : top metal)

(b) 3D view



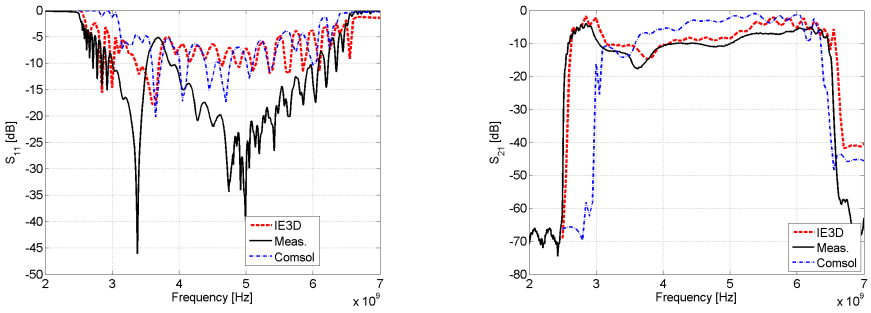
(c) Front Face

(d) Back Face

Figure 4.62. *Balanced CSSR structure with one split ring (ground plane is depicted in blue whereas upper metal is depicted in dark brown. The substrate between upper metal and ground plane has the following characteristics:* $\varepsilon_r = 2.33$, $h = 0.5$ *mm,* $tg\delta = 0.003$ *: (a) Topology, (b) 3D view, (c) Front Face (d) Bottom Face (dimensions are:* $R_{out} = 4.5$ *mm,* $G = 0.1$ *mm,* $C = 0.5$ *mm,* $W_{out} = 0.5$ *mm,* $W = 5$ *mm, distance between 2 adjacent cells fixed to 2 mm).*

(Short Open Through Line) [12]. Fig. 4.63 illustrates the comparison between simulations and experimental results for the left-hand and right-hand bands of the LWA created from a CRLH TL based on CSRRs. Discrepancies between measurements and simulations are explained by fabrication tolerances.

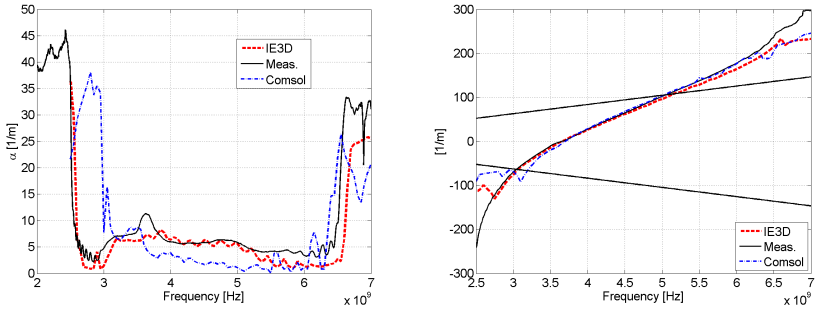
The leakage factor is extracted from 4.3 in Fig. 4.64(a) and the propagation constant is extracted from 4.4 in Fig. 4.64(b). The propagation characteristics exhibit a continuous transition between left and right leaky bands, giving rise to the disappearance of the gap in the scanning range. From the radiation cone, where the dispersion curve β penetrates in the radiation region, we can extract the leaky region between 3.15 GHz and 5 GHz for Comsol solver, between 3.05 GHz



(a) S_{11} *(b)* S_{21}

Figure 4.63. *S-parameters of TL loaded by 16 CSRRs of Fig. 4.62 measured (black solid), simulated with IE3D (red dashed) and with Comsol (blue dot-dashed) in left-hand and right-hand bands.*

and 5.15 GHz for IE3D simulation and between 3.05 GHz and 5.05 GHz for the measurements.



(a) Leakage factor α *(b)* Propagation constant β

Figure 4.64. *Propagation characteristics as calculated from the S-parameters shown in Fig. 4.63 using eqs. 4.4 and 4.3 of the TL loaded by 16 CSRRs depicted in Fig. 4.62. The calculations shown pertain to the measured case (black solid) and the IE3D case (red dashed) and with Comsol (blue dot-dashed) in the left-hand and right-hand bands. The magenta area represents the radiation cone defined by the free-space propagation constant* k_0.

Radiation performance. IE3D software is used to simulate the 3D radiation pattern of the TL based on the 16 cells from Fig. 4.62 in the leaky region. The structure is simulated assuming an infinite substrate. To validate the results of this software and to avoid the assumption of infinite substrate, the COMSOL solver is also used to simulate the radiation pattern of this structure. Fig. 4.66(a) and Fig. 4.66(b) show corresponding 2D views of the simulated radiation pattern for the leaky region in the ($\phi = 0°$) X-Z plane, validating the continuous frequency beam scanning for both leaky regions without stopband.

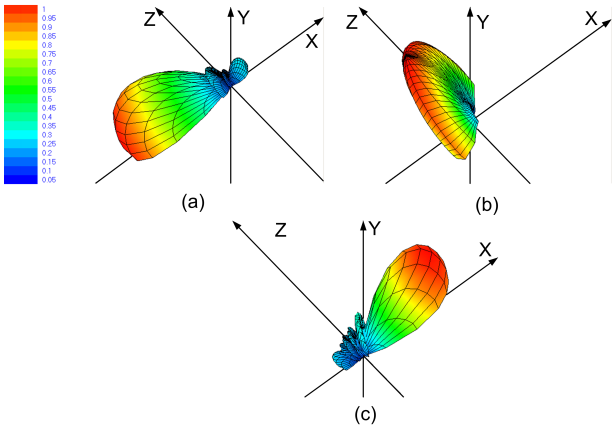
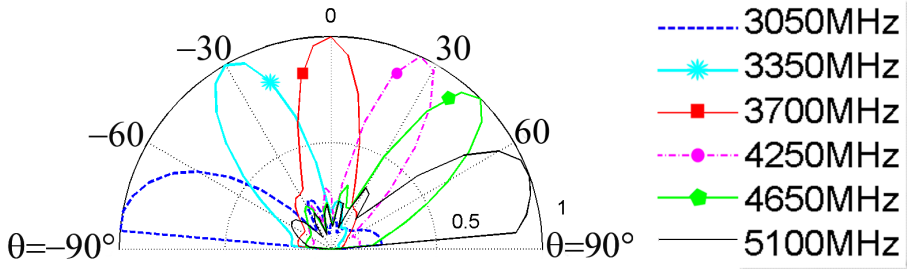
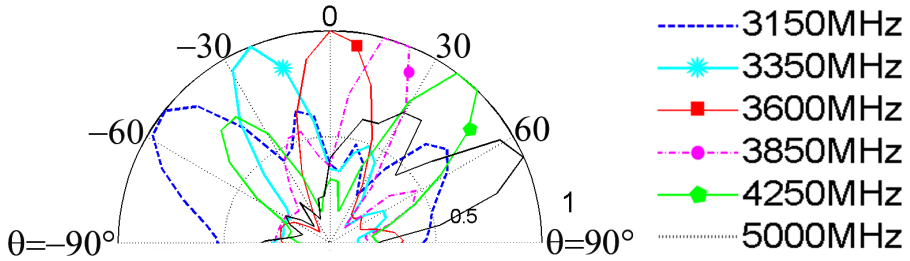


Figure 4.65. *Normalized 3D radiation patterns for the TL based on 16 cells of Fig. 4.62(a)(a) simulated with IE3D software assuming an infinite substrate at 3 frequencies in the leaky region. Color bar: blue corresponds to zero, red corresponds to 1 : (a) 3.1 GHz, (b) 3.7 GHz, (c) 5.1 GHz.*

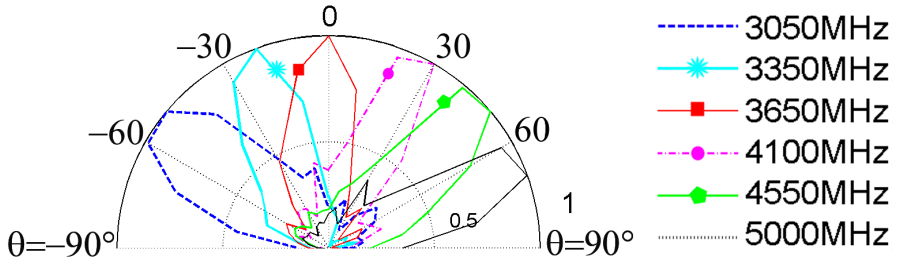
Fig. 4.65 shows 3D views of the simulated radiation pattern at three illustrative frequencies of interest in the leaky region. 3.1 GHz was first simulated because it is the lowest frequency of the left-leaky region, corresponding to $\beta = -k_0$, therefore to θ_{MB} = -90° from (4.5). Secondly 3.7 GHz is simulated because this frequency is the upper frequency of the left-leaky region, corresponding to $\beta = 0$, therefore to $\theta_{MB} = 0°$ from (4.5). In this case, the radiation is maximal in the broadside direction as predicted by the theory for the lowest frequency of the right-leaky region. Finally 5.1 GHz is simulated because this frequency is the upper frequency of the right-leaky region, corresponding to $\beta = k_0$, therefore to $\theta_{MB} = 90°$ from (4.5).



(a) IE3D Simulation



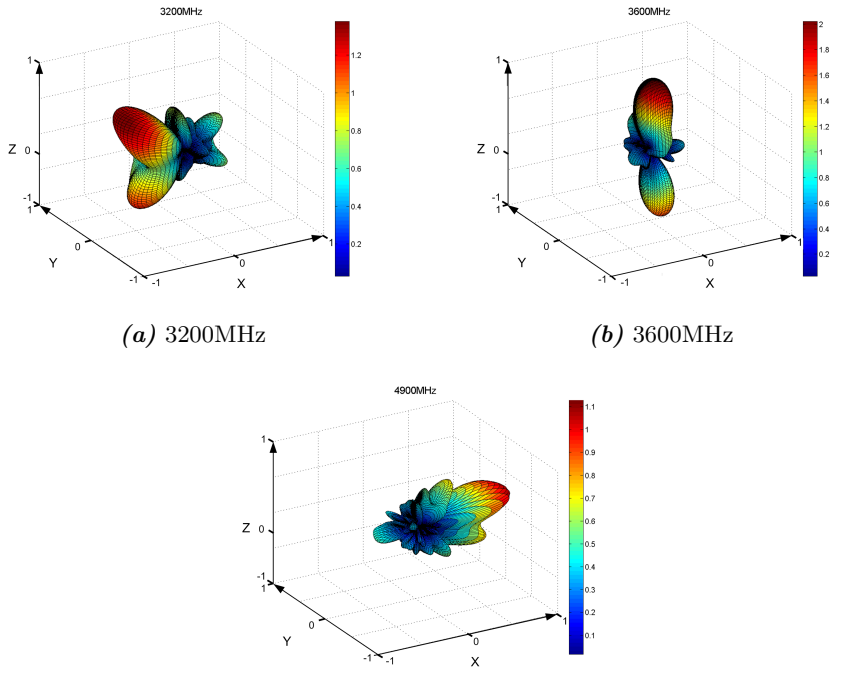
(b) Comsol Simulation



(c) Measurement

Figure 4.66. *Normalized 2D radiation pattern in ($\phi = 0°$) X-Z plane for the TL based on 16 cells of Fig. 4.62(a) (a) simulated with IE3D (with the assumption of infinite substrate), (b) with Comsol and (c) measured for different frequencies in the leaky region.*

The same analysis is presented using the COMSOL simulation in Fig. 4.67. Both approaches agree on a similar frequency scanning ability in both leaky regions. The antenna efficiency AF, illustrated in Fig. 4.68, is similar between IE3D and Comsol solvers.



(a) 3200MHz

(b) 3600MHz

(c) 4900MHz

Figure 4.67. *Normalized 3D radiation patterns for the TL based on the 16 cell structure of Fig. 4.62(a) simulated with COMSOL solver at 3 frequencies in the leaky region. Color bar: blue corresponds to the minimum, red corresponds to the maximum.*

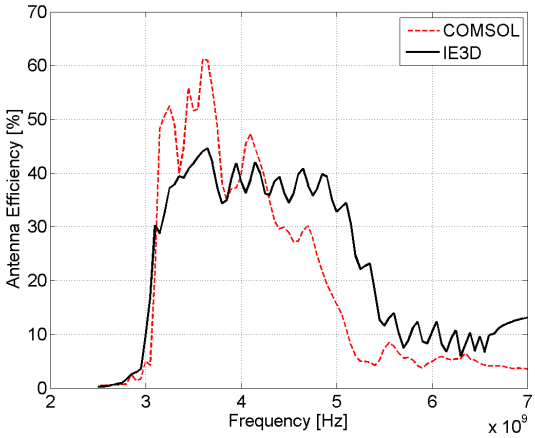


Figure 4.68. *Antenna efficiency AF of the cascade of 16 cells based on one split ring similar to the one depicted in Fig. 4.51(a) extracted from simulation with IE3D assuming an infinite substrate (solid) and COMSOL (dotted).*

To confirm this prediction, the radiation patterns are also measured from transmission measurements between a SATIMO524 QH800-008 Quad Ridge Horn Antenna and the antenna under test with the same VNA (used to extract the propagation characteristics) in an anechoic chamber (Fig. 4.69). The set-up is described in the section 4.2.2. The characteristics of the horn antenna are de-embedded following the methodology presented in [16]. Recall that Fig. 4.66(c) illustrates corresponding 2D views of the measured radiation pattern for the both leaky regions in the ($\phi = 0°$) X-Z plane, validating the uninterrupted frequency beam scanning in both leaky regions. Indeed, the qualitative agreement between Fig. 4.66(a), Fig. 4.66(b) and Fig. 4.66(c) is very good, given that in all likelihood there would occur frequency shifts between measurements and simulations due to fabrication tolerances.

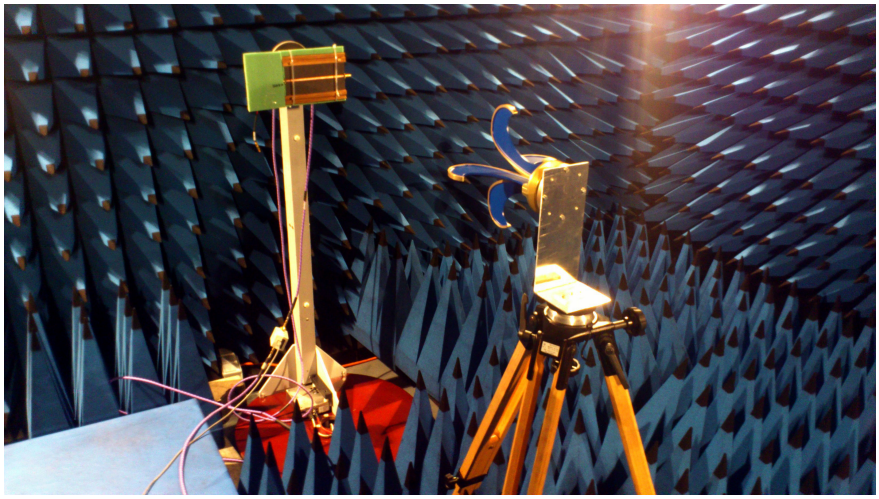


Figure 4.69. *Photos of the measurement set-up in the UCL anechoic chamber (on the left, antenna under test with the swivelling table inside the anechoic chamber and on the right, SATIMO 524 QH800-008 Quad Ridge Horn Antenna.*

Figs. 4.70, 4.71, 4.72 show 3D views of the measured radiation pattern at three illustrative frequencies of interest in both leaky regions. 3.05 GHz was first measured because it is close to the lowest frequency of the left-leaky region, corresponding to $\beta = -k_0$, therefore to $\theta_{\mathrm{MB}} = $ -90° from (4.5). Secondly 3.65 GHz is measured because this frequency is the upper frequency of the left-leaky region, corresponding to $\beta = 0$, therefore to $\theta_{\mathrm{MB}} = 0°$ from (4.5). Finally 5 GHz is measured because this frequency is close to the upper frequency of the right-leaky region, corresponding to $\beta = k_0$, therefore to $\theta_{\mathrm{MB}} = 90°$ from (4.5).

Moreover, the qualitative agreement between 3D views of Figs. 4.65, 4.67, 4.70, 4.71, 4.72 is quite good.

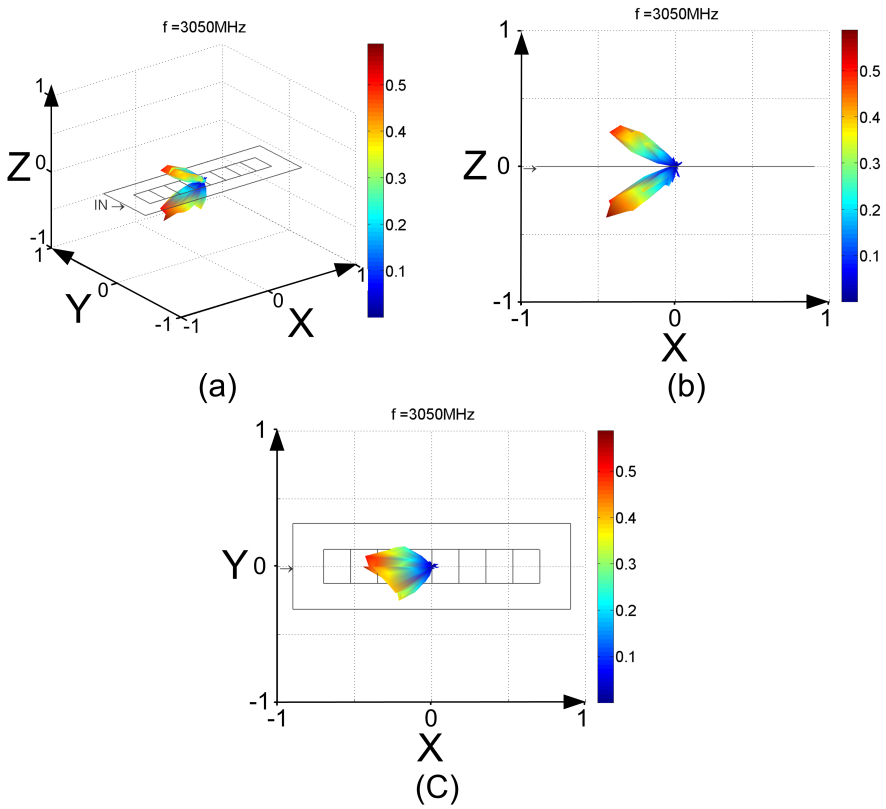


Figure 4.70. *(a) 3D view, (b) 3D view of ($\phi = 0°$) X-Z plane and (c) 3D top view along the z-axis of measurement of normalised radiation pattern of Fig. 4.61 at 3.05 GHz, corresponding to the lower frequency of the balanced leaky region. Color bar: dark blue corresponds to zero, dark red corresponds to 0.6.*

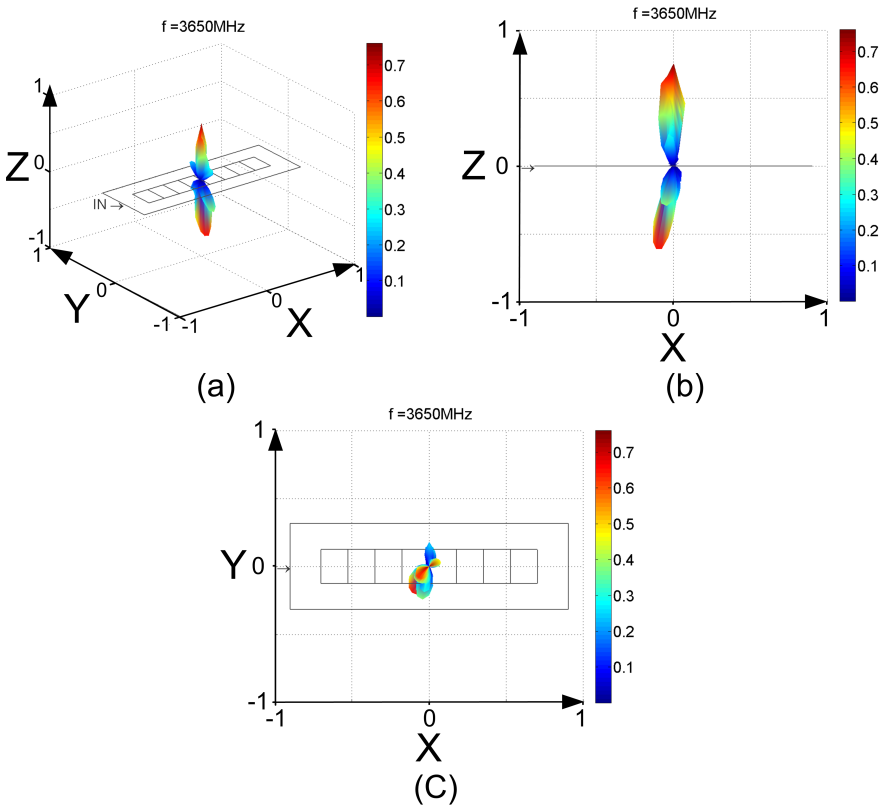


Figure 4.71. *(a) 3D view, (b) 3D view of ($\phi = 0°$) X-Z plane and (c) 3D top view along the z-axis of measurement of normalised radiation pattern of Fig. 4.61 at 3.65 GHz, corresponding to a frequency in the middle of the balanced leaky region. Color bar: dark blue corresponds to zero, dark red corresponds to 0.75.*

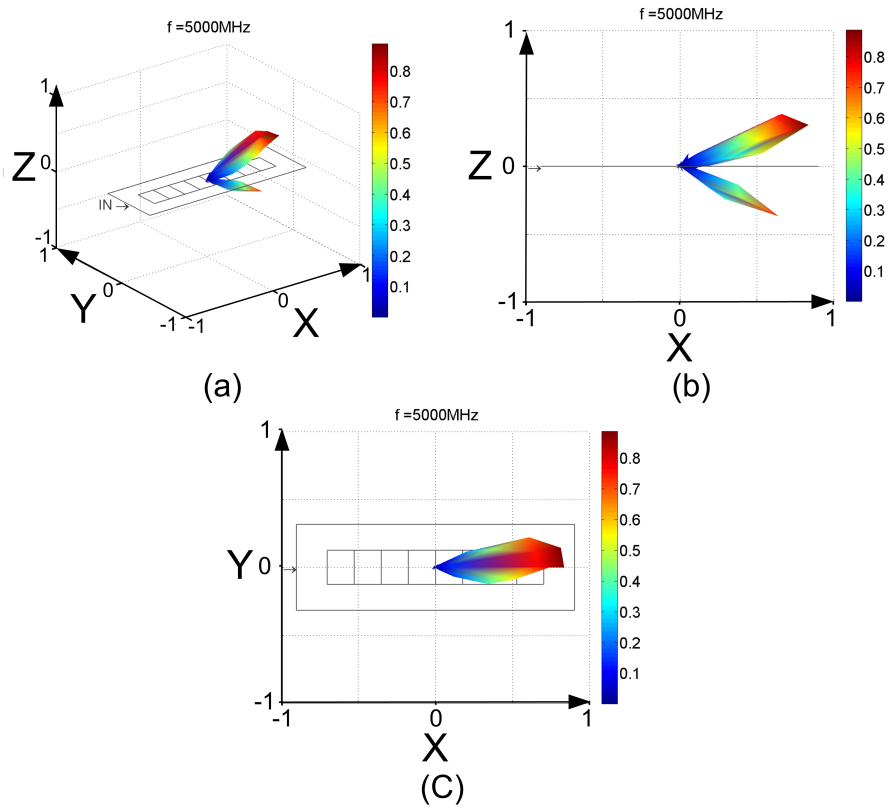


Figure 4.72. *3D view (a), 3D view of ($\phi = 0°$) X-Z plane (b) and 3D top view along the z-axis (c) of measurement of normalised radiation pattern of Fig. 4.61 at 5 GHz, corresponding to the upper frequency of the balanced leaky region. Color bar: dark blue corresponds to zero, dark red corresponds to 0.9.*

4.6 OTHER CANDIDATES OF RESONANT PLANAR LWA

This section is focused on an exhaustive list of other resonant type topologies than the CSRR cell proposed in Chapter 6. From the state of the art, various resonant structures similar to CSRR cell are chosen as candidates to be used for a one-dimensional LWA. Their dimensions are designed for operation in the same frequency band as the CSRR structure of section 6 (Fig. 4.1) and using the same substrate specifications. Tables 4.73 and 4.74 summarizes the main conclusions of the analyses of these structures with some of results presented in appendix E. For all theses simulations, the cell dimensions and substrate properties are similar to

those of the CSRR structure of Fig. 4.1. For a reason of thesis conciseness, the diverse dimensions are not detailed.

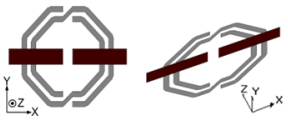
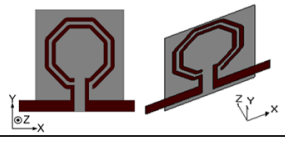
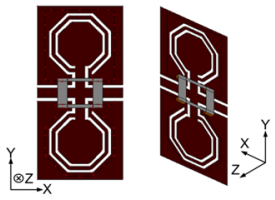
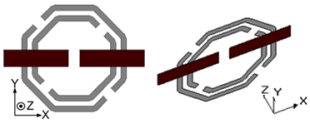
Resonant Candidates for Metamaterial LWAs		
Topology	***Properties***	***Appendix***
1. Nonbianisotropic Spiral Resonator		
	- : no radiation in the broadside direction, decrease of antenna efficiency with the number of turns	*E.2*
2. Open split ring resonators (OSRRs)		
	*- : poor antenna efficiency*	*E.3*
3. Open Complementary Split Ring Resonators (OCSRRs)		
	*- : poor antenna efficiency*	*E.4*
4. Double-split CSRR		
	*+ : possibility of balanced structure to realize a full-space scanning with frequency with radiation in the broadside direction, good antenna efficiency*	*E.5*

Figure 4.73. *Other candidates of resonant planar LWA (some results are presented in appendix E).*

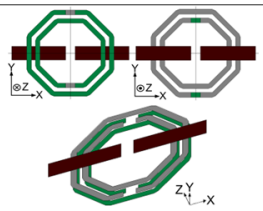
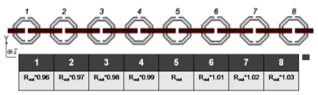
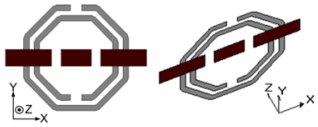
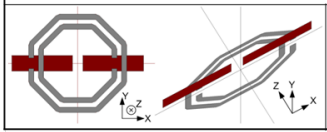
Resonant Candidates for Metamaterial LWAs		
Topology	**Properties**	**Appendix**
5. Double-layers CSRR		
	*+ : radiation in the broadside direction, possibility to create a electronic-tunable LWA by placing a ferroelectric film in the lower substrate*	*E.6*
6. Cascade of non-uniform CSRR cell		
	*+ : omnidirectional antenna using leaky waves, main radiation in the plane of the substrate*	*E.7*
7. CSRR with two gaps		
	*- : similar to CSRR with one gap, decrease of the LH band, no improve of the antenna efficiency,no LH band if gaps placed above the ring*	*E.8*
8. Rotation of CSRR by 90°		
	*+ : radiation in the broaside direction for a rotation of 90°* *- : poor antenna efficiency*	*E.9*

Figure 4.74. *Other candidates of resonant planar LWA (some results are presented in appendix E).*

4.7 CONCLUSION

This chapter has discussed radiation phenomena in a metamaterial transmission line based on series capacitive gaps and CSRRs periodically loading a host microstrip line and acting as a leaky-wave antenna. To the best of our knowledge, it is the first time that the leaky wave properties of this structure are analysed. Full wave simulation and measurement of this structure show, in the left-leaky region, a frequency beam steering simultaneously in the plane of the substrate, ($\theta = 90°$) X-Y plane, and in its normal plane, ($\phi = 0°$) X-Z plane.

Furthermore an analysis of different distances between CSRRs and the substrate edges shows that in narrow substrates destructive interference occurs between the free-space leaky wave radiation and the SW modes, reflected at substrate edges.

In the recent years, significant efforts have been directed in the creation a leaky wave antenna based on a fixed-frequency bias scanning. This chapter has presented the concept of ***electrical control of a LWA TL loaded by CSRRs and ferroelectric*** $Ba_{0.6}Sr_{0.4}TiO_3$ ***thin film placed on the serie gap***, realised on alumina substrate and silver metal layers, ***deposited with the inkjet technique***.

To prove the concept of fixed-frequency LWA based on tunable series capacitor, a similar structure ***using lumped varactor diodes***, is also analysed : full wave simulation and measurements have shown that the left-leaky region is translated to higher frequency as bias voltage increases. Full wave simulations has also proven the fixed-frequency bias scanning. Future works include the validation of this concept through the fabrication of BST LWA and its radiation measurements in anechoic chamber.

Next, this analysis considered the influence of the number of CSRR rings on the radiation properties. For an LWA loaded by a CSRR with a single ring, full wave simulation and measurement of this structure shows, in the left-leaky region, a frequency beam steering in the normal plane, ($\phi = 0°$) X-Z plane, so the number of CSRR rings plays a major role in the radiation shape of the antenna.

The author explains this phenomenon by the fact that near the upper frequency of the left-leaky region, LWAs loaded by CSRRs based on one split ring exhibit a main lobe oriented along broadside direction. This is contrary to LWAs loaded by CSRR based on two concentric split rings, which present a zero in this direction. The physical explanation will be analysed in the next chapter.

Afterwards, the roles played by the different CSRR dimensions on the antenna properties were considered. When designers must create an antenna for a specific applications, they must find a compromise of dimensions in order to facilitate the specifications of the technical requirements. Owing to the number of degrees of freedom in relation to the CSRR structure itself, the quantity of realizable CSRR-based structures could become exhaustive. The author wanted to answer to this inconvenience by creating a database of antenna properties as a function of the CSRR dimension.

This work is based on the IE3D parametric simulation of a cascade of 8 CSRR cells with a single ring. An exhaustive list of figures of merit are considered such as directivity, gain and matching impedance amongst others. For each parameter, the A balanced LWA based on CSRR with one ring has been created. Full-wave simulation and measurements have confirmed a full-spatial continuous frequency scanning.

Finally, LWAs based on resonant structures were investigated. The influence of the shape of the CSRR cell etched on the ground plane is highlighted. Depending on this profile, the spatial scanning exhibits the same behaviour as the classical LWA or LWA loaded by CSRR presented in the previous chapter, i.e. a frequency beam steering simultaneously in the plane of the substrate, ($\theta = 90°$) X-Y plane, and in its normal plane, ($\phi = 0°$) X-Z plane. A TL created by a cascade of OSRR cells and a CPW loaded by OCSRRs were tentatively studied as a candidate LWA but poor radiation performances invalidates the use of this kind of arrangement. Lastly, a non-linear cascade of CSRR is introduced where the size of the external CSRR ring is increased along the TL. From simulation results, it appears that this configuration leads to omnidirectional radiation in the substrate plane. This concept could be extended to improve the impedance adaptation.

This investigation is not completely exhaustive but offers several new LWA perspectives based on CSRR structure by creating specific radiation properties depending on the choice of resonant particle.

Bibliography

[1] D. Jackson and A. Oliner, *Leaky Wave Antennas.* in Balanis C.A. (Ed), Wiley, 2008, ch. Modern Antenna Handbook, pp. 325 – 368.

[2] G. Eleftheriades and M. Antoniades, *Antenna Applications of Negative Refractive Index Transmission Line (NRI-TL) Metamaterials.* in Balanis C.A. (Ed), Wiley, 2008, ch. Modern Antenna Handbook, pp. 677 – 736.

[3] C. Caloz and T. Itoh, *Electromagnetic metamaterial : Transmission line and microwave applications.* Wiley, 2006.

[4] I. Arnedo, J. Illescas, M. Flores, T. Lopetegi, M. Laso, F. Falcone, J. Bonache, J. Garcia-Garcia, F. Martin, J. Marcotegui, R. Marques, and M. Sorolla, "Forward and backward leaky wave radiation in split-ring-resonator-based metamaterials," *IET Microwave, Antennas, Propagation, Special Issue on Metamaterials LHM*, vol. 1, no. 1, pp. 65 – 68, Feb. 2007.

[5] S. Eggermont and I. Huynen, "Substrate edge effects in leaky wave antenna based on complementary split ring resonators," *Proc. IEEE Fourth European Conference on Antennas and Propagation (EUCAP2010)*, Apr. 2010, Barcelona, Spain.

[6] ——, "Leaky wave radiation phenomena in metamaterial transmission line based on complementary split ring resonators," *Microwave And Optical Technology Letters*, vol. 53, no. 9, pp. 2025 – 2029, Sep. 2011.

[7] ——, "Influence of number of split rings on the leaky radiation of a metamaterial transmission line based on complementary split ring resonators," *Microwave And Optical Technology Letters*, vol. 54, no. 4, pp. 867 – 875, 2012.

[8] M. S. R. Marques, F. Martin, *Metamaterials With Negative Parameters, Theory, Design and Microwave Applications.* Wiley, 2008.

[9] M. Gil, J. Bonache, I. Gil, J. Garcia-Garcia, and F. Martin, "On the transmission properties of left-handed microstrip lines implemented by complementary split rings resonators," *International Journal of Numerical Modelling : Electronic Networks, Devices and Fields*, vol. 19, no. 2, pp. 87 – 103, Mar. 2006.

[10] ©IE3D EM, Electromagnetic (EM) Design and Simulation Software, ©Mentor Graphics. [Online]. Available: http://www.mentor.com/electromagnetic-simulation

[11] ©COMSOL Multiphysics Finite Element Method solver. [Online]. Available: http://www.comsol.com/

[12] *Agilent AN 1287-3 Applying Error Correction to Network Analyzer Measurements, Application Note*, Agilent Technologies, USA, Mar. 2002.

[13] I. Huynen, C. Steukers, and F. Duhamel, "A wideband line-line dielectrometric method for liquids, soils, and planar substrates," *IEEE Transactions on Instrumentation and Measurement*, vol. 50, no. 5, pp. 1343 – 1348, Oct. 2001.

[14] D. M. Pozar, *Microwave Engineering.* Wiley, 1997.

[15] A. V. Vorst and D. Vanhoenacker-Janvier, *Bases de l'ingenierie Micro-Onde.* Deboeck Universite, 1996.

[16] C. Balanis, *Antenna Theory, 3rd edition.* Wiley, 2005.

[17] R. E. Collin, *Field Theory of Guided Waves.* New York, IEEE Press, 1991.

[18] A. Grbic and G. V. Eleftheriades, "Experimental verificiation of backward-wave radiation from a negative refractive index metamaterial," *Journal of Applied Physics*, vol. 92, no. 10, pp. 5930 – 5935, Nov. 2002.

[19] ——, "Experimental verification of backward-wave radiation from a negative refractive index metamaterial," *Journal of applied physics*, vol. 92, no. 10, pp. 5930 – 5935, Nov. 2002.

[20] B. Razavi, *RF Microelectronics.* Prentice Hall, 1997.

[21] D. Sievenpiper, J. Schaffner, J. J. Lee, and S. Livingston, "A steerable leaky-wave antenna using a tunable impedance ground plane," *IEEE Antennas and Wireless Propagation Letters*, vol. 1, pp. 179 – 182, 2002.

[22] G. Lovat, P. Burghignoli, and S. Celozzi, "A tunable ferroelectric antenna for fixed-frequency scanning applications," *IEEE Antennas and Wireless Propagation Letters*, vol. 5, pp. 353 – 356, 2006.

[23] D. F. Sievenpiper, "Forward and backward leaky wave radiation with large effective aperture from an electronically," *IEEE Transaction on Antennas and Propagation*, vol. 53, no. 1.

[24] A. Vélez, J. Bonache, and F. Martin, "Effects of varying the series capacitance in csrr-loaded metamaterial transmission lines," *Microwave And Optical Technology Letters*, vol. 49, no. 9, pp. 2245 – 2248, Sep. 2007.

[25] M. Gil, J. Bonache, and F. Martín, "Metamaterial filters: A review," *Metamaterials*, vol. 2, pp. 186 – 197, 2008.

[26] C. Marlier, "Projet de 2ème master, réalisation de métamatériaux accordables à base de céramiques," Université de Mons, Faculté Polytechnique de Mons, Tech. Rep., Jun. 2011, promoteur : Marc Debliquy.

[27] Z.-G. Y. (Editor), *Handbook of dielectric, piezoelectric and ferroelectric materials, Synthesis, properties and applications.* CRC Press, 2008.

[28] A. K. Tagantsev, V. O. Sherman, K. F. Astafiev, J. Venkatesh, and N. Setter, "Ferroelectric materials for microwave tunable applications," *Journal of Electroceramics*, vol. 11, pp. 5 – 66, 2003.

[29] S. Sedra and K. C. Smith, *Microelectronic Circuits: International edition.* OUP USA, 2010.

[30] D. Leblebici and Y. Leblebici, *Fundamentals of High-Frequency CMOS Analog Integrated Circuits.* Cambridge University Press, 2009.

[31] Skyworks, *SMV123x Series: Hyperabrupt Junction Tuning Varactors, datasheet*, Oct. 2009.

[32] *IE3DLibrary Users Manual, Version 12.0*, Zeland Software, Inc., Fremont, California, USA, Oct. 2006.

CHAPTER 5

INFLUENCE OF THE NUMBER OF RING ON THE BROADSIDE RADIATION OF CSRRS-LOADED LWA

This chapter presents the analysis of the radiation of the leaky wave antenna (LWA) based on CSRR. Considerable attention is given to the radiation at the upper frequency of the left-hand band for different geometrical configurations. Finally a sensitivity analysis with respect to the distance between rings is realised to help the understanding of the particular radiation of the CSRR-loaded LWA.

5.1 INTRODUCTION

The previous sections indicate a split of the radiation pattern into two different directions resulting into two apparent beams for the high frequency range of the left-leaky region for a LWA loaded by CSRRs with two rings. This phenomenon is not present for the low frequency range of its right-leaky region. This section analyses the electric and magnetic current distributions in the unit cell with the intent of predicting the radiation created by the upper level of metal and by the ground plane. This in turn will be seen to explain the behaviour of the radiation pattern. In the same time, a special attention is brought to the CSRR cell with one ring, because this structure does not present the same behavior in the left-leaky region than the LWA loaded by CSRRs with two rings. Next

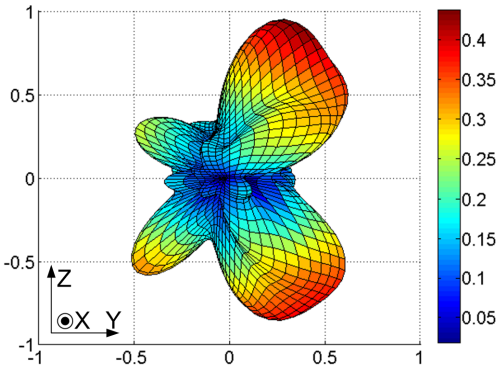
a sensitivity with respect to the distance between rings is created in the aim of better explaining the dipole representation of CSRRs with 1 and 2 rings.

5.2 CONTEXT OF THE WORK : RADIATION NEAR THE BROADSIDE

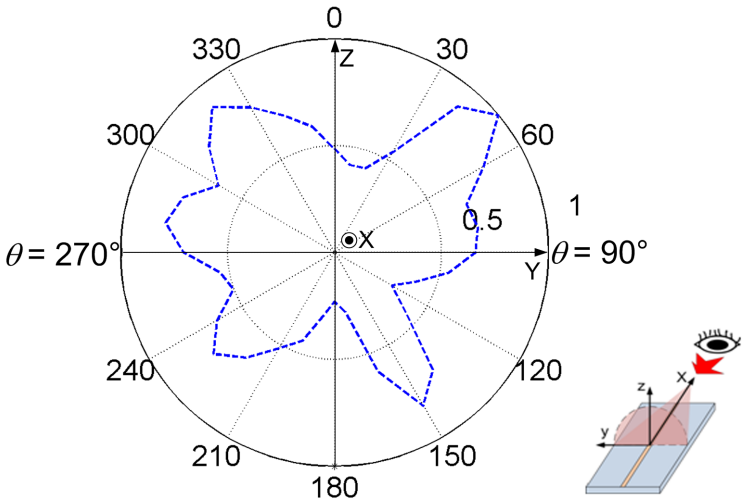
For CSRR-loaded LWA with two rings, the absence of maximal broadside radiation for upper frequencies of the left-leaky region is underlined in Fig. 5.1 by the view of the Y-Z ($\phi = 90°$) plane of simulated and experimental results. Fig. 5.1(a) shows the 3D view of the radiation pattern of CSRR cells of two split rings, for ($\phi = 90°$) Y-Z plane simulated with COMSOL at frequency f_u. Fig. 5.1(a) shows the corresponding 2D view of the measured radiation patterns.

For the same structure on the radiation near the lower frequency of the right-leaky region where β is close to zero, it is important to notice that the main lobe of the radiation pattern of Fig. 5.2 is oriented in the broadside direction following the prediction of (4.5).

Now, in order to compare the radiation properties that depend on the number of split rings, we could analyse the radiation pattern of the structure with a single ring, shown in Fig. 4.51, for the upper frequency f_u of the left-leaky region. Fig. 5.3(a) illustrates the 3D view of the radiation pattern of CSRR cells of one split ring, for ($\phi = 90°$) Y-Z plane simulated with COMSOL at frequency f_u. Fig. 5.3(b) shows the corresponding 2D view of the measured radiation patterns. It is clear that the main lobe is oriented along the Z-axis in the broadside direction as predicted by 4.5, contrary to the radiation pattern of the LWA created with CSRR with two split rings. The measurement in two different planes, i.e. ($\phi = 45°$) and ($\phi = 135°$) planes, shown in Fig. 5.4, confirms the main lobe is oriented along the Z plane for CSRR TL with one split ring.

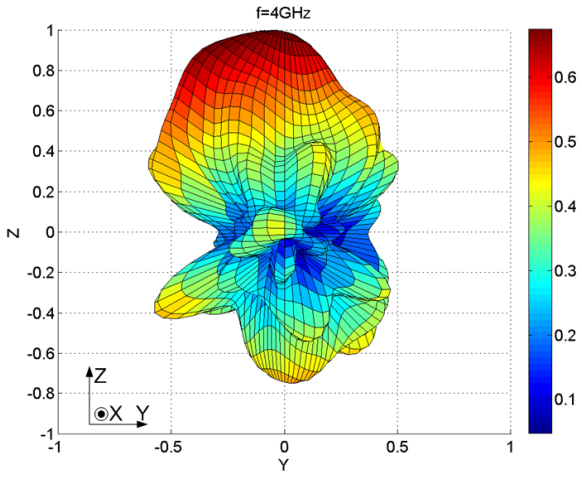


(a) COMSOL at 3.275 GHz

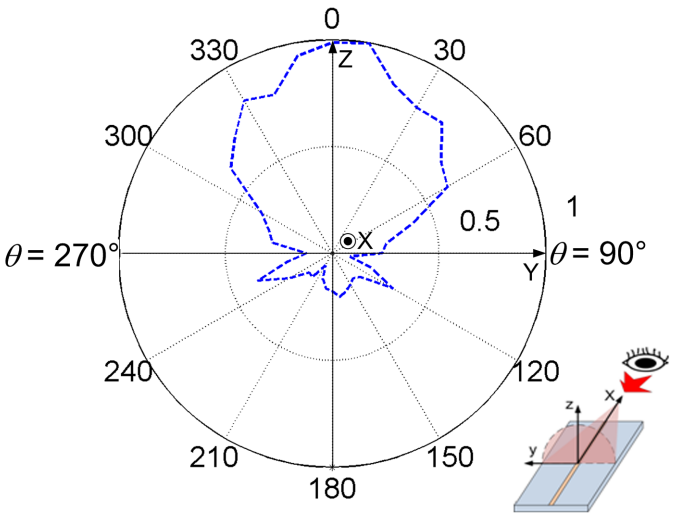


(b) Measurement at 2.92 GHz

Figure 5.1. *(a) 3D view of (ϕ = 90°) Y-Z plane of normalised radiation pattern for the TL based on 16 cells of Fig. 4.1(a)* ***with two rings*** *simulated with COMSOL at 3.275 GHz, corresponding to upper frequency of the* ***left-leaky region****. Color bar: dark blue corresponds to zero, dark red corresponds to 0.45. (b) Normalized 2D radiation pattern in (ϕ = 90°) Y-Z plane for the TL based on 16 cells of Fig. 4.2 measured at 2.92 GHz, corresponding to upper frequency of the left-leaky region.*

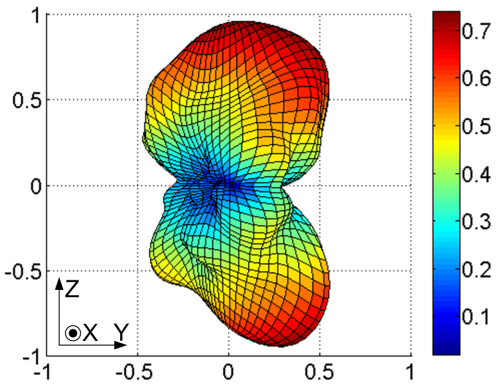


(a) COMSOL at 4 GHz

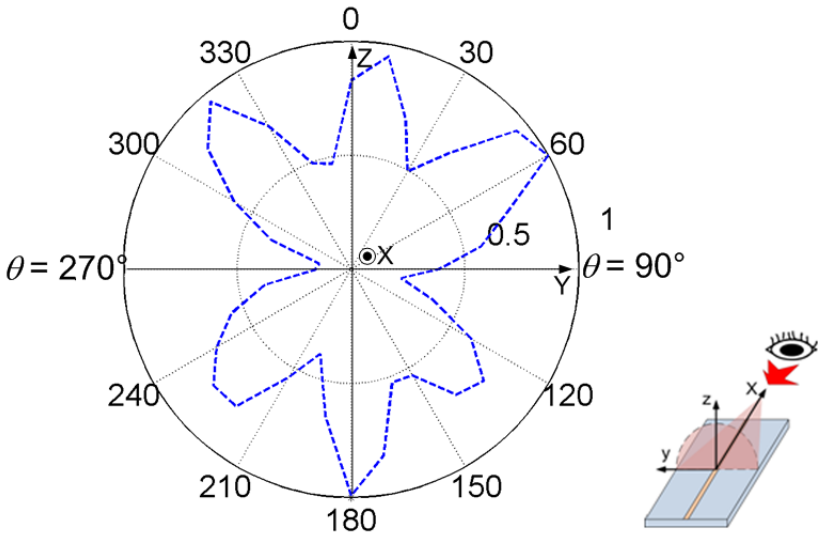


(b) Measurement at 4.8 GHz

Figure 5.2. *(a) 3D view of ($\phi = 90°$) Y-Z plane of normalised radiation pattern for the TL based on 16 cells of Fig. 4.1(a)* ***with two rings*** *simulated with COMSOL at 4 GHz, corresponding to lower frequency of the* ***right-leaky region****. Color bar: dark blue corresponds to 0.05, dark red corresponds to 0.675. (b) Normalized 2D radiation pattern in ($\phi = 90°$) Y-Z plane for the TL based on 16 cells of Fig. 4.2 measured at 4.8 GHz, corresponding to lower frequency of the right-leaky region.*



(a) COMSOL at 3.675 GHz



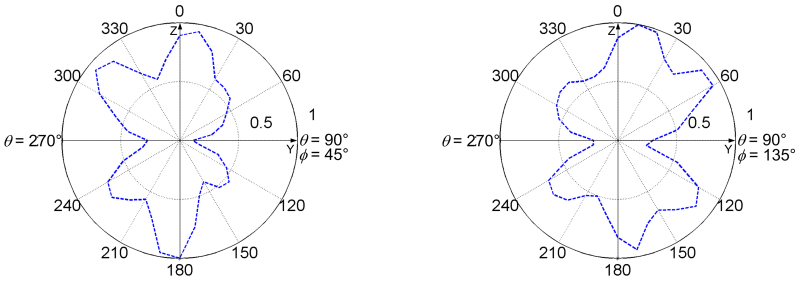
(b) Measurement at 4 GHz

Figure 5.3. *(a) 3D view of ($\phi = 90°$) Y-Z plane of normalised radiation pattern for the TL based on 16 cells similar to the one depicted in Fig. 4.51(a)* ***with a single ring*** *simulated with COMSOL at 3.675 GHz, corresponding to upper frequency of the* ***left-leaky region****. Color bar: dark blue corresponds to zero, dark red corresponds to 0.7. (b) Normalized 2D radiation pattern in ($\phi = 90°$) Y-Z plane for the TL based on 16 cells of Fig. 4.51 measured at 4 GHz, corresponding to upper frequency of the left-leaky region.*

Radiation in the broadside radiation			
CSRR with 2 rings		**CSRR with 1 ring**	
LH	*RH*	*LH*	*LH*
Null	Max	Max	Max

Table 5.1. *Summary of the behavior of the radiation beam in the broadside direction of LWA loaded by CSRR with two rings or with a single ring. The main beam presents a minimum (called "NULL" in the table) or a maximum (called "MAX") along the z-axis for the upper frequency of the left-leaky region (called "LH" in the table) or for the lower frequency of the right-leaky region (called "RH" in the table).*

We will try to explain the influence of the split ring on the broadside radiation. The table summarizes the results of these previous observations. We can know examine the distribution of electric and magnetic currents in these cases to understand these behaviours. We do not focus our attention in this analysis on the lower frequency range of the right-leaky region, indeed the radiation is not influenced by the CSRR ring, the radiation behavior is really similar between the structure with one or two rings.



(a) ($\phi = 45°$) plane ***(b)*** ($\phi = 135°$) plane

Figure 5.4. *Normalized 2D radiation pattern for the TL based on 16 cells similar to the one depicted in Fig. 4.51* ***with one ring*** *measured at 4 GHz, corresponding to upper frequency of the* ***left-leaky region*** *with (a) in ($\phi = 45°$) plane and (b) in ($\phi = 135°$) plane.*

5.3 IMPACT OF THE DISTRIBUTION OF ELECTRIC CURRENT

The behaviour of the radiation pattern for frequencies close to the upper limit of the left-leaky region can be explained by the distribution of the current density and the current vectors on the metallic strip joining two adjacent cells inside the 16-cells structure.

5.3.1 CSRR with two rings in the left-handed region

The inspection of the simulation of this metal strip, realized with IE3D presents a symmetrical distribution at a frequency of 3.17 GHz in Fig. 5.5, which could explain the radiation minimum in the broadside direction. As a result of this observation, this idea will be verified by considering a simple model based on electric dipoles to improve the understanding of the link between distribution current and the radiation phenomena.

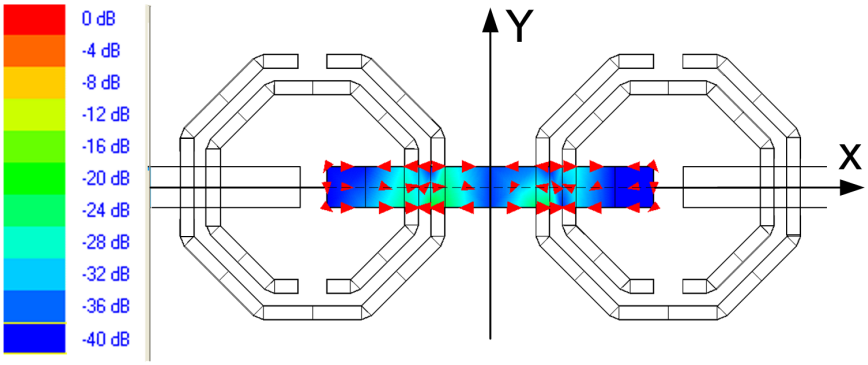


Figure 5.5. *Zoom of distribution of current density and current vectors on metallic strip joining adjacent cells, simulated with IE3D assuming an infinite substrate at 3.17 GHz, which is the upper frequency of the left-leaky region (Fig. 4.9). Color bar: current density is normalised with the maximum of the current on the upper metal level (maximal current density : 182.3 A/m) and is expressed in dB, blue color corresponds to lowest current density; red color corresponds to highest current density. Symmetry of current vectors at the same time around y-axis and x-axis is observed.*

At this frequency, broadside radiation should occur according to equation from (4.5) and Fig. 4.4(b) ($\beta \approx 0$). Due to the influence of CSRRs, current vectors are nearly symmetrical with respect to y-axis and anti-symmetrical with respect to x-axis. Let us assume an antenna consisting of cascaded sets of current dipoles. Each set consists of 8 infinitesimal horizontal dipoles: four of them are oriented along x-axis with the same magnitude, as shown in Fig. 5.6(a), and their four electric images reproduce the impact of the ground plane. The radiation

pattern $R(\theta, \phi)$ of this cascade is the product of the set pattern $E(\theta, \phi)$ and the array factor $AF(\theta, \phi)$ [1]. The far-field radiation pattern $E(\theta, \phi)$ is simulated for a set with COMSOL solver in Fig. 5.6(b) at 2.92 GHz. This corresponds to $\beta \approx 0$ for measurement results, therefore to $\theta_{\mathsf{MB}} \approx 0°$ from (4.5), expected maximal radiation in the broadside direction. A zero in the radiation pattern occurs at $\theta_{\mathsf{MB}} = 0°$. Symmetry of the current vectors in the metal strips around y-axis and their anti-symmetry around x-axis both create negative interference. This in turn inhibits the broadside radiation causing it to disappear. The array factor $AF(\theta, \phi)$ shown at the same frequency (based on measured propagation characteritics) in Fig. 5.6(c) is given by [2]:

$$AF(\theta, \phi) = \sum_{n+1}^{N} (I_n . e^{j(n-1)k_0 p sin\theta + j\xi_n}) \tag{5.1}$$

where $\xi_n = (n-1)k_0 p \sin\theta_{\mathsf{MB}}$ and $I_N = I_0 e^{-\alpha(n-1)p}$. N and p represent respectively the number of unit cells and period of the structure. The total far-field radiation pattern $R(\theta, \phi)$, equal to $E(\theta, \phi).AF(\theta, \phi)$ is illustrated in Fig. 5.6(d).

The main lobe of the array factor $AF(\theta, \phi)$ appears concentrated in the X-Z plane (Fig. 5.6(c)), which when combined with the zero observed at the broadside ($\theta_{\mathsf{MB}} = 0°$) for the set radiation pattern $E(\theta, \phi)$, yields the apparent radiation splitting of $R(\theta, \phi)$ observed in the plane of the substrate at Fig. 5.6(d). This prediction based on the current distribution of Fig. 5.6(a) is very similar to that observed in IE3D simulation (Fig. 4.9(c)) and in measurement (Fig. 4.15).

5.3.2 CSRR with two rings in the right-handed region

It is also possible to apply the same methodology to the lower frequency of the right-leaky region. In this case the current densities and current vectors of the metal strip between cells are analysed at 4.8 GHz, which corresponds to the lower frequency of the right-leaky region. The results of this analysis are shown in Fig. 5.7, all current vectors are oriented in the same direction along axis. Concerning frequencies for which the radiation appears in the broadside direction, it can be concluded that the left-leaky region is influenced by the CSRR, contrary to the right-leaky region. The model based on a cascade of eight dipoles is also applied in Fig. 5.8 with a good agreement between simulations (Fig. 4.11(a)), measurement and model (Fig. 5.8(d)). This model will be also validated in the next section.

5.3.3 CSRR with one ring in the left-handed region

A representation of the distribution of current density and current vectors on metallic strip joining adjacent cells, simulated with IE3D assuming an infinite substrate, is given in Fig. 5.9 at the upper frequency of the left-hand broadside for the case of the CSRR with one split ring. Inspection of Fig. 5.9 reveals that, unlike the case of CSRR with two split rings, any symmetry of current vectors is

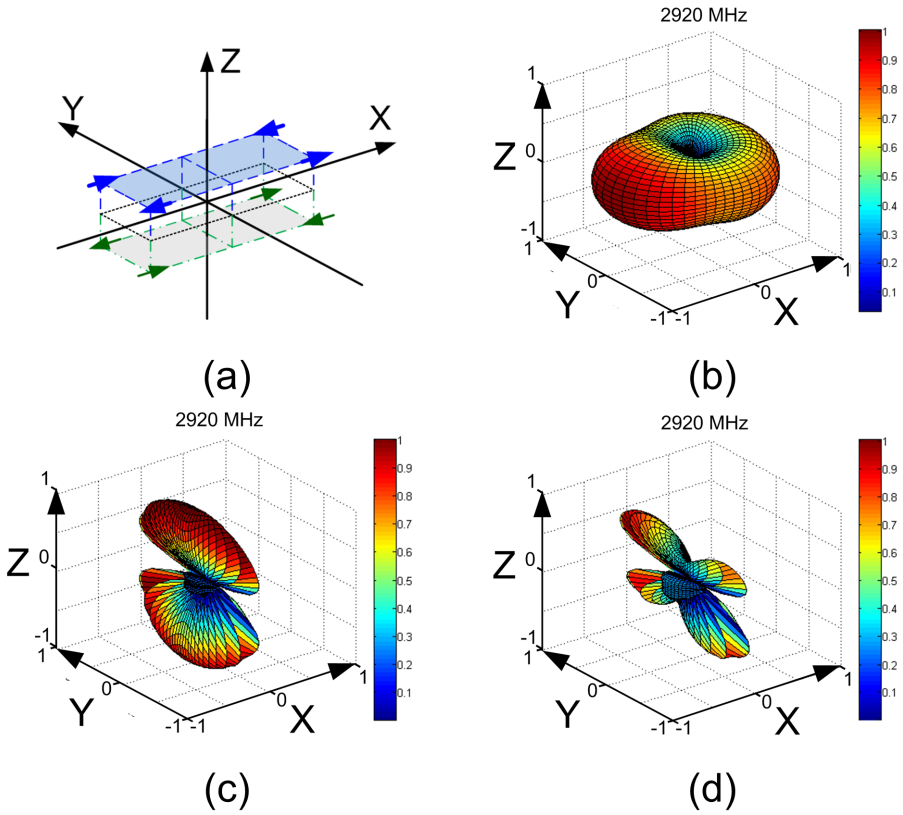


Figure 5.6. *(a) Geometry of eight opposite infinitesimal horizontal dipoles oriented along x-axis, (b) Normalised far-field pattern $E(\theta, \phi)$ of the geometry shown in Fig. 5.6(a) as simulated with COMSOL assuming distance between dipoles equal to 5 mm along the x axis, to 1.5 mm along the y axis, to 1 mm along the z axis at 2.92 GHz (c) Normalized array factor $AF(\theta, \phi)$ for 16 cells from (5.1) at 2.92 GHz, (d) Normalized total field $R(\theta, \phi)$ of 16-element array of Fig. 5.6(a), which is the product of $E(\theta, \phi)$ and $AF(\theta, \phi)$ at 2.92 GHz.*

not present. Indeed, all current vectors are oriented in the same direction along x-axis. We have to verify if this absence of symmetry can explain the presence of broadside radiation. Taking a similar approach to the previous analysis of the CSRR with two slit rings, we can conceptualize the antenna as cascaded sets of current dipoles. Each set consists of 8 infinitesimal horizontal dipoles and four of them are oriented along the x-axis with the same magnitude and same direction, as shown in Fig. 5.10(a). Also, their four electric images reproduce the electric ground. The radiation pattern $R(\theta, \phi)$ of this cascade is the product of the set pattern $E(\theta, \phi)$ and the array factor $AF(\theta, \phi)$ [1].

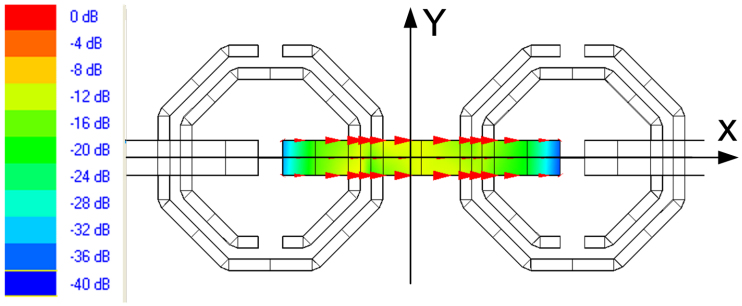
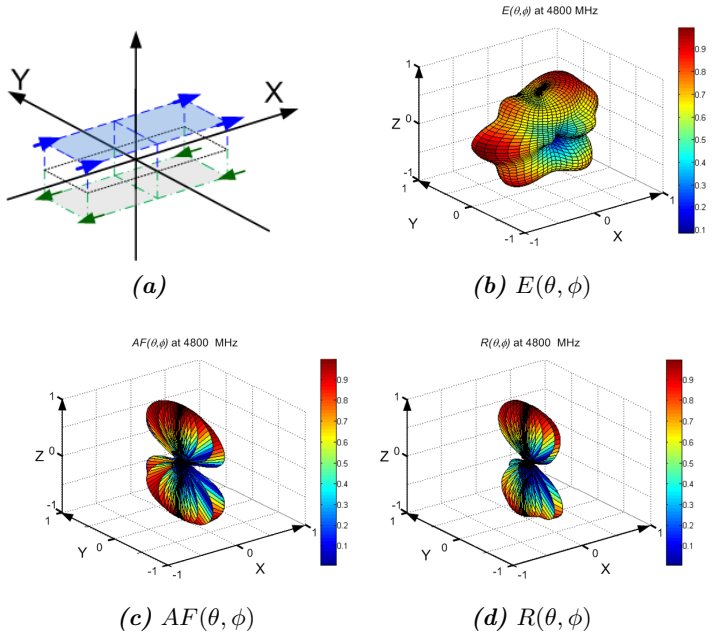


Figure 5.7. *Zoom of distribution of current density and current vectors on metallic strip joining adjacent cells, simulated with IE3D assuming an infinite substrate at 4.8 GHz, which is the lower frequency of the right-leaky region (Fig. F.5). Color bar: current density is normalised with the maximum of the current on the upper metal level and is expressed in dB, blue color corresponds to lowest current density; red color corresponds to highest current density. All current vectors are oriented in the same direction along axis.*

The 3D view of Fig. 5.10(b) depicts graphically the results of this normalised far-field pattern $E(\theta, \phi)$ given the geometry indicated in Fig. 5.10(a). These particular results arise from COMSOL simulations where it was assumed that the distance between dipoles equals to 5 mm along the x-axis, to 1.5 mm along the y-axis and to 1 mm along the z-axis. Contrary to the results of symmetrical sets of dipoles, this far-field pattern does not present zero radiation in the broadside direction. The array factor, illustrated in Fig. 5.10(c), is calculated at 4 GHz, which follows from equation 5.1 and is based on measured propagation characteristics. Globally the array factor of the cascade model of the CSRR-loaded TL with one split ring is similar to the results obtained with two split rings. Fig. 5.10(d) shows the total radiation pattern $R(\theta, \phi)$. The main lobe of the array factor $AF(\theta, \phi)$ is mainly oriented in the Y-Z plane, which, combined with the main lobe of the set radiation pattern $E(\theta, \phi)$, yields the broadside radiation observed in $R(\theta, \phi)$ and is similar to that observed in COMSOL simulation (Fig. F.9(a) and Fig. 5.3(a)) and in measurement (Fig. 4.55(b) and 5.3(b)).

Furthermore the number of rings does not influence only the radiation pattern. The comparison of the antenna efficiency AF, provided by COMSOL and IE3D software and shown in Fig. 5.11, indicates that there is a lower efficiency for a TL based on two split rings than for a TL based on one split ring.

We can see in the results presented in the appendix C and in Figs. 4.58, 4.57 that the differences in the radiation behaviour due to the presence of different numbers of rings are only observed for the case of the left-hand region. Indeed the analysis of the right-hand region, presented in the appendix C, is similar to the results of the CSRR with two split rings, presented in the section 4.2.2. To clarify, the right-hand region is mainly influenced by the parasitic parts of the LC



(a) ***(b)*** $E(\theta, \phi)$

(c) $AF(\theta, \phi)$ ***(d)*** $R(\theta, \phi)$

Figure 5.8. *(a) Geometry of eight opposite infinitesimal horizontal dipoles oriented along x-axis, (b) Normalised far-field pattern $E(\theta, \phi)$ of the geometry shown in Fig. 5.8(a) as simulated with COMSOL assuming distance between dipoles equal to 5 mm along the x-axis, to 1.5 mm along the y-axis, to 1 mm along the z-axis at 4.8 GHz (c) Normalized array factor $AF(\theta, \phi)$ for 16 cells from (5.1) at 4.8 GHz, (d) Normalized total field $R(\theta, \phi)$ of 16-elements array of Fig. 5.8(a), which is the product of $E(\theta, \phi)$ and $AF(\theta, \phi)$ at 4.8 GHz.*

model (presented in the chapter 2), i.e. the series inductance of the microstrip line and the parallel capacitance between the line and the ground plane. Thus the topology of the CSRR does not influence the right-hand region.

5.4 IMPACT OF THE DISTRIBUTION OF MAGNETIC CURRENT

A similar analysis is performed for the electric field distribution across the rings. Once again, it is expected that this distribution show characteristics, explaining the radiation minimum at the upper frequency of the left-leaky region. This is also verified by inspection by creating a simple model based on a magnetic current loop.

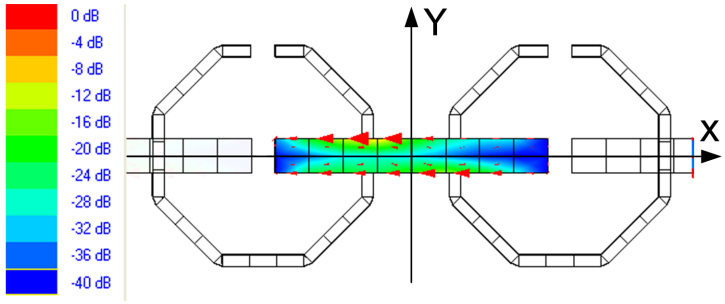


Figure 5.9. *Zoom of distribution of current density and current vectors on metallic strip joining adjacent cells, simulated with IE3D assuming an infinite substrate at 4.14 GHz, the upper frequency of the left-leaky region (Fig. 4.56(c)).Color bar: current density is normalised with the maximum of the current on the upper metal level ((maximal current density : 197.8 A/m)) and is expressed in dB. Blue color corresponds to lowest current density; red color corresponds to highest current density. All current vectors are oriented in the same direction along x-axis.*

5.4.1 CSRR with two rings in the left-handed region

Fig. 5.12 shows the components E_X and E_Y of electric field distribution across 3 adjacent rings, for the configuration of Fig. 4.1. It is observed that for the two concentric rings, a non zero and antisymetric electric field distribution is present all around the ring perimeter, assumed to be squared for simplicity. As a consequence, a magnetic current loop is created in each cell of the structure. Each branch of the ring carries an equivalent magnetic current that is opposite on two adjacent parallel branches, as illustrated in Fig. 5.13(a).

We can use this modelling tool with the same methodology described in the previous section to analyse the impact of this magnetic current loop on the radiation pattern of the complete antenna. As a consequence, the corresponding far-field radiation pattern $E(\theta, \phi)$ of the cell, predicted by COMSOL at the upper frequency f_u of the simulated left-leaky band ($f_u = 3.275$ GHz), shows a zero in the broadside direction (Fig. 5.13(b)), which combined with the array factor $AF(\theta, \phi)$ computed at that frequency, illustrated in Fig. 5.13(c), yields the apparent radiation splitting of $R(\theta, \phi)$ observed in COMSOL simulation (Fig. 5.13(d)).

5.4.2 CSRR with two rings in the right-handed region

The same methodology is applied to the lower frequency of the RH band. Fig. 5.14 shows the components E_X and E_Y of electric field distribution across 3 adjacent rings for this frequency. Both electric field components are in the same direction along X, are opposite along Y. In the previous case, the two rings are

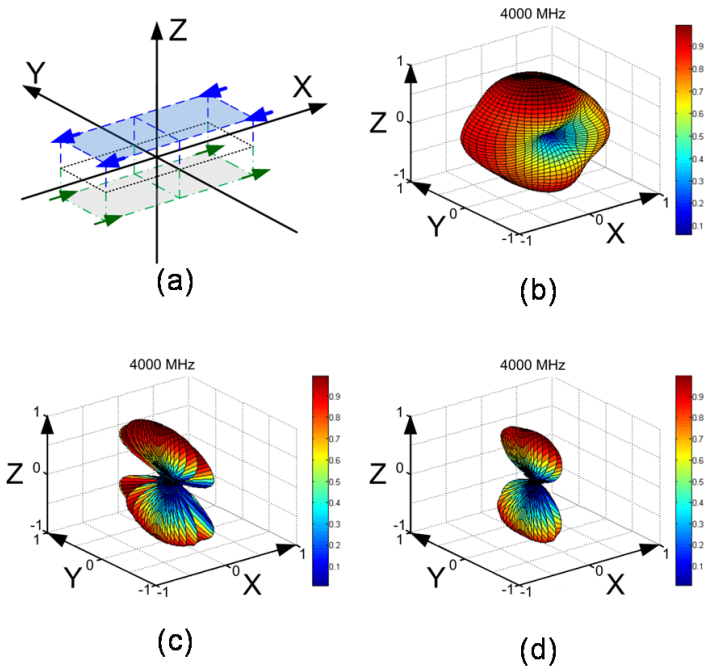


Figure 5.10. *(a) Geometry of eight opposite infinitesimal horizontal dipoles oriented along the x-axis, (b) Normalised far-field pattern $E(\theta, \phi)$ of geometry Fig. 5.10(a) simulated with COMSOL assuming with distance between dipoles equal to 5 mm along x-axis, to 1.5 mm along y-axis, to 1 mm along z-axis at 4 GHz (c) Normalized array factor $AF(\theta, \phi)$ for 16 cells from eq. (5.1) at 4 GHz, (d) Normalized total field $R(\theta, \phi)$ of 16-element array of Fig. 5.10(a), product of $E(\theta, \phi)$ and $AF(\theta, \phi)$ at 4 GHz.*

strongly coupled because the upper frequency of the left-leaky region is close to the CSRR resonance frequency. In this case the inner ring does not seem to carry the radiated energy and the E_x electric field is globally higher on the left part of the CSRR than in the right part as presented in the model of Fig. 5.15(a). The corresponding far-field radiation pattern $E(\theta, \phi)$, predicted by COMSOL at the lower frequency f_L of the measured right-leaky band ($f_L = 4.8$ GHz), shows a maximum at the broadside direction (Fig. 5.15(b)), which combined with the array factor $AF(\theta, \phi)$ computed at that frequency (Fig. 5.15(c)), predicts again the maximal radiation of $R(\theta, \phi)$ in the broadside direction (Fig. 5.15(d)), as observed in measurement (Fig. 5.2(b)).

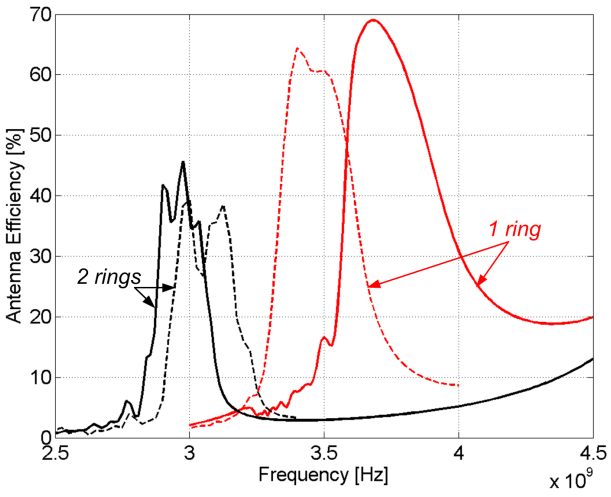
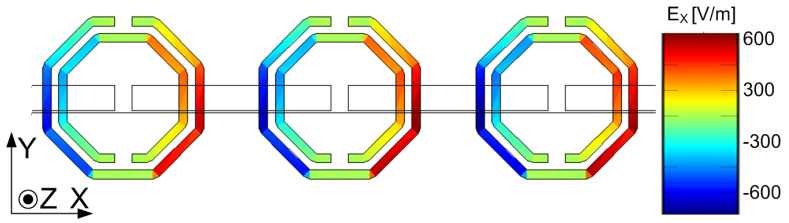


Figure 5.11. *Antenna efficiency AF of a cascade of 16 cells based on one split ring (red) of Fig. 4.51(a) and on two split rings (black) of Fig. 4.1(a) extracted from simulation with IE3D assuming an infinite substrate (solid) and COMSOL (dotted).*

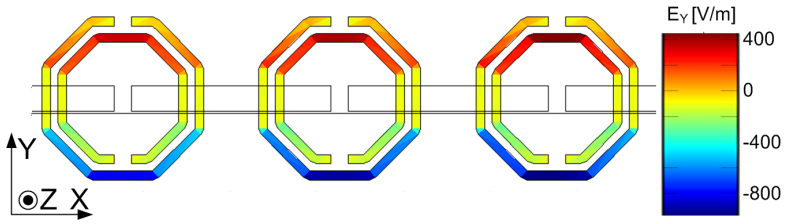
5.4.3 CSRR with one ring in the left-handed region

A similar analysis is performed for the electric field distribution across the rings for each configuration. Fig. 5.16 shows the components E_X and E_Y of electric field distribution across 3 adjacent rings for the configuration with one split ring (as depicted in Fig. 4.51).

For the case of the single ring cells, there is almost no electric field on the top branch of the ring (Fig. 5.16), meaning that no magnetic current is present on that branch. As a consequence, the top and bottom currents do not compensate themselves, which means that the corresponding far-field radiation pattern $E(\theta, \phi)$ of the cell computed at corresponding upper frequency, (f_u = 3.275 GHz), of the simulated left-leaky band exhibits a significant radiation in the broadside direction (Fig. 5.17(b)). To calculate $R(\theta, \phi)$, the previous results are multiplied to the array factor $AF(\theta, \phi)$ calculated at the same frequency (depicted in Fig. 5.17(c)). It is clear that the main radiation lobe of $R(\theta, \phi)$ is oriented along the z-axis in the broadside direction as observed in the COMSOL simulation (depicted in Fig. 5.17(d)).



(a) E_X



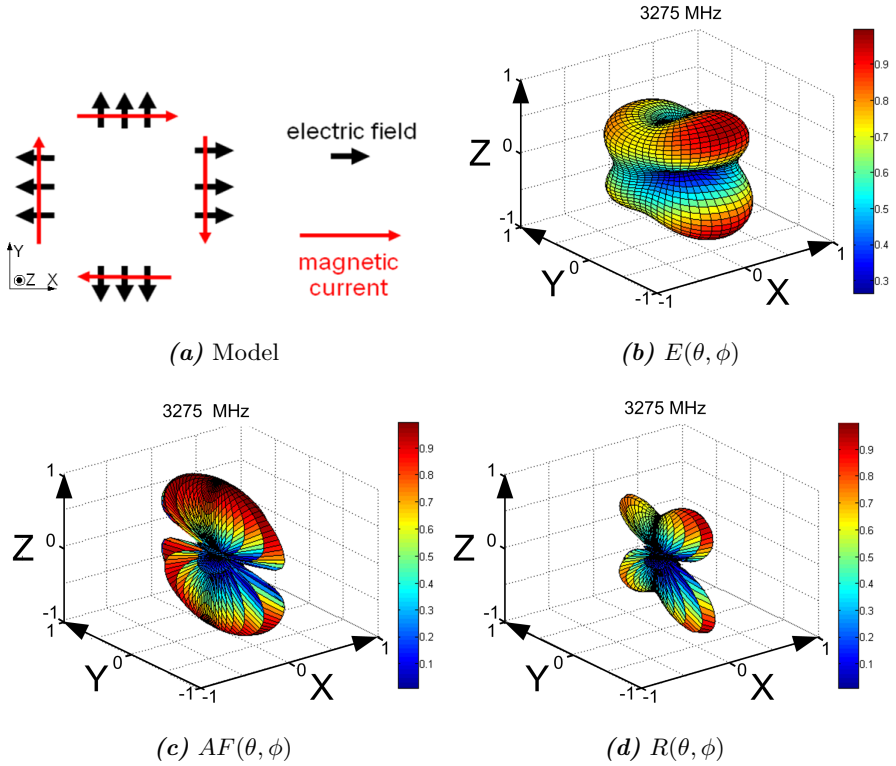
(b) E_Y

Figure 5.12. *Zoom of electric field distribution across the rings of 3 adjacent cells of Fig. 4.1, as simulated with COMSOL at 3.275 GHz which is the upper frequency of left-leaky region : (a)* E_X *and (b)* E_Y

5.5 APPLICATION TO A BALANCED CSRR-LOADED LWAS

We applied the same analysis to the balanced structure, presented in section 4.5.3.3 and illustrated in Fig. 4.61. A representation of the distribution of current density and current vectors on metallic strip joining adjacent cells, simulated with IE3D assuming an infinite substrate, is given in Fig. 5.18 at the upper frequency of the left-hand broadside. Current vectors present a symmetry along y-axis but not around x-axis. This behaviour is in accordance with the explanation presented in the section 5.3, which means that the antenna can radiate in the broadside direction along the z-axis.

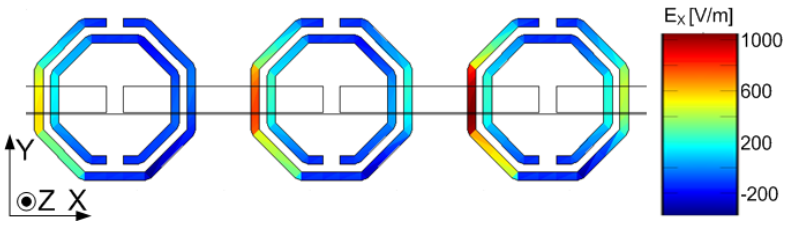
A similar analysis is performed for the electric field distribution across the rings. Fig. 5.19 shows the components E_X and E_Y of electric field distribution across 3 adjacent rings, for this balanced configuration. On one hand, the symmetry of the E_x component along the y-axis does not contribute to the broadside radiation. On the other hand, the E_y component does not present any symmetry along the x-axis or the y-axis, so the radiation in the broadside direction is mainly created by this component.



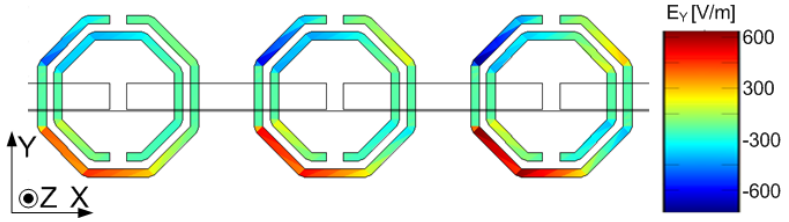
(a) Model ***(b)*** $E(\theta, \phi)$

(c) $AF(\theta, \phi)$ ***(d)*** $R(\theta, \phi)$

Figure 5.13. *(a) Schematic view of current and electric field distribution for CSRR structure based on two split rings for the upper frequency of left-leaky region (thick black arrows represent the electric field across the rings, thin red arrows represent the magnetic current created by the electric field across the ring). (b) Normalised far-field pattern* $E(\theta, \phi)$ *of the square model described in (a) as simulated with COMSOL at 3.275 GHz which is the upper frequency of measured left-leaky region. (d) Normalized array factor* $AF(\theta, \phi)$ *for 15 cells from (5.1) at 3.275 GHz based on the measured dispersion diagram. (c) Normalized total field* $R(\theta, \phi)$ *of 15-elements array of (a), which is the product of* $E(\theta, \phi)$ *of (b) and* $AF(\theta, \phi)$ *similar to (d) at 3.275 GHz.*

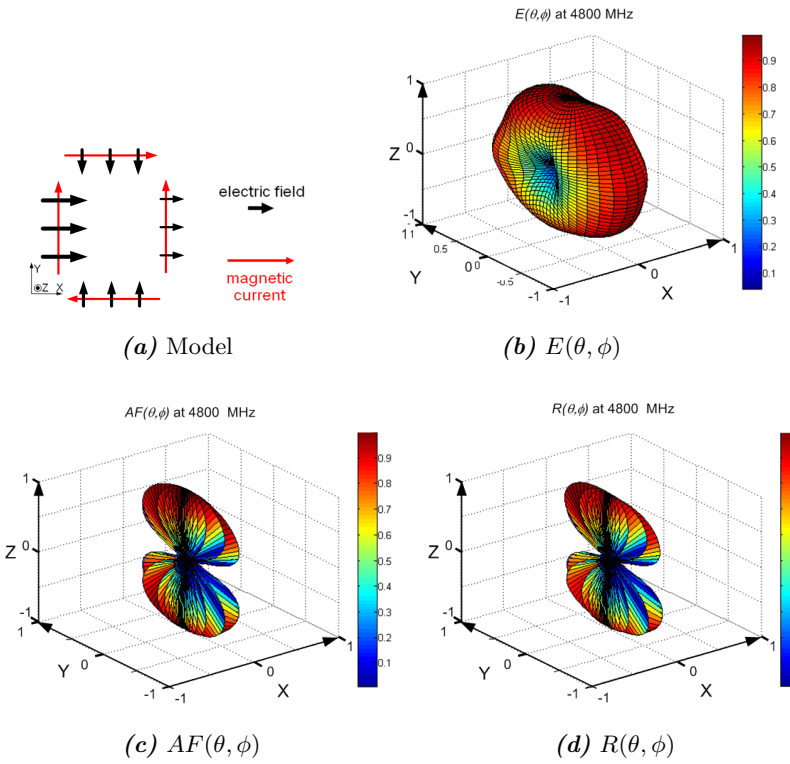


(a) E_X



(b) E_Y

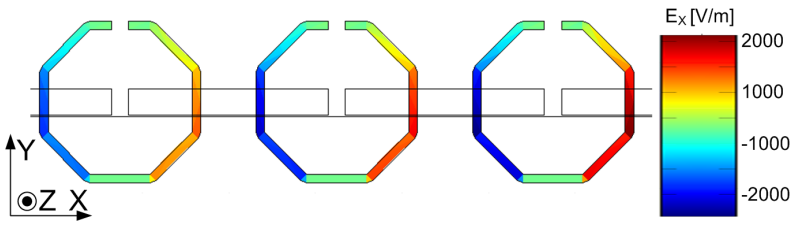
Figure 5.14. *Zoom of electric field distribution across the rings of 3 adjacent cells of Fig. 4.1, simulated with COMSOL at the lower frequency of right-leaky region, at 4 GHz : (a)* E_X *and (b)* E_Y



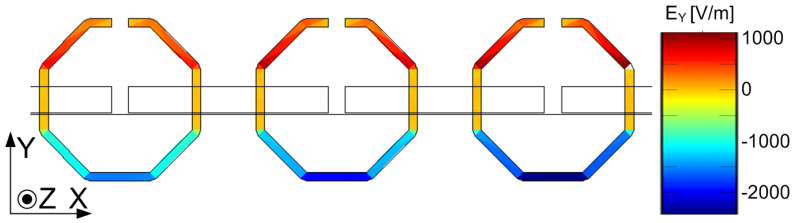
(a) Model ***(b)*** $E(\theta, \phi)$

(c) $AF(\theta, \phi)$ ***(d)*** $R(\theta, \phi)$

Figure 5.15. *(a) Schematic view of current and electric field distribution for CSRR structure based on two split rings for the upper frequency of left-leaky region (thick black arrows represent the electric field across the rings, thin red arrows represent the magnetic current created by the electric field across the ring). (b) Normalised far-field pattern* $E(\theta, \phi)$ *of the square model described in (a) as simulated with COMSOL at 4.8 GHz which is the lower frequency of the measured right-leaky region. (c) Normalized array factor* $AF(\theta, \phi)$ *for 15 cells from (5.1) at 4.8 GHz based on the measured dispersion diagram. (d) Normalized total field* $R(\theta, \phi)$ *of 15-elements array of (a), which is the product of* $E(\theta, \phi)$*, shown in (b) and* $AF(\theta, \phi)$ *shown in (c) at 4.8 GHz.*

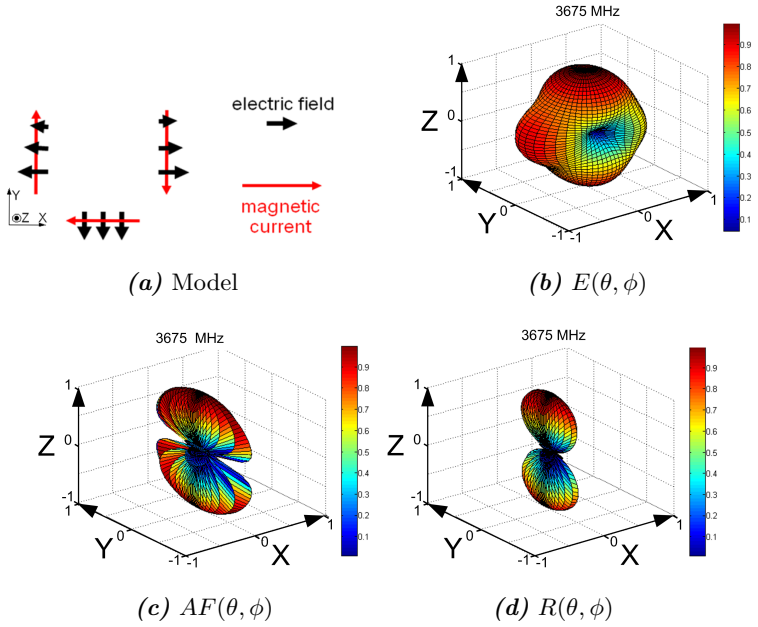


(a) E_X



(b) E_Y

Figure 5.16. *Zoom of electric field distribution across the rings of 3 adjacent cells of Fig. 4.51 each consisting of one split ring, simulated with COMSOL at the upper frequency of left-leaky region, at 3.275 GHz : (a)* E_X *and (b)* E_Y *.*



(a) Model ***(b)*** $E(\theta, \phi)$

(c) $AF(\theta, \phi)$ ***(d)*** $R(\theta, \phi)$

Figure 5.17. *(a) Schematic view of current and electric field distribution for CSRR structure based on one split ring (thick black arrows represent the electric field across the rings, thin red arrows represent the magnetic current created by the electric field across the ring). (b) Normalised far-field pattern* $E(\theta, \phi)$ *of the square model implied by (a) simulated for the single ring structure at the upper measured frequency of left leaky region, at 3.675 GHz with COMSOL. (c) Normalized array factor* $AF(\theta, \phi)$ *for 15 cells from eq. (5.1) at 3.675 GHz based on the dispersion diagram simulated with COMSOL. (d) Normalized total field* $R(\theta, \phi)$ *of 15-elements array depicted in Fig. (a).* $R(\theta, \phi)$ *corresponds to the product of* $E(\theta, \phi)$*, shown in Fig. (b), and of* $AF(\theta, \phi)$*, shown in Fig. (c), for CSRR structure based on one ring at 3.675 GHz.*

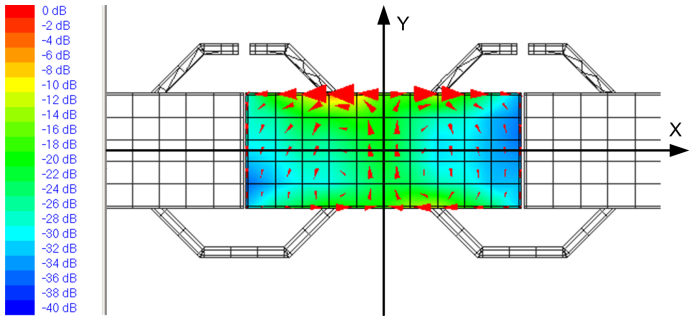
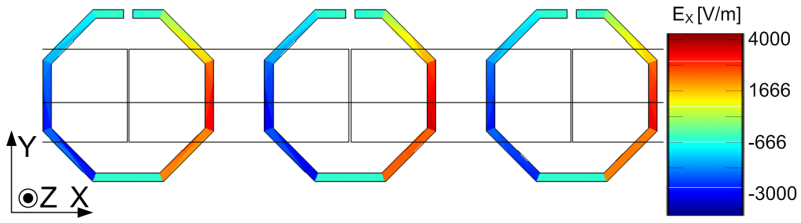
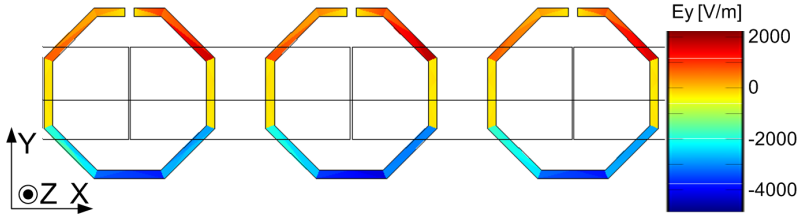


Figure 5.18. *Zoom of distribution of current density and current vectors on metallic strip joining adjacent cells, simulated with IE3D assuming an infinite substrate at 3.7 GHz, which is the upper frequency of the left-leaky region and the lower frequency of the right-leaky region (Fig. 4.66(a)). Color bar: current density is normalised with the maximum of the current on the upper metal level (maximal current density : 63.139 A/m) and is expressed in dB, blue color corresponds to lowest current density; red color corresponds to highest current density. Symmetry of current vectors around y-axis is observed, but not around x-axis.*



(a) E_X



(b) E_Y

Figure 5.19. *Zoom of electric field distribution across the rings of 3 adjacent cells of Fig. 4.62(a), as simulated with COMSOL at 3.6 GHz which is the upper frequency of left-leaky region : (a)* E_X *and (b)* E_Y

5.6 SENSITIVITY ANALYSIS WITH RESPECT OF THE DISTANCE BETWEEN RINGS

5.6.1 Analysis of the figures of merit

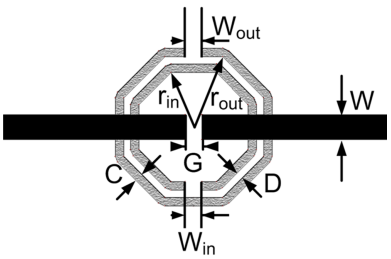
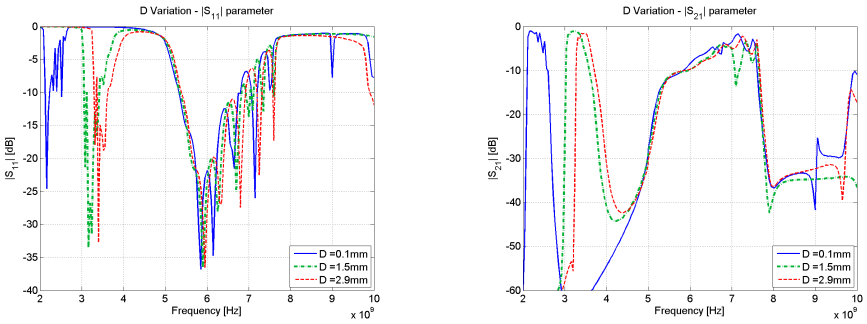


Figure 5.20. *CSSR structure (ground plane is depicted in grey whereas upper metal is depicted in black. The substrate between upper metal and ground plane has the following characteristics: $\varepsilon_r = 2.33$, $h = 0.5$ mm, $tg\delta = 0.003$: (a) Layout (initial dimensions are: $r_{in} = 3.5$ mm, $r_{out} = 4.5$ mm, $G = 1$ mm, $C = 0.5$ mm, $D = 0.5$ mm, $W_{out} = 1$ mm, $W_{in} = 1$ mm, $W = 1.47$ mm) (b) 3D view, (c) View of transmission line created by a cascade of 8 cells with source (distance between CSRRs : 2.5 mm).*

This section presents the influence of the distance, D, between two rings, presented in Fig 5.20 on the figures of merit. The definitions of the figures of merit are described in section 4.5.3. D is increased from 0.1 mm to 2.9 mm by step of 0.35 mm, the others dimensions are fixed to the dimensions described in Fig. 5.20. The D influence on the figure of merits is presented from Fig. 5.21 to Fig. 5.29 for the left-leaky region.

The analysis of the amplitude of the S-parameters could conclude that the dimension, D, has more effect on the LH band than the RH band, it makes sense, following the theory of the metametariel TL. Indeed the D dimension influence the LC circuit of the ring, this LC circuits does not influence the RH band region. Globally the antenna characteristics, as antenna efficiency and gain, are improved with an increase of the D dimension, so when the coupling between the two rings decreases.



(a) S_{11} *(b)* S_{21}

Figure 5.21. *S-parameters of TL loaded by 8 CSRRs for both leaky regions for three values of the space D between two adjacent CSRR cells : the minimum, the middle and the maximum of its interval (the others cell dimensions are fixed to the dimensions described in Fig. 5.20).*

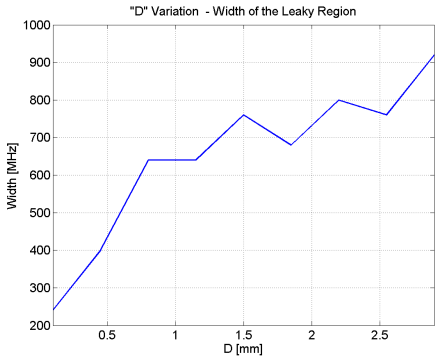


Figure 5.22. *Influence of the space D between rings on the width of the leaky region defined as the difference between the lower and the upper frequency of the leaky region for left-leaky region, described in section 4.5.3 (the antenna is based on 8 CSRRs, the others cell dimensions are fixed to the dimensions described in Fig. 5.20).*

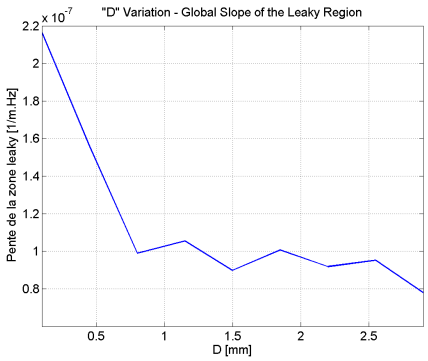


Figure 5.23. *Influence of the space D between rings on the slope of the leaky region, defined in eq. 4.16 for left-leaky region, described in section 4.5.3 (the antenna is based on 8 CSRRs, the others cell dimensions are fixed to the dimensions described in Fig. 5.20).*

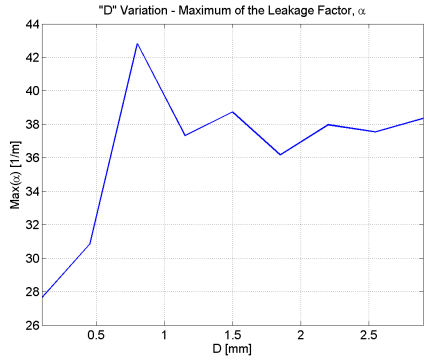


Figure 5.24. *Influence of the space D between rings on the maximum of the leakage factor defined as the maximum of leakage factor, α, for left-leaky region, described in section 4.5.3 (the antenna is based on 8 CSRRs, the others cell dimensions are fixed to the dimensions described in Fig. 5.20).*

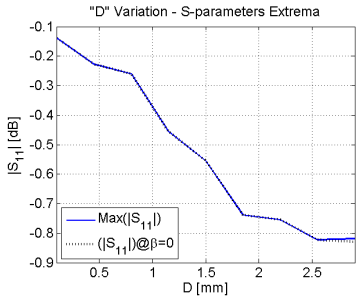


Figure 5.25. *Influence of the space D between rings on the extrema of the S_{11}-parameter defined as the maximum of the S_{11} magnitude for the leaky region, compared to S_{11}-parameter at the edges of the leaky region, described in section 4.5.3 for the left-leaky region (the antenna is based on 8 CSRRs, the others cell dimensions are fixed to the dimensions described in Fig. 5.20).*

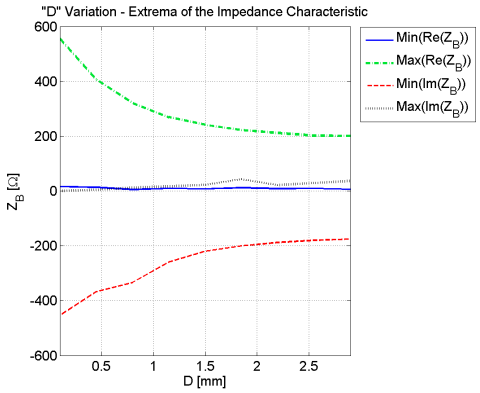


Figure 5.26. *Influence of the space D between rings on the extrema of the characteristics impedance Z_B defined as the maximum and the minimum the real and imaginary parts of the characteristic impedance Z_B for the leaky region defined in eq. 4.18 described in section 4.5.3 for the left-leaky region (the antenna is based on 8 CSRRs, the others cell dimensions are fixed to the dimensions described in Fig. 5.20).*

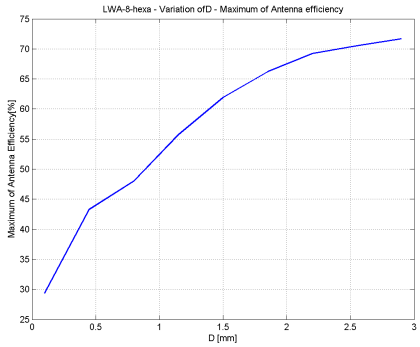


Figure 5.27. *Influence of the space D between rings on the maximum of the antenna efficiency defined as the maximum of antenna efficiency described in section 4.5.3 for the leaky region (the antenna is based on 8 CSRRs, the others cell dimensions are fixed to the dimensions described in Fig. 5.20).*

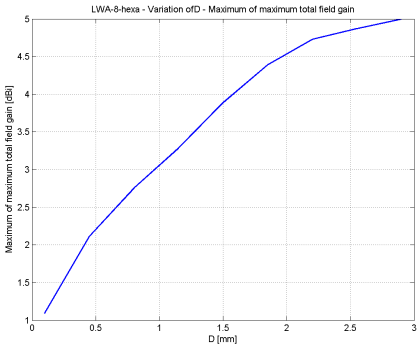


Figure 5.28. *Influence of the space D between rings on the maximum of the total field gain defined as the maximum of the maximum total field gain, described in section 4.5.3 for the left-leaky region (the antenna is based on 8 CSRRs, the others cell dimensions are fixed to the dimensions described in Fig. 5.20).*

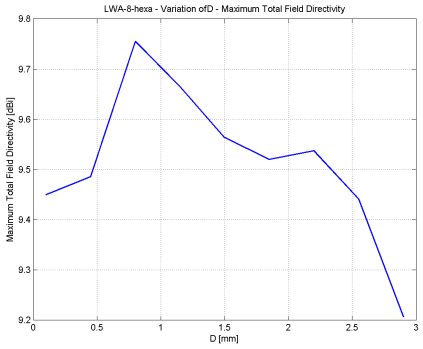


Figure 5.29. *Influence of the space D between rings on the maximum of the total field directivity defined as the maximum of the maximum total field directivity, described in section 4.5.3 (the antenna is based on 8 CSRRs, the others cell dimensions are fixed to the dimensions described in Fig. 5.20).*

5.6.2 Comparison of radiation shapes

Fig. 5.30 and Fig. 5.31 illustrate a comparison of the radiation pattern and of the distribution of electric and magnetic currents for different distances, D, between two rings. Each illustration, extracted from IE3D simulation, is depicted at the frequency f_u, i.e. the upper frequency of the left-leaky region.

From this comparison, we can extract the followings :

- The first conclusion is that when the distance D increases, the maximum of radiation occurs closer to the broadside direction
- Second, for small distance D, the distribution of electric currents is also clearly asymmetrical. This asymmetry disappears when the distance D is increased.
- The last conclusion is that the presence of the high coupling between the two rings, illustrated by the distribution of the electric field, and so, the presence of a high resonance is clearly visible for the lowest distance D, contrary to the highest ones.

The previous section has demonstrated the link between the current distribution and the radiation pattern. Now, from this comparison, we can conclude that the distribution of the electric field would influence the electric current distribution of the structure and so its radiation pattern.

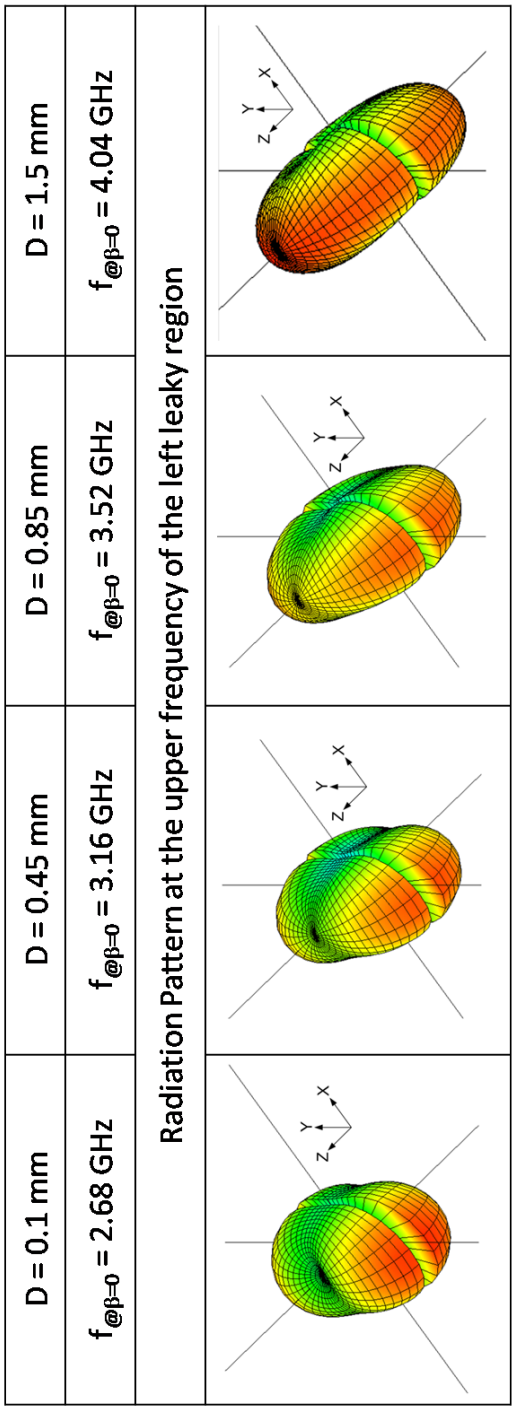


Figure 5.30. *Influence of the space D between rings on the radiation pattern at the upper frequency of the left-leaky region (the antenna is based on 8 CSRRs, the others cell dimensions are fixed to the dimensions described in Fig. 4.1).*

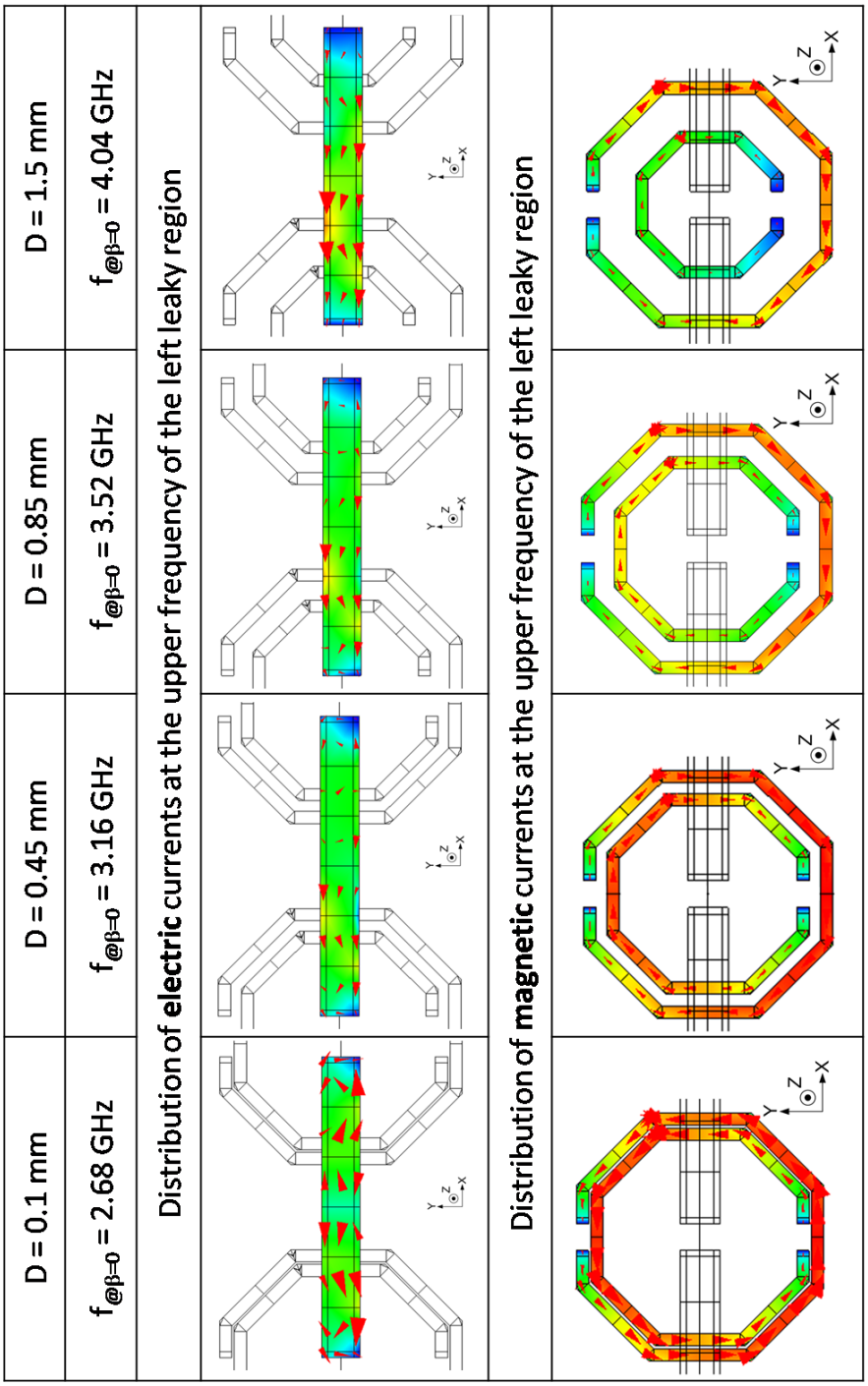
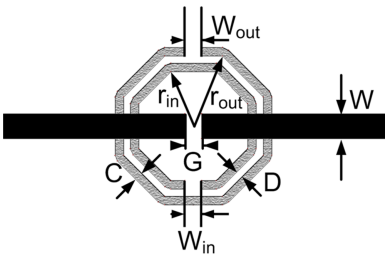
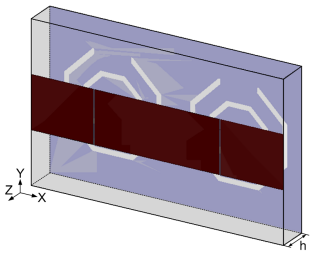


Figure 5.31. *Influence of the space D between rings on the distribution of the electric and magnetic currents at the upper frequency of the left-leaky region (the antenna is based on 8 CSRRs, the others cell dimensions are fixed to the dimensions described in Fig. 4.1).*

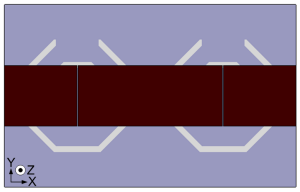
5.6.3 Balanced CSRR-loaded LWAs with two split rings



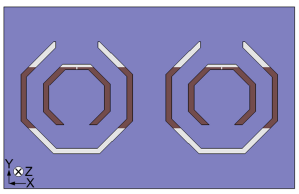
(a) Topology (grey : slot, black : top metal)



(b) 3D view



(c) Front Face



(d) Back Face

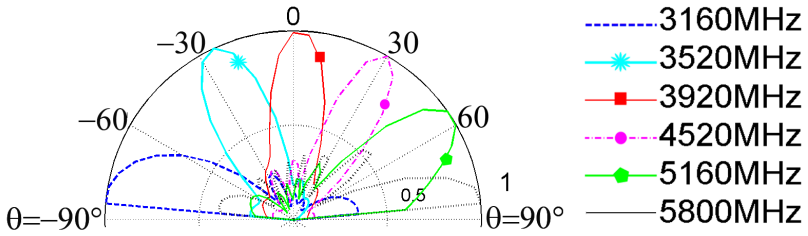
Figure 5.32. *Balanced CSSR structure with two split rings (ground plane is depicted in blue whereas upper metal is depicted in dark brown. The substrate between upper metal and ground plane has following characteristics: $\varepsilon_r = 2.33$, $h = 0.5$ mm, $tg\delta = 0.003$: (a) Topology, (b) 3D view, (c) Front Face (d) Bottom Face (dimensions are: $R_{out} = 4.5$ mm, $R_{in} = 2.5$ mm, $G = 0.1$ mm, $C = 0.5$ mm, $W_{out} = W_{in} = 3$ mm, $W = 5$ mm, $D = 1.5$ mm, distance between 2 adjacent cells fixed to 2 mm).*

For the sake of completeness, a balanced structure based on CSRRs with two rings has been designed for the same frequency range using the previous conclusions. This structure is based on the structure present in the section 4.5.3.3. A second ring is added inside the first ring. **The distance D between these two rings is chosen high enough to avoid the coupling phenomena, to avoid the kill of the broadside radiation.**

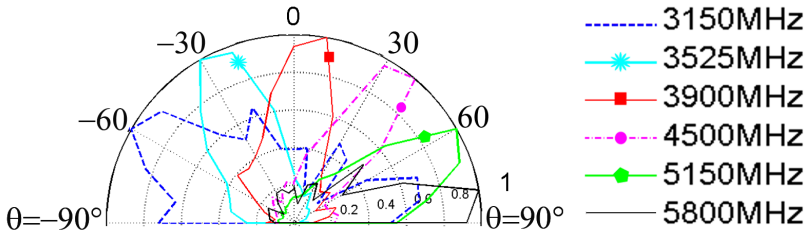
The simulated and measured results are presented in annex G. In this design, the full-space scanning frequency range extends from approximately 3.12 GHz to 6.8 GHz, with the broadside transition at 3.9 GHz.

Fig. 5.33 shows corresponding 2D views of the simulated and measured radiation pattern for the leaky region in the ($\phi = 0°$) X-Z plane, validating the continuous frequency beam scanning for both leaky regions without stop-band. **The broadside transition frequency presents a radiation pattern with**

a maximum in the broadside direction, contrary to the structure presented in the chapter 6.



(a) IE3D Simulation



(b) Measurement

Figure 5.33. *Normalized 2D radiation pattern in ($\phi = 0°$) X-Z plane for the TL based on 16 cells of Fig. 5.32(a). (a): simulation with IE3D with the assumption of infinite substrate and (b) measurements for different frequencies in the leaky region.*

5.7 CONCLUSION

This chapter has discussed radiation phenomena in a metamaterial transmission line based on series capacitive gaps and CSRRs periodically loading a host microstrip line and acting as a leaky-wave antenna. In the previous chapter, for the case of double ring cells, full wave simulation and measurement of this structure showed, in the left-leaky region, a frequency beam steering simultaneously in the plane of the substrate, ($\theta = 90°$) X-Y plane, and in its normal plane, ($\phi = 0°$) X-Z plane. Here, we explain this phenomenon by the fact that the radiation pattern near the upper frequency of the left-leaky region is related to the number of concentric split rings of the CSRRs and the direction of the main lobe of the LWA. Near this frequency, LWAs loaded by CSRR based on one split ring exhibit a main lobe oriented along broadside direction, contrary to LWAs loaded by CSRR based on two concentric split rings, which present a null in this direction. The physical explanation for this second case is the particular current

distribution on metal strips, which creates a null in the total radiated field in the broadside direction.

A sensitivity analysis with respect to the distance between rings has demonstrated the influence of the ring resonance on the electric currents. More the distance D is high, more the resonance is weak, less the distribution of electric currents is asymmetrical.

Bibliography

[1] C. Balanis, *Antenna Theory, 3rd edition.* Wiley, 2005.

[2] C. Caloz and T. Itoh, *Electromagnetic metamaterial : Transmission line and microwave applications.* Wiley, 2006.

[3] I. Huynen, *Bases de l'ingénérie micro-onde, ELEC2700.* Université catholique de Louvain, 2006.

CHAPTER 6

CONCLUSION AND FUTURE WORKS

These last decades have seen the emergence of the metamaterial concept. Metamaterial structures present physical properties that do not exist in the nature, especially in the area of microwave RF engineering. As introduced in the first chapter, these left-handed cells provide added degrees of freedom for system designers and have facilitated amongst other things:

- A considerable decrease in the size of microwave components such as filters or couplers,
- An increase in system bandwidth, useful for ultra wide band applications,
- An easy insertion of electrical-tunable elements, these elements could influence the physical properties of an antenna with a simple DC voltage applied to the circuit.

The ultimate objective of this research was the use of metamaterial structures to design a reflective RF tag with a direction of radiation differing from the normal in the plane of the tag. Inspiration was taken from the article [1], which concerned the concept of the left-hand transmission line, which had one of its extremities shorted and the other matched to a 50-Ohm impedance. This TL presents a phase velocity in opposition to the direction indicated by its Poynting vector in the left-hand region. This property is the consequence of the inverse

combination of the classical TL elements, based on discrete components. This kind of TL is called a Composite Right/Left Hand TL because it offers a left-hand behaviour for the lower frequencies and the classical right handed behaviour at higher frequencies.

This thesis analyses a transmission line based on Complementary Split Ring Resonators, presented in [2]. This TL produces a similar frequency behaviour than the metamaterial TL proposed in [1]. Two concentric split rings, referred to as a *Complementary Split Ring Resonator*, are etched, for example, on the back of the substrate of a host line. This structure can be viewed as an electric dipole excited by an electric field while exhibiting negative values of dielectric permittivity around its resonance. The first chapter present some applications of this structure in the antenna environment : improving impedance matching issues, filtering undesirable frequencies for ultra wide band applications or decreasing the size of patch antennas.

The second chapter presents the basic concepts governing the operation of one-dimensional leaky wave antennas (LWAs), behaving as a guiding structure along which a wave propagates and leaks out gradually energy in the form of coherent radiation. LWAs present the advantage of offering sharp directional beams with respect to frequency of operation. Three kinds of LWAs exist: uniform, periodic and quasi-periodic. They differ in the geometrical shape of the transverse cross section. The periodic structures present periodical discontinuities along the propagation axes. Their radiation modes are higher order modes, contrary to uniform antenna where the fundamental mode radiates. These modes could create forward and backward radiation. The quasi-uniform structure also presents discontinuities along the propagation constant but the periodicity of this modulation is smaller than the wavelength of the guided travelling waves. In this last category, metamaterial antennas present a fundamental mode which radiates. Furthermore it is possible to balance the cell and create, as a result, a full continuous frequency scanning from the backward to the forward direction.

The third chapter presents and analyses the somewhat unexpected radiation performances of a TL loaded by CSRRs used as an LWA. Indeed the full wave simulations and measurements in an anechoic chamber show in the left-leaky region, a frequency beam steering simultaneously in the plane of the substrate, and in its normal plane. This behaviour does not occur in the right leaky region, where instead the structure radiates as a conventional LWA. An explanation proposed was the presence of surface waves, propagating along the substrate. Indeed the theoretical calculation and nearfield measurements show the presence of surface waves in the structure. These waves could create a radiation once they meet an interface with free space, such as substrate edges. Full wave simulations have shown that a parasitic radiation would appear if the substrate edges are

too close to the radiating elements of the antenna but the abnormal behaviour of this antenna was not explained because it occurs whatever the distance between the substrate edges and the TL.

CSRRs with two rings can be used to decrease the working frequency of the LWA or to decrease the physical dimensions of the antenna. In both cases, this means a negative interference near the broadside frequency. The proposed application is the design of low profile and highly directive detectors with a direction of radiation different from the normal to the plane of the tag, to be used in monitoring and access control systems. Recent solutions include progressive antennas, antenna networks [3] and antennas with metamaterials [4, 5]. The novel solution described in this work proposes a frequency scanning without the addition of electronic tuning. Unfortunately this structure presents the drawback of backside radiation however it can be used with the solution proposed in [6, 7] to suppress the radiation from one side by placing a long metallic trough on the ground plane in front of the CSRR cell.

For the designer of the RF front-end, the bandwidth required by LWAs to perform full scanning, could translate into an implementation too costly. Indeed, it is less expensive to maintain a given value of quality factor over a bandwidth of 1 MHz than over 1 GHz. An electronic tunable solution, i.e. a beam scanning control achieved by a DC voltage or current instead of using a frequency variation, could therefore be an alternate solution. The focus was on two solutions: one using ferromagnetic nanowired membranes, and the other using a ferroelectric material coupled with CSRRs.

The first solution, presented in the annexe A uses a frequency scanning obtained by a left-handed behaviour induced by the negative permeability of a porous insulating alumina membrane filled with ferromagnetic nanowires by electro deposition. A practical implementation of such structure must resolve two challenges: (i) the application of the high external tuning DC magnetic field without interference with the antenna radiation, and (ii) the realisation of a long structure to obtain a good directivity.

The second solution is placed within the continuity of the work of the third chapter; a tunable element is placed on the TL gap. This ferroelectric component, tuned with a DC voltage applied between the two ports, is a $Ba_{0.6}Sr_{0.4}TiO_3$ thin film placed on the series gap, placed on an alumina substrate and silver metal layers, realized with the inkjet technique. This last fabrication technique has the advantage of creating low cost multiple coating structures. This is significant because it is more difficult to realize these kinds of structure with conventional lithography techniques. The main challenge is to maintain the ferroelectric properties of the BST thin film, with a size of the BST grain smaller than 100 nm with the repartition of the crystal domain such that the ferroelectric properties of the thin film is preserved. The aid and expertise in this process from the University of Mons is greatly acknowledged here.

The concept of tuning the CSRR gap element with a voltage by using a SMD varactor, i.e. an inverse polarized diode, has been investigated. Full wave simulation and measurements have shown that the left-leaky region is shifted higher in frequency as the bias voltage increases. Full wave simulations have also proven the fixed-frequency bias scanning.

This work also considers other resonant structures similar to the CSRR structure and which could be good candidates to be part of a metamaterial LWA. This approach is described in the fifth chapter and the analyzed cells are : non-bianisotropic spiral resonators, open split ring resonators, open complementary split ring resonators, balanced double split ring CSRRs, double-layers CSRRs, a cascade of non uniform CSRR cells, CSRR cells with two gaps on the microstrip and CSRRs with a single ring etched on the ground plane. Two more promising structures are the double split ring CSRR and the CSRR with a single ring etched on the ground plane. These present a high efficiency without having a radiation null in the broadside direction at the upper frequency of the left leaky region. Their LC models are equivalent to the CSRR model and they also present a left and right hand regions. Full wave simulations and measurements in an anechoic chamber confirm these conclusions for the CSRR cell with a single ring etched on the ground plane.

A parametric study on a single ring CSSR structure has been realised to show the influence of each dimension on the antenna properties, in order to facilitate a design in view of the high number of degrees of freedom. The metamaterial detractors claim the bad impact of the leakage on the metamaterial components. In relation to this, this work also has the objective to give the opportunity to a RF designer to choose, for example, the dimensions of a filter, in order to reduce this disadvantageous radiation leakage.This parametric analysis allows for the realisation of a single ring CSRR balanced structure, i.e. for which the stop-band between the left and the right regions vanishes. Hence, the structure offers a continuous frequency scanning and this is confirmed by the full-wave simulation and measurement in an anechoic chamber, this confirms that this structure could be an good candidate for metamaterial LWAs such as the structure of Caloz's group presented in [8]. This approach has also been used for the CSRR structure with two rings. This work has hence shown that using a modified geometry of the CSSR enables a reduction in the impact of the CSRR resonance near the upper frequency of the left-hand region. This creates a full-space scanning with the radiation split near this frequency. Measurement in an anechoic chamber then confirms this behaviour.

In the fourth chapter, attention was focused on the current distribution on the CSRR and on the metal strip. The current distribution of the current of the strip presents a symmetry both along x and y axis. As a result, it was necessary

to develop a simple model with current dipoles, similar to the theory presented in [9]. The array of dipoles reproduces the radiation pattern behaviour of the antenna. It was then observed that for two concentric rings, a non zero and antisymetric electric field distribution is present all around the ring perimeter. Using the same model, which was developed previously in this work, and the same methodology, the same conclusion is reached: in the left-leaky region, a frequency beam steering occurs simultaneously in the plane of the substrate, and in its normal plane. The presence of these various symmetries is explained by the proximity of the resonance frequency of the ring. This resonance frequency indeed defines the upper frequency of the left-hand region. A sensitivity analysis w.r.t. the distance between two rings highlight the influence of the coupling between the two rings on the radiation null in the broadside direction.

The set of obtained results during this thesis would suggest some perspectives and recommendations for the future use of these kinds of antennas for diverse applications:

1. For the reflector applications, our simulations have clearly demonstrated that, independently of the metametarial TL topology, the structure creates a parasitic beam as well as the desired lobe and this behaviour is explained in Fig. 6.1. This parasitic behaviour was not admissible by the application environment, i.e. a warehouse with metallic shelves with a localization system on the ceiling. Indeed the parasitic radiation could distort the localization results through echo of the parasitic beams on the metallic shelves.

2. To create a more complete localization tool, an electrically controlled structure could switch from a single ring structure to a double ring structure and so could present two antenna radiation characteristics. This could be achieved using a diode.

3. To realize a ferromagnetic tunable LWA at a fixed frequency, the length of the porous insulating alumina membrane filled with ferromagnetic nanowires must be greater than two wavelengths of the guided wave in the substrate. A powerful hard permanent magnet, e.g., an Sm-Co, could be placed underneath the structure and create a sufficient magnetic field to influence the nanowire substrate.

4. To realize a ferroelectric tunable LWA at a fixed frequency with the inkjet technique, the synthesis of a ferroelectric or antiferroelectric material must be investigated more deeply.

5. To change the directivity and possibly the beam direction in the substrate, an array of TLs loaded by CSRR could be realized, based on a similar structure to [10]. A suitable application for this idea could be low profile detectors implemented in monitoring and access control systems such as radar and MIMO-based systems for user-tracking or location-based services in WiFi networks [11].

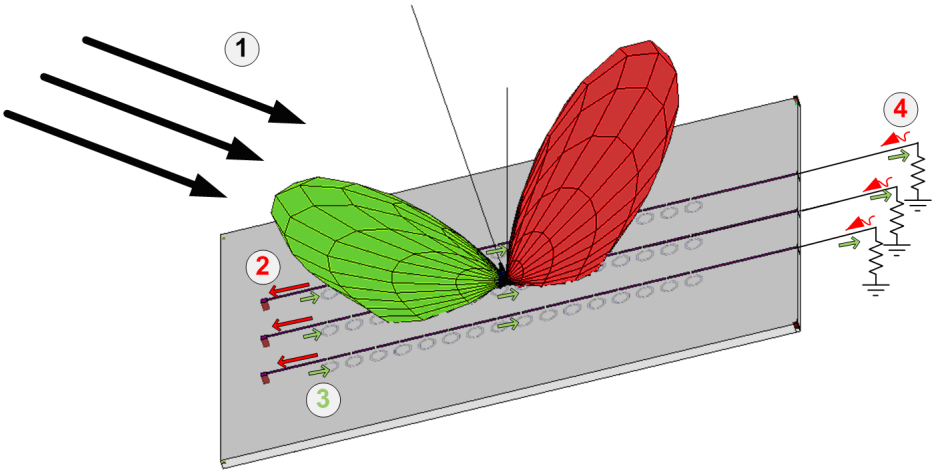


Figure 6.1. *Schematic of a reflector based on a TL loaded by CSRR, one of its extremities is shorted, the other is matched to a 50-Ohm impedance, this structure is inspired by [1]. (1) The plane wave, with a frequency in the left leaky region, is incident to the TL, which creates a wave in the guided structure with a negative propagation constant and this guided wave is depicted with a large red arrow. (2) This wave propagates until the short end creating a parasitic beam, depicted on the right in red. (3) A second wave, depicted with a small green arrow, is reflected on the short end this wave creating the reflected beam, depicted on the left in green. (4) The reflected wave is absorbed by the 50Ω impedance, however a small quantity of this wave is reflected. This part is presented with a small red arrow and also contributes to the parasitic beam depicted in red.*

6. In the analysis on the other candidates for resonant cells for LWA application, a second candidate, the balanced double split ring CSRR, merits investigation by theoretical analysis and measurement. The cascade of non uniform CSRR cells has presented high antenna efficiency however its matching factor is poor. Other non-linear profiles could be analyzed to find a wideband solutions.

7. The geometrical analysis realized on the CSRR with one single ring could be extended. The influence of each dimensions on the different factors of merit have been described but a transversal analysis must be realised to discover the dependence between the impacts of each dimensions : select the optimum of each dimension for some figures of merit does not bring to the best solution, indeed the optimum of one dimension could destroy

the optimum obtained with another dimension. So to give a useful tool for a RF designer, it is necessary to determine the coupled influence of dimensions on desired performances.

8. The analysis of the last chapter proves that a symmetrical structure kills the radiation on the broadside direction in the left-leaky region. Indeed a null in the broadside direction appears for a structure with two or three rings, but not a single ring. A modal analysis as presented in [12] could try to better understand this phenomena.

Bibliography

[1] S. L. C. Caloz and T. Itoh, "A novel leaky-wave retrodirective reflector using short/ matched terminations," *Proceedings of European Microwave Conference*, pp. 1071–1074, Oct. 2003, Munich, Germany.

[2] M. Gil, J. Bonache, J. Garcia-Garcia, and F. Martin, "Composite right/left handed (crlh) transmission lines based on complementary split ring resonators (csrrs) and applications," *Proc. Metamaterials 2007*, pp. 22–24, Oct. 2007, Roma, Italy.

[3] C. Balanis, *Antenna Theory, 3rd edition.* Wiley, 2005.

[4] S. Lim, C. Caloz, and T. Itoh, "Electronically scanned composite right/left handed microstrip leaky-wave antenna," *IEEE Microwave and Wireless Components Letters*, vol. 14, no. 6, pp. 277 – 279, Jun. 2004.

[5] S. S. Lim, C. Caloz, and T. Itoh, "Metamaterial-based electronically controlled transmission-line structure as a novel leaky-wave antenna with tunable radiation angle and beamwidth," *Transaction on Microwave Theory Techniques*, vol. 12, no. 12, pp. 2678 – 2690, Dec. 2004.

[6] A. Grbic and G. V. Eleftheriades, "Experimental verificiation of backward-wave radiation from a negative refractive index metamaterial," *Journal of Applied Physics*, vol. 92, no. 10, pp. 5930 – 5935, Nov. 2002.

[7] ——, "Experimental verification of backward-wave radiation from a negative refractive index metamaterial," *Journal of applied physics*, vol. 92, no. 10, pp. 5930 – 5935, Nov. 2002.

[8] C. Caloz and T. Itoh, *Electromagnetic metamaterial : Transmission line and microwave applications.* Wiley, 2006.

[9] ——, "Array factor approach of leaky-wave antennas and application to 1-d/2-d composite right/left-handed (crlh) structures," *IEEE Microwave and Wireless Components Letters*, vol. 14, no. 6, pp. 274 – 276, Jun. 2004.

[10] H. V. Nguyen, S. Abielmona, A. Rennings, and C. Caloz, "Pencil-beam full-space scanning 2d crlh leaky-wave antenna array," *Proceedings of European Microwave Conference.*

[11] C. Caloz, D. R. Jackson, and T. Itoh, *Leaky-Wave Antennas.* in Frank B. Gross (Ed), Mc Graw Hill, 2011, ch. Frontiers in Antennas : Next Generation, Design and Engineering, pp. 339 – 410.

[12] S. Paulotto, P. Baccarelli, F. Frezza, and D. R. Jackson, "Full-wave modal dispersion analysis and broadside optimization for a class of microstrip CRLH leaky-wave antennas," *IEEE Transactions on Microwave Theory and Techniques*, vol. 56, no. 12, pp. 2826–2837, Dec. 2008.

APPENDIX A

MAGNETIC TUNABILITY OF METAMATREIAL LEAKY-WAVE ANTENNA BASED ON NANOWIRED MEMBRANES

THis annex presents the novel concept of an electronically controlled leaky wave antenna. Two distinct approaches are considered in this thesis, namely ferroelectric materials as well as CSRRs in conjunction with ferromagnetic materials. The objective is the creation of frequency independent LWAs with an alternative scanning mechanism to frequency tuning. Concerning the LWA realized on ferromagnetic materials, I have collaborated and made simulations for the conference proceeding [1].

Ferromagnetic nanowired membranes are good candidates for miniaturized tunable and non-reciprocal devices. We propose a novel topology for leaky-wave antennas, where broadside scanning is obtained by a left-handed behaviour induced by negative permeability of the substrate. The ferromagnetic nature of wires allows beam scanning at fixed frequency by applying an external magnetic DC field.

A.1 INTRODUCTION

Ferromagnetic nanowired substrates (Fig. A.1(a)) offer, due to their excellent material properties, the ability to build tunable planar devices for very high frequencies, as nowadays requested for wireless communication and automotive systems. The advantages of such materials compared to classical ferrites [2, 3] are a higher operation frequency, a higher saturation magnetization and a higher resonant frequency. They are tunable in frequency by applying an external mag-

netic field [4]. The nanowires as ferromagnetic inclusions influence the permittivity and permeability of the composite substrate. The focus of this section lies on the feasibility of Leaky-Wave Antennas (LWAs) based on such a nanowired substrate. First of all, we show the influence of an applied external magnetic field on the permeability of the artificial substrate. The permeability is negative in a certain frequency range, when the porosity, as well as the height of the nanowires in the substrate, are chosen large enough. By adding a shunt inductance to the configuration, a left-handed material is created which is the basic requirement to create a leaky-wave antenna.

A.2 TOPOLOGY OF FERROMAGNETIC NANOWIRED SUBSTRATE

The so-called "nanowired substrate" of Fig. A.1(a) consists of a porous insulating alumina membrane filled with ferromagnetic nanowires by electrodeposition. The cylindrical pores of diameter D are randomly distributed and electromagnetic waves can propagate untroubled for a nanowire diameter smaller than skin depth [5]. Fig. A.1(b) shows the equivalent circuit of the nanowired substrate with an added shunt inductance, the basic material for our investigation, and Fig. A.1(c) the concept of its realisation in a microstrip line technology. This structure is similar to Fig. 2.1(b). The parallel inductance is a stub connecting the microstrip with the ground plane. The series capacitance, usually created with a gap, is replaced by a substrate with negative permeability. Indeed the microstrip created on the nanowire substrate has the behaviour of LC circuit in function of frequency.

The studied membrane is a 6 μm thick alumina membrane with a porosity of 40 %. The material of the ferromagnetic nanowires is Cobalt and their height is 3.6 μm. As already mentioned, the material properties are tunable by applying an external magnetic DC field. Fig. A.2(a) shows this influence on the real part and Fig. A.2(b) on the imaginary part of the effective permeability of the nanowired substrate by applying different field values between 6 kOe and 10 kOe compared to the one with no applied external field. The curves are shifted on the x-axis to lower frequencies, when the external magnetic field is applied. This phenomenon occurs due to the dipolar coupling of the nanowires inside the membrane [6]. The negative behaviour of μ will induce a negative inductance as imaginary part of series impedance Z shown in Fig. A.1(b). The value of L_{shunt} is chosen for obtaining a total shunt admittance of the cell behaving as a negative capacitance in the frequency range of interest.

A.3 FREQUENCY TUNED LEAKY-WAVE BEHAVIOUR AT ZERO DC MAGNETIC FIELD

The interest of metamaterials is used here for the possibility of scanning the azimuth angle Θ from backward ($\Theta = -90°$) to forward ($\Theta = 90°$) propagation [8, 9] for leaky wave antennas. Fig. A.3(a) shows the simulation of propaga-

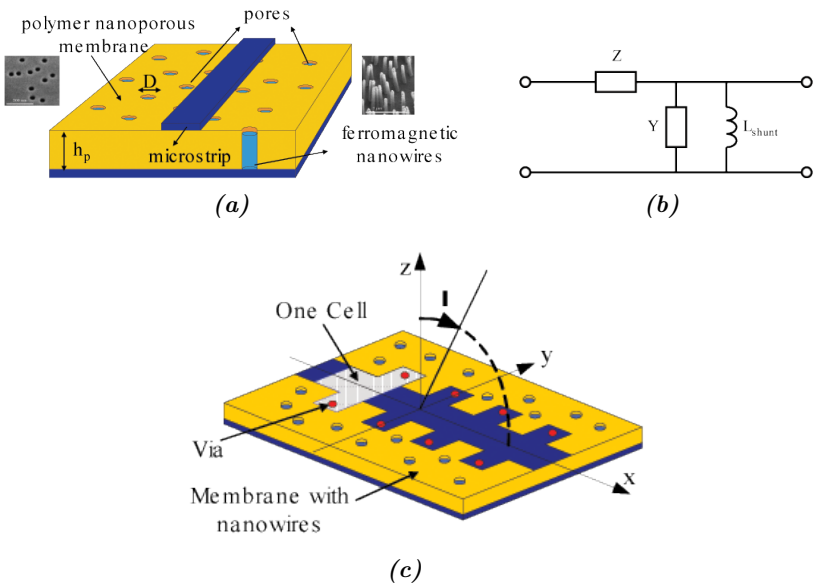


Figure A.1. *(a) : Microstrip line on ferromagnetic nanowired substrate, (b) : Equivalent circuit with shunt inductance (c) : Concept of double negative material in microstrip line technology. Stubs with vias form parallel inductor* L_{shunt}.

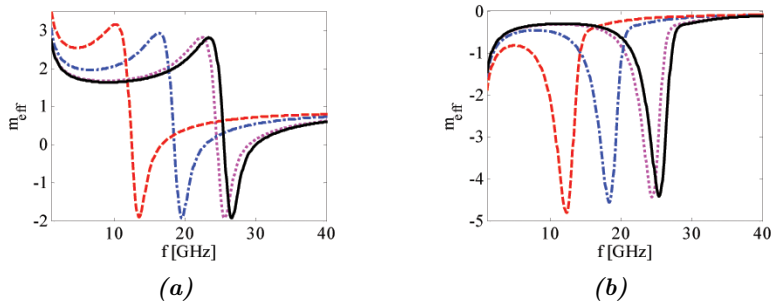
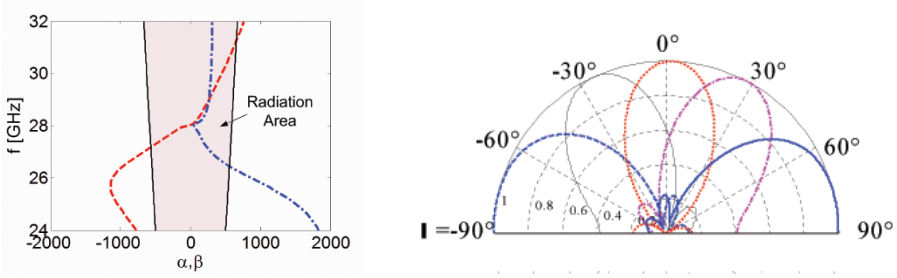


Figure A.2. *Effective permeability with applied external magnetic field: 0 Oe (solid), 6 kOe (dashed), 8 kOe (dashdotted), 10 kOe (dotted) (a) : Real part (b) : Imaginary part. Simulations use a variational approach detailed in [7].*

tion constant β and leakage constant α for 15 cells on the substrate of section 2, cascading the basic cell as highlighted in Fig. A.1(c). Left-handed propagation occurs from about $f = 26\ GHz$ to $f = 28\ GHz$, indeed in the range where μ is negative (solid curve in Fig. A.2(a)). From leaky-wave theory radiation occurs



(a) *(b)*

Figure A.3. *(a) : Dispersion Diagram with radiation cone area with α (dash-dotted) and β (dashed) for a 15 cells LWA and (b) : Radiation pattern for five frequencies in the radiation cone: $f_{BW} = 27.14\ GHz$ (dashed), $f_1 = 29.14\ GHz$ (thin dotted), $f_0 = 28.04\ GHz$ (thick dotted), $f_2 = 29.14\ GHz$ (dashdotted) and $f_{FW} = 31.24\ GHz$ (solid).*

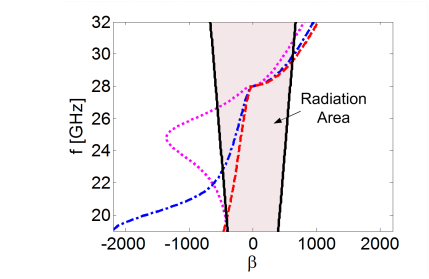
when propagation constant $|\beta|$ is lower than free space propagation constant $|k_0|$, i.e. within the radiation cone area (Fig. A.3(a)). The main beam direction is given by $\Theta = \arcsin \beta/k_0$. The radiation pattern shown in Fig. A.3(b) has been calculated using the array factor approach [8] for five frequencies inside the radiation zone of Fig. A.3(a). The antenna scans from endfire to backfire, depending on the sign of β ($\Theta = -90°$ for $\beta = -|k_0|$ at $f_{BW} = 27.14\ GHz$, $\Theta = 0°$ for $\beta = 0$ at $f_0 = 28.04\ GHz$, and $\Theta = 90°$ for $\beta = |k_0|$ at $f_{FW} = 31.24\ GHz$).

A.4 LEAKY-WAVE BEHAVIOR BASED ON EXTERNAL DC MAGNETIC FIELD TUNING

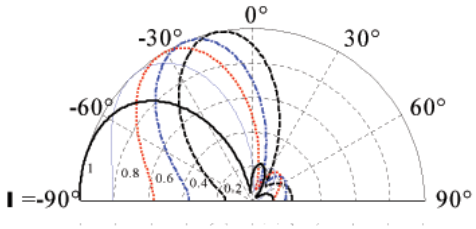
This section analyses the influence of an applied external DC magnetic field on the LWA behaviour. Fig. A.4(a) shows this influence on the propagation constant β of the previous structure with applied DC fields of 6 kOe, 8 kOe and 10 kOe. Contrary to the previous case, the scanning of the beamdirection is now possible at one single frequency thanks to the tuning by a DC magnetic field. A radiation pattern has been calculated (Fig. A.4(b)), based on the cells of the previous section, but for one frequency with five different applied external magnetic fields. The frequency of 26.64 GHz has been chosen to have a maximal angle variation with DC field values from 6 kOe to 10 kOe while remaining in the radiation area. A beam scanning from $\Theta = -90°$ to $\Theta = -10°$ is obtained.

A.5 CONCLUSION

In this section, we proposed a novel architecture of planar, integrated and tunable leaky-wave antenna, where broadside scanning is obtained by a left-handed



(a)



(b)

Figure A.4. *(a) : Propagation Constant β with applied external magnetic field 6 kOe (dashed), 8 kOe (dashdotted), 10 kOe (dotted) and (b) :Calculated radiation pattern in the X-Z plane for a single frequency $f = 26.64\ GHz$ with different applied magnetic fields: $H_{DC} = 6$ kOe (dashed), $H_{DC} = 9$ kOe (dashdotted), $H_{DC} = 9.5$ kOe (dotted), $H_{DC} = 9.75$ kOe (thin solid) and $H_{DC} = 10$ kOe (thick solid).*

behaviour induced by negative permeability of the substrate. The ferromagnetic nature of nanowires allows beam scanning of the LWA antenna at fixed frequency in the Ka band, by applying an external DC magnetic field. This is an advantage because narrow band emission and reception modules can be used. The biggest challenge of this structure is to find a solution to apply the high external DC magnetic field without interfering with the antenna radiation. The realization of long structure, necessary to improve the LWA directivity, is also another challenge for the prototype realization.

Bibliography

[1] J. Spiegel, S. Eggermont, and I. Huynen, "Investigation on ferromagnetic nanowired substrates for leaky-wave antennas," *Proceedings of Metamaterial's 2008*, 2008, Pampluna, Spain.

[2] T. Kodera and C. Caloz, "Uniform ferrite-loaded open waveguide structure with crlh response and its application to a novel backfire-to-endfire leaky-wave antenna," *IEEE Transactiobs on Magnetics*, vol. 57, no. 4, pp. 784 – 795, Apr. 2009.

[3] M. Tsutsumi and K. Okubo, "Left-handed characteristics of ferrite microstrip line magnetized to wave propagation," *IEEE Transactiobs on Magnetics*, vol. 45, no. 10, pp. 4207 – 4210, Oct. 2009.

[4] I. Huynen, G. Goglio, D. Vanhoenacker, and A. V. Vorst, "A novel nanostructured microstrip device for tunable stopband filtering applications at microwaves," *IEEE Microwave and Guided Wave Letters*, vol. 9, no. 10, pp. 401 – 403, October 1999.

[5] J. Spiegel, J. de la Torre, M. Darques, L. Piraux, and I. Huynen, "Permittivity model for ferromagnetic nanowired substrate," *IEEE Microwave and Wireless Components Letters*, vol. 17, no. 7, pp. 492 – 494, Jul. 2007.

[6] A. Encinas-Oropesa, M. Demand, L. Piraux, U. Ebels, and I. Huynen, "Effect of dipolar interaction on the ferromagnetic resonance properties in arrays of magnetic nanowires," *Journal of Applied Physics*, vol. 89, no. 11, pp. 6704–6707, Jun. 2001.

[7] A. Berk, "Variational principles for electromagnetic resonators and waveguides," *IEEE Transactions on Antennas and Propagation*, vol. 4, pp. 104–111, 1956.

[8] C. Caloz and T. Itoh, *Electromagnetic metamaterial : Transmission line and microwave applications*. Wiley, 2006.

[9] F. Qureshi, M. Antoniades, and G. Eleftheriades, "A compact and low-profile metamaterial ring antenna with vertical polarization," *IEEE Antennas and Wireless Propagations Letters*, vol. 4, pp. 333–336, 2005.

APPENDIX B

FERROELECTRIC TUNABLE LWA : FIRST INVESTIGATION

This annex presents the first results about the fabrication of the ferroelectric tunable CSRR-based leaky wave antenna, realized with the inkjet technique. This is the subject of the section 4.4.

B.1 INTRODUCTION

This appendix is focused on the ferroelectric tunability of a resonant-type leaky wave antenna. Our approach is to influence the serie capacitance C_g of the CSRR-loaded unit cell of Fig. 4.39 by the introduction of a varactor, based on a ferroelectric thin ($< 1\mu m$) or thick ($\simeq 10\,\mu$m) film of Barium Strontium Titanate (BST), placed on the gap of the microstrip line, as illustrated in Fig. 4.39.

Our approach is to insert this tunable capacitance in the CSRR-loaded leaky wave TL presented in the chapter 6 based on a ferroelectric BST thin film. This work has been done in collaboration of Céline Marlier, Marc Debliquy, Maurice Gonon and Nathalie Maury from the University of Mons, Belgium. The context of this work was the topic of a student project of second bachelor and of a student project of second master [1]. This section summarizes its main results.

B.2 FERROELECTRIC MATERIALS

A ferroelectric material is a material that possesses dipole moments in its lattice structure and that can show a spontaneous permanent polarization. This state is more or less equivalent to what can be observed in ferromagnetic materials but from an electrical point of view. This polarisation can be changed by applying

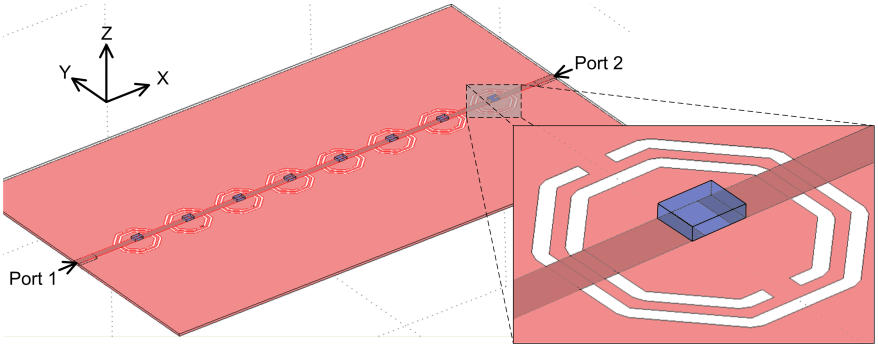


Figure B.1. *Conceptual 3D view of TL based on 8 CSSR cells with serie tunable components (ground plane is depicted in rose, the tunable component is depicted in blue, whereas upper metal is depicted in grey).*

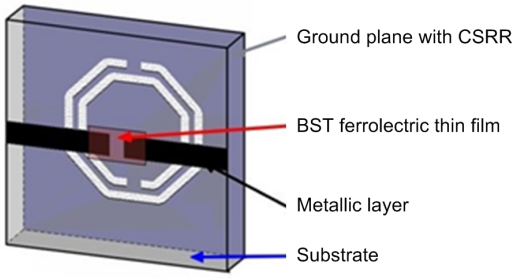


Figure B.2. *Conceptual 3D view of CSSR structure with BST ferroelectric thin film (ground plane is depicted in grey, BST film is depicted in rose, whereas upper metal is depicted in black).*

an electric field, following a hysteresis loop shown in Fig. B.3. The dipole moments tend to orient themselves according to the applied field. The configuration where most moments are aligned (83% for poly-cristal) is called the saturation polarization. If the applied field is removed, the remnant polarization is called the residual spontaneous polarization, P_s. The electric field, necessary to cancel this polarization, is called the coercive force, E_c [2].

The ferroelectric materials are also characterized by a large dielectric permittivity. The electrical, mechanical and optical properties of a ferroelectric material strongly depend on the applied electric field and the temperature. A ferroelectric material is characterised by two states, in function of the temperature T. The temperature limit between this two states is named the Curie Temperature, T_C. If $T < T_C$, the material presents a ferroelectric state with a spontaneous polar-

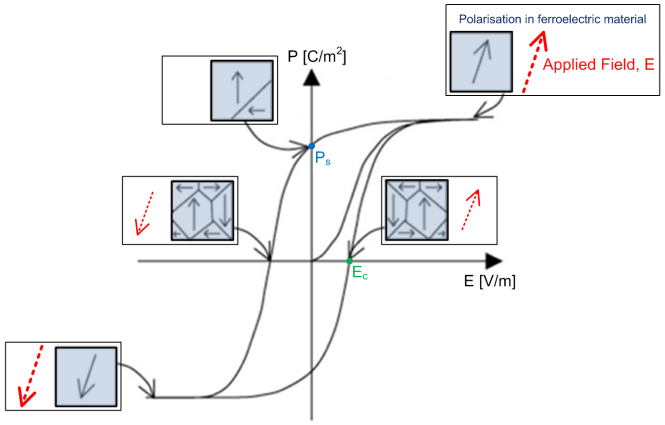


Figure B.3. *Typical Ferroelectric (Electric Field E,Polarisation P) hysteresis loop (the material polarisation is drawn in function of the applied electric field for four noticeable points, P_s is the residual spontaneous polarization, E_c is called the coercive force) [1].*

ization and a dependence of the dielectric constant on temperature and applied voltage. If $T > T_c$, the material presents a paraelectric state without a spontaneous polarization. Indeed a paraelectric material can be polarized by an applied application but when it is removed, the polarization disappears. A paraelectric material is not characterized by a hysteresis loop, but by a linear law.

One of the applications of ferroelectric materials is the realization of tunable capacitance, they are also used for their piezzoeletric ability and for their large value of permittivity. The permittivity of this capacitance is chosen at room temperature in order to present the largest variation of permittivity with the applied voltage. For a fixed applied voltage, this variation is maximum at the Curie temperature, i.e. at the transition between the paraelectric and ferroelectric states.

So the ideal case is a material with a Curie temperature close to room temperature. The Curie temperature of $BaTiO_3$, a ferroelectric material, is around 120Â°C. In order to approach the ideal case, the structure of $BaTiO_3$ is modified for example by the substitution of Ba^{2+} with Sr^{2+} or with Ca^{2+} or by the substitution of Ti^{4+} with Zr^{4+} [3]. The solution, chosen in this project, is the composition $Ba_{1-x}Sr_xTiO_3$. Depending on the strontium proportion, its Curie temperature varies from 100K (Curie Temperature of Sr_xTiO_3) to 400K (Curie Temperature of $BaTiO_3$). As shown in Fig. B.4, the chosen composition $Ba_{0.6}Sr_{0.4}TiO_3$ has a high permittivity value at room temperature.

An example of tunable capacitance is illustrated in Fig. B.5(a). This capacitance is created from a ceramic layer of Barium Strontium Titanate (BST),

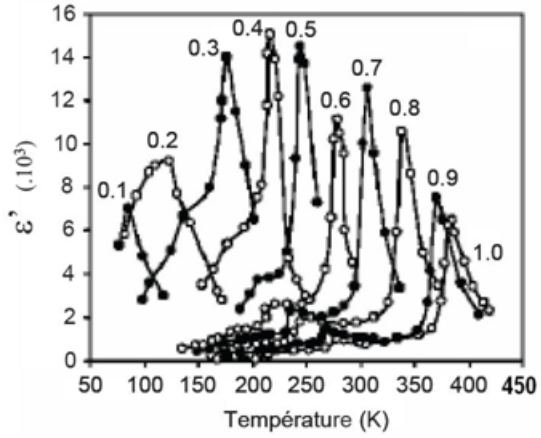


Figure B.4. *Permittivity of ceramic $BaSrTiO_3$ material versus temperature for different mole fraction of Ba [3].*

on which interdigital electrodes are placed. Fig. B.5(b,c) show the value of the capacitance as a function of applied DC voltage and geometrical parameters of the interdigital capacitance. Maximum capacitance appears for zero voltage, it decreases whatever the voltage value. Geometrical parameters of the interdigital electrodes has also a significant effect on the variation of the capacitance because large electrical fields are needed : the smaller distance between electrodes, S, more the larger capacitance variations with DC voltage as illustrated in Fig. B.5.

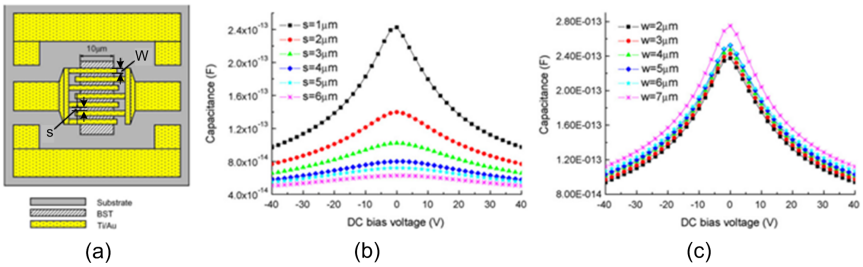


Figure B.5. *(a) Topology of a planar interdigital capacitor with BST thin film ($W = 3\mu m$, $S = 1\mu m$). Capacitance versus applied DC voltage of the interdigital capacitor of (a) measured at 2 GHz (b) for different values of S (from 1 to 6 μm) and (c) for different values of W (from 2 to 7 μm) [4].*

To obtain a good variation of the capacitance in the configuration illustrated in Fig. B.2, the electric field is of the order of magnitude of 10^5 V/m. The

two chosen arrangements are shown in Fig. B.6. In the first configuration of Fig. B.6(a), the BST thick film is deposited on the conductive layers of the electrodes. To obtain this field for reasonable DC voltage, the thickness of the BST layer is around 10 microns. Then the electric field, applied along the film across the gap, is mainly horizontal and the capacitance variation depends on the length of the gap between the two conductive layers. In this topology, the gap has to be small. For the second configuration, shown in Fig. B.6(b), the DC voltage is applied across the film thickness, the electric field is mainly vertical, this makes the capacitance variation depending on the thickness of the BST film, as a result relatively small DC voltages are sufficient for effective tuning. To obtain this field for reasonable DC voltage, the thickness of the BST layer is around one micron.

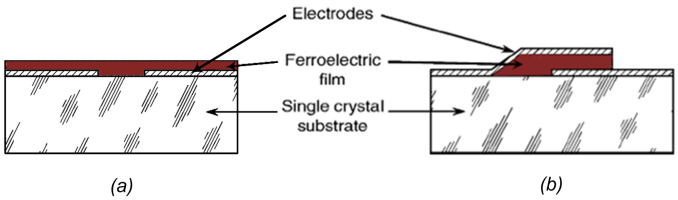


Figure B.6. *Section view of two configurations of planar capacitance with BST thin film (a) : planar, (b) : trilayer [5].*

So the first part of this project is focused on the deposition of thin film of $Ba_{0.6}Sr_{0.4}TiO_3$, with a thickness of 500 nm, deposited on the CSRR cell. The CSRR cell is fabricated on alumina substrate with the inkjet technology. The first section will describe the first step of the fabrication of the ferroelectric film. The second section will present the first experimental results, done with the inkjet printer.

B.3 EXPERIMENTAL RESULTS OF BST THIN FILM

Configuration of Fig. B.6 is based on the "thin film" technology. This technology has two advantages : low production cost and low tuning voltage [5]. Firstly, the use of ferroelectric films enables the integration of the microwave circuits (as phase shifter and antennas) on only one substrate thus substantially reducing the size, mass, and cost of the circuits. Secondly, if the electric field, applied to the BST material, is of the order of magnitude of 10^5 V/m, the voltage across the material must be around 1000 V for 1 cm thick bulk. However, for 10 μm thick film, the voltage across the material is around 10 V to generate the same electric field.

The material properties, especially for ferroelectric material, are affected by the fact that the material is presented as a bulk or as a thin film on crystal

substrate. For example, the dielectric permittivity is smaller for thin films than for bulk materials (sometimes more than an order of magnitude lower). This phenomenon is called size effect. The dependence of dielectric permittivity or electric tunability of the ferroelectric sample on its size (especially the thickness of a ferroelectric film) is of primary concern.

The RF sputtering technique, described in [1], is used to create the thin film because this technique has the advantage of dense deposition and not so high annealing temperature. This last property is interesting in this project because of the silver ink deposition used for the conductive layers of the CSRR-ferroelectric cell of Fig. B.2. Indeed the melting temperature of silver ink is 961.78Â°C, higher temperature than the annealing temperature of sputtering.

The drawback of the RF sputtering deposition is the following : by different methods, ferroelectric material is ejected from a target and is deposited onto a substrate, such as alumina substrate. Unfortunately, the composition of the thin film is not exactly the same as the target. The difference is due because of the sputtering yield of the different elements. So to create a $Ba_{0.6}Sr_{0.4}TiO_3$ thin film, the necessary exact composition of the target has to be chosen by trial and error.

The chosen substrate is an alumina substrate because of its low permittivity (interesting for antenna), its good behaviour in RF frequency and low cost. This substrate can also suffer without damages the annealing treatments used after the deposition. Indeed an annealing treatment is necessary to transform the amorphous BST deposit in its perovskite crystal state.

B.4 EXPERIMENTAL RESULTS OF INK-JET SILVER PRINTING ON ALUMINA SUBSTRATE

Silver is the selected metal because of its good conductivity (highest electrical conductivity of any element and the highest thermal conductivity of any metal), its good resistance to oxidation (cause of loss of electrical conductivity) and its high fusion temperature (961.78Â°C), higher temperature than the annealing temperature of BST sputter deposition technique. Two techniques are used to realize the silver deposition by physical vapour deposition, followed by laser ablation to create the slot on the ground plane, and by inkjet technique, followed by an annealing, to create the upper metal layer of the microstrip line.

Metal-inkjet printing is similar to the technique widely used in office and home printers and is an innovative fabrication technique of printed electronic circuits for high resolution and low cost metallization on various substrate. The aim of this technique is to deposit the metallic ink following a specific pattern based on a non-impact dot-matrix digital printing technology [6]. A piezoelectric material throws metallic droplets from a small orifice in a print head over the alumina substrate. This deposit uses the IJ242-54 conductive silver/copper ink (90 % Silver nanoparticules, 10 % Copper nanoparticules with glass particles for cohesion) from Cima Nano Tech with the inkjet printer Dimatix Fujifilm.

After the ink-jet deposit, a thermal sintering process welds particles together at temperatures below their melting point, resulting in an evaporation of liquid, creating continuous conductivity and thus percolating paths. This annealing is divided in three parts : an increased ramp from 25Â°C to 250Â°C by 2Â°C/min, a stable period at 250Â°C during 35 minutes, a decreased ramp from 250Â°C to 25Â°C by 5Â°C/min.

The layout of the upper metal layer, presented in Fig. B.2, is deposited on alumina substrate (substrate thickness = 0.63 mm, substrate permittivity = 6), the layout and photos of this fabrication are shown in Fig. B.7 (dimensions are : G = 1 mm, W = 0.825 mm, L = 10 mm). A drawback of this method is the reproducibility of the exact dimensions (good scaling factor), asking a long optimisation process of the circuit dot-matrix. Unfortunately, the RF measurements have not been possible, due to the sample breakage during the cutting process.

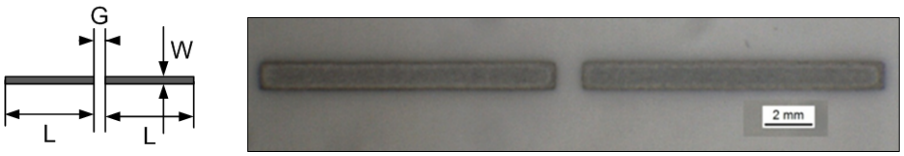


Figure B.7. *Layout (a) and Photos (b) of ink-jet silver deposition of a microstrip gap on alumina substrate (G = 1 mm, W = 0.825 mm, L = 10 mm, alumina substrate thickness = 0.63 mm, alumina substrate permittivity = 6) [1].*

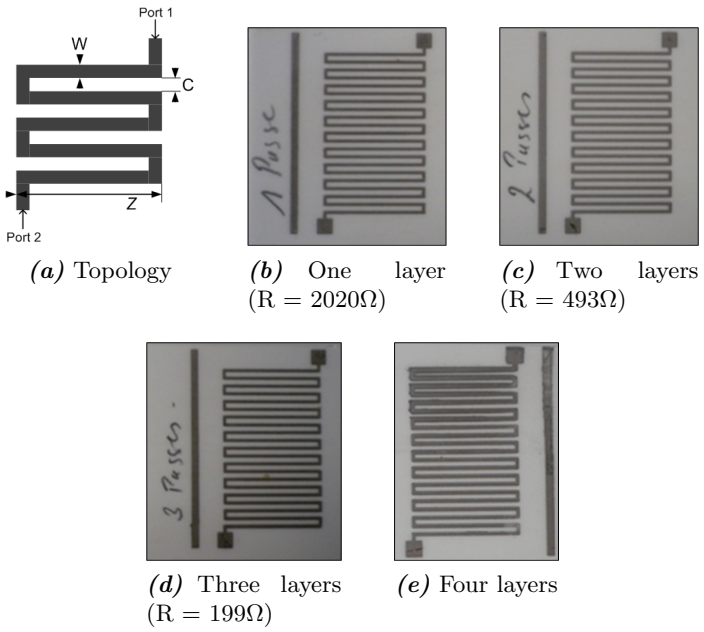
Additionally to the RF measurements, the resistivity of the silver inkjet printing is measured by the creation of microstrip meander line. The objective is to compare the line resistivity as a function of the different printing successive layers on top of each over. The measured parameter is the sheet resistance, R_s, also used for semiconductor doping, metal deposition, resistive paste printing and glass coating. For a thin film, assumed uniform in thickness, the expression of R_s is :

$$R_s = R \,.\, \frac{W}{L} \qquad [\Omega/\square] \tag{B.1}$$

Where R is the measured resistance between the two access of the meander line, W and L is respectively the width and the length of the line.

Fig. B.8 shows the topology and photos of the meander line realisation fabricated on alumina substrate (meander line composed by 21 sections lines with Z = 15 mm, W = 300 μm, C = 300 μm, alumina substrate thickness = 0.63 mm, alumina substrate permittivity = 6). Resistivity decreases as the number of printing successive layers increases. Indeed the sheet resistance is equal to 1.887 $\Omega/\square$ for one layer, equal to 0.46 $\Omega/\square$ for two layers, to 0.1858 $\Omega/\square$ for three layers. Unfortunately, for four successive ink layers, the inkjet deposit becomes unusable

because printing inaccuracy increases too much as illustrated in Fig B.8(e). To help the comparison, the conventional photolithography used for circuits presented in the chapter 6 presents a sheet resistance around 1 mΩ/□, so significantly less than the inkjet technique.



(a) Topology

(b) One layer (R = 2020Ω)

(c) Two layers (R = 493Ω)

(d) Three layers (R = 199Ω)

(e) Four layers

Figure B.8. *Layout and Photos of a deposited silver patterns for different printing successive layers on top of each over (meander line composed by 21 sections lines with Z = 15 mm, W = 300 µm, C = 300 µm, alumina substrate thickness = 0.63 mm, alumina substrate permittivity = 6) [1].*

B.5 CONCLUSION

This section has presented the early stages of the fabrication process of TL loaded by CSRRs and ferroelectric thin film. The chosen composition of the ferroelectric thin film is $Ba_{0.6}Sr_{0.4}TiO_3$, presenting a high permittivity peak at room temperature. The RF sputtering technique is used to deposit the thin film because this technique has the advantage of dense deposition and not so high annealing temperature. It is followed by annealing treatment. Alumina substrate is chosen because of its low permittivity for antenna application and because it is not damaged by the annealing treatment used after the sputter deposition technique. In a first step, interdigital capacitors are realized to test the tunable

capability of the BST samples and to extract the BST thin film permittivity. The extracted value corresponds to the classical value.

The second part of this project concerns the metallic line fabrication based on the metal inkjet technique. This new technique has the advantages of high resolution and low cost metallization on various substrate. Silver is the selected metal because of its good conductivity, its good resistance to oxidation (cause of loss of electrical conductivity) and its high fusion temperature, higher temperature than the annealing temperature of BST sputter deposition technique. The resistivity of the silver inkjet printing is measured by the creation of microstrip meander line, in order to provide a comparison of the resistivity versus as the number of the printing successive layers. Resistivity decreases as the number of printing successive layers increases, but the increase of printing successive layers suffers from a precision decrease.

RF measurements are not be possible, because of delay in the fabrication process. A radiation analysis of a TL loaded by CSRRs and lumped serie varactors is developed in parallel with this work, in the aim to examine the electronic control of tunable serie capacitor on the LWA radiation performances.

Bibliography

[1] C. Marlier, "Projet de 2ème master, réalisation de métamatériaux accordables à base de céramiques," Université de Mons, Faculté Polytechnique de Mons, Tech. Rep., Jun. 2011, promoteur : Marc Debliquy.

[2] O. G. Vendik and S. P. Zubko, *Ferroelectrics as Constituents of Tunable Metamaterials.* in F. Capolino, CRC Press Inc, 2009, ch. Theory and Phenomena of Metamaterials, Metamaterial Handbook, pp. 33–1 – 33–40.

[3] V. Reymond, "Nouvelles couches minces et multicouches dérivés de batio3 : Optimisation des propriétés diélectriques," Ph.D. dissertation, Université de Bordeaux, Ecole doctorale des sciences chimiques, 2004.

[4] J. Zhang, H. Zhang, S. L. S.G., Z. Xu, and K. Chen, "The effect of physical design parameters on the rf and microwave performance of the bst thin film planer interdigitated varactors," *Sensors and Actuators A, ScienceDirect, Elsevier*, vol. 141, pp. 231 – 237, 2007.

[5] A. K. Tagantsev, V. O. Sherman, K. F. Astafiev, J. Venkatesh, and N. Setter, "Ferroelectric materials for microwave tunable applications," *Journal of Electroceramics*, vol. 11, pp. 5 – 66, 2003.

[6] A. Kamyshny, J. Steinke, and S. Magdassi, "Metal-based inkjet inks for printed electronics," *The Open Applied Physics Journal*, vol. 4, pp. 19 – 36, 2011.

APPENDIX C

RIGHT-LEAKY REGION OF CSRR-LOADED TL WITH ONE SPLIT RING

This annex will present the results of the radiation performance of the right-leaky region of the CSRR-loaded TL antenna with on split ring. The analysis of the left-hand region is the subject of the section 4.5.

C.1 INTRODUCTION

The analysed structure is a TL loaded by gaps and CSRRs. The topology of the CSRR is based on one split ring as viewed in Fig. 4.50. The schematic of the TL is showed in C.1 with source. The structure is lying on a Rogers RT5870 RF substrate ($\varepsilon_r = 2.33$, $h = 0.5$ mm, $tg\delta = 0.003$). The parameters of the cell are: $r_{out} = 4.5$ mm, $G = 1$ mm, $C = 0.5$ mm, $D = 0.5$ mm, $W_{out} = 1$ mm, $W_{in} = 1$ mm, $W = 1.47$ mm. The methodology of the extraction of the propagation characteristics are described in the section 4.2. Full wave simulation of the structure is based on the IE3D software and COMSOL Multiphysics Finite Element Method solver. The measured 2D radiation patterns of CSRR-based TL with one split ring are obtained from transmission measurements between a Rohde & Schwarz HL024A1/S1 Crossed Log-Periodic Antenna and the antenna under test using the Agilent PNA-X N5242A Vector Network Analyser.

C.2 PROPAGATION CHARACTERISTICS

Fig. 4.52 presents the comparison of S parameters for a TL loaded by 16 CSRRs with one split ring. Structure based on CSRRs of two split rings creates a right-hand bands at lower frequencies (in Fig. 4.52), but the frequency shift is smaller

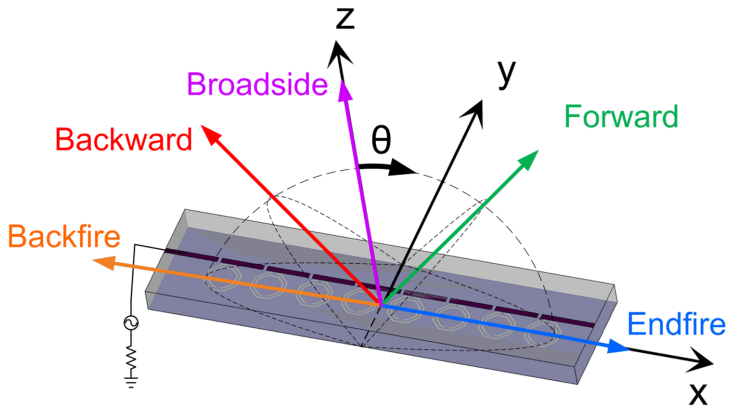


Figure C.1. *View of transmission line created by a cascade of 8 cells with source and specific axes (distance between CSRRs : 2.5 mm).*

than in the left-hand band (Fig. 4.5 : CSRR with two split rings, Fig. 4.52 : CSRR with one split ring). Leakage factor is extracted from equation 4.3 in Fig. 4.53(c) and the propagation constant is extracted from equation 4.4 in Fig. 4.53(d). From the radiation cone, the right-leaky region is determined to be between 5.25 GHz and 7.73 GHz for IE3D simulation and between 5.147 GHz and 7.475 GHz for measurement.

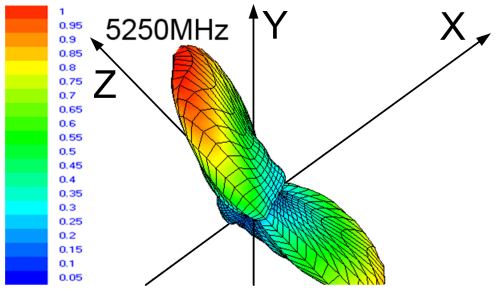
C.3 RADIATION PERFORMANCES

The simulated and measured radiation patterns are showed in Fig. 4.57 in the ($\phi = 0°$) X-Z plane to verify the frequency scanning from $\beta = 0$ (where the main beam is oriented in the broadside direction of Fig. C.1) to $\beta = k_0$ (where the main beam is oriented in the endfire direction of Fig. C.1).

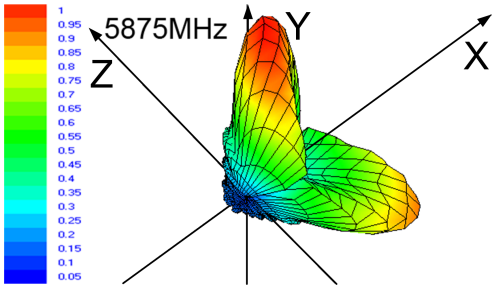
Fig. C.2 presents the 3D view of the radiation pattern simulated by IE3D. It is noticed that the behaviour of TL with one split ring is similar to TL with two split rings (Fig. 4.11).

Fig.C.3 presents the same analysis for the COMSOL simulation, the frequency scanning is also similar to the COMSOL results for TL based on two split rings (Fig. 4.11).

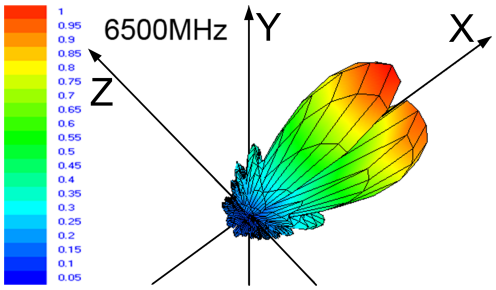
Fig. C.4(b) shows the measured radiation pattern for the ($\phi = 90°$) Y-Z plane. The main beam is not split into two parts, which is similar to the case of the CSRR with two split rings at the lower frequency of the right-hand band (Fig. 4.16). The measurement in two different planes, i.e. ($\phi = 45°$) and ($\phi = 135°$) planes, shown in Fig. C.5, confirms the main lobe is oriented along the Z plane for the case of CSRR TL with one split ring.



(a) 5250MHz



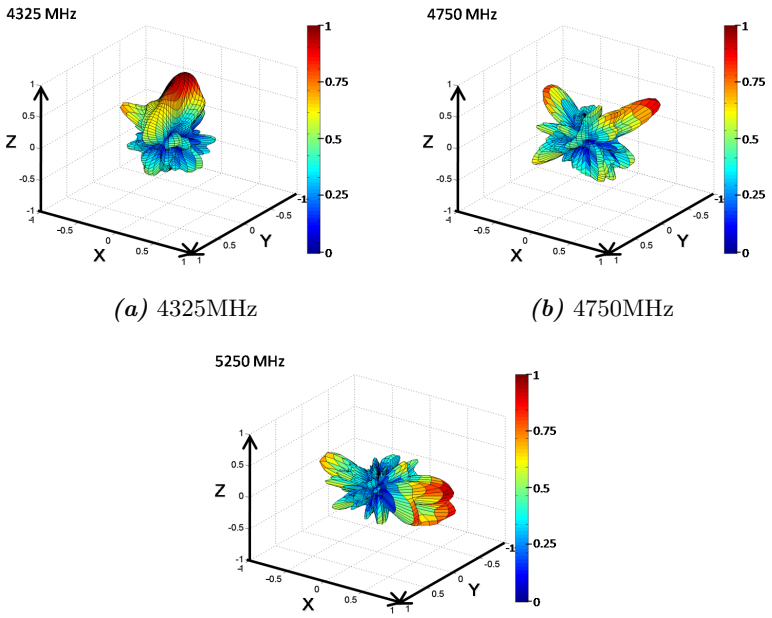
(b) 5875MHz



(c) 6500MHz

Figure C.2. *Normalized 3D radiation pattern for the TL based on 16 CSRRs with one split ring of Fig. 4.50(a) simulated with IE3D assuming an infinite substrate at 3 frequencies in the right-leaky region. Color bar: blue corresponds to zero, red corresponds to 1.*

In order to verify the model of the TL comprising sets of dipoles, which explains broadside radiation at the lower frequency of the right-handed band, Fig. C.6 illustrates the zoom of distribution of current density and current vectors on metallic strip joining adjacent cells. This was simulated at the lower frequency of the right-leaky region, i.e. 5.25 GHz, using the IE3D software under the normal



(a) 4325MHz *(b)* 4750MHz

(c) 5250MHz

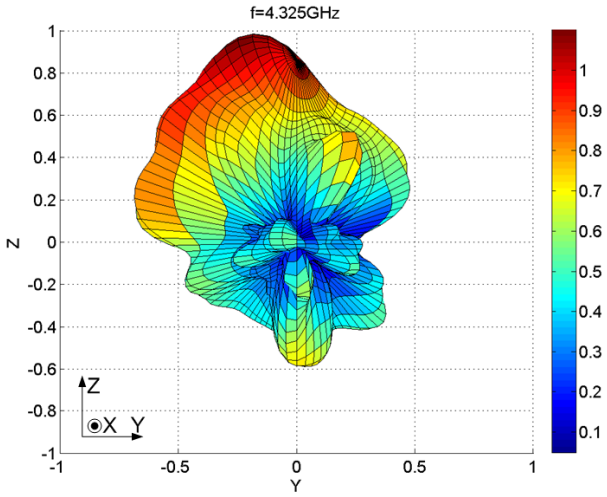
Figure C.3. *Normalized 3D radiation pattern for the TL based on 16 CSRRs with one split ring of Fig. 4.50(a) simulated with COMSOL at 3 frequencies in the right-leaky region. Color bar: blue corresponds to zero, red corresponds to 1.*

assumption of infinite substrate. In a similar manner to Fig 5.10, for the case of the right-leaky region, all vectors are orientated along the x-axis.

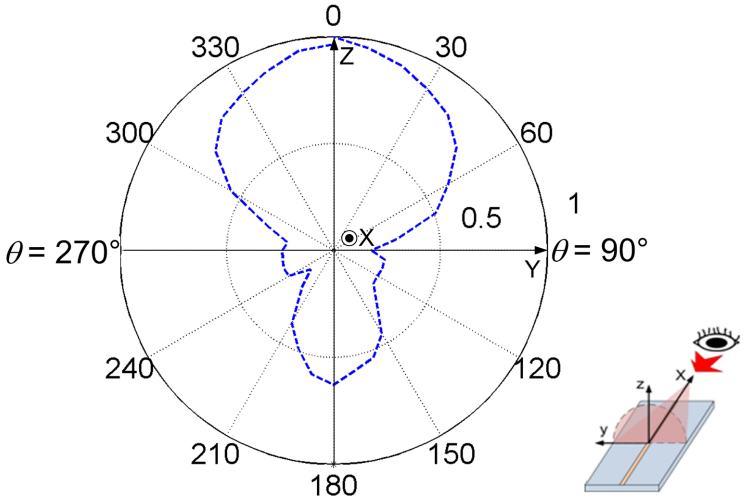
To conclude, the influence of the number of rings on the radiation pattern is negligible in the right-hand band. The radiation efficiency, illustrated in Fig. 4.59, is quite the same whatever the number of rings.

C.4 CONCLUSION

This appendix presents the propagation characteristics and radiation performances of a TL loaded by 16 CSRRs with one split ring in the right-hand region. These results are compared to the same results for TL loaded by 16 CSRRS with two split rings. To conclude, the influence of the number of rings on the radiation pattern is negligible in the right-hand band.

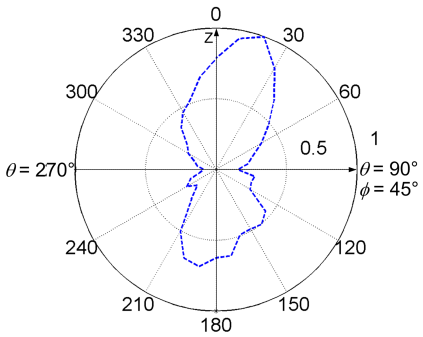


(a) COMSOL at 4.325 GHz

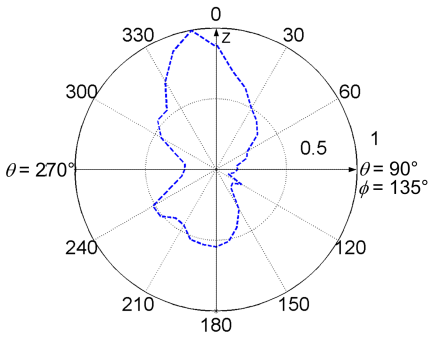


(b) Measurement at 4.8 GHz

Figure C.4. *(a) 3D view of ($\phi = 90°$) Y-Z plane of normalised radiation pattern for the TL based on 16 cells with one split ring of Fig. 4.50(a) simulated with COMSOL at 4.325 GHz, corresponding to lower frequency of the right-leaky region. Color bar: dark blue corresponds to zero, dark red corresponds to 1. (b) Normalized 2D radiation pattern in ($\phi = 90°$) Y-Z plane for the TL based on 16 cells with one split ring of Fig. 4.50(a) measured at 5.15 GHz, corresponding to the lower frequency of the right-leaky region.*



(a) ($\phi = 45°$) plane



(b) ($\phi = 135°$) plane

Figure C.5. *Normalized 2D radiation pattern for the TL based on 16 cells of Fig. 4.2 measured at 5.15 GHz, corresponding to upper frequency of the left-leaky region (a) in ($\phi = 45°$) plane and (b) in ($\phi = 135°$) plane.*

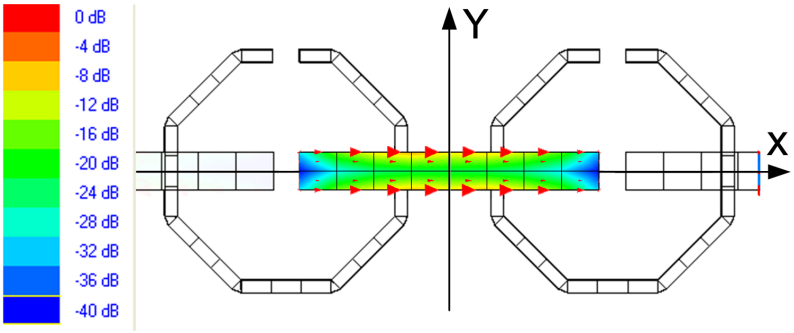
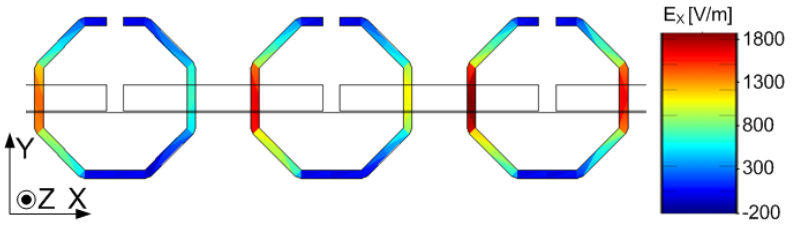
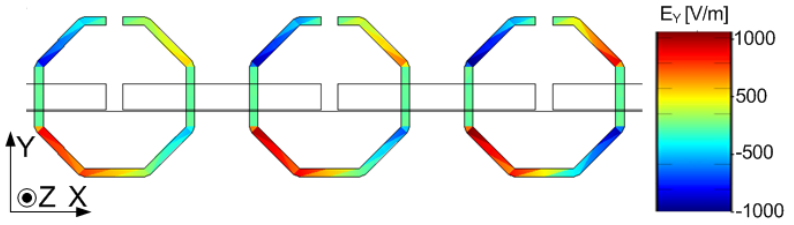


Figure C.6. *Zoom of distribution of current density and current vectors on metallic strip joining adjacent cells, simulated with IE3D assuming an infinite substrate at 5.25 GHz, lower frequency of the right-leaky region (Fig. C.2(a)). Color bar: current density is normalised with the maximum of the current on the upper metal level and is expressed in dB, blue color corresponds to lowest current density; red color corresponds to highest current density (maximal current density : 174.14 A/m). All current vectors are oriented in the same direction along axis.*

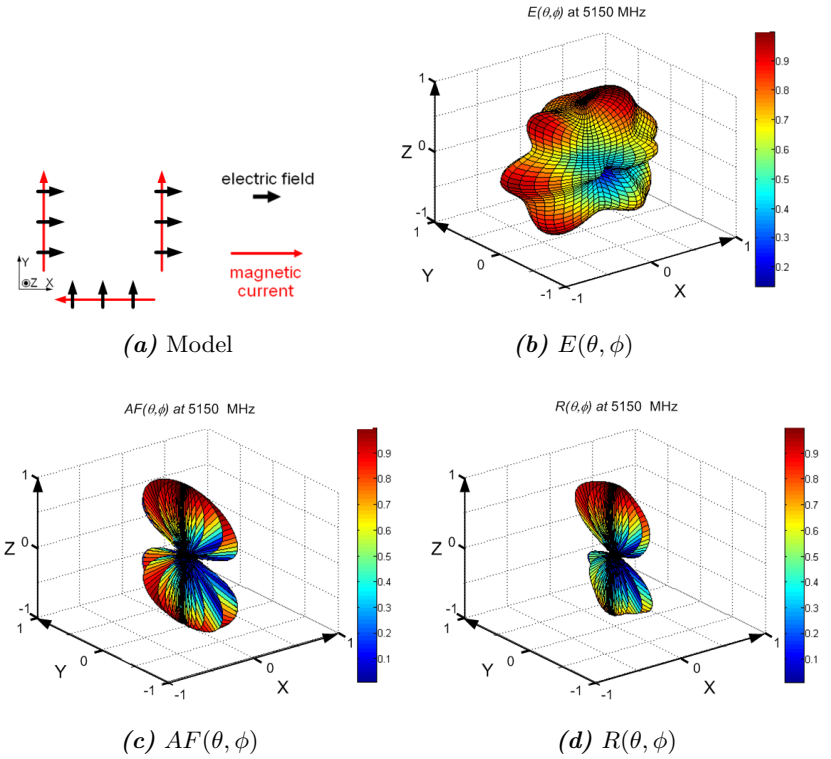


(a) E_X



(b) E_Y

Figure C.7. *Zoom of electric field distribution across the rings of 3 adjacent single ring cells of Fig. 4.50, simulated with COMSOL at the lower frequency of right-leaky region, at 4.325 GHz : (a)* E_X *and (a)* E_Y



(a) Model ***(b)*** $E(\theta, \phi)$

(c) $AF(\theta, \phi)$ ***(d)*** $R(\theta, \phi)$

Figure C.8. *(a) Schematic view of current and electric field distribution for CSRR structure based on one split ring for the lower frequency of the right-hand region(thick black arrows represent the electric field across the rings, thin red arrows represent the magnetic current created by the electric field across the ring). (b) Normalised far-field pattern* $E(\theta, \phi)$ *of the square model described in (a) simulated with COMSOL for the single ring structure at 5.1 GHz which is the lower measured frequency of right-leaky region. (c) Normalized array factor* $AF(\theta, \phi)$ *for 15 cells from (5.1) at 5.1 GHz based on the measured dispersion diagram. (c) Normalized total field* $R(\theta, \phi)$ *of 15-elements array of (a), product of* $E(\theta, \phi)$ *(shown in (b)) and* $AF(\theta, \phi)$ *(shown in (c)) for CSRR structure based on one ring at 5.1 GHz.*

APPENDIX D

PARAMETRIC STUDY OF CSRR-BASED LWA

This annex presents the results of the parametric study of the CSRR-based LWA.

D.1 FIGURES OF MERIT

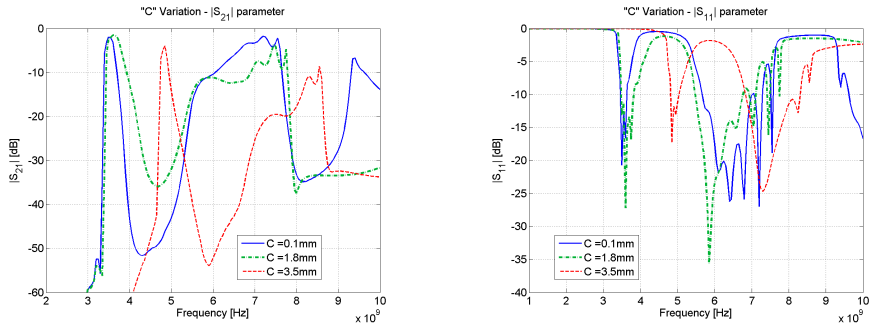
The figures of merit are described in the section 4.5.3.

The figures of merit have the objective to analyse the radiation performances (as directivity, gain and efficiency), the impedance matching of the TL (to realize the matching load at the LWA end to absorb the no-radiated energy and to improve the input matching to optimize the input energy), to compare the frequency scanning between the left and the right leaky regions.

D.2 WIDTH C OF THE SLOT

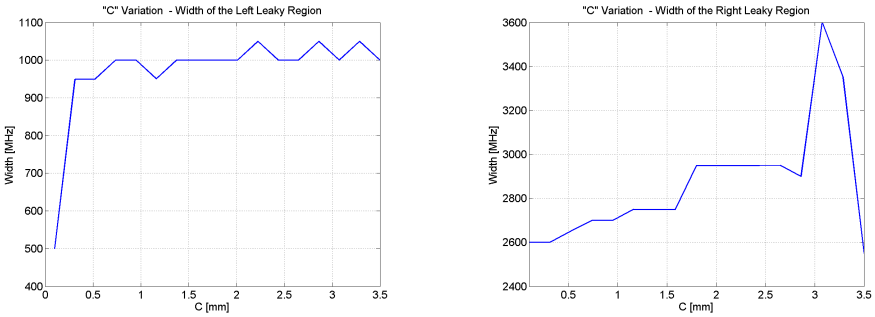
This section presents the influence of width, C, of the slot on the figures of merit. C is increased from 0.1 mm to 3.5 mm in steps of 0.2125 mm. The others dimensions are fixed to the dimensions described in Fig. 4.60. The influence of C on the figure of merit is presented from Fig. D.1 to Fig. D.9 for both leaky regions.

Conclusion : The increase of C moves the LH and RH bands to higher frequencies. The higher C is, the lower the capacitance of the LC network of the CSRR and the capacitance between the series elements and the CSRR are. C does not influence much the width of both leaky regions. The global slope for the LH band is not really influenced by C, but an increase of C creates an increase



(a) *(b)*

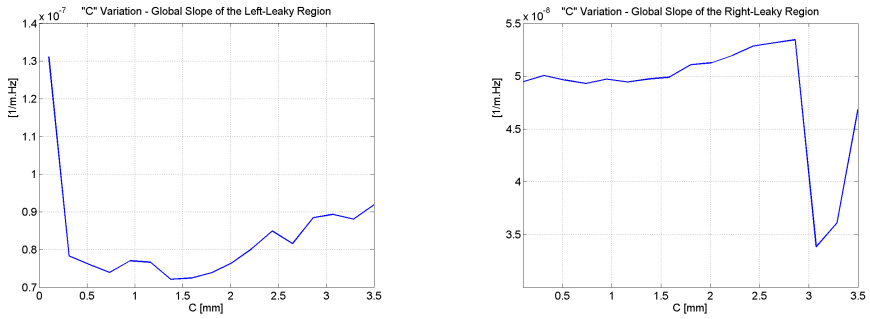
Figure D.1. *S-parameters of TL loaded by 8 CSRRs for both leaky regions for three values of the width C of the CSRR slot : the minimum, the middle and the maximum of its interval (the others cell dimensions are fixed to the dimensions described in Fig. 4.60).*



(a) LH region ***(b)*** RH region

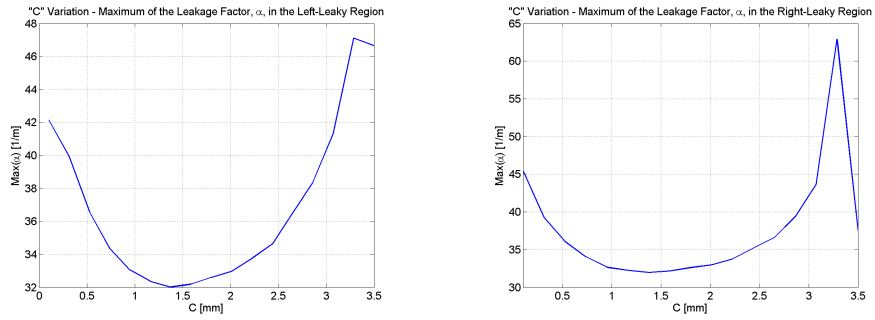
Figure D.2. *Influence of the width C of the CSRR slot on the width of the leaky region defined as the difference between the lower and the upper frequency of the leaky region for both leaky regions (the antenna is based on 8 CSRRs, the others cell dimensions are fixed to the dimensions described in Fig. 4.60).*

of the global slope for the RH band. The leakage factor presents a minimum around $C = 1.5$ mm for both leaky regions. The interval of the characteristic impedance decreases weakly with an increase of C in the left-leaky region but increases strongly with an increase of C in the right-leaky region. An increase of C induces a decrease of the maximum of S_{11}-parameter for both leaky regions. The minimum of S_{11}-parameter presents a maximum at approximately $C =$



(a) LH region *(b)* RH region

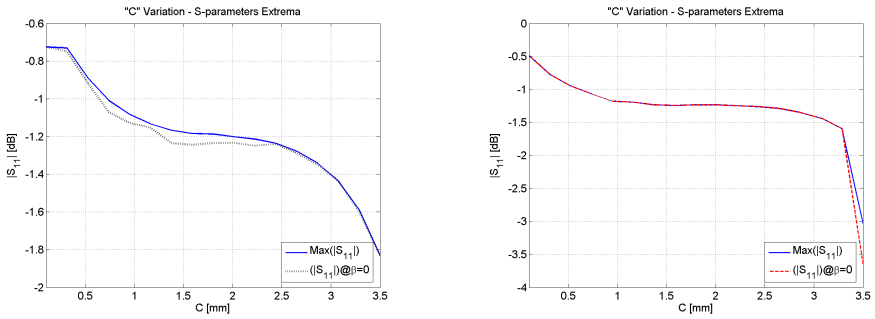
Figure D.3. *Influence of the width C of the CSRR slot on the slope of the leaky region, defined in eq. 4.16 for both leaky regions (the antenna is based on 8 CSRRs, the others cell dimensions are fixed to the dimensions described in Fig. 4.60).*



(a) LH region *(b)* RH region

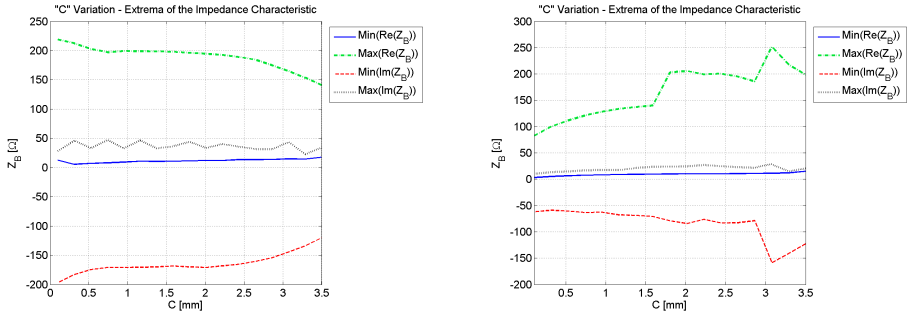
Figure D.4. *Influence of the width C of the CSRR slot on the maximum of the leakage factor, α, for the leaky region (the antenna is based on 8 CSRRs, the others cell dimensions are fixed to the dimensions described in Fig. 4.60).*

3 mm for the left-leaky region and a minimum at approximately $C = 0.2$ mm for the right-leaky region. The antenna efficiency AF increases with an increase of C for both leaky regions. The maximal gain presents a maximum at approximately $C = 2$ mm for the left-leaky region and at approximately $C = 3$ mm for the right-leaky region. The maximal directivity presents a maximum at approximately $C = 3$ mm for the left-leaky region and at approximately $C = 2.5$ mm for the right-leaky region.



(a) LH region *(b)* RH region

Figure D.5. *Influence of the width C of the CSRR slot on the extrema of the S_{11}-parameter defined as the maximum magnitude for the leaky region, compared to S_{11}-parameter at the edges of the leaky region (the antenna is based on 8 CSRRs, the others cell dimensions are fixed to the dimensions described in Fig. 4.60).*

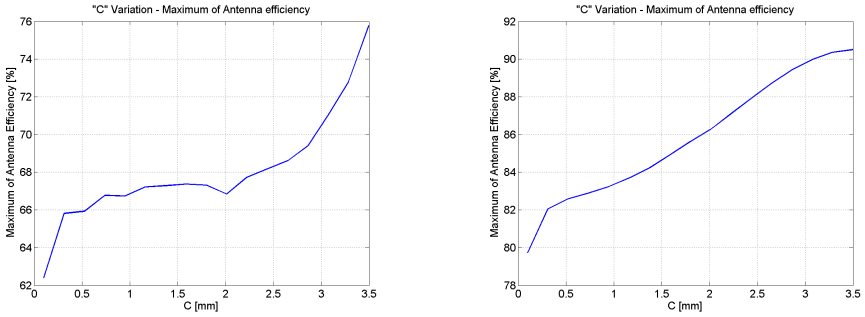


(a) LH region *(b)* RH region

Figure D.6. *Influence of the width C of the CSRR slot on the extrema of the characteristics impedance Z_B defined as the maximum and the minimum the real and imaginary parts of the characteristic impedance Z_B for the leaky region defined in eq. 4.18 (the antenna is based on 8 CSRRs, the others cell dimensions are fixed to the dimensions described in Fig. 4.60).*

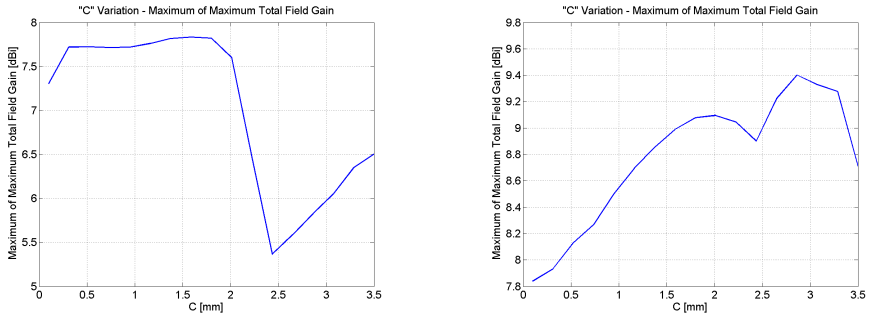
D.3 OUTER RADIUS R_{OUT} OF THE OUTER RING

This section presents the influence of the outer radius, R_{out}, of the outer ring on the figures of merit. R_{out} is increased from 3.7 mm to 10 mm by step of 0.7 mm,



(a) LH region *(b)* RH region

Figure D.7. *Influence of the width C of the CSRR slot on the maximum of the antenna efficiency defined as the maximum of antenna efficiency AF for the leaky region (the antenna is based on 8 CSRRs, the others cell dimensions are fixed to the dimensions described in Fig. 4.60).*

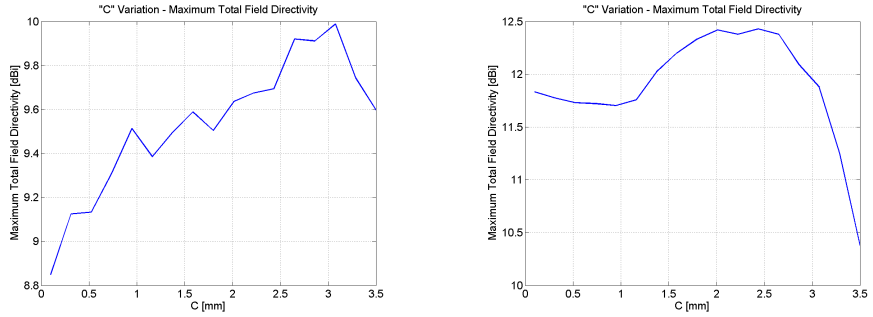


(a) LH region *(b)* RH region

Figure D.8. *Influence of the width C of the CSRR slot on the maximum of the total field gain defined as the maximum of the maximum total field gain for the leaky region (the antenna is based on 8 CSRRs, the others cell dimensions are fixed to the dimensions described in Fig. 4.60).*

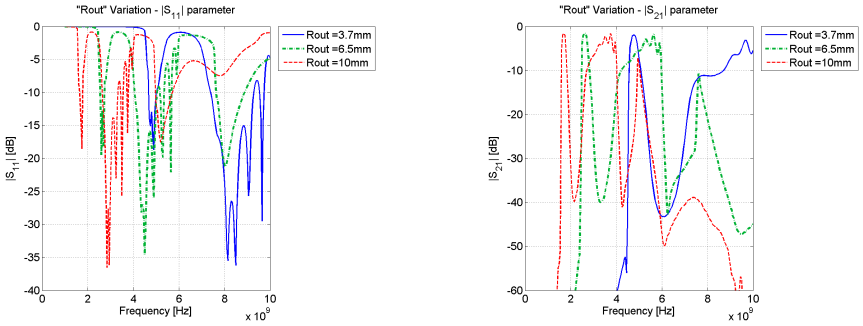
the others dimensions are fixed to the dimensions described in Fig. 4.60. The R_{out} influence on the figure of merits is presented from Fig. D.10 to Fig. D.18 for both leaky regions.

The increase of R_{out} moves the LH and RH bands in lower frequency. The influence of R_{out} on the width of the leaky regions is the highest : an increase of R_{out} creates a decrease of this width and an increase of the global slope



(a) LH region *(b)* RH region

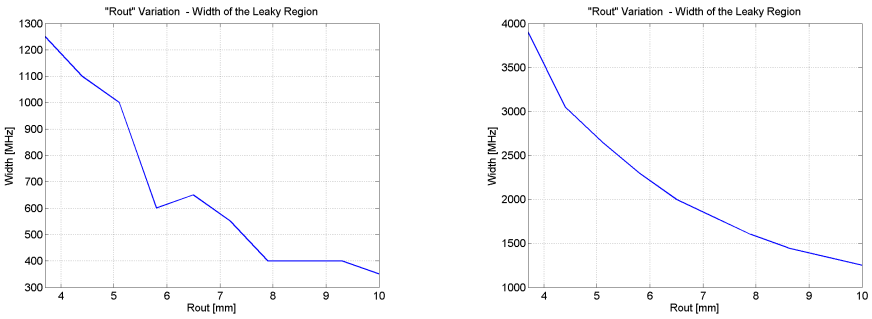
Figure D.9. *Influence of the width C of the CSRR slot on the maximum of the total field directivity defined as the maximum of the maximum total field directivity for the leaky region (the antenna is based on 8 CSRRs, the others cell dimensions are fixed to the dimensions described in Fig. 4.60).*



(a) S_{11} *(b)* S_{21}

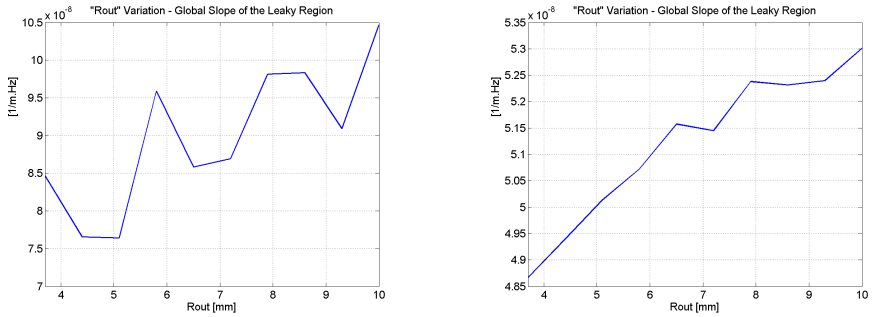
Figure D.10. *S-parameters of TL loaded by 8 CSRRs for both leaky regions for three values of the outer radius R_{out} : the minimum, the middle and the maximum of its interval (the others cell dimensions are fixed to the dimensions described in Fig. 4.60).*

for both leaky regions. The leakage factor increases in the both leaky regions for an increase of R_{out}. The interval of the characteristic impedance increases weakly with an increase of R_{out} in the left-leaky region but decreases weakly with an increase of R_{out} in the right-leaky region. The extrema of S_{11}-parameter is not really influenced by R_{out} for both leaky regions. The maximal antenna efficiency decreases with an increase of R_{out} for the left-leaky region and presents



(a) LH region *(b)* RH region

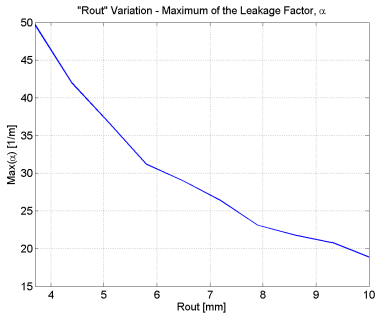
Figure D.11. *Influence of the outer radius R_{out} of the CSRR ring on the width of the leaky region defined as the difference between the lower and the upper frequency of the leaky region for both leaky regions (the antenna is based on 8 CSRRs, the others cell dimensions are fixed to the dimensions described in Fig. 4.60).*



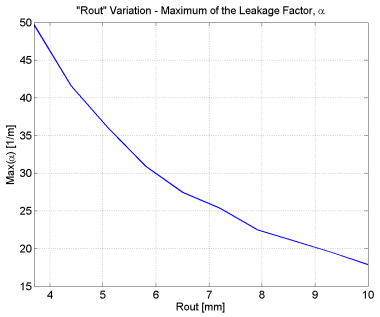
(a) LH region *(b)* RH region

Figure D.12. *Influence of the outer radius R_{out} of the CSRR ring on the slope of the leaky region, defined in eq. 4.16 for both leaky regions (the antenna is based on 8 CSRRs, the others cell dimensions are fixed to the dimensions described in Fig. 4.60).*

a maximum around $R_{out} = 5$ mm. The maximal gain and the directivity decrease with an increase of R_{out} for both leaky regions.

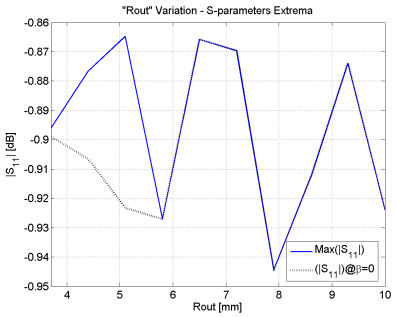


(a) LH region

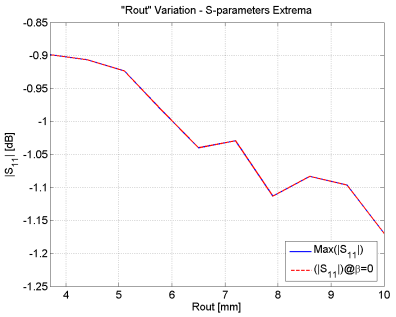


(b) RH region

Figure D.13. *Influence of the outer radius R_{out} of the CSRR ring on the maximum of the leakage factor defined as the maximum of leakage factor, α, for the leaky region (the antenna is based on 8 CSRRs, the others cell dimensions are fixed to the dimensions described in Fig. 4.60).*

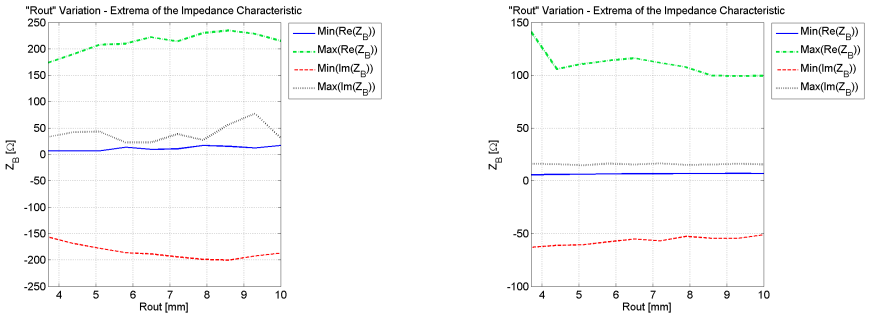


(a) LH region



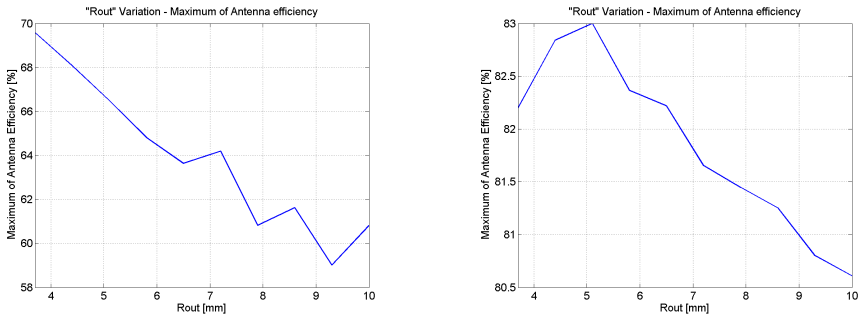
(b) RH region

Figure D.14. *Influence of the outer radius R_{out} of the CSRR ring on the extrema of the S_{11}-parameter defined as the maximum of the S_{11} magnitude for the leaky region, compared to S_{11}-parameter at the edges of the leaky region (the antenna is based on 8 CSRRs, the others cell dimensions are fixed to the dimensions described in Fig. 4.60).*



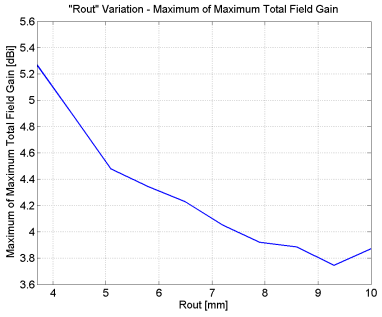
(a) LH region ***(b)*** RH region

Figure D.15. *Influence of the outer radius R_{out} of the CSRR ring on the extrema of the characteristics impedance Z_B defined as the maximum and the minimum the real and imaginary parts of the characteristic impedance Z_B for the leaky region defined in eq. 4.18 (the antenna is based on 8 CSRRs, the others cell dimensions are fixed to the dimensions described in Fig. 4.60).*

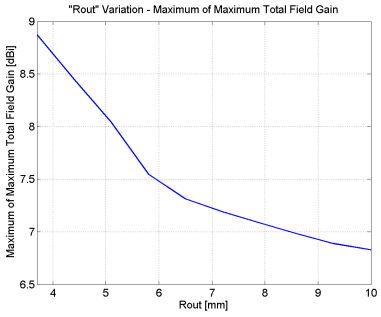


(a) LH region ***(b)*** RH region

Figure D.16. *Influence of the outer radius R_{out} of the CSRR ring on the maximum of the antenna efficiency defined as the maximum of antenna efficiency for the leaky region (the antenna is based on 8 CSRRs, the others cell dimensions are fixed to the dimensions described in Fig. 4.60).*

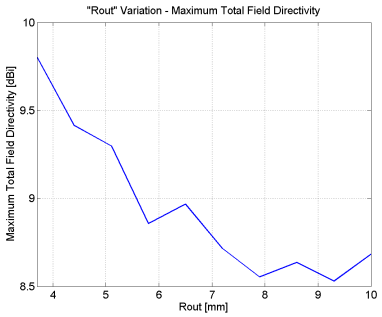


(a) LH region

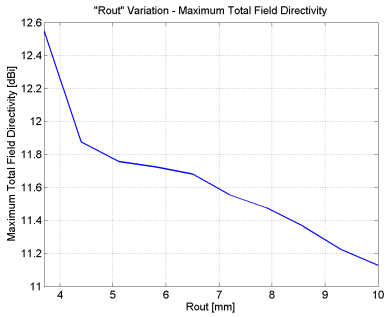


(b) RH region

Figure D.17. *Influence of the outer radius R_{out} of the CSRR ring on the maximum of the total field gain defined as the maximum of the maximum total field gain for the leaky region (the antenna is based on 8 CSRRs, the others cell dimensions are fixed to the dimensions described in Fig. 4.60).*



(a) LH region

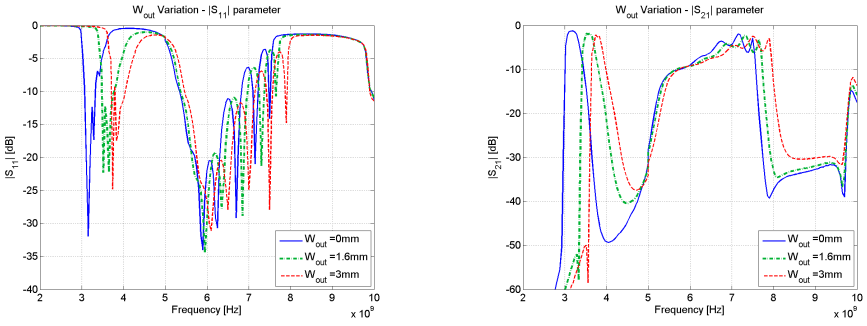


(b) RH region

Figure D.18. *Influence of the outer radius R_{out} of the CSRR ring on the maximum of the total field directivity defined as the maximum of the maximum total field directivity for the leaky region (the antenna is based on 8 CSRRs, the others cell dimensions are fixed to the dimensions described in Fig. 4.60).*

D.4 OPENING W_{OUT} OF THE RING

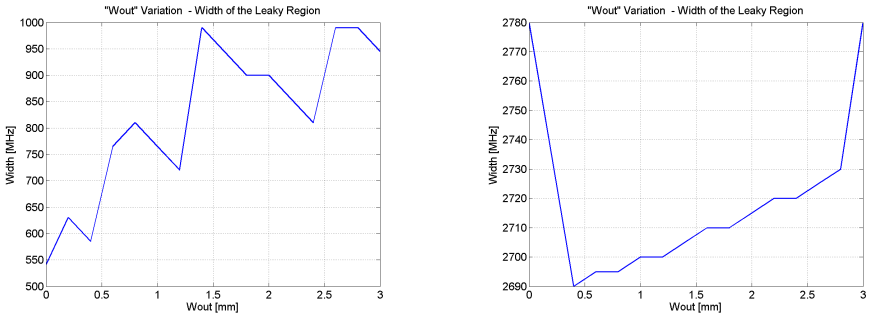
This section presents the influence of the opening, W_{out}, of the ring on the figures of merit. W_{out} is increased from 0.0025 mm to 3 mm by step of 0.2 mm, the others dimensions are fixed to the dimensions described in Fig. 4.60. The W_{out} influence on the figure of merits is presented from Fig. D.19 to Fig. D.27 for both leaky regions.



(a) S_{11} *(b)* S_{21}

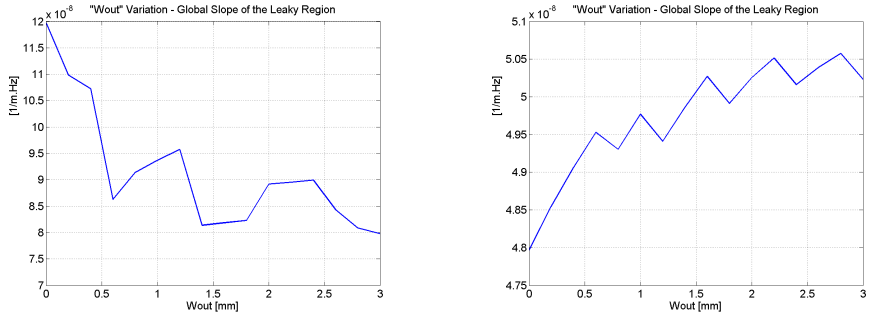
Figure D.19. *S-parameters of TL loaded by 8 CSRRs for both leaky regions for three values of the opening W_{out} of the CSRR ring : the minimum, the middle and the maximum of its interval (the others cell dimensions are fixed to the dimensions described in Fig. 4.60).*

The increase of W_{out} moves the LH band in higher frequency, the RH band is more and less the same. Indeed W_{out} influences only the CSRR structure. An increase of W_{out} creates an increase of the width of the leaky region for both regions. The parameter W_{out} does not influence the global slope in the RH band, for the LH band, an increase of W_{out} creates a decrease of the global slope. The leakage factor decreases weakly for an increases of W_{out} for both leaky regions. The interval of the characteristic impedance decreases with an increase of W_{out} in the both leaky regions. For both leaky regions, the maximum of S_{11}-parameter decreases with an increase of W_{out} and the minimum of of S_{11}-parameter is not influenced by W_{out}. The antenna efficiency increases with an increase of W_{out} for the left-leaky region and is maximal around $W_{out} = 5$ mm for the right leaky-region. An increase of W_{out} induces a increases of the maximal gain and the maximal directivity for the left-leaky region and their decreases for the right leaky region.



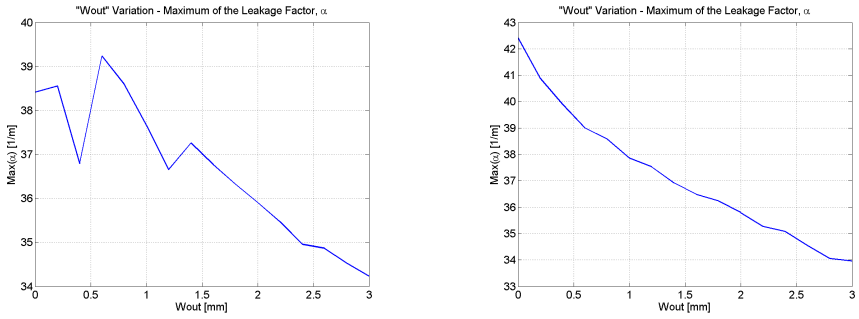
(a) LH region *(b)* RH region

Figure D.20. *Influence of the opening W_{out} of the CSRR ring on the width of the leaky region defined as the difference between the lower and the upper frequency of the leaky region for both leaky regions (the antenna is based on 8 CSRRs, the others cell dimensions are fixed to the dimensions described in Fig. 4.60).*



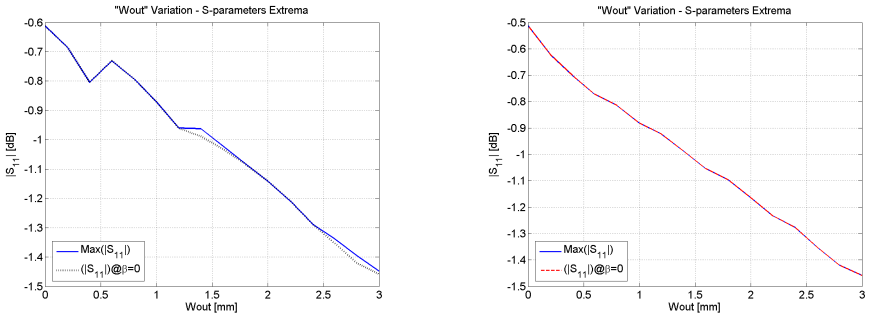
(a) LH region *(b)* RH region

Figure D.21. *Influence of the opening W_{out} of the CSRR ring on the slope of the leaky region, defined in eq. 4.16 for both leaky regions (the antenna is based on 8 CSRRs, the others cell dimensions are fixed to the dimensions described in Fig. 4.60).*



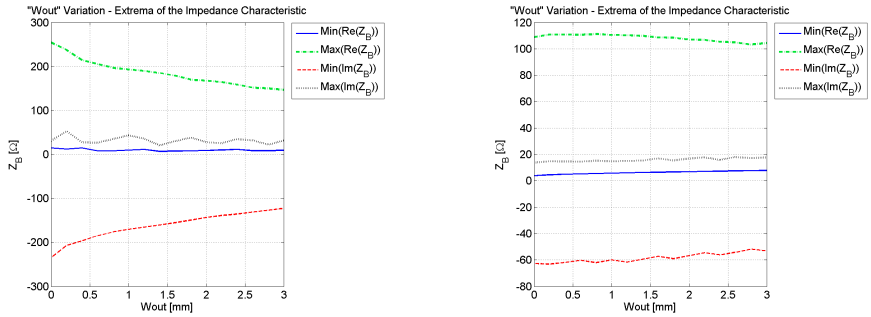
(a) LH region *(b)* RH region

Figure D.22. *Influence of the opening W_{out} of the CSRR ring on the maximum of the leakage factor defined as the maximum of leakage factor, α, for the leaky region (the antenna is based on 8 CSRRs, the others cell dimensions are fixed to the dimensions described in Fig. 4.60).*



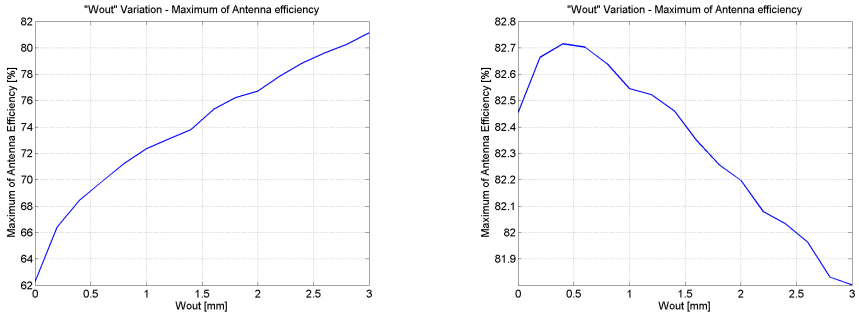
(a) LH region *(b)* RH region

Figure D.23. *Influence of the opening W_{out} of the CSRR ring on the extrema of the S_{11}-parameter defined as the maximum of the S_{11} magnitude for the leaky region, compared to S_{11}-parameter at the edges of the leaky region (the antenna is based on 8 CSRRs, the others cell dimensions are fixed to the dimensions described in Fig. 4.60).*



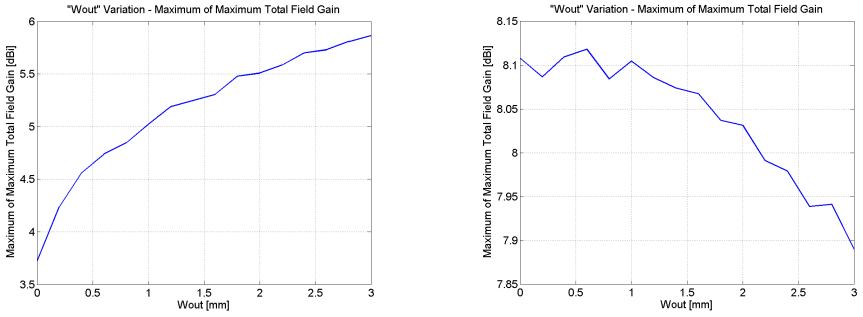
(a) LH region *(b)* RH region

Figure D.24. *Influence of the opening W_{out} of the CSRR ring on the extrema of the characteristics impedance Z_B defined as the maximum and the minimum the real and imaginary parts of the characteristic impedance Z_B for the leaky region defined in eq. 4.18 (the antenna is based on 8 CSRRs, the others cell dimensions are fixed to the dimensions described in Fig. 4.60).*



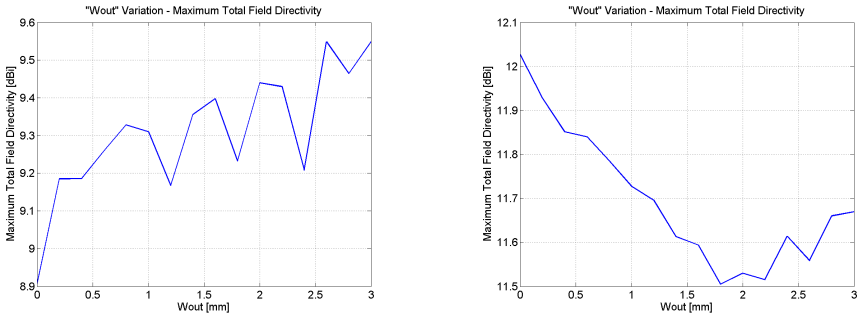
(a) LH region *(b)* RH region

Figure D.25. *Influence of the opening W_{out} of the CSRR ring on the maximum of the antenna efficiency defined as the maximum of antenna efficiency for the leaky region (the antenna is based on 8 CSRRs, the others cell dimensions are fixed to the dimensions described in Fig. 4.60).*



(a) LH region *(b)* RH region

Figure D.26. *Influence of the opening W_{out} of the CSRR ring on the maximum of the total field gain defined as the maximum of the maximum total field gain for the leaky region (the antenna is based on 8 CSRRs, the others cell dimensions are fixed to the dimensions described in Fig. 4.60).*

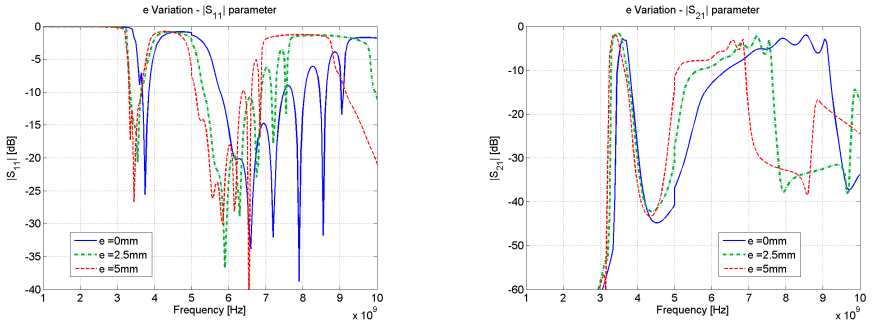


(a) LH region *(b)* RH region

Figure D.27. *Influence of the opening W_{out} of the CSRR ring on the maximum of the total field directivity defined as the maximum of the maximum total field directivity for the leaky region (the antenna is based on 8 CSRRs, the others cell dimensions are fixed to the dimensions described in Fig. 4.60).*

D.5 SPACE E BETWEEN TWO CELLS

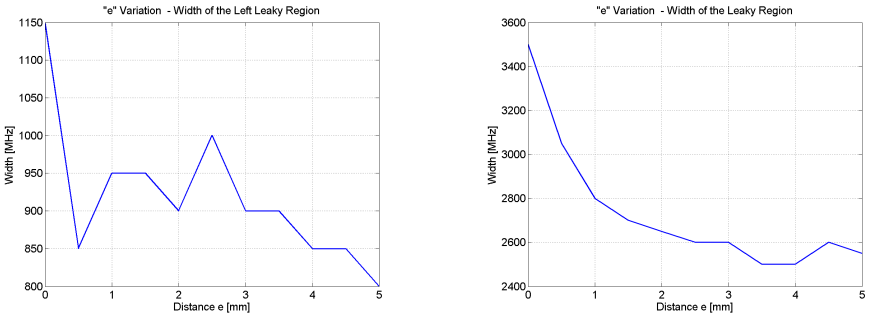
This section presents the distance, e, between two cells, of the slot on the figures of merit. e is increased from 0 mm (the distance between the radius is equal to 0 mm, the distance between two sides is in fact equal to 0.76 mm) to 5 mm by step of 0.5 mm, the others dimensions are fixed to the dimensions described in Fig. 4.60. The e influence on the figure of merits is presented from Fig. D.28 to Fig. D.36 for both leaky regions.



(a) S_{11} ***(b)*** S_{21}

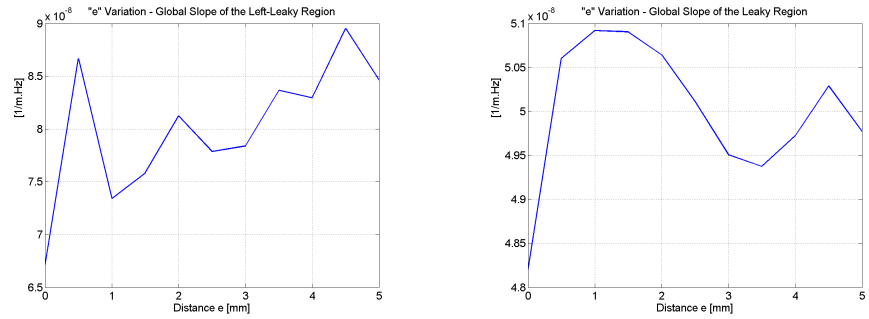
Figure D.28. *S-parameters of TL loaded by 8 CSRRs for both leaky regions for three values of the space e between two adjacent CSRR cells : the minimum, the middle and the maximum of its interval (the others cell dimensions are fixed to the dimensions described in Fig. 4.60).*

The increase of e moves the LH and RH bands in lower frequency, especially the higher frequency of the RH band decreases a lot with the increase of e. The width of the leaky region decreases with an increase of e. The global slope of the left-leaky region increases with an increase of e. The global slope of the right-leaky region presents a maximum around e = 1.25 mm. The leakage factor decreases with a increase of e for both leaky regions. The interval of the characteristic impedance decreases with an increase of e in the left-leaky region but is not really influenced by e in the right-leaky region. The maximum of S_{11}-parameter is not really influenced by e for the left-leaky region. The minimum of S_{11}-parameter is maximal for $e = 1$ mm for the left leaky region and is not influenced for the right-leaky region. An increase of e creates a decrease of the antenna efficiency for both leaky regions. The maximal decreases with an increase of e for the left-leaky region and increases with an increase of e for the right-leaky region. An increase of e creates an increase of the maximal directivity for both leaky regions.



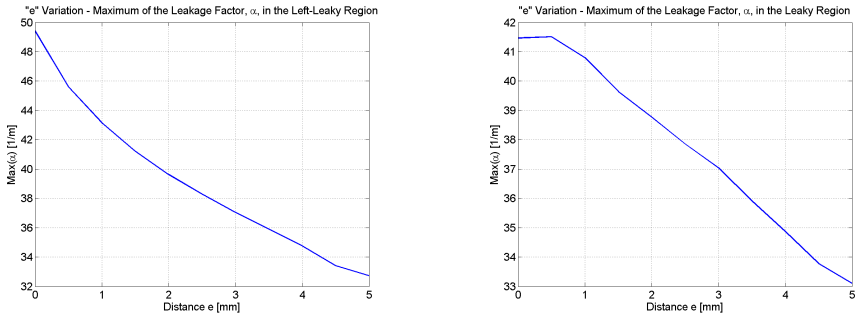
(a) LH region ***(b)*** RH region

Figure D.29. *Influence of the space e between two adjacent CSRR cells on the width of the leaky region defined as the difference between the lower and the upper frequency of the leaky region for both leaky regions (the antenna is based on 8 CSRRs, the others cell dimensions are fixed to the dimensions described in Fig. 4.60).*



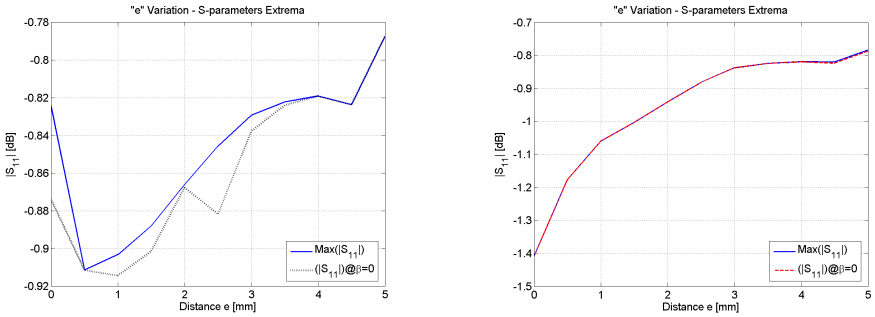
(a) LH region ***(b)*** RH region

Figure D.30. *Influence of the space e between two adjacent CSRR cells on the slope of the leaky region, defined in eq. 4.16 for both leaky regions (the antenna is based on 8 CSRRs, the others cell dimensions are fixed to the dimensions described in Fig. 4.60).*



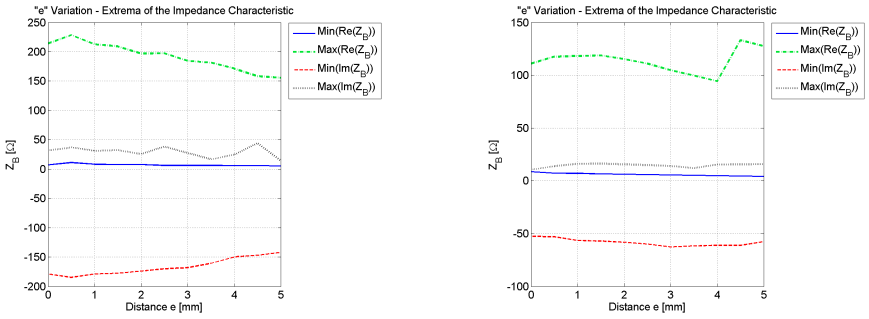
(a) LH region *(b)* RH region

Figure D.31. *Influence of the space e between two adjacent CSRR cells on the maximum of the leakage factor defined as the maximum of leakage factor, α, for the leaky region (the antenna is based on 8 CSRRs, the others cell dimensions are fixed to the dimensions described in Fig. 4.60).*



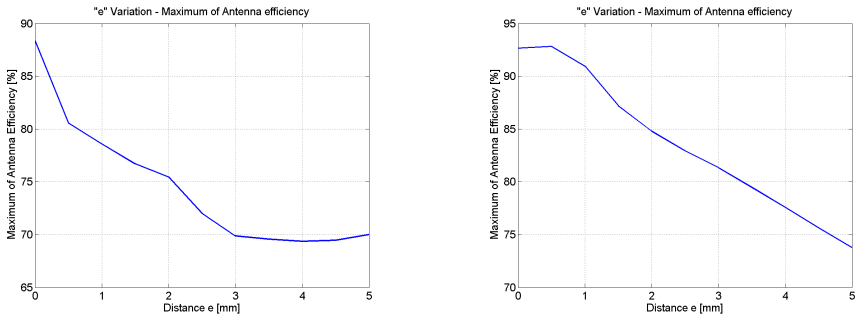
(a) LH region *(b)* RH region

Figure D.32. *Influence of the space e between two adjacent CSRR cells on the extrema of the S_{11}-parameter defined as the maximum of the S_{11} magnitude for the leaky region, compared to S_{11}-parameter at the edges of the leaky region (the antenna is based on 8 CSRRs, the others cell dimensions are fixed to the dimensions described in Fig. 4.60).*



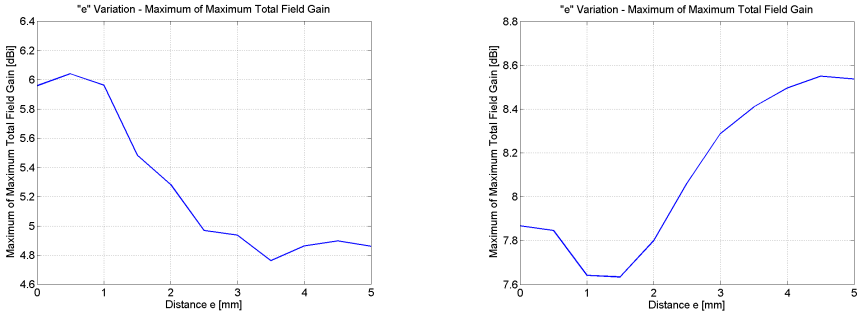
(a) LH region ***(b)*** RH region

Figure D.33. *Influence of the space e between two adjacent CSRR cells on the extrema of the characteristics impedance Z_B defined as the maximum and the minimum the real and imaginary parts of the characteristic impedance Z_B for the leaky region defined in eq. 4.18 (the antenna is based on 8 CSRRs, the others cell dimensions are fixed to the dimensions described in Fig. 4.60).*



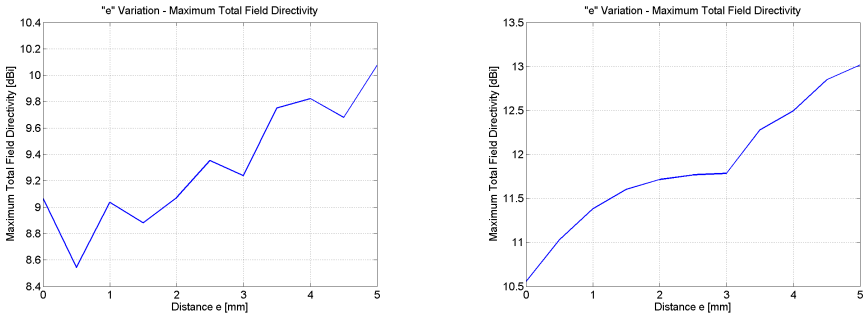
(a) LH region ***(b)*** RH region

Figure D.34. *Influence of the space e between two adjacent CSRR cells on the maximum of the antenna efficiency defined as the maximum of antenna efficiency for the leaky region (the antenna is based on 8 CSRRs, the others cell dimensions are fixed to the dimensions described in Fig. 4.60).*



(a) LH region *(b)* RH region

Figure D.35. *Influence of the space e between two adjacent CSRR cells on the maximum of the total field gain defined as the maximum of the maximum total field gain for the leaky region (the antenna is based on 8 CSRRs, the others cell dimensions are fixed to the dimensions described in Fig. 4.60).*

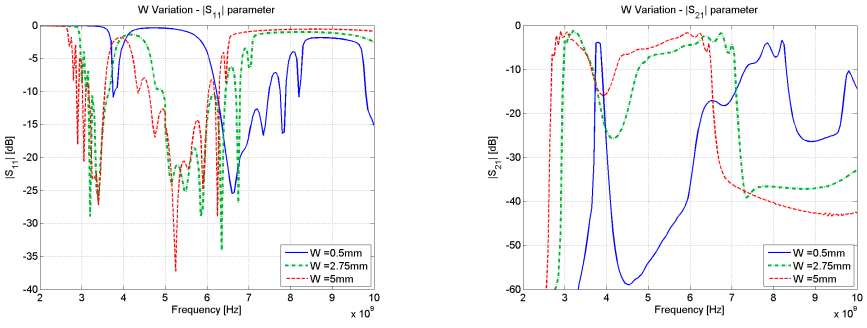


(a) LH region *(b)* RH region

Figure D.36. *Influence of the space e between two adjacent CSRR cells on the maximum of the total field directivity defined as the maximum of the maximum total field directivity for the leaky region (the antenna is based on 8 CSRRs, the others cell dimensions are fixed to the dimensions described in Fig. 4.60).*

D.6 WIDTH W OF THE METAL STRIP LINE

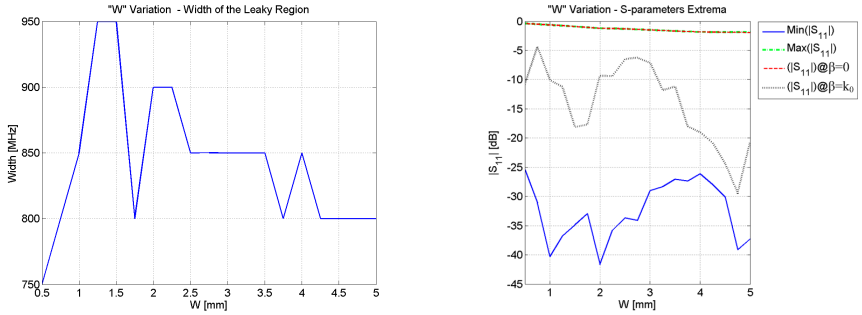
This section presents the influence of width, W, of the metal strip line on the figures of merit. w is increased from 0.5 mm to 5 mm by step of 0.25 mm, the others dimensions are fixed to the dimensions described in Fig. 4.60. The W influence on the figure of merits is presented from Fig. D.37 to Fig. D.45 for both leaky regions.



(a) S_{11} ***(b)*** S_{21}

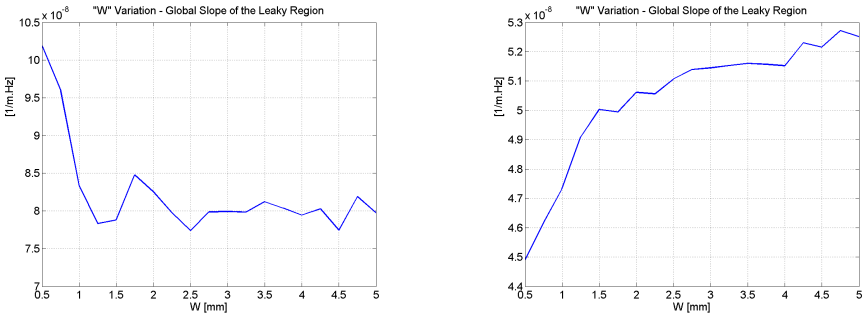
Figure D.37. *S-parameters of TL loaded by 8 CSRRs for both leaky regions for three values of the width W of the metal strip line : the minimum, the middle and the maximum of its interval (the others cell dimensions are fixed to the dimensions described in Fig. 4.60).*

The increase of W moves the LH and RH bands in lower frequency (the shift is higher for the RH band). The width and the global slope of the left-leaky region is not really influenced by the parameter W, the width of the right leaky region increases and the global slope decreases for an decrease of W. The leakage factor, the interval of the characteristic impedance and the maximal gain decrease for an increase of W for both leaky regions. The maximum of the S_{11}-parameter decreases with an increase of W for both leaky regions, the minimum of the S_{11}-parameter decreases with an increase of W for the left-leaky region and does not present a specific behaviour for a modification of this parameter for the right leaky region. The maximal antenna efficiency presents a maximum around W = 3 mm for the left-leaky region, its value decreases with an increase of W for the right-leaky region. The maximal directivity increases with an increase of W for the left-leaky region and decreases with an increase of W for the right-leaky region.



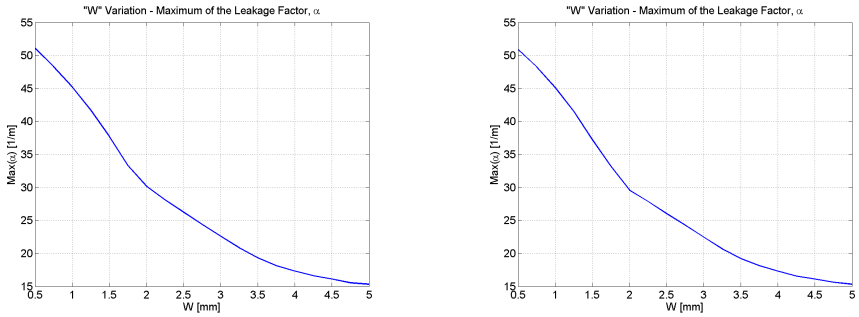
(a) LH region *(b)* RH region

Figure D.38. *Influence of the width W of the metal strip line on the width of the leaky region defined as the difference between the lower and the upper frequency of the leaky region for both leaky regions (the antenna is based on 8 CSRRs, the others cell dimensions are fixed to the dimensions described in Fig. 4.60).*



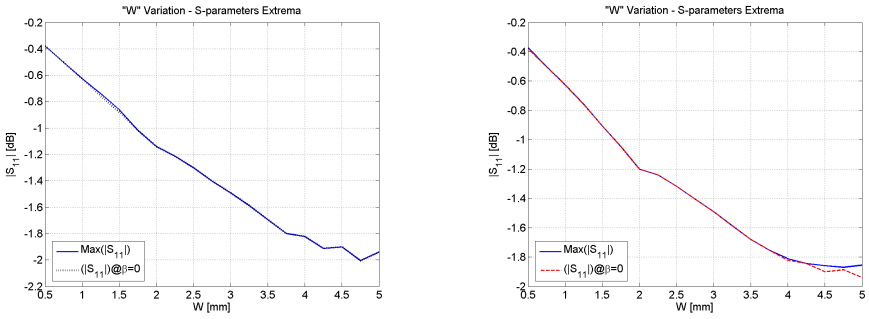
(a) LH region *(b)* RH region

Figure D.39. *Influence of the width W of the metal strip line on the slope of the leaky region, defined in eq. 4.16 for both leaky regions (the antenna is based on 8 CSRRs, the others cell dimensions are fixed to the dimensions described in Fig. 4.60).*



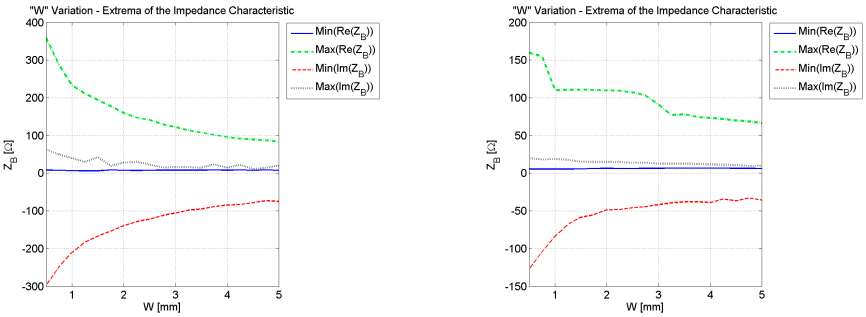
(a) LH region *(b)* RH region

Figure D.40. *Influence of the width W of the metal strip line on the maximum of the leakage factor defined as the maximum of leakage factor, α, for the leaky region (the antenna is based on 8 CSRRs, the others cell dimensions are fixed to the dimensions described in Fig. 4.60).*



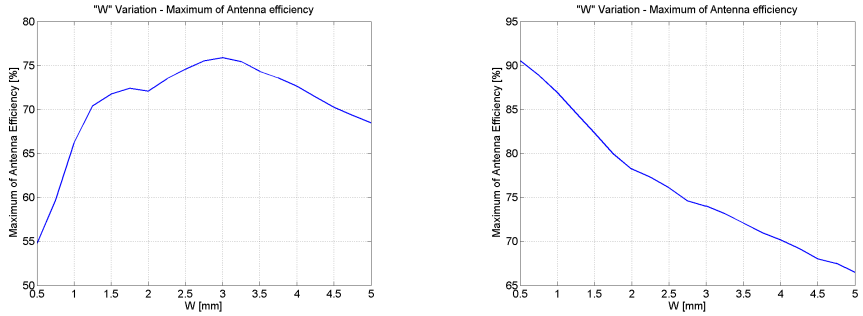
(a) LH region *(b)* RH region

Figure D.41. *Influence of the width W of the metal strip line on the extrema of the S_{11}-parameter defined as the maximum of the S_{11} magnitude for the leaky region, compared to S_{11}-parameter at the edges of the leaky region (the antenna is based on 8 CSRRs, the others cell dimensions are fixed to the dimensions described in Fig. 4.60).*



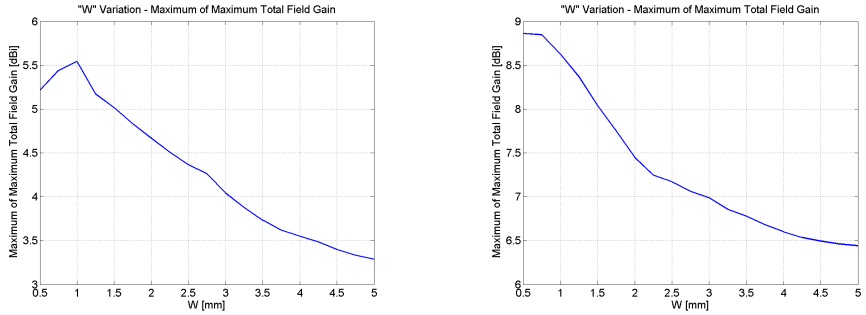
(a) LH region ***(b)*** RH region

Figure D.42. *Influence of the width W of the metal strip line on the extrema of the characteristics impedance Z_B defined as the maximum and the minimum the real and imaginary parts of the characteristic impedance Z_B for the leaky region defined in eq. 4.18 (the antenna is based on 8 CSRRs, the others cell dimensions are fixed to the dimensions described in Fig. 4.60).*



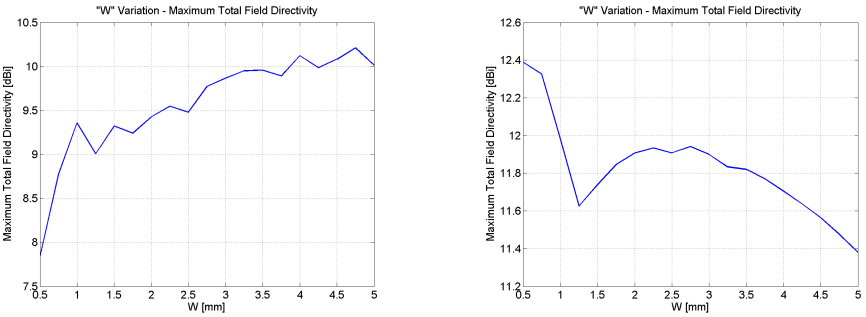
(a) LH region ***(b)*** RH region

Figure D.43. *Influence of the width W of the metal strip line on the maximum of the antenna efficiency defined as the maximum of antenna efficiency for the leaky region (the antenna is based on 8 CSRRs, the others cell dimensions are fixed to the dimensions described in Fig. 4.60).*



(a) LH region *(b)* RH region

Figure D.44. *Influence of the width W of the metal strip line on the maximum of the total field gain defined as the maximum of the maximum total field gain for the leaky region (the antenna is based on 8 CSRRs, the others cell dimensions are fixed to the dimensions described in Fig. 4.60).*

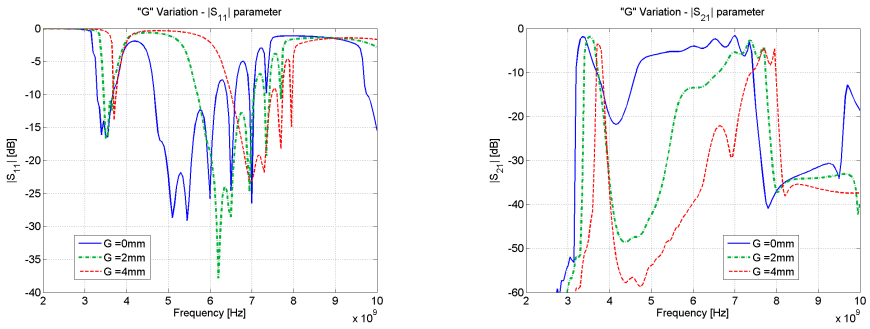


(a) LH region *(b)* RH region

Figure D.45. *Influence of the width W of the metal strip line on the maximum of the total field directivity defined as the maximum of the maximum total field directivity for the leaky region (the antenna is based on 8 CSRRs, the others cell dimensions are fixed to the dimensions described in Fig. 4.60).*

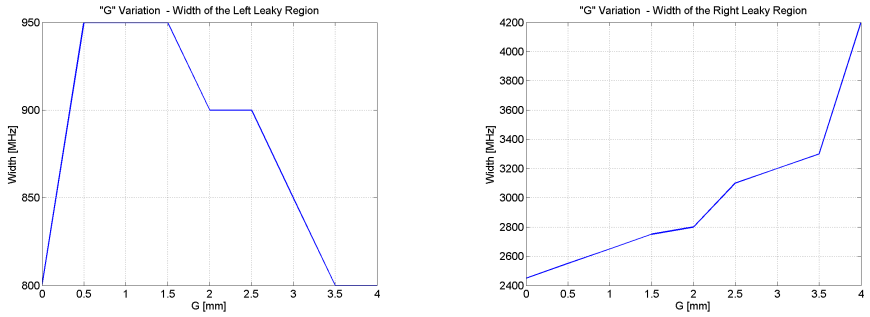
D.7 SIZE G OF THE GAP

This section presents the influence of size, G, of the gap on the figures of merit. G is increased from 0.002 mm to 4 mm by step of 0.5 mm, the others dimensions are fixed to the dimensions described in Fig. 4.60. The G influence on the figure of merits is presented from Fig. D.46 to Fig. D.54 for both leaky regions.



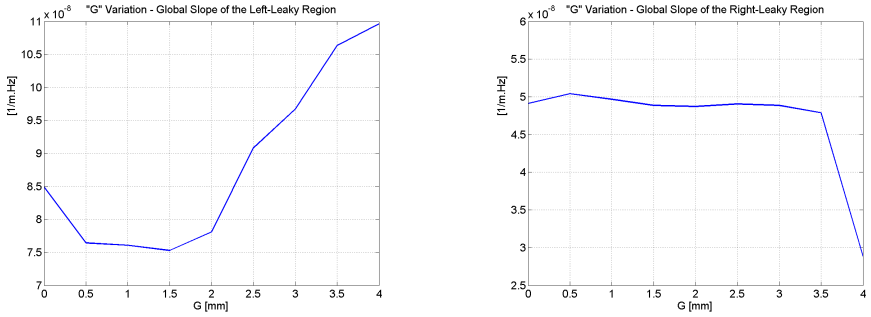
(a) S_{11} *(b)* S_{21}

Figure D.46. *S-parameters of TL loaded by 8 CSRRs for both leaky regions for three values of the size G of the gap : the minimum, the middle and the maximum of its interval (the others cell dimensions are fixed to the dimensions described in Fig. 4.60).*



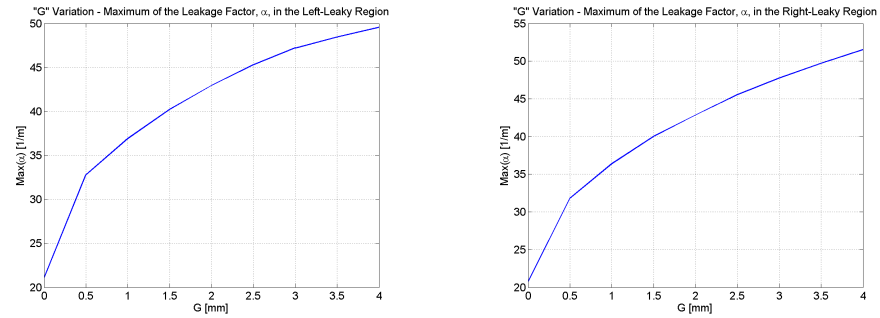
(a) LH region *(b)* RH region

Figure D.47. *Influence of the size G of the gap on the width of the leaky region defined as the difference between the lower and the upper frequency of the leaky region for both leaky regions (the antenna is based on 8 CSRRs, the others cell dimensions are fixed to the dimensions described in Fig. 4.60).*



(a) LH region *(b)* RH region

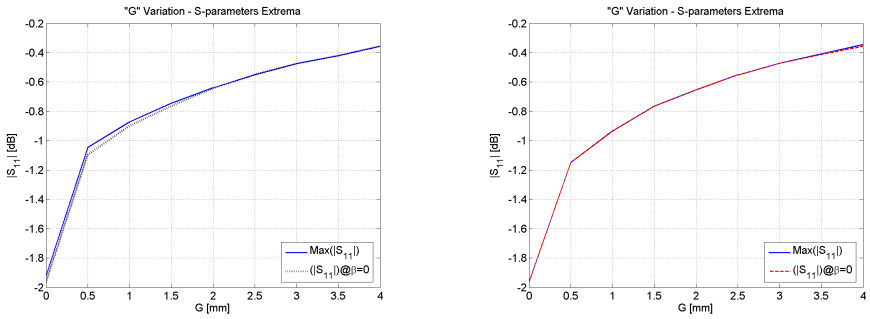
Figure D.48. *Influence of the size G of the gap on the slope of the leaky region, defined in eq. 4.16 for both leaky regions (the antenna is based on 8 CSRRs, the others cell dimensions are fixed to the dimensions described in Fig. 4.60).*



(a) LH region *(b)* RH region

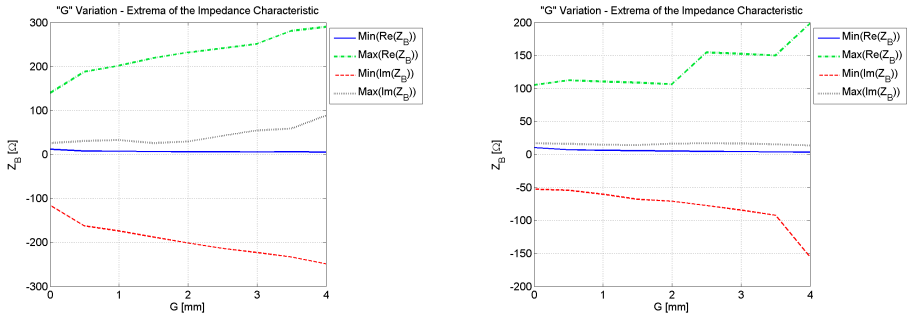
Figure D.49. *Influence of the size G of the gap on the maximum of the leakage factor defined as the maximum of leakage factor, α, for the leaky region (the antenna is based on 8 CSRRs, the others cell dimensions are fixed to the dimensions described in Fig. 4.60).*

The lower frequencies of the RH and LH bands are moved in higher frequency with an increase of G. Indeed the parameter G influences mainly the serie capacitance C_g of the unit cell influencing then the lower frequencies of each LH bands. An increase of G does not really influence the width of the left-leaky region. Contrary, an increase of G creates an increase of the width and a decrease of the global slope of the right leaky region. The global slope of the left-leaky region increases with an increase of G. The leakage factor, the interval of the characteristic impedance, the extrema of S_{11}-parameter, the antenna efficiency



(a) LH region *(b)* RH region

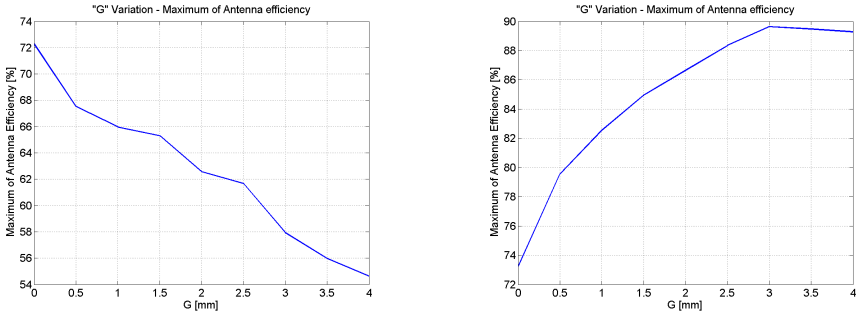
Figure D.50. *Influence of the size G of the gap on the extrema of the S_{11}-parameter defined as the maximum of the S_{11} magnitude for the leaky region, compared to S_{11}-parameter at the edges of the leaky region (the antenna is based on 8 CSRRs, the others cell dimensions are fixed to the dimensions described in Fig. 4.60).*



(a) LH region *(b)* RH region

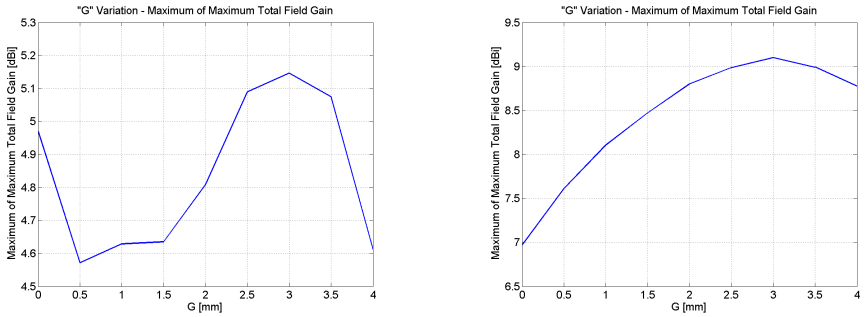
Figure D.51. *Influence of the size G of the gap on the extrema of the characteristics impedance Z_B defined as the maximum and the minimum the real and imaginary parts of the characteristic impedance Z_B for the leaky region defined in eq. 4.18 (the antenna is based on 8 CSRRs, the others cell dimensions are fixed to the dimensions described in Fig. 4.60).*

increase with an increase of G for both leaky regions. The maximal gain presents a maximum around $G = 3$ mm for the left and right-leaky regions. The directivity decreases with an increase of G for the left-leaky region and presents a maximum around $G = 3.5$ mm for the right-leaky region.



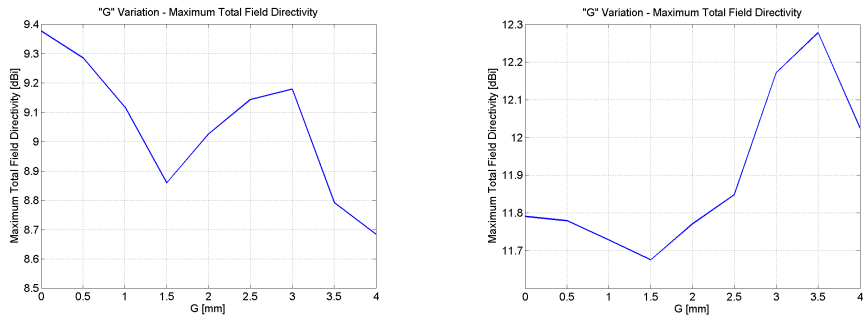
(a) LH region *(b)* RH region

Figure D.52. *Influence of the size G of the gap on the maximum of the antenna efficiency defined as the maximum of antenna efficiency for the leaky region (the antenna is based on 8 CSRRs, the others cell dimensions are fixed to the dimensions described in Fig. 4.60).*



(a) LH region *(b)* RH region

Figure D.53. *Influence of the size G of the gap on the maximum of the total field gain defined as the maximum of the maximum total field gain for the leaky region (the antenna is based on 8 CSRRs, the others cell dimensions are fixed to the dimensions described in Fig. 4.60).*

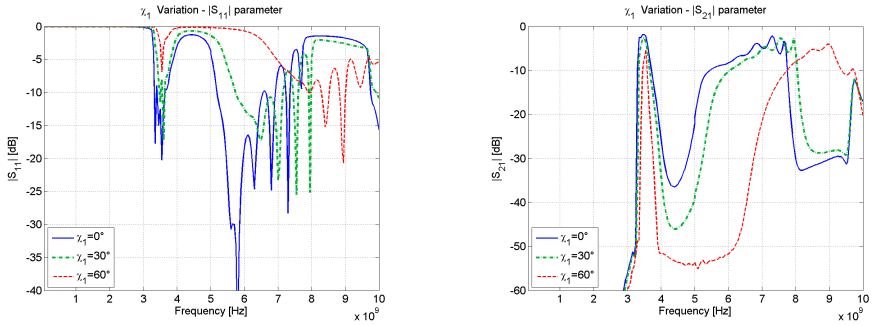


(a) LH region ***(b)*** RH region

Figure D.54. *Influence of the size G of the gap on the maximum of the total field directivity defined as the maximum of the maximum total field directivity for the leaky region (the antenna is based on 8 CSRRs, the others cell dimensions are fixed to the dimensions described in Fig. 4.60).*

D.8 OPENING ANGLE χ_1 OF THE RING

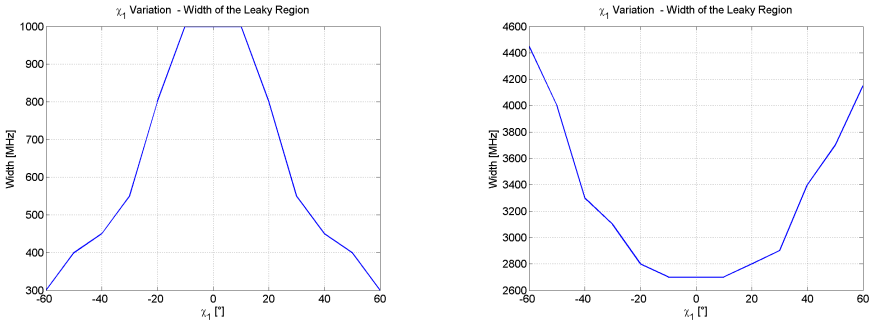
This section presents the the opening angle, χ_1, of the ring on the figures of merit. χ_1 is increased from -60° to 60° by step of 10°, the others dimensions are fixed to the dimensions described in Fig. 4.60. The extraction of the figure of merits are not possible for χ_1 angles bigger than 60° and smaller than -60° because the TL has not the characteristics of a LH TL, the left-handed band does not exist for these values. The χ_1 influence on the figure of merits is presented from Fig. D.55 to Fig. D.63 for both leaky regions.



(a) S_{11} *(b)* S_{21}

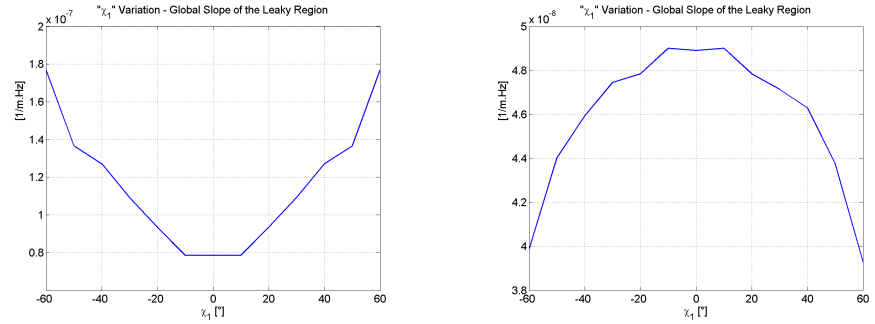
Figure D.55. *S-parameters of TL loaded by 8 CSRRs for both leaky regions for three values of the opening angle χ_1 of the CSRR ring : the minimum, the middle and the maximum of its interval (the others cell dimensions are fixed to the dimensions described in Fig. 4.60).*

The LH band is not influenced by the value of the parameter χ_1. Contrary the RH band is moved in higher frequency for an increase of χ_1 from 0° to 60°. An increase of χ_1 from 0° to 60° creates a decrease of the width and an increase of the global slope of the left-leaky region and an increase of the width and a decrease of the global slope of the right-leaky region. The leakage factor increases with an increase of χ_1 for both leaky regions. The impedance characteristic Z_B is the only one of figures of merit which creates an asymmetric response for an modification of χ_1, Z_B presents a maximum around 30° for the left-leaky region and a maximum around -50° for the right-leaky region. The minimum of S_{11}-parameter increases with an increase of χ_1 for the left-leaky region but does not present a specific behaviour for a modification of χ_1 for the right-leaky region. The maximal antenna efficiency presents a maximum around $\chi_1 = 20°$ for the left-leaky region and around χ_1 = -20° for the right-leaky region. The maximal gain presents two maximums around $\chi_1 = +40°$ and $\chi_1 = -40°$ for the left-leaky region. The maximal gain increases with an increase of χ_1 for the right-leaky region. The directivity presents two extrema for the left-leaky region : a



(a) LH region *(b)* RH region

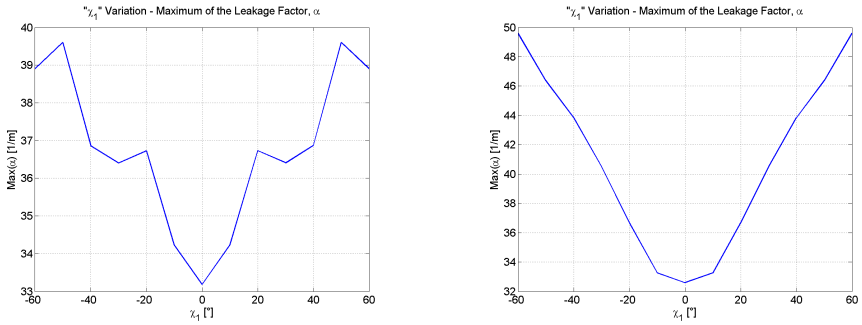
Figure D.56. *Influence of the opening angle χ_1 of the CSRR ring on the width of the leaky region defined as the difference between the lower and the upper frequency of the leaky region for both leaky regions (the antenna is based on 8 CSRRs, the others cell dimensions are fixed to the dimensions described in Fig. 4.60).*



(a) LH region *(b)* RH region

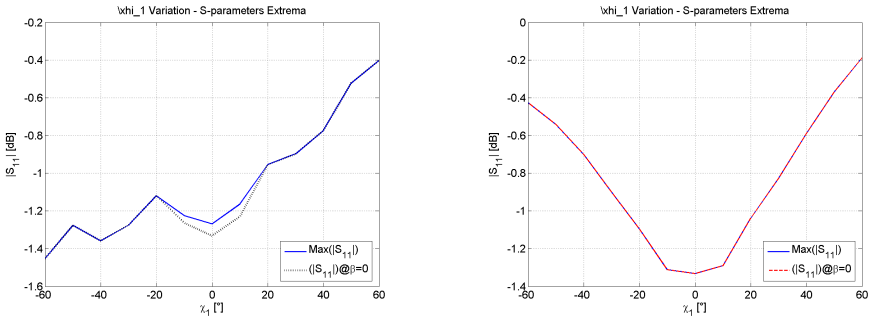
Figure D.57. *Influence of the opening angle χ_1 of the CSRR ring on the slope of the leaky region, defined in eq. 4.16 for both leaky regions (the antenna is based on 8 CSRRs, the others cell dimensions are fixed to the dimensions described in Fig. 4.60).*

minimum around $\chi_1 = 10°$ and a maximum around $\chi_1 = 50°$. For the right-leaky region, the directivity presents a maximum around $\chi_1 = 0°$.



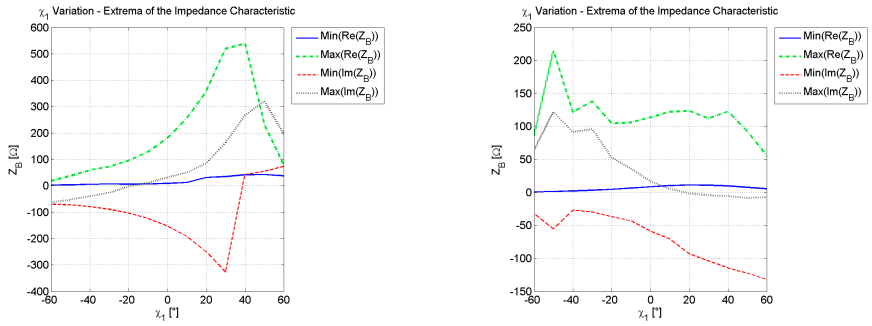
(a) LH region *(b)* RH region

Figure D.58. *Influence of the opening angle χ_1 of the CSRR ring on the maximum of the leakage factor defined as the maximum of leakage factor, α, for the leaky region (the antenna is based on 8 CSRRs, the others cell dimensions are fixed to the dimensions described in Fig. 4.60).*



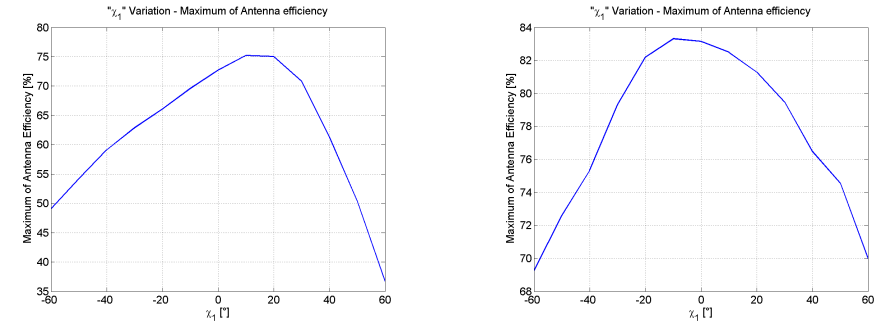
(a) LH region *(b)* RH region

Figure D.59. *Influence of the opening angle χ_1 of the CSRR ring on the extrema of the S_{11}-parameter defined as the maximum of the S_{11} magnitude for the leaky region, compared to S_{11}-parameter at the edges of the leaky region (the antenna is based on 8 CSRRs, the others cell dimensions are fixed to the dimensions described in Fig. 4.60).*



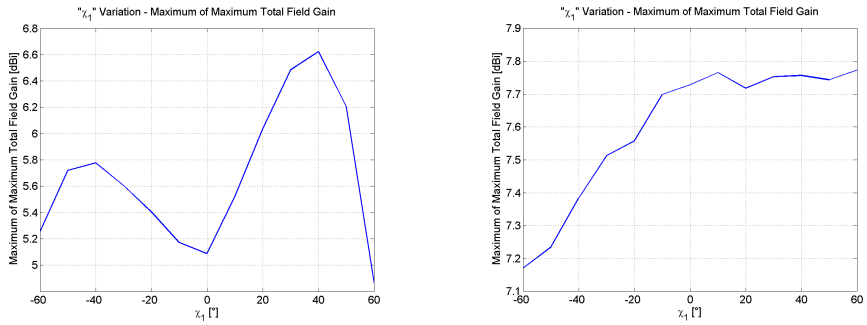
(a) LH region ***(b)*** RH region

Figure D.60. *Influence of the opening angle χ_1 of the CSRR ring on the extrema of the characteristics impedance Z_B defined as the maximum and the minimum the real and imaginary parts of the characteristic impedance Z_B for the leaky region defined in eq. 4.18 (the antenna is based on 8 CSRRs, the others cell dimensions are fixed to the dimensions described in Fig. 4.60).*



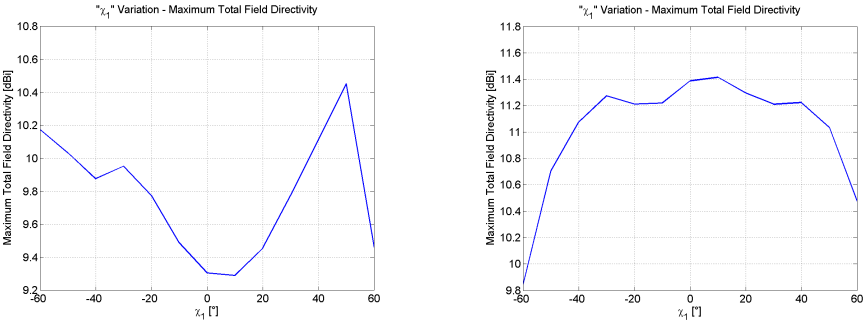
(a) LH region ***(b)*** RH region

Figure D.61. *Influence of the opening angle χ_1 of the CSRR ring on the maximum of the antenna efficiency defined as the maximum of antenna efficiency for the leaky region (the antenna is based on 8 CSRRs, the others cell dimensions are fixed to the dimensions described in Fig. 4.60).*



(a) LH region *(b)* RH region

Figure D.62. *Influence of the opening angle χ_1 of the CSRR ring on the maximum of the total field gain defined as the maximum of the maximum total field gain for the leaky region (the antenna is based on 8 CSRRs, the others cell dimensions are fixed to the dimensions described in Fig. 4.60).*

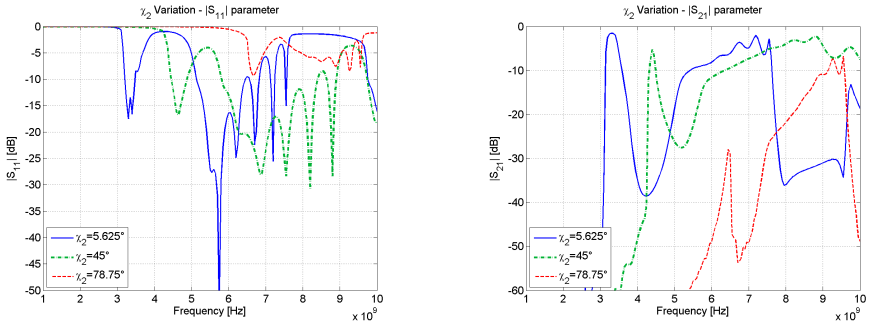


(a) LH region *(b)* RH region

Figure D.63. *Influence of the opening angle χ_1 of the CSRR ring on the maximum of the total field directivity defined as the maximum of the maximum total field directivity for the leaky region (the antenna is based on 8 CSRRs, the others cell dimensions are fixed to the dimensions described in Fig. 4.60).*

D.9 OPENING ANGLE χ_2 OF THE RING

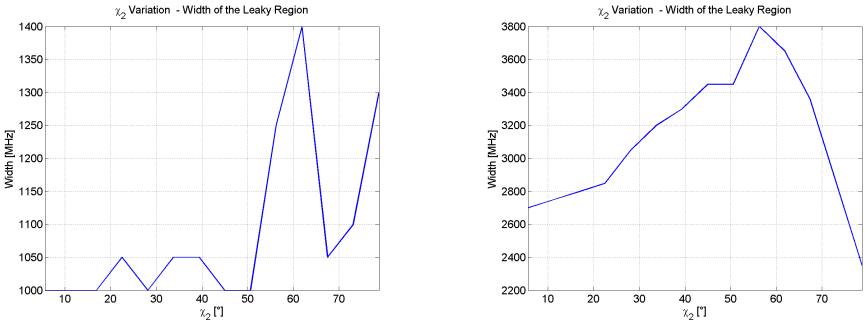
This section presents the the opening angle, χ_2, of the ring on the figures of merit. χ_2 is increased from 5.625° to 78.75° by step of 5.625°, the others dimensions are fixed to the dimensions described in Fig. 4.60. The extraction of the figure of merits are not possible for χ_1 angles smaller than 5.625° and bigger than 78.75° because the TL has not the characteristics of a LH TL, the left-handed band does not exist for these values. The χ_2 influence on the figure of merits is presented from Fig. D.64 to Fig. D.72 for both leaky regions.



(a) S_{11} *(b)* S_{21}

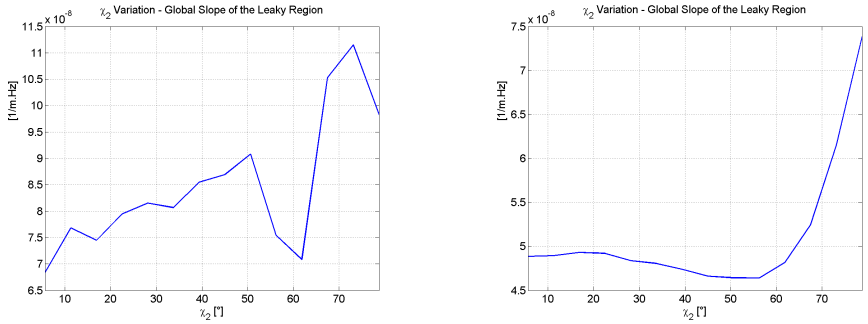
Figure D.64. *S-parameters of TL loaded by 8 CSRRs for both leaky regions for three values of the opening angle χ_2 of the CSRR ring : the minimum, the middle and the maximum of its interval (the others cell dimensions are fixed to the dimensions described in Fig. 4.60).*

An increase of the parameter χ_2 moves the LH and RH bands in higher frequencies. The width of the left-leaky region and its global slope increase with an increase of χ_2. The influence of χ_2 presents a optimal maximum for the right-leaky region around 56.25°. An increase of χ_2 induces an increase of the global slope of the right-leaky region. The leakage factor presents a minimum around χ_2=50° for the left-leaky region and around 60° for the right-leaky region. The interval of the characteristic impedance decreases with an increase of χ_2 for both leaky regions. The maximum of S_{11}-parameter presents a maximum around χ_2 = 50° for both leaky region. More precisely, the maximum of S_{11}-parameter presents two extrema for the left-leaky region : a minimum around χ_2 = 50° and a maximum around χ_2 = 60°. The minimum of S_{11}-parameter presents a maximum around χ_2 = 60° for the left-leaky region and increases with an increase of χ_2 for the right-leaky region. The antenna efficiency presents a maximum around χ_2 = 60° for both leaky regions. The maximal gain presents a maximum around χ_2 = 50° for the left-leaky region and decreases with an increase of χ_2 for the right-leaky region. The directivity presents a maximum around χ_2 = 40°



(a) LH region ***(b)*** RH region

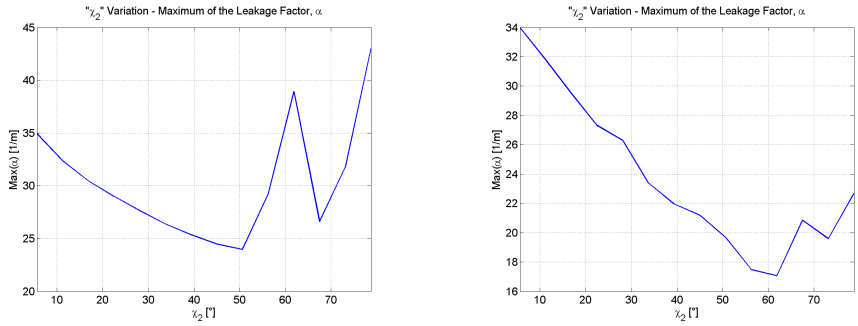
Figure D.65. *Influence of the opening angle χ_2 of the CSRR ring on the width of the leaky region defined as the difference between the lower and the upper frequency of the leaky region for both leaky regions (the antenna is based on 8 CSRRs, the others cell dimensions are fixed to the dimensions described in Fig. 4.60).*



(a) LH region ***(b)*** RH region

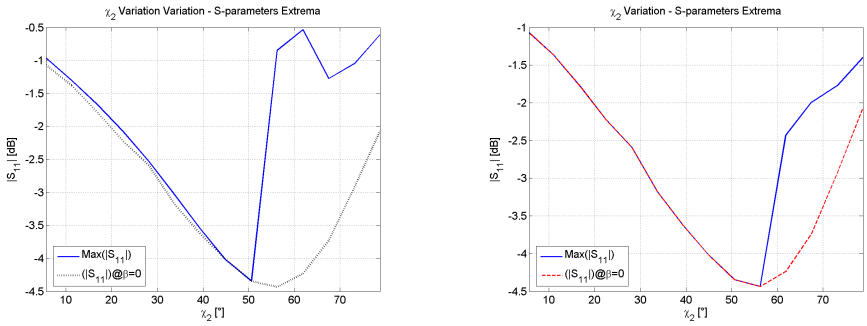
Figure D.66. *Influence of the opening angle χ_2 of the CSRR ring on the slope of the leaky region, defined in eq. 4.16 for both leaky regions (the antenna is based on 8 CSRRs, the others cell dimensions are fixed to the dimensions described in Fig. 4.60).*

for the left-leaky region and decreases with an increase of χ_2 for the right-leaky region.



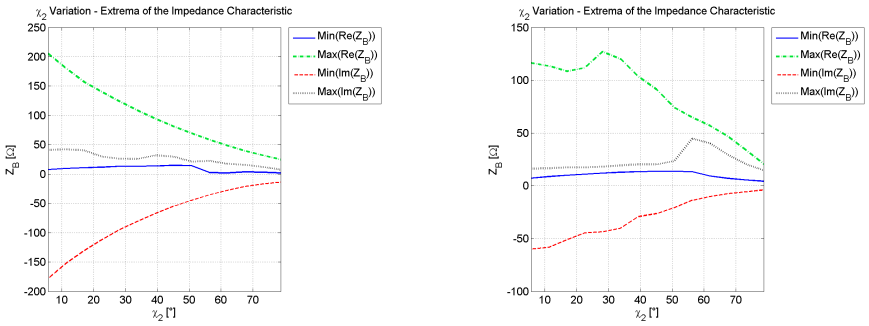
(a) LH region *(b)* RH region

Figure D.67. *Influence of the opening angle χ_2 of the CSRR ring on the maximum of the leakage factor defined as the maximum of leakage factor, α, for the leaky region (the antenna is based on 8 CSRRs, the others cell dimensions are fixed to the dimensions described in Fig. 4.60).*



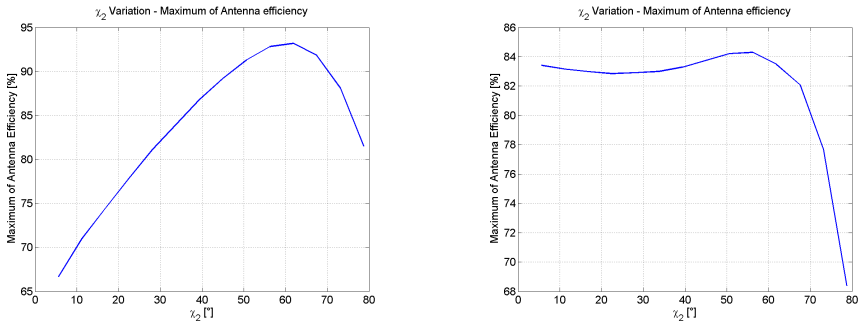
(a) LH region *(b)* RH region

Figure D.68. *Influence of the opening angle χ_2 of the CSRR ring on the extrema of the S_{11}-parameter defined as the maximum of the S_{11} magnitude for the leaky region, compared to S_{11}-parameter at the edges of the leaky region (the antenna is based on 8 CSRRs, the others cell dimensions are fixed to the dimensions described in Fig. 4.60).*



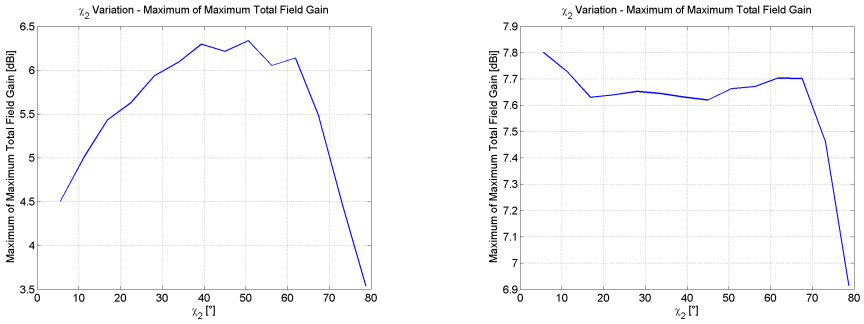
(a) LH region ***(b)*** RH region

Figure D.69. *Influence of the opening angle χ_2 of the CSRR ring on the extrema of the characteristics impedance Z_B defined as the maximum and the minimum the real and imaginary parts of the characteristic impedance Z_B for the leaky region defined in eq. 4.18 (the antenna is based on 8 CSRRs, the others cell dimensions are fixed to the dimensions described in Fig. 4.60).*



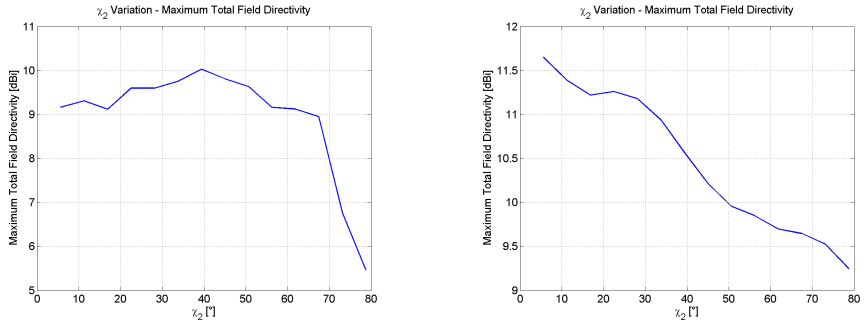
(a) LH region ***(b)*** RH region

Figure D.70. *Influence of the opening angle χ_2 of the CSRR ring on the maximum of the antenna efficiency defined as the maximum of antenna efficiency for the leaky region (the antenna is based on 8 CSRRs, the others cell dimensions are fixed to the dimensions described in Fig. 4.60).*



(a) LH region *(b)* RH region

Figure D.71. *Influence of the opening angle χ_2 of the CSRR ring on the maximum of the total field gain defined as the maximum of the maximum total field gain for the leaky region (the antenna is based on 8 CSRRs, the others cell dimensions are fixed to the dimensions described in Fig. 4.60).*



(a) LH region *(b)* RH region

Figure D.72. *Influence of the opening angle χ_2 of the CSRR ring on the maximum of the total field directivity defined as the maximum of the maximum total field directivity for the leaky region (the antenna is based on 8 CSRRs, the others cell dimensions are fixed to the dimensions described in Fig. 4.60).*

D.10 CONCLUSION

- **Width of the leaky region :** Globally, whatever the analysed parameters, the width of the leaky region is smaller in the LH bands than in the RH bands. For the LH band, the parameter that influences this width the most is R_{out} with less influence from the parameters are W and G. For the RH band, the parameter that influences this width the most is R_{out}, with less influence from the parameter, C. For the LH band, an increase of the width can be induced by an increase of C, W, χ_2 and W_{out} whereas a decrease of the width can be induced by an increase of R_{out}, e and χ_1. For the RH band, an increase of the width can be induced by an increase of C, W_{out}, G, χ_1 whereas a decrease of the width can be induced by an increase of R_{out}, e and W.

- **Slope of the leaky region :** The slope of the right leaky region is smaller than the slope in the left-leaky region. For the LH band, the parameter influencing the most this slope is χ_1, with a lesser influence from the parameter, C. For the RH band, the parameter influencing the most this slope is χ_2, with less influence from W_{out}. For the LH band, an increase of the global slope can be induced by an increase of R_{out}, e, G, χ_1 and χ_2, whereas a decrease of the width can be induced by an increase of W_{out}. For the RH band, an increase of the global slope can be induced by an increase of C, R_{out}, W, χ_2, whereas a decrease of the width can be induced by an increase of G, χ_1.

- **Maximum of the leakage factor :** The maximum of the leakage factor is in the same range for the LH and RH bands. For the LH band, the parameter influencing the most this maximum is W_{out} with less influence from the paramter, R_{out}. For the RH band, the parameter influencing the most this maximum is W, with less influence from the parameters: W_{out} and e. For both bands, an increase of the maximum of the leakage factor can be induced by an increase of R_{out}, G, χ_1 where a decrease of the width can be induced by an increase of W_{out}, e and W.

- **Maximum of the S_{11}-parameter :** Globally the circuit matching is influenced in the same way in the left-leaky region as in the right-leaky region. Analysis of table D.1 shows that the extrema of S_{11}-parameter is mostly influenced by χ_2 and W and weakly influenced by R_{out} and C for the left-leaky region. Analysis of table D.2 shows that the extrema of S_{11}-parameter is mostly influenced by χ_2 and weakly influenced by W_{out} and R_{out} for the right-leaky region. A decrease in the maximum of S_{11}-parameter is obtained with a decrease in G and χ_2 for the left leaky region. The parameters C and χ_2 influence the extrema of the maximum of S_{11}-parameter in this leaky region. For the right-leaky region, a decrease in the the maximum of S_{11}-parameter is obtained with an increase in C, W_{out}

and W and a decrease in G and e. The parameter χ_2 influence the extrema of the maximum of S_{11}-parameter in this leaky region.

- **Characteristic impedance, Z_B :** The left-leaky region induces a higher characteristic impedance, Z_B than the right leaky region. Analysis of table D.3 shows that the real part of Z_B is mostly influenced by χ_1 and weakly influenced by W and R_{out} for the left-leaky region. Analysis of table D.4 shows that the real part of Z_B is mostly influenced by C and weakly influenced by W_{out} and R_{out} for the right-leaky region. Tables D.5 and D.6 show that the parameter χ_1 is the parameter with the most influence on the imaginary part of Z_B for both leaky regions. These tables also show that the parameters, e and R_{out}, have a lesser influence on this figure of merit. A decrease in the interval of the impedance characteristic is obtained with an increase of C, W_{out}, e, W and χ_2 and a decrease of R_{out}, G and χ_1 for the left leaky region. For the right-leaky region, a decrease of the interval of the impedance characteristic is obtained with an increase of R_{out}, W_{out}, W and χ_2 and a decrease of C and G.

- **Antenna Efficiency :** Globally the maximal antenna efficiency AF in the left-leaky region is smaller than in the right-leaky region. Analysis of table D.7 shows that the maximal antenna efficiency AF is mostly influenced by χ_1 and weakly influenced by R_{out} for the left-leaky region. Analysis of table D.8 shows that the maximal antenna efficiency AF is mostly influenced by W and weakly influenced by W_{out} for the right-leaky region. An increase in the maximal antenna efficiency AF is obtained with an increase in C, W_{out} and a decrease in R_{out}, G and e for the left leaky region. The parameters W, χ_1 and χ_2 create extrema of the antenna efficiency AF in the left-leaky region. For the right-leaky region, an increase in the maximal antenna efficiency AF is obtained with an increase in C, G and a decrease of e, W and χ_2. The parameters R_{out}, W_{out} and χ_1 influence the extrema of the antenna efficiency AF in this leaky region.

- **Maximal Gain :** The maximal gain is higher in the right leaky region than in the left one. Analysis of table D.9 shows that the maximal gain is mostly influenced by χ_2 and weakly influenced by G for the left-leaky region. Analysis of table D.10 shows that the maximal gain is mostly influenced by W and weakly influenced by W_{out} for the right-leaky region. An increase in the maximal gain is obtained with an increase in W_{out} and a decrease in R_{out}, W and e for the left leaky region. The parameters C, G, χ_1 and χ_2 influence the extrema of the gain in the left-leaky region. For the right-leaky region, an increase in the maximal gain is obtained with an increase in e and a decrease of R_{out}, W_{out}, W and χ_2. The parameters C, G and χ_1 influence the extrema of the maximal gain in this leaky region.

- **Maximal Directivity :** The maximal directivity is higher in the right leaky region than in the left one. Analysis of table D.11 shows that the

Left-Leaky Region						
	Max(S_{11}) [dB] vs frequency			**Min(S_{11}) [dB] vs frequency**		
	Min	Max	Δ	Min	Max	Δ
C	-1,83	-0,73	1,11	-18,62	-13,07	5,55
R_{out}	-0,94	-0,86	0,08	-18,69	-8,37	10,32
W_{out}	-1,45	-0,61	0,84	-22,64	-15,08	7,56
e	-0,91	-0,79	0,12	-26,68	-12,74	13,94
W	-2,01	-0,38	1,63	-38,87	-5,54	33,33
G	-1,92	-0,36	1,57	-19,48	-7,11	12,36
χ_1	-1,45	-0,40	1,05	-23,88	-3,10	20,78
χ_2	-4,35	-0,53	3,81	-29,36	-9,26	20,10

Table D.1. *Comparison of the S_{11} extrema for the left-leaky region (the red and blue color are used to indicate respectively the maximum and minimum value in each column).*

maximal directivity is mostly influenced by χ_2 and weakly influenced by W_{out} for the left-leaky region. Analysis of table D.12 shows that the maximal directivity is mostly influenced by e and weakly influenced by W_{out} for the right-leaky region. An increase in the maximal directivity is obtained with an increase in e, W_{out} and W and a decrease in R_{out} and G for the left leaky region. The parameters C, χ_1 and χ_2 influence the extrema of the directivity in the left-leaky region. For the right-leaky region, an increase in the maximal directivity is obtained with an increase in e and a decrease in R_{out}, W_{out}, W and χ_2. The parameters C, G and χ_1 influence the extrema of the maximal directivity in this leaky region.

Right-Leaky Region						
	Max(S_{11}) [dB]			**Min(S_{11}) [dB]**		
	Min	Max	Δ	Min	Max	Δ
C	-3,04	-0,49	2,55	-46,75	-24,72	22,03
R_{out}	-1,17	-0,90	0,27	-40,60	-32,78	7,82
W_{out}	-1,46	-0,51	0,95	-35,72	-31,15	4,57
e	-1,41	-0,78	0,63	-43,04	-34,66	8,38
W	-1,87	-0,37	1,50	-41,66	-25,44	16,23
G	-1,97	-0,34	1,62	-41,38	-23,17	18,21
χ_1	-1,33	-0,19	1,15	-51,08	-10,74	40,34
χ_2	-4,44	-1,07	3,37	-54,31	-8,50	45,81

Table D.2. *Comparison of the S_{11} extrema for the right-leaky region (the red and blue color are used to indicate respectively the maximum and minimum value in each column).*

Left-Leaky Region						
	Max(Re(Z_B)) [Ω]			**Min(Re(Z_B)) [Ω]**		
	Min	Max	Δ	Min	Max	Δ
C	140,43	218,94	78,51	5,59	17,51	11,93
R_{out}	173,73	234,93	61,20	6,54	16,84	10,30
W_{out}	146,87	254,25	107,39	6,91	14,54	7,63
e	155,76	228,49	72,73	5,29	11,00	5,71
W	83,98	359,67	275,68	6,26	8,91	2,65
G	139,55	289,79	150,25	5,03	11,88	6,85
χ_1	18,50	538,73	520,23	2,98	42,50	39,52
χ_2	24,51	205,68	181,18	1,69	14,68	12,99

Table D.3. *Comparison of the $Re(Z_B)$ extrema for the left-leaky region (the red and blue color are used to indicate respectively the maximum and minimum value in each column).*

Right-Leaky Region						
	Max(Re(Z_B)) [Ω]			**Min(Re(Z_B))** [Ω]		
	Min	Max	Δ	Min	Max	Δ
C	82,15	251,86	169,70	3,19	14,99	11,79
R_{out}	99,20	141,05	41,85	5,71	6,94	1,23
W_{out}	103,27	111,19	7,92	3,77	7,81	4,04
e	94,25	133,22	38,97	4,13	8,59	4,46
W	66,74	159,75	93,01	5,45	6,77	1,32
G	105,09	198,37	93,28	3,41	10,31	6,90
χ_1	55,66	214,70	159,04	0,76	11,18	10,42
χ_2	20,71	127,03	106,32	4,23	13,74	9,51

Table D.4. *Comparison of the Re(Z_B) extrema for the right-leaky region (the red and blue color are used to indicate respectively the maximum and minimum value in each column).*

Left-Leaky Region						
	Max(Im(Z_B)) [Ω]			**Min(Im(Z_B))** [Ω]		
	Min	Max	Δ	Min	Max	Δ
C	22,61	47,08	24,47	-196,83	-120,45	76,38
R_{out}	22,67	77,32	54,65	-200,37	-156,48	43,88
W_{out}	20,28	52,68	32,40	-235,34	-122,58	112,76
e	14,26	44,15	29,89	-184,94	-142,15	42,79
W	11,27	63,16	51,89	-297,81	72,74	370,55
G	25,41	88,68	63,26	-249,09	-115,90	133,19
χ_1	-62,06	319,83	381,90	-327,21	74,20	401,41
χ_2	7,58	42,19	34,61	-178,56	-13,78	164,78

Table D.5. *Comparison of the Im(Z_B) extrema for the left-leaky region (the red and blue color are used to indicate respectively the maximum and minimum value in each column).*

Right-Leaky Region						
	Max(Im(Z_B)) [Ω]			**Min(Im(Z_B))** [Ω]		
	Min	Max	Δ	Min	Max	Δ
C	9,85	28,31	18,46	-159,02	-58,83	100,18
R_{out}	14,73	16,42	1,70	-63,06	-51,12	11,94
W_{out}	13,84	17,86	4,02	-63,19	-51,79	11,40
e	10,44	16,14	5,69	-62,70	-52,59	10,11
W	9,67	19,78	10,11	-127,56	-32,90	94,66
G	13,58	16,87	3,29	-155,55	-52,85	102,69
χ_1	-8,46	121,88	130,34	-132,22	-27,22	105,00
χ_2	14,62	44,49	29,87	-60,05	-3,99	56,06

Table D.6. *Comparison of the $Im(Z_B)$ extrema for the right-leaky region (the red and blue color are used to indicate respectively the maximum and minimum value in each column).*

Left-Leaky Region			
	Max(Ant.Eff.) [%]		
	Min	Max	Δ
C	62,38	75,79	13,41
R_{out}	59,01	69,59	10,58
W_{out}	62,23	81,12	18,88
e	69,36	88,35	18,99
W	54,71	75,88	21,17
G	54,64	72,29	17,65
χ_1	36,69	75,23	38,54
χ_2	66,66	93,20	26,54

Table D.7. *Comparison of the antenna efficiency AF extrema for the left-leaky region (the red and blue color are used to indicate respectively the maximum and minimum value in each column).*

Right-Leaky Region			
	Max(Ant.Eff.) [%]		
	Max	Min	Δ
C	79,73	90,50	10,78
R_{out}	80,61	83,00	2,39
W_{out}	81,80	82,71	0,91
e	73,77	92,83	19,06
W	66,49	90,56	24,07
G	73,21	89,64	16,43
χ_1	69,25	83,31	14,06
χ_2	68,39	84,30	15,90

Table D.8. *Comparison of the antenna efficiency AF extrema for the right-leaky region (the red and blue color are used to indicate respectively the maximum and minimum value in each column).*

Left-Leaky Region			
	Max(Gain) [dBi]		
	Max	Min	Δ
C	5,36	7,83	2,47
R_{out}	3,72	5,86	2,15
W_{out}	3,72	5,86	2,15
e	4,76	6,04	1,28
W	3,29	5,54	2,25
G	4,57	5,15	0,57
χ_1	4,86	6,62	1,76
χ_2	3,54	6,34	2,80

Table D.9. *Comparison of the gain extrema for the left-leaky region (the red and blue color are used to indicate respectively the maximum and minimum value in each column).*

Right-Leaky Region			
	Max(Gain) [dBi]		
	Max	Min	Δ
C	7,84	9,40	1,56
R_{out}	6,83	8,87	2,04
W_{out}	7,89	8,12	0,23
e	7,63	8,55	0,92
W	6,44	8,86	2,42
G	6,97	9,10	2,13
χ_1	7,17	7,77	0,60
χ_2	6,91	7,80	0,89

Table D.10. *Comparison of the gain extrema for the right-leaky region (the red and blue color are used to indicate respectively the maximum and minimum value in each column).*

Left-Leaky Region			
	Max(Directivity) [dBi]		
	Max	Min	Δ
C	8,85	9,99	1,14
R_{out}	8,53	9,80	1,27
W_{out}	8,90	9,55	0,64
e	8,54	10,08	1,53
W	7,83	10,21	2,38
G	8,68	9,38	0,69
χ_1	9,29	10,45	1,16
χ_2	5,46	10,02	4,56

Table D.11. *Comparison of the directivity extrema for the left-leaky region (the red and blue color are used to indicate respectively the maximum and minimum value in each column).*

Right-Leaky Region			
	Max(Directivity) [dBi]		
	Max	Min	Δ
C	10,38	12,43	2,05
R_{out}	11,13	12,55	1,42
W_{out}	11,50	12,03	0,52
e	10,55	13,02	2,46
W	11,38	12,39	1,01
G	11,68	12,28	0,60
χ_1	9,84	11,41	1,58
χ_2	9,25	11,65	2,41

Table D.12. *Comparison of the directivity extrema for the right-leaky region (the red and blue color are used to indicate respectively the maximum and minimum value in each column).*

APPENDIX E

OTHER CANDIDATES OF RESONANT PLANAR LWA

This annex presents the analysis of the radiation characteristics realised on other resonant planar LWA. For all theses simulations, the cell dimensions and substrate properties are similar to those of the CSRR structure of Fig. 4.1.

E.1 INTRODUCTION

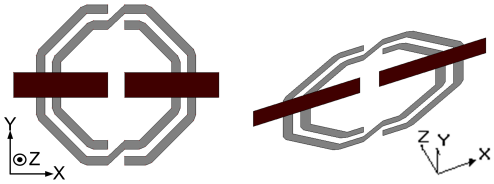
This section is focused on an exhaustive list of other resonant type topologies than the CSRR cell, as called in the chapter 6. From the state of the art, various resonant structures similar to CSRR cell are chosen as candidates to be used for a one-dimensional LWA. Their dimensions are designed for operation in the same frequency band as the CSRR structure of Chapter6 (Fig. 4.1) and using the same substrate specifications. For all theses simulations, the cell dimensions and substrate properties are similar to those of the CSRR structure of Fig. 4.1. For a reason of thesis conciseness, the diverse dimensions are not detailed.

E.2 NONBIANISOTROPIC SPIRAL RESONATOR

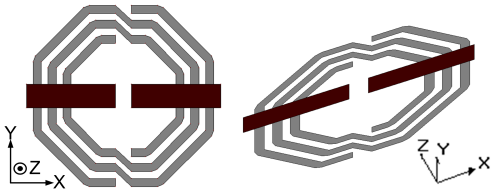
The first structure is the nonbianisotropic spiral resonator [1], illustrated in Fig. E.1 for different numbers of turns. The radiation behaviour is similar to the unbalanced CSRR cell with two rings. Fig. E.1(d) shows the influence of the number of turns. The antenna efficiency AF decreases when the number of turns increases and this behaviour is probably linked with the higher coupling between the slot. The first structure is the nonbianisotropic spiral resonator [1], illustrated in Fig. E.1 for different numbers of turns. The radiation behaviour

is similar to the unbalanced CSRR cell with two rings. Fig. E.1(d) shows the influence of the number of turns. The antenna efficiency AF decreases when the number of turns increases and this behaviour is probably linked with the higher coupling between the slot.

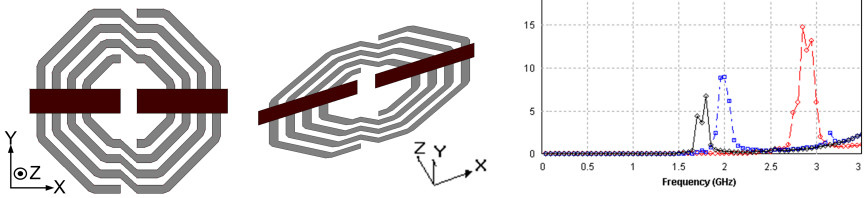
A transmission line is created from a cascade of nonbianisotropic spiral resonators presented in Fig. E.1. Fig. E.2(a) and Fig. E.2(b) illustrate the simulated S parameters for the left-hand band of this LWA for different number of turns. The propagation characteristic, extracted from the S-parameters, is shown in Fig. E.3. The left leaky region should exist between 2.75 GHz and 3.05 GHz for two turns, between 1.95 GHz and 2.1 GHz for three turns, between 1.75 GHz and 1.85 GHz for four turns. Radiations patterns are shown in Fig. E.4 for two turns, in Fig. E.5 for three turns, in Fig. E.6 for four turns. At the upper frequency of the left leaky region, the radiation behaviour is similar to the LWA based on CSRR presented in Fig. 4.1, the radiation seems be equally splitted into two different directions resulting in two apparent beams in the plane of the substrate: one beam steering from $\phi = 180°$ to $\phi = 90°$ and the other steering from $\phi = 180°$ to $\phi = 90°$.



(a) 2 turns

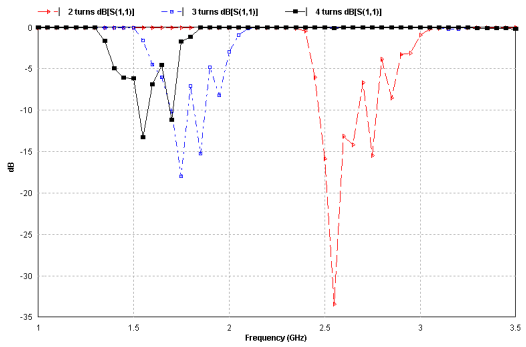


(b) 3 turns

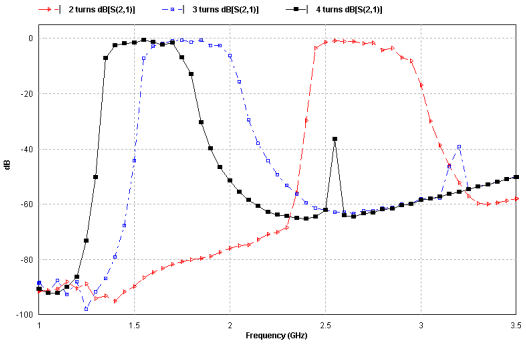


(c) 4 turns ***(d)*** Antenna Efficiency *AF*

Figure E.1. *Nonbianisotropic spiral resonator, inspired by [1] - Topology of one cell (a) for two turns, (b) three turns and (c) four turns - (d) Antenna efficiency AF of TL loaded by 8 nonbianisotropic spiral resonators of an LWA extracted from simulation with IE3D assuming an infinite substrate for cell with two turns (red dashed), with three turns (blue dashdot) and with four turns (black solid).*

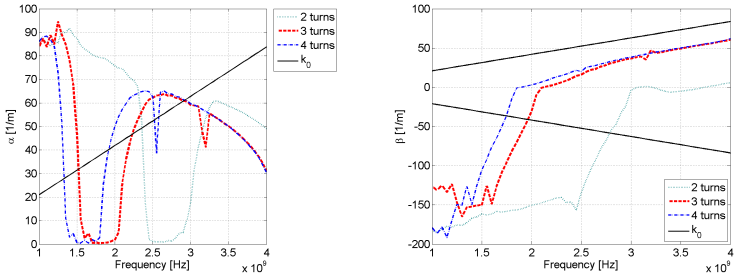


(a) S_{11} parameter



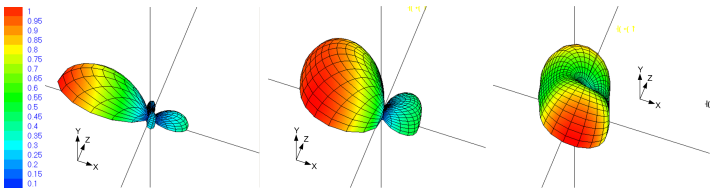
(b) S_{21} parameter

Figure E.2. *Comparison of S-parameters extracted from IE3D simulation assuming an infinite substrate for the left-hand band between a cascade of TL loaded by 8 nonbianisotropic spiral resonators of an LWA, presented in Fig. E.1 extracted from simulation with IE3D assuming an infinite substrate for cell with two turns (red dashed), with three turns (blue dashdot) and with four turns (black solid).*



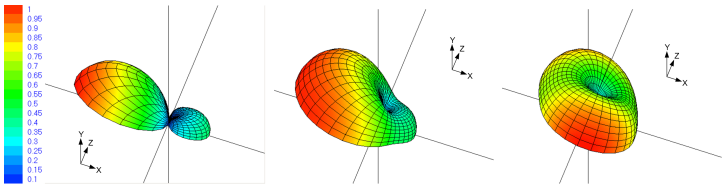
(a) Leakage factor α ***(b)*** Propagation constant β

Figure E.3. *Comparison of the propagation characteristics extracted from IE3D simulation assuming an infinite substrate for the left-hand band between a cascade of TL loaded by 8 nonbianisotropic spiral resonators of an LWA, presented in Fig. E.1 extracted from simulation with IE3D assuming an infinite substrate for cell with 2, 3 and 4 turns.*



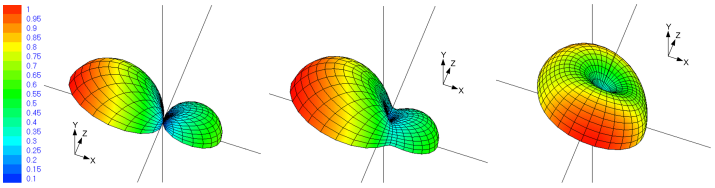
(a) 2.75 GHz ***(b)*** 2.9 GHz ***(c)*** 3.05 GHz

Figure E.4. *Normalized 3D radiation pattern for the cascade of TL loaded by 8 nonbianisotropic spiral resonators of an LWA* WITH TWO TURNS *illustrated in Fig. E.1(a) simulated with IE3D software assuming an infinite substrate at 3 frequencies in the left-leaky region. Color bar: blue corresponds to zero, red corresponds to 1 : (a) 2.75 GHz, (b) 2.9 GHz, (c) 3.05 GHz.*



(a) 1.95 GHz ***(b)*** 2 GHz ***(c)*** 2.1 GHz

Figure E.5. *Normalized 3D radiation pattern for the cascade of TL loaded by 8 nonbianisotropic spiral resonators of an LWA* WITH THREE TURNS *illustrated in Fig. E.1(b) simulated with IE3D software assuming an infinite substrate at 3 frequencies in the left-leaky region. Color bar: blue corresponds to zero, red corresponds to 1 : (a) 1.95 GHz, (b) 2 GHz, (c) 2.1 GHz.*



(a) 1.7 GHz ***(b)*** 1.75 GHz ***(c)*** 1.85 GHz

Figure E.6. *Normalized 3D radiation pattern for the cascade of TL loaded by 8 nonbianisotropic spiral resonators of an LWA* WITH FOUR TURNS *illustrated in Fig. E.1(c) simulated with IE3D software assuming an infinite substrate at 3 frequencies in the left-leaky region. Color bar: blue corresponds to zero, red corresponds to 1 : (a) 1.7 GHz, (b) 1.75 GHz, (c) 1.85 GHz.*

E.3 OPEN SPLIT RING RESONATORS (OSRRS)

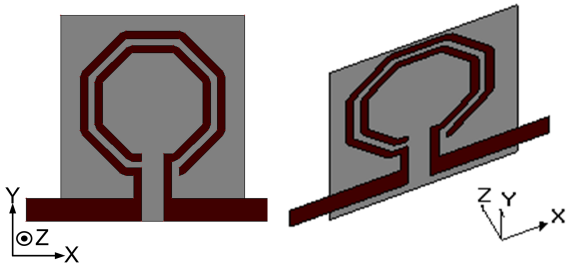


Figure E.7. *Topology of open split ring resonators (OSRRs), inspired by [2].*

The second structure, which may be viewed as a grouping of similar structures, is depicted in Fig. E.7 and presented in [2]. These structures go under the name of open split ring resonators (OSRRs). The analysis realised on this structure presents a poor antenna efficiency AF (under 5%), this kind of structure does not seem to be a good candidate for a leaky wave antenna.

A transmission line is created from a cascade of 8 OSRR cells presented in Fig. E.7. Fig. E.9(a) illustrates the simulated S parameters for the left-hand band of this LWA. The propagation characteristic, extracted from the S-parameters, is shown in Fig. E.9(b). The left leaky region should exist between 2.74 GHz and 3.14 GHz, but the antenna efficiency, presented in Fig. E.9(c), is really low at this bandwidth. Indeed the current distribution, shown in Fig. E.8, does not present the current distribution of a leaky wave antenna.

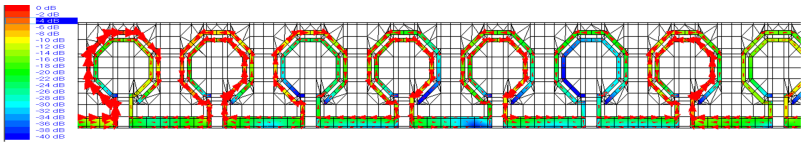
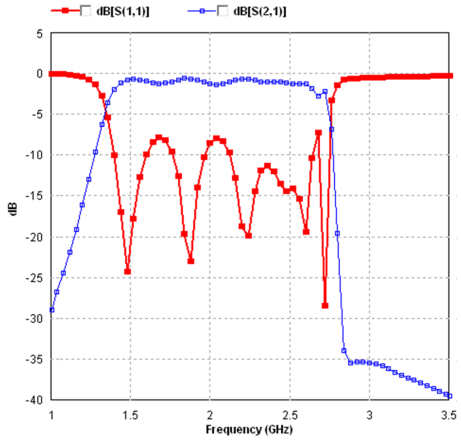


Figure E.8. *Zoom of distribution of current density and current vectors on metallic strip joining adjacent cells for the LWA of Fig. E.7, simulated with IE3D assuming an infinite substrate at 3.05 GHz, which is the middle frequency of the left-leaky region (Fig. E.9(b)). Color bar: current density is normalised with the maximum of the current on the upper metal level (maximal current density : 39.066 A/m) and is expressed in dB, blue color corresponds to lowest current density; red color corresponds to highest current density.*

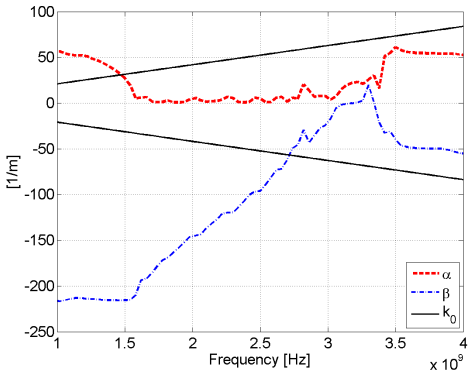
E.4 OPEN COMPLEMENTARY SPLIT RING RESONATORS (OCSRRS)

The next structure, which may be viewed as a grouping of similar structures, is depicted in Fig. E.10 and presented in [2]. These structures go under the name of open complementary split ring resonators (OCSRRs), the dual of the previous structure. The analysis realised on this structure presents a poor antenna efficiency AF (under 5%), this kind of structure does not seem to be a good candidate for a leaky wave antenna.

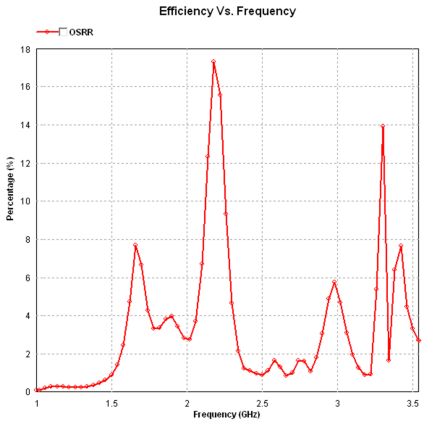
A CPW loaded by OCSRRs is created from a cascade of 8 OCSRRs cells presented in Fig. E.10. Fig. E.12(a) illustrates the simulated S parameters for the left-hand band of this LWA. The propagation characteristic, extracted from the S-parameters, is shown in Fig. E.12(b). The left leaky region should exist between 2.75 GHz and 3.35 GHz, but the antenna efficiency, presented in Fig. E.12(c), is really low at this bandwidth. Globally the structure has the same behaviour than the previous one (Fig. E.11).



(a) S parameters



(b) Propagation Characteristics



(c) Antenna efficiency

Figure E.9. *(a) S-parameters, (b) Propagation Characteristcs and (c) Antenna efficiency of a cascade of 8 OSRR cells, illustrated in Fig. E.7 simulated with IE3D assuming an infinite substrate for the left-hand band.*

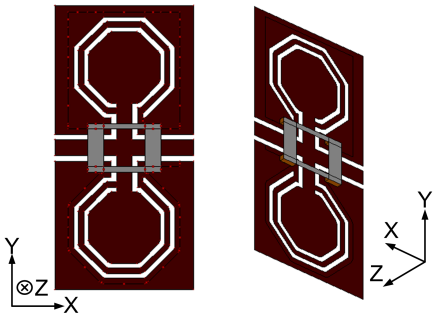


Figure E.10. *Topology of CPW loaded with a pair of open complementary split ring resonators (OCSRRs), inspired by [2].*

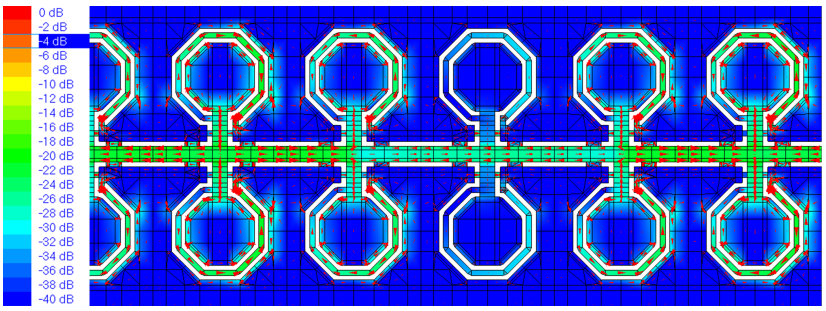
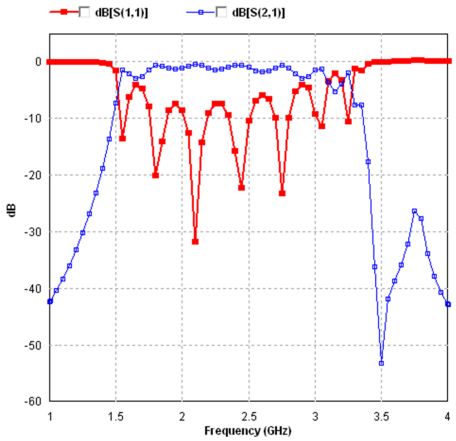
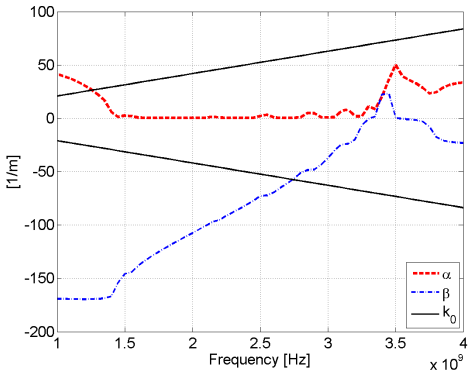


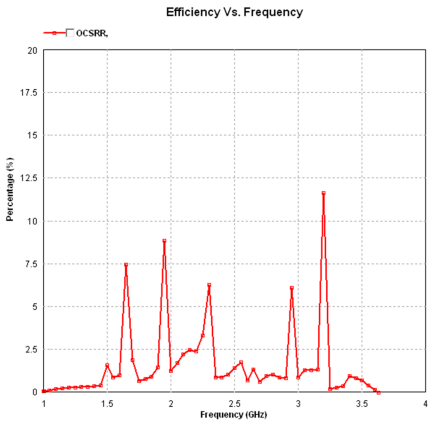
Figure E.11. *Zoom of distribution of current density and current vectors on metallic strip joining adjacent cells for the LWA of Fig. E.10, simulated with IE3D assuming an infinite substrate at 3.2 GHz, which is the middle frequency of the left-leaky region (Fig. E.12(b)). Color bar: current density is normalised with the maximum of the current on the upper metal level (maximal current density : 39.066 A/m) and is expressed in dB, blue color corresponds to lowest current density; red color corresponds to highest current density.*



(a) S parameters



(b) Propagation Characteristics



(c) Antenna efficiency

Figure E.12. *(a) S-parameters, (b) Propagation Characteristcs and (c) Antenna efficiency of a cascade of 8 OSRR cells, illustrated in Fig. E.10 simulated with IE3D assuming an infinite substrate for the left-hand band.*

E.5 BALANCED DOUBLE-SPLIT CSRR

This structure concerns the double-split CSRR, inspired by [1], illustrated in Fig. E.13(a). This structure is balanced, i.e. the stop-band between the left and the right regions is suppressed, with as its result that the spatial lobe scanning from backward to forward quadrants is continuous with frequency. It also presents a higher antenna efficiency AF (around 40% in the left leaky region) as well as a continuous full-space scanning. The propagation characteristics, shown in Fig. E.13(b), exhibit a continuous transition between left and right leaky bands. The radiation pattern, illustrated in Fig. E.15 for three frequencies of interest in the leaky region, is maximal in the broadside direction at 5.62 GHz as predicted by the theory for the lowest frequency of the right-leaky region. This structure is therefore a good candidate to be used for a LWA.

A transmission line is created from a cascade of 8 Double-split CSRR presented in Fig. E.13(a). Fig. E.14(a) and Fig. E.14(b) illustrate the S parameters simulated with IE3D assuming an infinite substrate for the left-hand band of this balanced LWA.

The antenna efficiency, presented in Fig. E.14(c) and is higher than the same LWA created with CSRR presented in the Fig. 4.1.

E.6 DOUBLE-LAYERS COMPLEMENTARY SPLIT RING RESONATOR

This next structure is inspired by the broadside-coupled SRR presented in [3]. A transmission line is loaded by 2 CSRRs juxtaposed in opposite directions as illustrated in Fig. E.16(a). The first CSRR is covered by a dielectric layer. On the ground plane of this second layer, the second CSRR is etched. The left leaky region is shifted higher in frequency and the antenna efficiency AF, shown in Fig. E.16(b), is similar to the one-layer case presented in 4.2.2. However the radiation at the upper frequency of the left leaky region presented a maximum along the Y axis as illustrated in Fig. E.18.

A transmission line is loaded by 2 CSRRs juxtaposed in opposite directions as illustrated in Fig. E.16(a). S parameter of this structure is shown in Fig. E.17. From this simulation, the propagation characteristics is extracted in Fig. E.17(b). The analysis of the propagation factor β predicts a left leaky region between 3.59 GHz and 4.2 GHz.

E.7 CASCADE OF NON-UNIFORM CSRR CELL

The concept behind this type of structure is to realise an omnidirectional antenna in the plane of the substrate in a large bandwidth. The TL is realised with a microstrip loaded with the same CSRRs that are presented in Fig. 4.1. Its radiation pattern must also suppress the broadside radiation over the whole left-handed region. But the size of the external ring is increased along the TL. The growing step is chosen by iteration so that the matching of the first cell

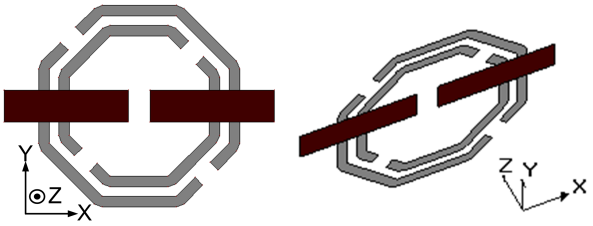
was enough at the resonance frequency of the last cell (Fig. E.19(b)), each cell presents a different theoretical direction angle of the main beam, so the structure becomes an omnidirectional antenna. **This structure could not be called a leaky wave antenna because it does not present the phenomenon of beam scanning with an increase of frequency, even if the radiation is created by leaky waves.** Furthermore the main drawback of this structure is slight increase in S_{11} in the left-leaky region. However the antenna presents a good antenna efficiency AF despite this poor matching (Fig. E.21(a)) and an omnidirectional radiation in the plane of the substrate (Fig. E.21(b)).

The TL is realised with a microstrip loaded with the same CSRRs than presented in Fig. 4.1, but the size of the external ring is increased along the TL. The topology presented in Fig. E.19(a). The propagation characteristics could be extracted from the S-parameters of Fig. E.19(b) and E.19(c). The analysis of Fig. E.20 shows that the structure could be radiate between 2.88 and 3.14 GHz, this corresponds to the maximum of the antenna efficiency of Fig. E.21(a). But the antenna doesn't have the LWA behaviour, i.e. a beam scanning with a frequency variation (Fig. E.22).

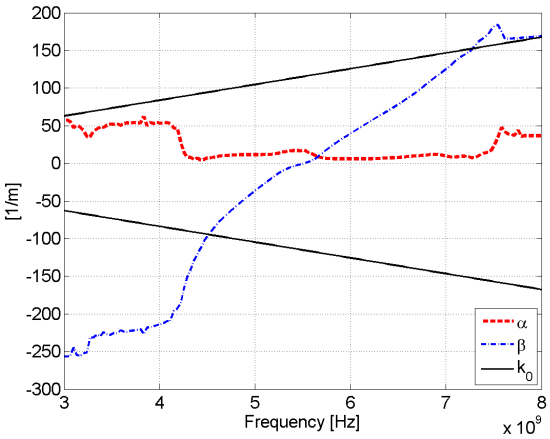
E.8 CSRR WITH TWO GAPS

A transmission line is created from a cascade of 8 CSRR cells with two gaps presented in Fig. E.23(a). The periodic leaky wave radiation a the periodic interface between free space and metallic layer, so the objective is to introduce more gaps in the metal layers and compare the antenna efficiency. Fig. E.24 illustrates the comparison between simulation and experimental results for the left-hand band of the LWA created from a CRLH TL based on CSRRs. The left-hand region decreases because of the introduction of this gap, this is explained by the LC model of the CSRR. The lower frequency of the left-hand region is fixed by the serie capacitance, and yet the serie capacitance of Fig. E.23(a) is taken in place by the serie of two gaps, so this capacitance is smaller than those in Fig. 4.1. The propagation characteristics, extracted from the IE3D simulation, are presented in Fig. E.25. The left-leaky region should be between 3.05 GHz and 3.275GHz. But the antenna efficiency is not affected by the add of this gap, (Fig. E.23(b)).

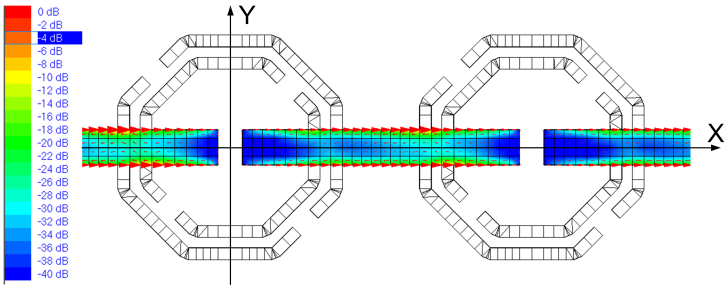
It is interesting to note that the position of this gap could be created a bad interference between the CSRR and the microstrip. Fig. E.26(a) presents the same structure of Fig. E.23(a) except that the two gaps are placed just above the ring. Fig. E.26(b) and Fig. E.26(c) show that in this case the structure doesn't present a left-hand region.



(a) Topology

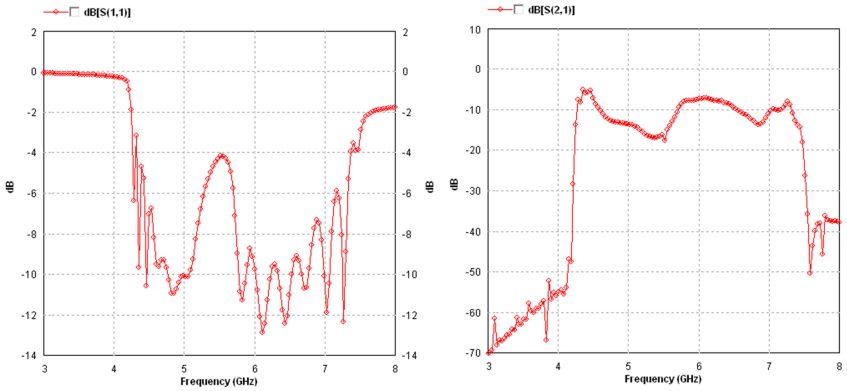


(b) Propagation Characteristic

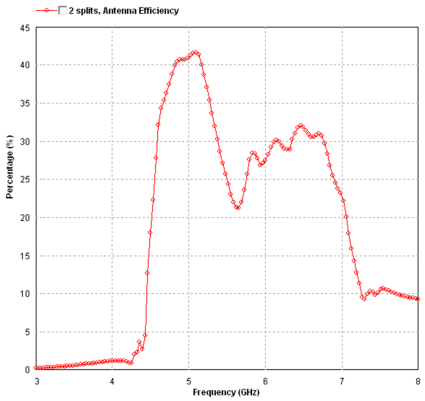


(c) Distribution of current at 5.62 GHz

Figure E.13. *a) Topology of Balanced Double-split CSRR, inspired by [1], (b) Propagation characteristics of the TL loaded by 8 CSRRs depicted in Fig. E.13(a), (c) Zoom of distribution of current density and current vectors on metallic strip joining adjacent cells, simulated with IE3D assuming an infinite substrate at 5.62 GHz, which is the upper frequency of the left-leaky region (Fig. E.13(a)). Color bar: current density is normalised with the maximum of the current on the upper metal level (maximal current density : 223.3 A/m) and is expressed in dB, blue color corresponds to lowest current density; red color corresponds to highest current density. All current vectors are oriented in the same direction along x-axis.*



(a) S_{11} parameter ***(b)*** S_{21} parameter



(c) Antenna efficiency

Figure E.14. *(a), (b) S-parameters and (c) Antenna efficiency of a cascade of 8 Double-split CSRR, illustrated in Fig. E.13(a) simulated with IE3D assuming an infinite substrate for the left-hand band.*

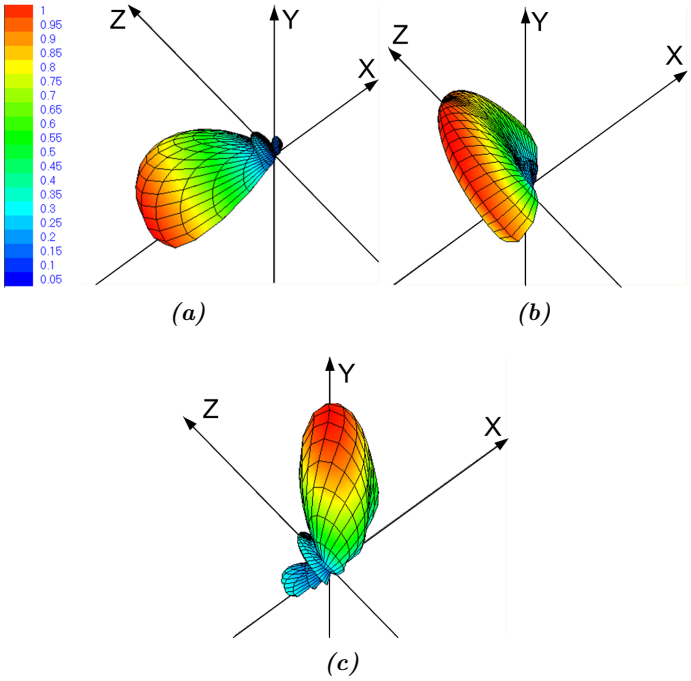
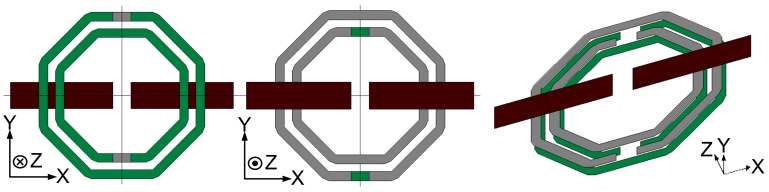
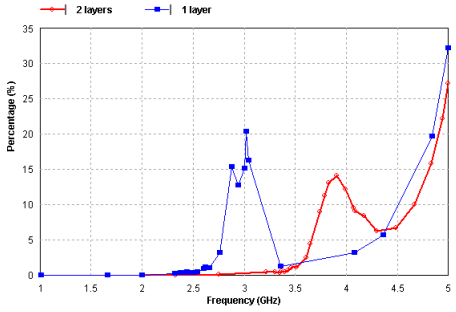


Figure E.15. *Normalized 3D radiation pattern for the TL based on 8 cells of Fig. E.13(a)(a) simulated with IE3D software assuming an infinite substrate at 3 frequencies in the left-leaky region. Color bar: blue corresponds to zero, red corresponds to 1 : (a) 4.64 GHz, (b) 5.62 GHz, (c) 6.425 GHz.*

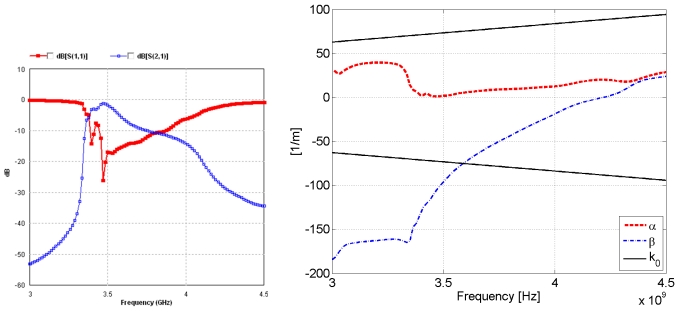


(a) Topology



(b) Antenna Efficiency *AF*

Figure E.16. *(a) Topology of double-layer complementary split ring resonator, inspired by [3] ; (b) Comparison of antenna efficiency AF extracted from simulation with IE3D assuming an infinite substrate between a cascade of 8 cells based on CSRR of Fig. 4.1 (in blue, called, "1 layer") and a cascade of 8 cells based on broadside-coupled double CSRR of Fig. E.16(a) with the same dimensions and substrate characteristics (in red, called, "2 layers").*



(a) *S* parameters ***(b)*** Propagation Characteristics

Figure E.17. *(a) S-parameters and (b) Propagation characteristics of a cascade of 8 double-layers CSRR, illustrated in Fig. E.16(a) simulated with IE3D assuming an infinite substrate for the left-hand band.*

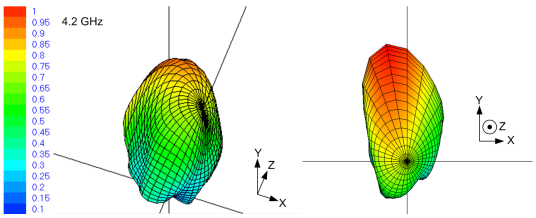
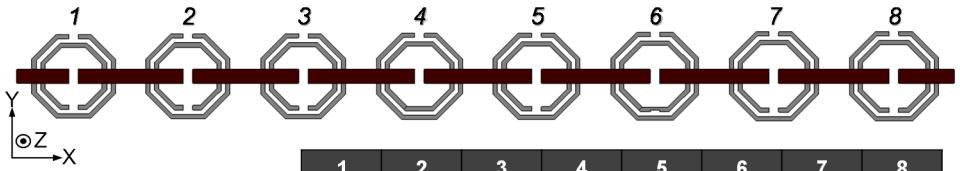
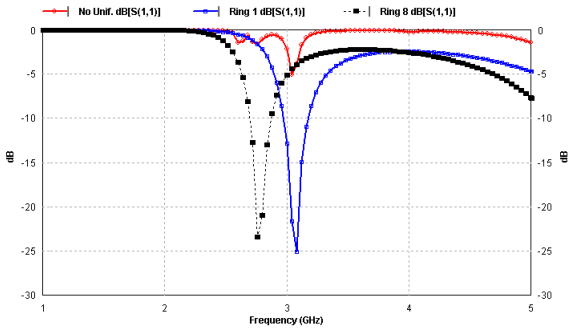


Figure E.18. *Normalized 3D radiation pattern for the cascade of double-layer complementary split ring resonator illustrated in Fig. E.16(a) simulated with IE3D software assuming an infinite substrate at the upper frequency of the left-leaky region, i.e. 3 GHz. Color bar: blue corresponds to zero, red corresponds to 1.*

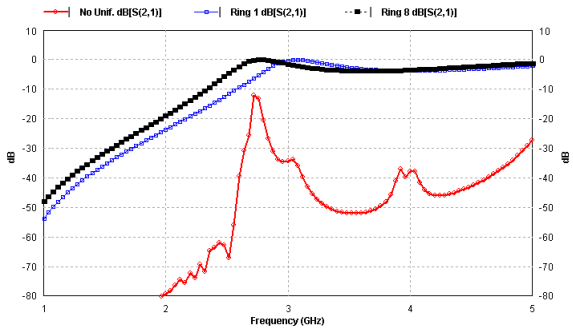


1	2	3	4	5	6	7	8
R_{out}*0.96	R_{out}*0.97	R_{out}*0.98	R_{out}*0.99	R_{out}	R_{out}*1.01	R_{out}*1.02	R_{out}*1.03

(a) Topology



(b) S_{11}-parameter



(c) S_{21}-parameter

Figure E.19. *Cascade of non-uniform CSRR cell (the external ring increases following the table in the view of the topology : (a) Topology, (b) and (c) S parameters extracted from simulation with IE3D assuming an infinite substrate (red solid with circles : simulation of TL illustrated in (a), blue solid with squares : simulation of the first cell only, black dash with full squares : simulation of the last cell only).*

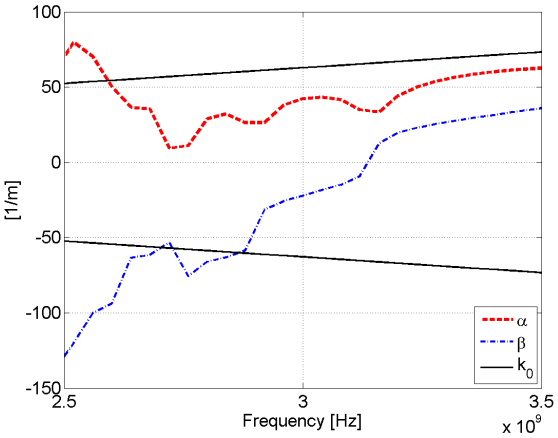
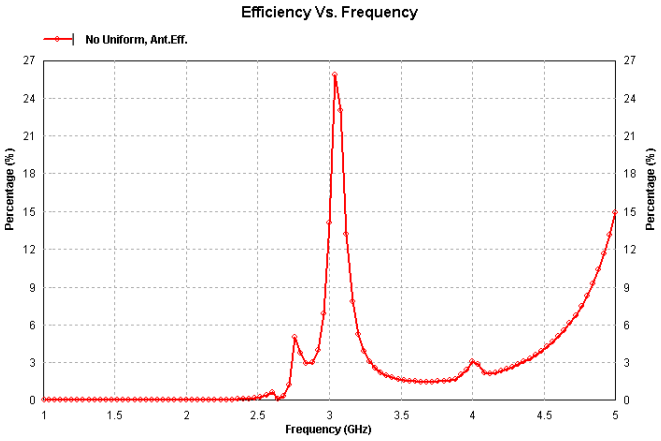
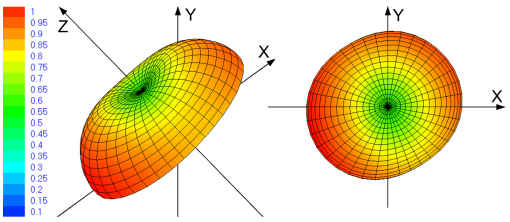


Figure E.20. *Propagation characteristics of the cascade of non-uniform CSRR cell, illustrated in Fig. E.16(a) and simulated with IE3D assuming an infinite substrate for the left-hand band.*

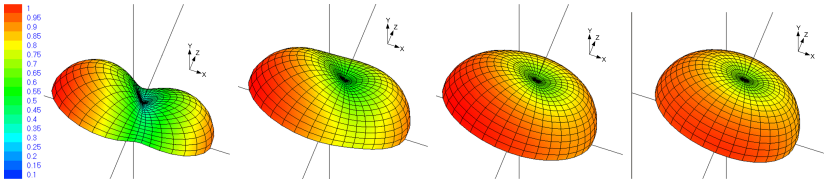


(a) Antenna Efficiency *AF*



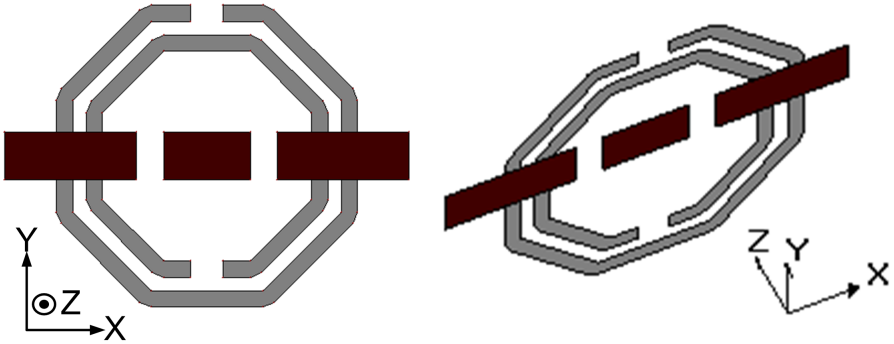
(b) Radiation Pattern at 3 GHz

Figure E.21. *(a) Antenna efficiency AF of the cascade of 8 non-uniform CSRR cells, illustrated in Fig. E.19(a) simulated with IE3D assuming an infinite substrate for the left-hand band. (b) Normalized 3D radiation pattern for the cascade of 8 non-uniform CSRR cells, illustrated in Fig. E.19(a) simulated with IE3D assuming an infinite substrate at 3 GHz. The antenna efficiency AF in the left-leaky region is maximal for this frequency. Color bar: blue corresponds to zero, red corresponds to 1.*

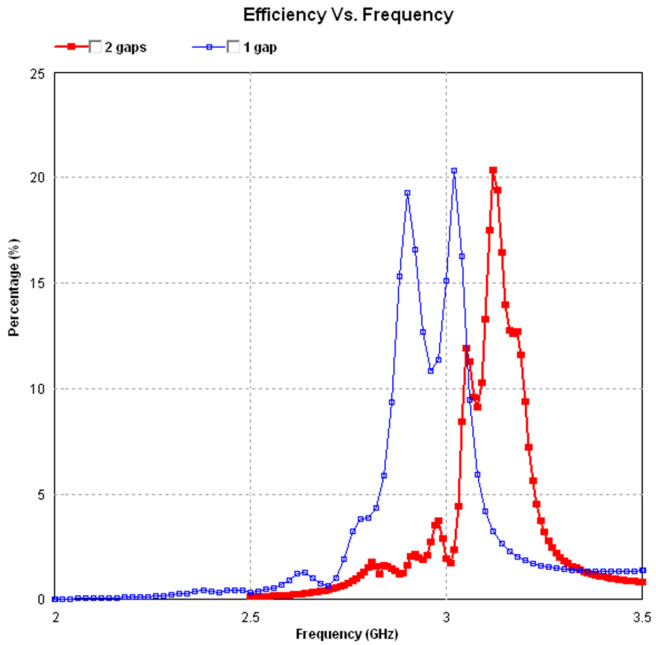


(a) 2.88 GHz ***(b)*** 2.96 GHz ***(c)*** 3.04 GHz ***(d)*** 3.12 GHz

Figure E.22. *Normalized 3D radiation pattern for the cascade of non-uniform CSRR cell, illustrated in Fig. E.16(a) simulated with IE3D software assuming an infinite substrate at 4 frequencies in the left-leaky region. Color bar: blue corresponds to zero, red corresponds to 1.*

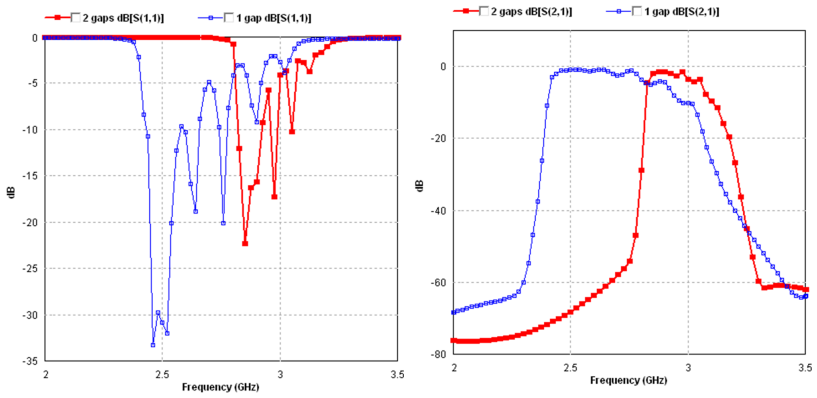


(a) Topology



(b) Antenna efficiency

Figure E.23. *Cascade of 8 CSRR cells with two gaps : (a) Topology, (b) Antenna efficiency extracted from simulation with IE3D assuming an infinite substrate with two gaps (in red, called "2 gaps"), illustrated in Fig. E.23(a) and a cascade of 8 CSRRs (in blue, called "1 gap") with one gap, illustrated in Fig. 4.1.*



(a) S_{11} parameter *(b)* S_{21} parameter

Figure E.24. *(a), (b) Comparison of S-parameters extracted from IE3D simulation assuming an infinite substrate for the left-hand band between a cascade of 8 CSRRs with two gaps (in red, called "2 gaps"), illustrated in Fig. E.23(a) and a cascade of 8 CSRRs (in blue, called "1 gap") with one gap, illustrated in Fig. 4.1.*

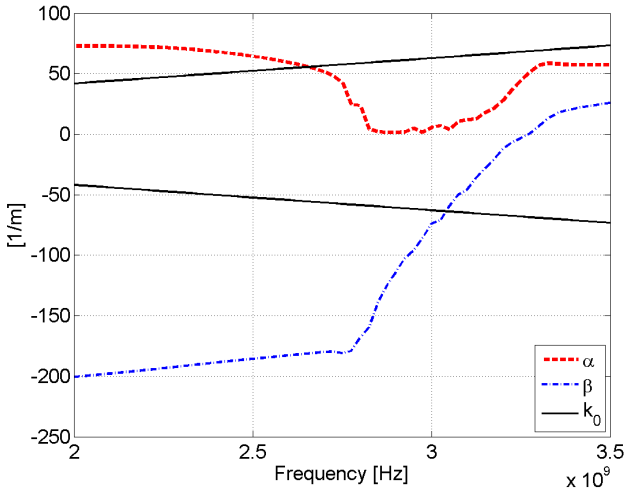
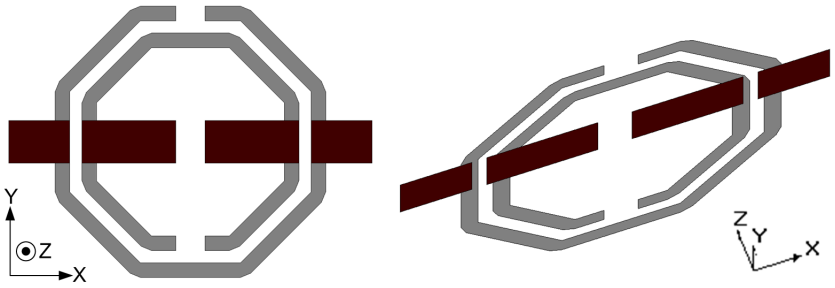
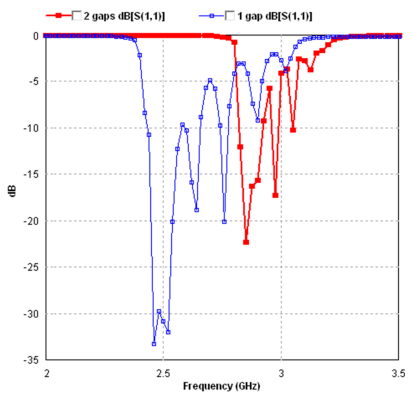


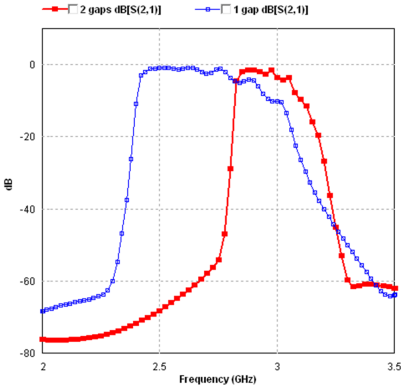
Figure E.25. *Propagation characteristics of a cascade of 8 CSRRs with two gaps, illustrated in Fig. E.23(a) and simulated with IE3D assuming an infinite substrate for the left-hand band.*



(a) Topology



(b) S_{11} parameter

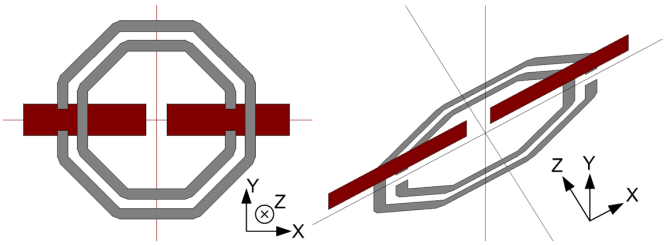


(c) S_{21} parameter

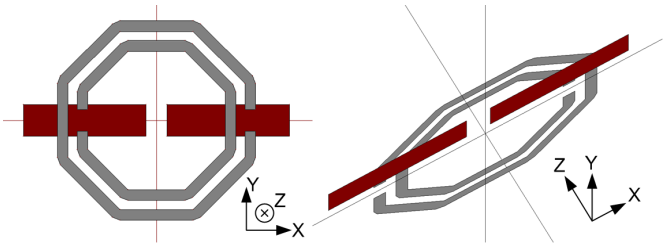
Figure E.26. *(a) Topology (the topology is the same than Fig. E.23(a), except that the two gaps are placed just above the ring) (b) Comparison of S-parameters extracted from IE3D simulation assuming an infinite substrate for the left-hand band between a cascade of 8 CSRRs with two gaps (in red, called "2 gaps"), illustrated in Fig. E.26(a) and a cascade of 8 CSRRs (in blue, called "1 gap") with one gap, illustrated in Fig. 4.1.*

E.9 ROTATION OF CSRR

The CSRR structure of Fig. 4.1 is rotated by 90° and -90°, the results are illustrated in Fig.E.27. S-parameters and the antenna efficiency are illustrated for the LH region in Fig.E.28 and compared to the CSRR structure presented in the third chapter with two rings. The radiation pattern, illustrated in Fig. E.29 for an angle of 90° and in Fig. E.30 for an angle of -90° for three frequencies of interest in the left leaky region. It is interesting to note that for an rotation angle of 90°, the radiation pattern is maximal in the broadside direction at the upper frequency of the left-leaky region. Fig. E.31 illustrates the distribution of eletric and magnetic current density and current vectors on metallic strip joining adjacent cells and rings for the magnetic and electric distribution. That explains the interesting behaviour of the radiation pattern for the rotation of 90, indeed all vectors are oriented in the same direction. So this structure is therefore a good candidate to be used for a LWA.



(a) Topology of a CSRR rotation by 90°



(b) Topology of a CSRR rotation by -90°

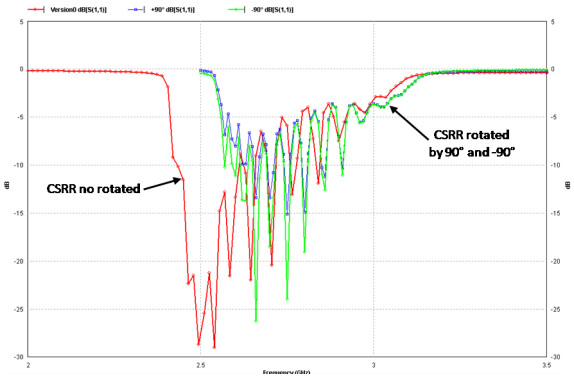
Figure E.27. *Rotation of CSRR (a) Topology with a rotation of 90°, (b) Topology with a rotation of -90°, the dimensions are described in Fig. 4.1.*

Bibliography

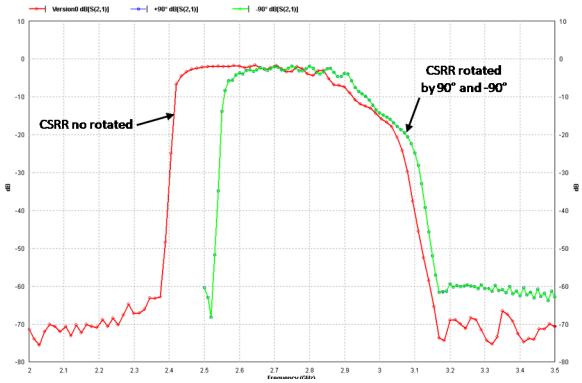
[1] M. S. R. Marques, F. Martin, *Metamaterials With Negative Parameters, Theory, Design and Microwave Applications.* Wiley, 2008.

[2] M. Sindreu, F. Aznar, A. Vélez, J. Bonache, and F. Martín, "Analysis and applications of osrr- and ocsrr-loaded transmission lines: A new path for the design of compact transmission line metamaterials," *Metamaterials (Elsevier)*, no. 4, 2010, pages =.

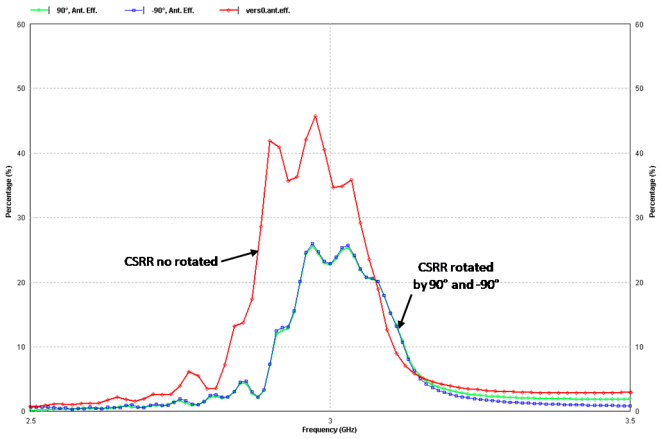
[3] R. Marques, F. Mesa, J. Martel, and F. Medina, "Comparative analysis of edge- and broadside- coupled split ring resonators for metamaterial design-theory and experiments," *IEEE Transactions on Antennas and Propagation*, vol. 51, no. 10, 2003, month =.



(a) $|S_{11}|$

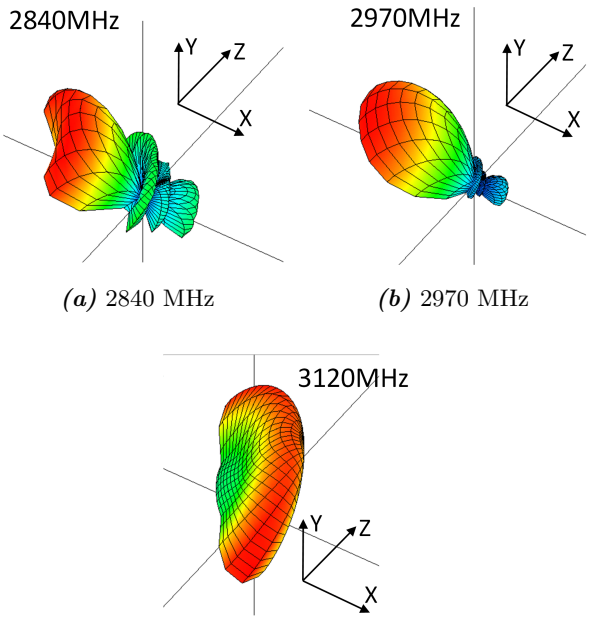


(b) $|S_{21}|$



(c) Antenna Efficiency *AF*

Figure E.28. *Comparison of S-parameters and antenna efficiency AF extracted from IE3D simulation assuming an infinite substrate for the left-hand band between a cascade of TL loaded by 8 CSRR rotated by 0°, 90° and -90°, presented in Fig. E.27.*

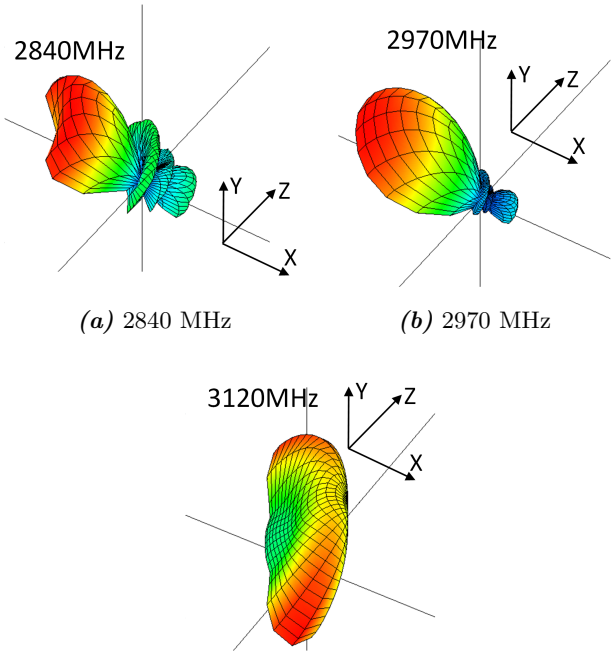


(a) 2840 MHz

(b) 2970 MHz

(c) 3120 MHz

Figure E.29. *Normalized 3D radiation pattern for the TL based on 8 cells of Fig. E.27(a) with a* ***CSRR cell rotated by 90°*** *simulated with IE3D software assuming an infinite substrate at 3 frequencies in the left-leaky region. Color bar: blue corresponds to zero, red corresponds to 1 : (a) 2.84 GHz, (b) 2.97 GHz, (c) 3.12 GHz.*



(a) 2840 MHz ***(b)*** 2970 MHz

(c) 3120 MHz

Figure E.30. *Normalized 3D radiation pattern for the TL based on 8 cells of Fig. E.27(b) with a* ***CSRR cell rotated by -90°*** *simulated with IE3D software assuming an infinite substrate at 3 frequencies in the left-leaky region. Color bar: blue corresponds to zero, red corresponds to 1 : (a) 2.84 GHz, (b) 2.97 GHz, (c) 3.12 GHz.*

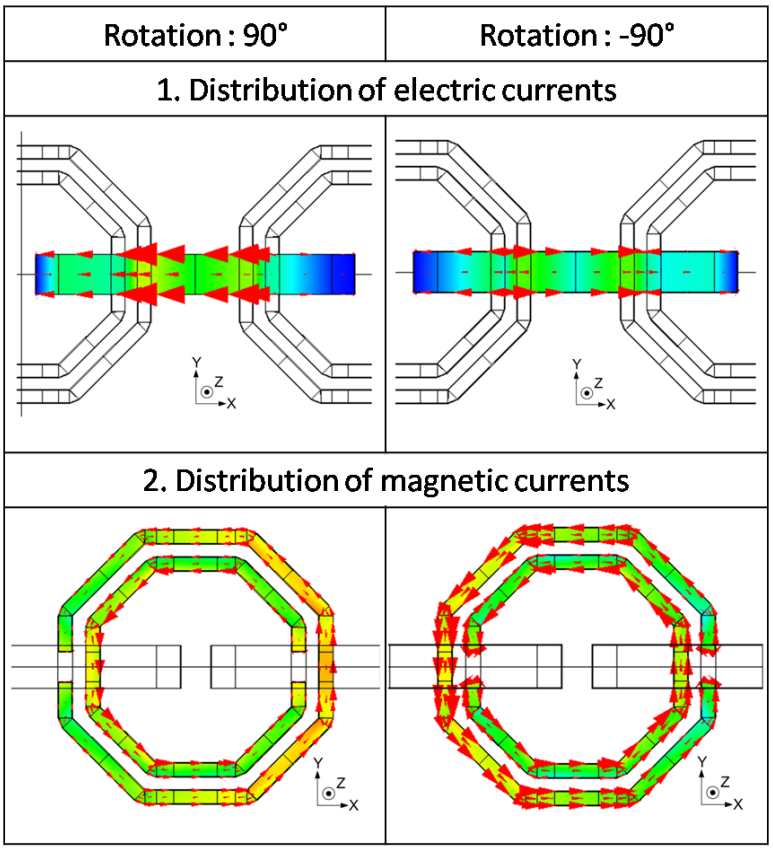


Figure E.31. *Comparison of the distribution of eletric and magnetic current density and current vectors on metallic strip joining adjacent cells and rings, simulated with IE3D assuming an infinite substrate at the upper frequency of the left-leaky region for two rotation angles. Color bar: current density is normalised with the maximum of the current on the upper metal level and is expressed in dB, blue color corresponds to lowest current density; red color corresponds to highest current density.*

APPENDIX F

RESULTS OF COMSOL SIMULATION

For a reason of thesis compactness, this annex presents the results of the COMSOL simulation of CSRR-loaded LWAs with one and two rings. Discrepancies between COMSOL simulation and measurements are explained by the influence of too simplified meshing, indeed the simulated structure must be long enough to radiate the main part of the energy, but it includes small dimensions around the CSRR. So for memory reasons, we had to accept to decrease the meshing characteristics of the simulation. That creates a shift in lower frequencies of the S-parameters, but globally the analysis of the propagation characteristics, and the radiation performances, presented in the next section, have presented quite the same behaviour except this frequency shift, so we have kept this simulation for the section of the physical explanation.

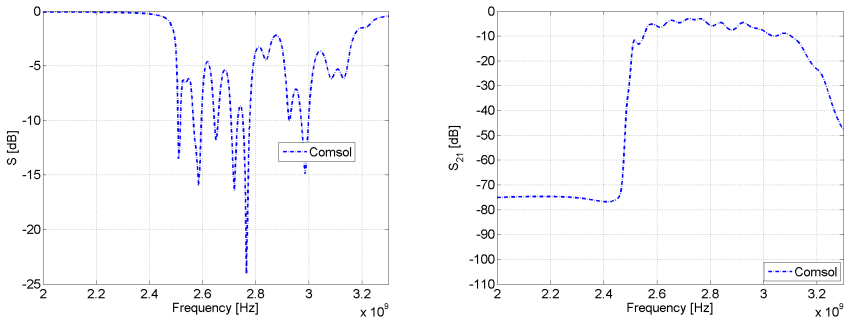
F.1 CSRR-LOADED LWAS WITH TWO RINGS

F.1.1 Left-leaky region

Fig. F.1 illustrates the COMSOL simulation for the left-hand band of the LWA created from a CRLH TL based on CSRRs. Fig. F.2 illustrates the leakage factor α and the propagation constant β of the equivalent TL, extracted from the S-parameters of the cascade of 16 cells similar to Fig. 4.1(c).

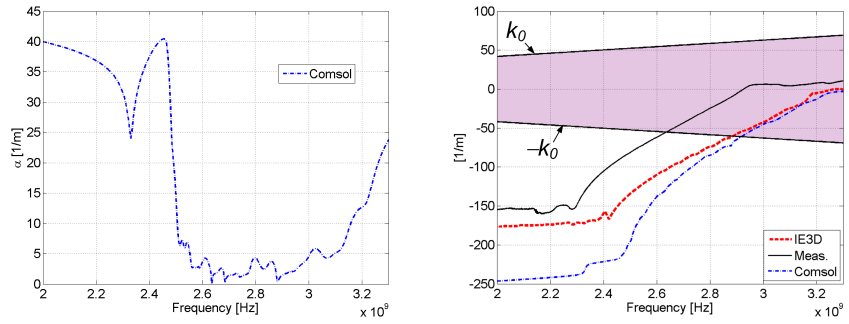
Fig. F.3 validates the behaviour of the radiation pattern with the COMSOL software. It shows 3D views of the radiation pattern at three illustrative frequencies of interest in the left-leaky region :

- The radiation pattern was first simulated at 2.9 GHz because it is the lowest frequency of the left-leaky region, corresponding to $\beta = -k_0$, therefore to θ_{MB} = -90° from (4.5).



(a) S_{11} *(b)* S_{21}

Figure F.1. *S-parameters of TL loaded by 16 CSRRs of Fig. 4.1 simulated with COMSOL (blue dashdot) in the left-hand band. This figure must be compared to Fig. 4.3.*



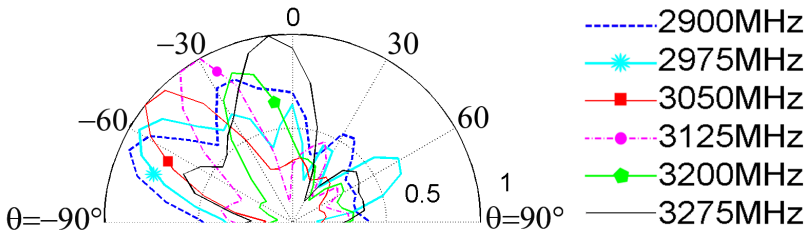
(a) Leakage factor α *(b)* Propagation constant β

Figure F.2. *Propagation characteristics as calculated from the S-parameters shown in Fig. F.1 using eqs. 4.4 and 4.3 of the TL loaded by 16 CSRRs depicted in Fig. 4.1. The calculations shown pertain to the COMSOL case (blue dashdot) in the left-hand band. The magenta area represents the radiation cone defined by the free-space propagation constant k_0. This figure must be compared to Fig. 4.4.*

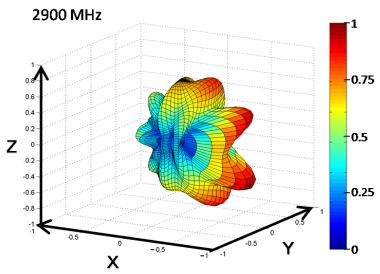
- Secondly 3.05 GHz was used because this frequency is in the middle of the left-leaky region.

- Finally 3.275 GHz was used because this frequency is the upper frequency of the left-leaky region, corresponding to $\beta = 0$, therefore to $\theta_{\mathsf{MB}} = 0°$ from (4.5).

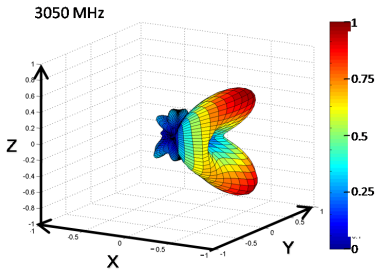
It is clear that the full-wave simulator based on finite substrate predicts a significantly different radiation pattern in the $\theta = 0°$ Y-Z plane. However the splitting into two different directions resulting into two apparent beams is ***predicted by both IE3D and COMSOL softwares***.



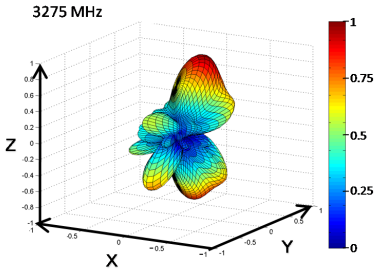
(a) Normalized 2D radiation pattern



(b) 2900MHz ($\beta = -k_0$)



(c) 3050MHz

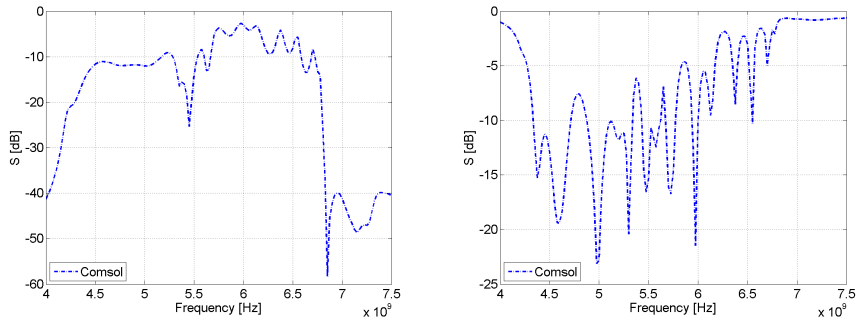


(d) 3275MHz ($\beta \approx 0$)

Figure F.3. *Normalized 2D and 3D radiation pattern for the TL based on 16 cells of Fig. 4.1(a) simulated with COMSOL solver at 3 frequencies in the left-leaky region. Color bar: blue corresponds to the minimum, red corresponds to the maximum.*

F.1.2 Right-leaky region

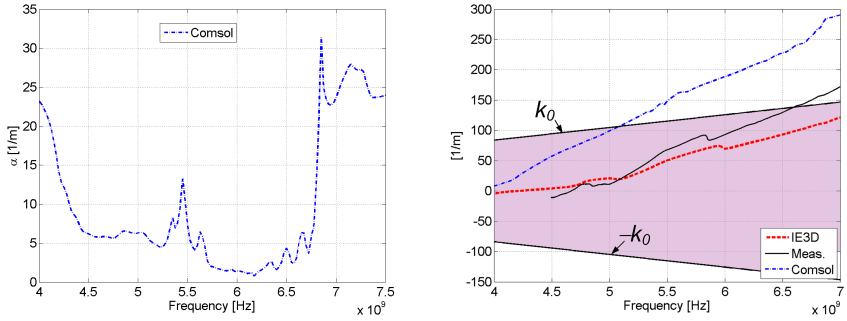
Fig. F.4 illustrates the COMSOL simulation for the right-hand band of the LWA created from a CRLH TL based on CSRRs. Fig. F.5 illustrates the leakage factor α and the propagation constant β of the equivalent TL, extracted from the S-parameters of the cascade of 16 cells similar to Fig. 4.1(c).



(a) S_{21} *(b)* S_{11}

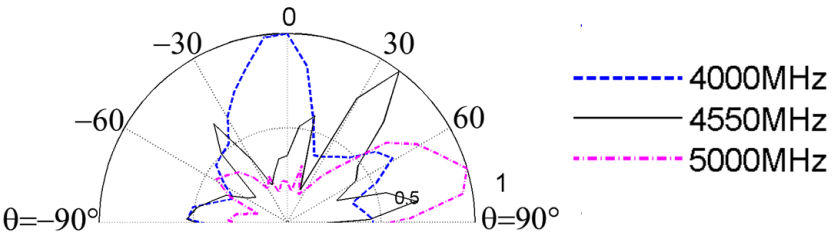
Figure F.4. *S-parameters of TL loaded by 16 CSRRs of Fig. 4.1 simulated with COMSOL (blue dashdot) in the right-hand band. This figure must be compared to Fig. 4.4.*

The same analysis of radiation pattern is presented using the COMSOL simulation in Fig. F.6. This approach agrees on a frequency scanning ability in the right-hand region.

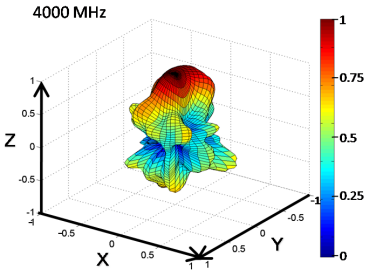


(a) α *(b)* β

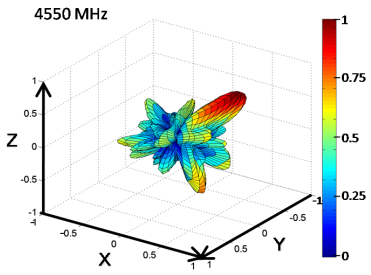
Figure F.5. *Propagation characteristics as calculated from the S-parameters shown in Fig. F.4 using eqs. 4.4 and 4.3 of the TL loaded by 16 CSRRs depicted in Fig. 4.1. The calculations shown pertain to the measured case (black solid), the IE3D case (red dashed) and the COMSOL case (blue dashdot) in the right-hand band. The magenta area represents the radiation cone defined by the free-space propagation constant* k_0*. This figure must be compared to Fig. F.5.*



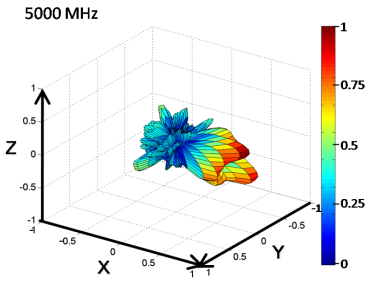
(a) Normalized 2D radiation pattern



(b) 4000 MHz ($\beta = 0$)



(c) 4550 MHz



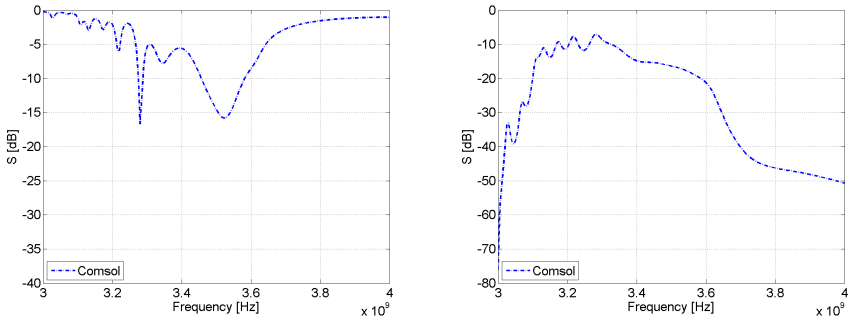
(d) 5000 MHz ($\beta = k_0$)

Figure F.6. *Normalized 2D and 3D radiation pattern for the TL based on 16 cells of Fig. 4.1(a) simulated with COMSOL at 3 frequencies in the right-leaky region. Color bar: blue corresponds to zero, red corresponds to 1.*

F.2 CSRR-LOADED LWAS WITH ONE RING

F.2.1 Left-leaky region

Fig. F.7 shows the S-parameters performed with COMSOL solver. The propagation characteristics are extracted from S-parameters by the methodology explained in section 4.2. Fig. F.11 shows the leakage factor α and the propagation constant β of the equivalent TL, extracted from the S-parameters simulated for the cascade of 16 cells similar to Fig. 4.1(c). We can now analyse the radiation pattern in the right-leaky region. From these propagation characteristics, the leakage radiation appears to occur between 3.3 GHz and 3.71 GHz for the case of the COMSOL solver.

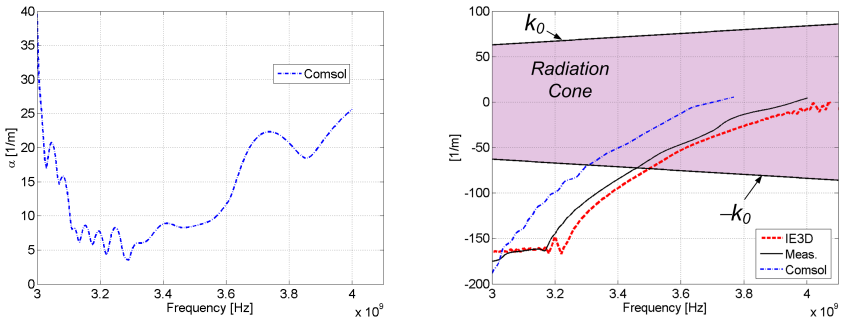


(a) S_{11} *(b)* S_{21}

Figure F.7. *S-parameters of TL loaded by 16 CSRRs with one ring of Fig. 4.50 in the left-hand band simulated with COMSOL (blue dashdot). This figure must be compared to Fig. 4.52.*

Fig. 4.55(a) shows corresponding 2D views of the simulated radiation pattern in the (ϕ = 0°) X-Z plane, demonstrating their frequency scanning capability. In accordance with Fig. 4.53(b) and with equation 4.5, the main beam scanning occurs from θ = -90° to θ = 0° with increasing frequency in the left-leaky region. Indeed, the qualitative agreement between Fig. 4.55(a), Fig. F.9(a) and Fig. 4.55(b) is very good, especially given that there is always inherently a frequency shift between measurements and simulation due to fabrication tolerances and meshing influence.

In order to facilitate the comparison with radiation patterns of CSRRs with two split rings, the simulated 3D radiation pattern is shown in Fig. F.9 for three frequencies in the left-leaky region region. The results derived from the IE3D software differ with the results derived from the COMSOL solver for the radiation pattern in the (ϕ = 90°) X-Y plane, due to the impact of infinite



(a) Leakage factor α *(b)* Propagation constant β

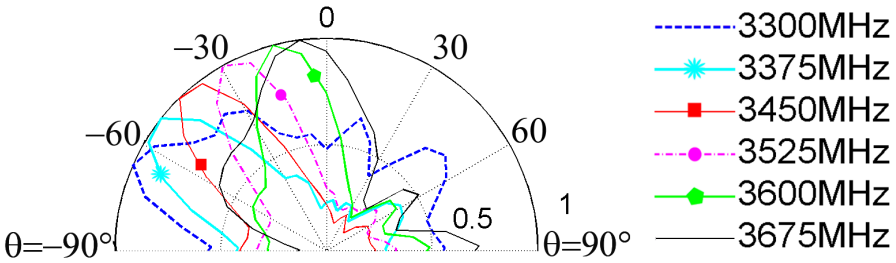
Figure F.8. *Propagation characteristics as calculated from the S-parameters shown in Fig. 4.52 in the left-hand band using eqs. 4.4 and 4.3 of the TL loaded by 16 CSRRs with one split ring depicted in Fig. 4.50. The calculations shown pertain to the COMSOL case (blue dashdot) in the left-hand band. The magenta area represents the radiation cone defined by the free-space propagation constant k_0. This figure must be compared to Fig. 4.53.*

substrate. However, globally the leaky wave behaviour is the same and in fact the antenna behaves like the classical leaky antenna introduced in the chapter 3.

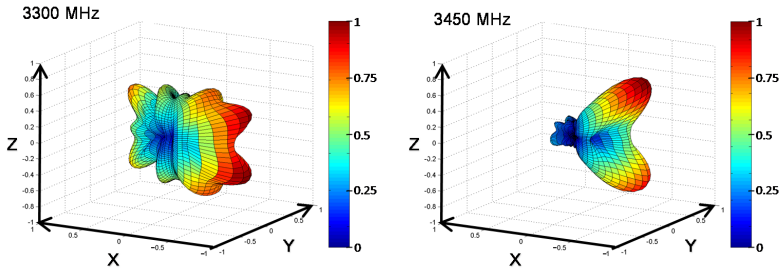
F.2.2 Right-leaky region

Fig. F.10 shows the S-parameters performed with COMSOL solver. The propagation characteristics are extracted from S-parameters by the methodology explained in section 4.2. Fig. F.11 shows the leakage factor α and the propagation constant β of the equivalent TL, extracted from the S-parameters simulated for the cascade of 16 cells similar to Fig. 4.1(c). We can now analyse the radiation pattern in the right-leaky region. From the radiation cone, the right-leaky region is determined to be between 4.325 GHz and 5.85 GHz for COMSOL simulation.

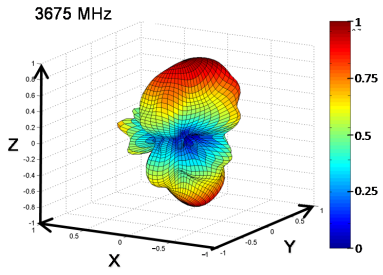
The simulated radiation patterns are shown in Fig. F.12 in the ($\phi = 0°$) X-Z plane to verify the frequency scanning from $\beta = 0$ (where the main beam is oriented in the broadside direction of Fig. 4.1(c)) to $\beta = k_0$ (where the main beam is oriented in the endfire direction of Fig. 4.1(c)). The COMSOL results of 3D radiation pattern are shown in the appendix C)



(a) Normalised 2D radiation pattern

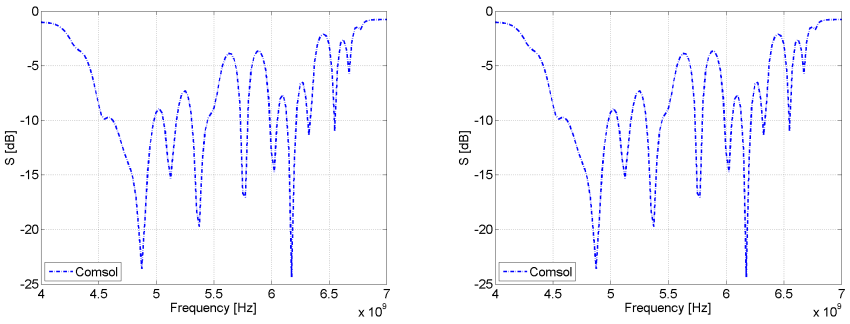


(b) 3300MHz *(c)* 3450MHz



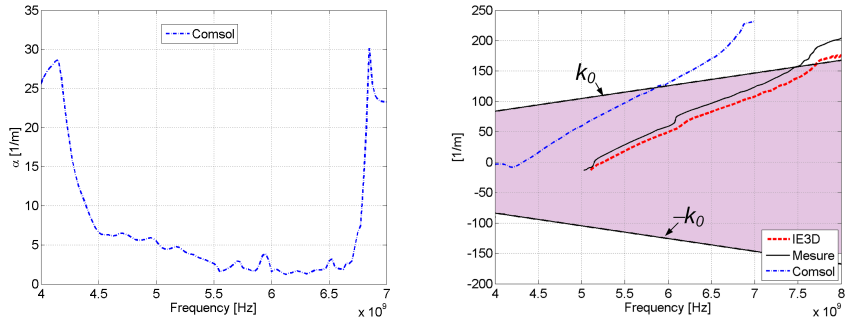
(d) 3675MHz

Figure F.9. *Normalized 2D and 3D radiation pattern for the TL based on 16 cells similar to the one depicted in Fig. 4.51(a) simulated with COMSOL at 3 frequencies in the left-leaky region. Color bar: blue corresponds to the minimum, red corresponds to the maximum.*



(a) S_{11} ***(b)*** S_{21}

Figure F.10. *S-parameters of TL loaded by 16 CSRRs with one ring of Fig. 4.50 in the right-hand band simulated with COMSOL (blue dashdot). This figure must be compared to Fig. 4.52.*



(a) Leakage factor α ***(b)*** Propagation Constant β

Figure F.11. *Propagation characteristics as calculated from the S-parameters shown in Fig. 4.52 in the right-hand band using eqs. 4.4 and 4.3 of the TL loaded by 16 CSRRs with one split ring depicted in Fig. 4.50. The calculations shown pertain to the COMSOL case (blue dashdot) in the right-hand band. The magenta area represents the radiation cone defined by the free-space propagation constant k_0. This figure must be compared to Fig. 4.53.*

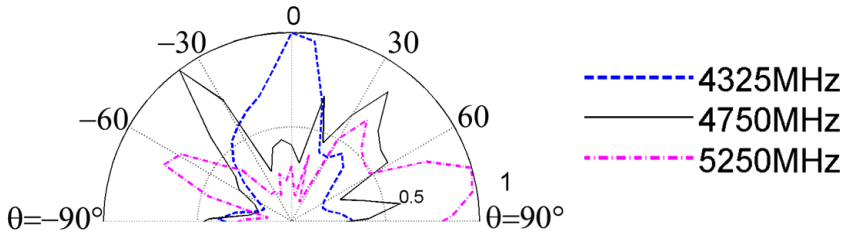


Figure F.12. *Normalized 2D radiation pattern in ($\phi = 0°$) X-Z plane for the TL based on 16 cells similar to the one depicted in Fig. 4.50(a) simulated with COMSOL for different frequencies in the right-leaky region.*

APPENDIX G

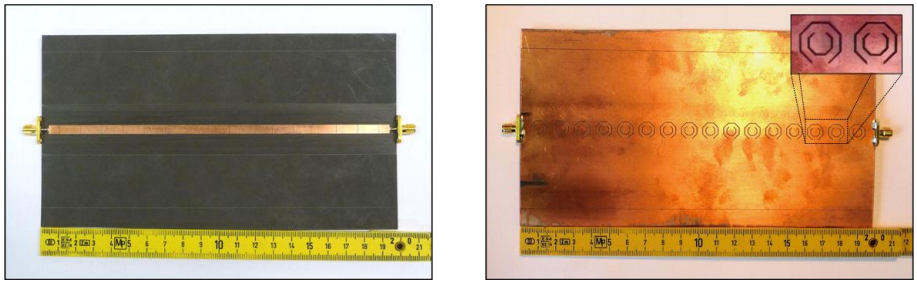
BALANCED CSRR-BASED LWA WITH TWO RINGS

This annex presents the analysis realised on an balanced metamaterial LWA based on CSRR with two rings.

G.1 TOPOLOGY AND PROPAGATION CHARACTERISTICS

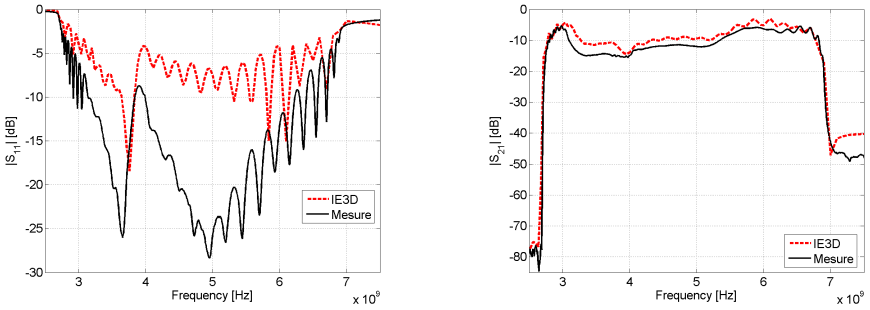
Using the method described in the section 4.5.3.3, a balanced structure with two rings is also realized. Due to fabrication tolerances, the width C of the slot and the outer radius R_{out} of the ring are also fixed respectively to 0.5 mm and 5 mm. The aim is to decrease the lower frequency of the RH region and to decrease the higher frequency of the LH band. A high value of W and of D, a low value of G and χ_1 would cause a decrease in the stop-band. After optimisation, the results are shown in Fig. G.3.

Setup Environment : *S-parameters are simulated with the IE3D software (with the assumption of infinite substrate and ground planes) and are measured using a Agilent PNA-X N5242A Vector Network Analyser and a 40 GHz Universal Test Fixture. The calibration is realised with an N4691-60006 Agilent Electronic Calibration (ECal) Module based on a SOTL technique (Short Open Through Line) [1]. Fig. G.2 illustrates the comparison between simulation and experimental results for the left-hand and right-hand bands of the LWA created from a CRLH TL based on CSRRs.*



(a) Front Face *(b)* Back Face

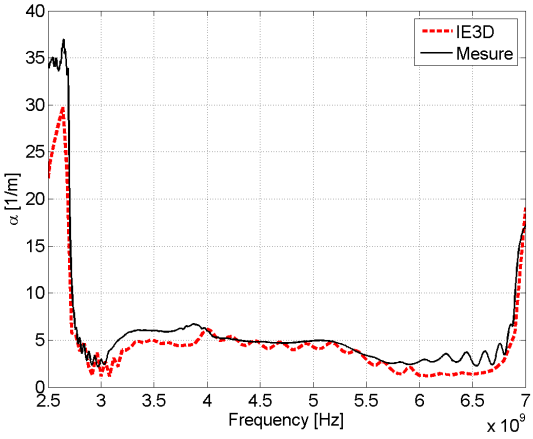
Figure G.1. *Photos of the cascade of 16 cells, corresponding to the layout described in Fig. G.3. (a) : strip metal and (b) : ground plane (antenna length = 20cm).*



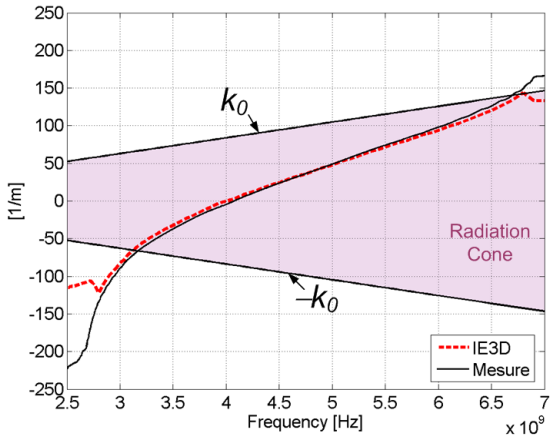
(a) S_{11} *(b)* S_{21}

Figure G.2. *S-parameters of the TL loaded by 16 CSRRs of Fig. G.3 measured (black solid), simulated with IE3D (red dashed) in left-hand and right-hand bands.*

The leakage factor is extracted from 4.3 in Fig. G.3(a) and the propagation constant is extracted from 4.4 in Fig. G.3(b). The propagation characteristics exhibit a continuous transition between left and right leaky bands, giving rise to the suppression of the gap in the scanning range. From the radiation cone, the full-space leaky region is determined to be between 3.17 GHz and 6.7 GHz for IE3D simulation and between 3.12 GHz and 6.8 GHz for the measurements.



(a) Leakage factor α



(b) Propagation constant β

Figure G.3. *Propagation characteristics as calculated from the S-parameters shown in Fig. G.2 using eqs. 4.4 and 4.3 of the TL loaded by 16 CSRRs depicted in Fig. G.3. The calculations shown pertain to the measured case (black solid) and the IE3D case (red dashed) in the left-hand and right-hand bands. The magenta area represents the radiation cone defined by the free-space propagation constant* k_0.

G.2 RADIATION PERFORMANCE

IE3D software is used to simulate the 3D radiation pattern of the TL based on the 16 cells from Fig. 4.62 in the leaky region. Fig. 5.33(a) shows corresponding 2D views of the simulated radiation pattern for the leaky region in the ($\phi = 0°$) X-Z plane, validating the continuous frequency beam scanning for both leaky regions without stopband. In order to confirm the beneficial nature of this behaviour, Fig. G.4 shows 3D views of the simulated radiation pattern at three illustrative frequencies of interest in the leaky region.

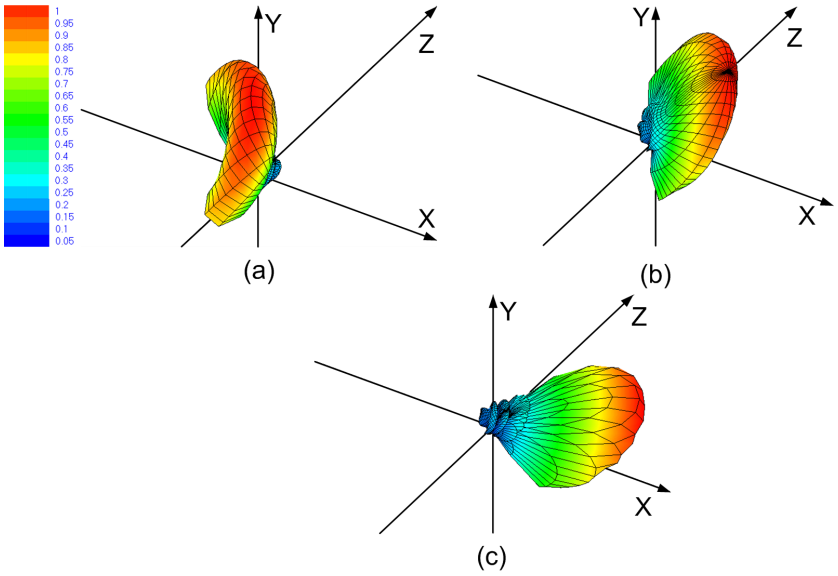


Figure G.4. *Normalized 3D radiation pattern for the TL based on 16 cells of Fig. 5.32(a) simulated with IE3D software assuming an infinite substrate at 3 frequencies in the leaky region. Color bar: blue corresponds to zero, red corresponds to 1 : (a) 3.44 GHz, (b) 3.92 GHz, (c) 4.84 GHz.*

A representation of the distribution of current density and current vectors on metallic strip joining adjacent cells, simulated with IE3D assuming an infinite substrate, is given in Fig. G.5 at the upper frequency of the left-hand broadside. Inspection of this figure reveals that, unlike the case of unbalanced CSRR with two split rings, no symmetry of current vectors is present. Indeed, all current vectors are oriented in the same direction along x-axis.

Setup Environment : *To confirm this prediction, the radiation patterns are also measured from transmission measurements between a an HL024A1-S1 Rohde & Schwarz Crossed Log-Periodic Antenna and the antenna under test with the same VNA (used to extract the propagation*

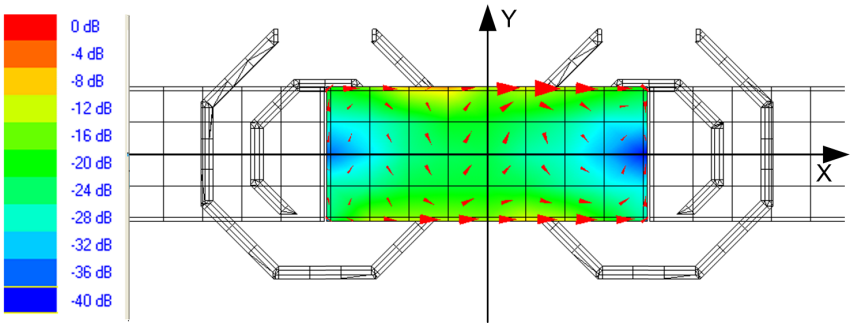


Figure G.5. *Zoom of distribution of current density and current vectors on metallic strip joining adjacent cells, simulated with IE3D assuming an infinite substrate at 3.92 GHz, which is the upper frequency of the left-leaky region and the lower frequency of the right-leaky region (Fig. G.4). Color bar: current density is normalised with the maximum of the current on the upper metal level (maximal current density : 55.788 A/m) and is expressed in dB, blue color corresponds to lowest current density; red color corresponds to highest current density.*

characteristics) in an anechoic chamber. The set-up is described in the section 4.2.2. The characteristics of the horn antenna are de-embedded following the methodology presented in [2]. |

Measured radiation patterns for the same structure are shown at three frequencies corresponding to :

- **backward** radiation angles : Fig. G.7,
- **broadside** radiation angles: Fig. G.8,
- **forward** radiation angles: Fig. G.9.

Good agreement can be observed between measurement and simulation predictions. As predicted by the simulated distribution current and explained in [3], the balanced condition suppresses the resonance effect of the LH cell, allowing for radiation in the broadside direction.

Tunable ferrolectric LWA based on one ring : We have used this cascade of 16 cells with lumped diodes as described in the section 4.4.4.1 with the kind of varactors SMV1232 [4] to verify the concept of an electrically tunable LWAs based on CSRR. A DC bias voltage from 0 to 40 V has been used to modify the serie capacitor of the CSRR cell. Full-wave simulation and measurement of S-parameters have demonstrated the influence of the serie capacitor on the S-parameters in the left and right-hand regions. Unfortunately, contrary to the prediction o the COMSOL solver, the measurement in the anechoic chamber has not presented the expected scanning at a fixed frequency scanning in the left-hand region, the reason is probably that the resonance frequency of the varactors was too low, so the concept is not yet validated.

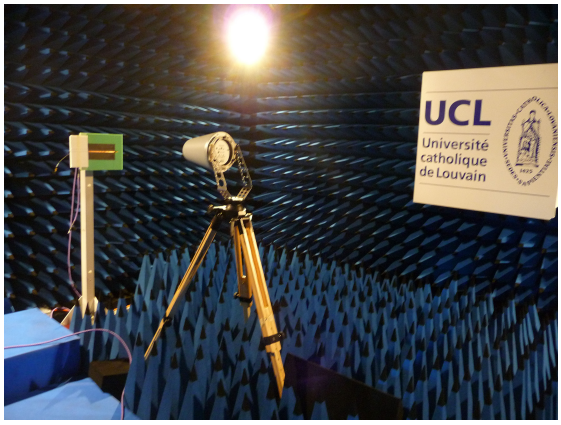


Figure G.6. *Photos of the measurement set-up in the UCL anechoic chamber (on the left, antenna under test with the swivelling table inside the anechoic chamber and on the right, HL024A1-S1 Rohde & Schwarz Crossed Log-Periodic Antenna.*

Bibliography

[1] *Agilent AN 1287-3 Applying Error Correction to Network Analyzer Measurements, Application Note*, Agilent Technologies, USA, Mar. 2002.

[2] C. Balanis, *Antenna Theory, 3rd edition.* Wiley, 2005.

[3] C. Caloz and T. Itoh, *Electromagnetic metamaterial : Transmission line and microwave applications.* Wiley, 2006.

[4] Skyworks, *SMV123x Series: Hyperabrupt Junction Tuning Varactors, datasheet*, Oct. 2009.

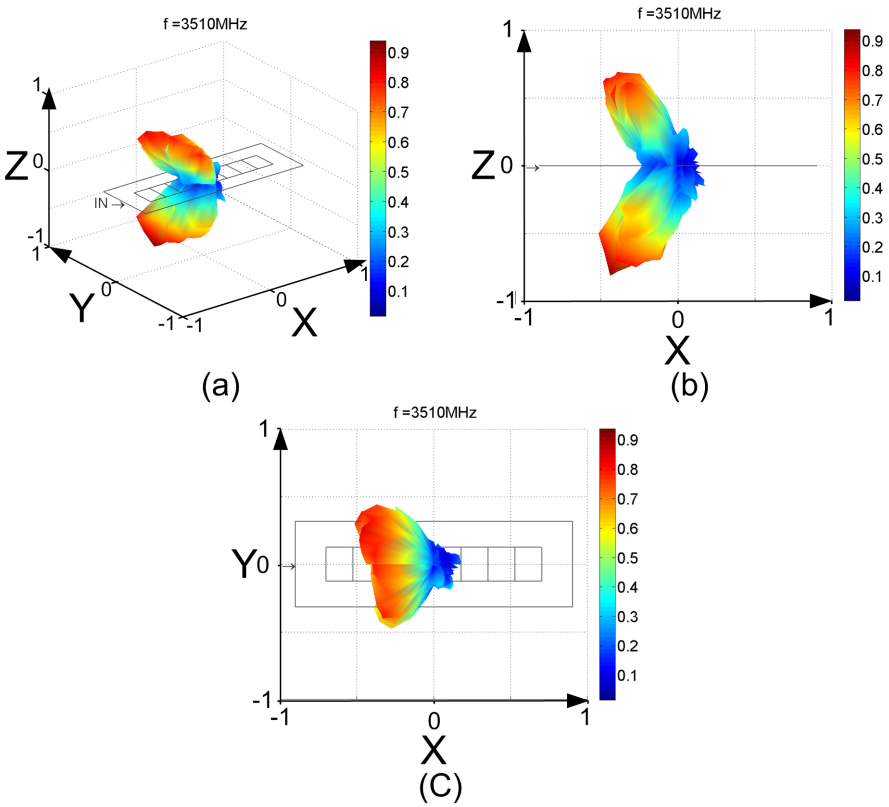


Figure G.7. *(a) 3D view, (b) 3D view of ($\phi = 0°$) X-Z plane and (c) 3D top view along the z-axis (c) of measurement of normalised radiation pattern of Fig. G.1 at 3.51 GHz, corresponding to a frequency in the middle of the left-leaky region. Color bar: dark blue corresponds to zero, dark red corresponds to 0.9.*

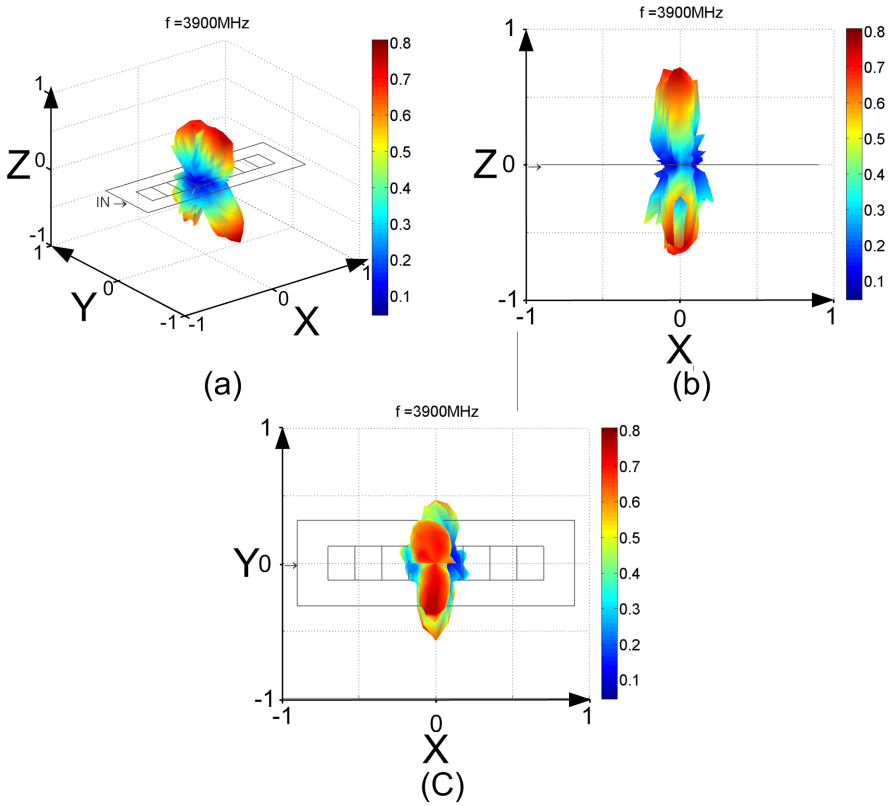


Figure G.8. *(a) 3D view, (b) 3D view of ($\phi = 0°$) X-Z plane and (c) 3D top view along the z-axis (c) of measurement of normalised radiation pattern of Fig. G.1 at 3.9 GHz, corresponding to a frequency corresponding to the broadside direction of the leaky region. Color bar: dark blue corresponds to zero, dark red corresponds to 0.8.*

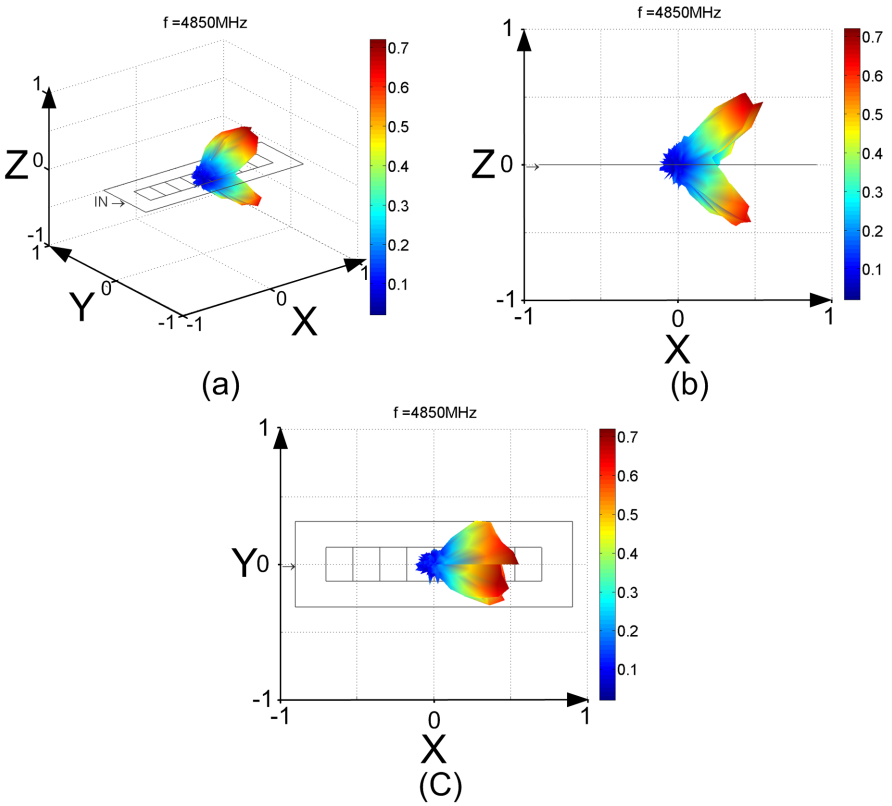


Figure G.9. *(a) 3D view, (b) 3D view of ($\phi = 0°$) X-Z plane and (c) 3D top view along the z-axis (c) of measurement of normalised radiation pattern of Fig. G.1 at 4.85 GHz, corresponding to a frequency in the middle of the right-leaky region. Color bar: dark blue corresponds to zero, dark red corresponds to 0.7.*